University of Wollongong

Research Online

University of Wollongong Thesis Collection 2017+

University of Wollongong Thesis Collections

2018

Evolution of microstructure and texture during deformation and annealing of transformation-induced plasticity high Mn steel

Sudipta Pramanik
University of Wollongong

Follow this and additional works at: https://ro.uow.edu.au/theses1

University of Wollongong

Copyright Warning

You may print or download ONE copy of this document for the purpose of your own research or study. The University does not authorise you to copy, communicate or otherwise make available electronically to any other person any copyright material contained on this site.

You are reminded of the following: This work is copyright. Apart from any use permitted under the Copyright Act 1968, no part of this work may be reproduced by any process, nor may any other exclusive right be exercised, without the permission of the author. Copyright owners are entitled to take legal action against persons who infringe their copyright. A reproduction of material that is protected by copyright may be a copyright infringement. A court may impose penalties and award damages in relation to offences and infringements relating to copyright material. Higher penalties may apply, and higher damages may be awarded, for offences and infringements involving the conversion of material into digital or electronic form.

Unless otherwise indicated, the views expressed in this thesis are those of the author and do not necessarily represent the views of the University of Wollongong.

Recommended Citation

Pramanik, Sudipta, Evolution of microstructure and texture during deformation and annealing of transformation-induced plasticity high Mn steel, Doctor of Philosophy thesis, School of Mechanical, Materials, Mechatronic and Biomedical Engineering, University of Wollongong, 2018.
https://ro.uow.edu.au/theses1/388

Research Online is the open access institutional repository for the University of Wollongong. For further information contact the UOW Library: research-pubs@uow.edu.au

UNIVERSITY
OF WOLLONGONG
AUSTRALIA

School of Mechanical, Materials, Mechatronic and Biomedical Engineering
Faculty of Engineering and Information Sciences

Evolution of microstructure and texture during deformation and annealing of transformation-induced plasticity high Mn steel

Sudipta Pramanik, B.E, M.E

This thesis is presented as a part of the requirement for the award of the degree of
Doctor of Philosophy
University of Wollongong

October 2018

Table of Contents

Certificate

I, Sudipta Pramanik, state that the present thesis, submitted by me for the partial fulfilment for the requirements of the award of Doctor of Philosophy, in the School of Mechanical, Materials, Mechatronic and Biomedical Engineering, Faculty of Engineering and Information Sciences, University of Wollongong, is solely my work unless otherwise acknowledged or referenced. This thesis has not been submitted for qualifications of any degree at any other academic institution.

Sudipta Pramanik

October 2018

Abstract

An as-cast Fe-17Mn-3Al-2Si-1Ni-0.06C (wt. %) high Mn steel slab was subjected to hot rolling to 52% thickness reduction and quenched to room temperature. Thereafter, the hot-rolled plate was plane strain compressed to 5, 10, 15 and 20% thickness reductions at room temperature and cold-rolled to a further 42, 66 and 88% thickness reductions. The samples after 42% cold rolling were isochronally annealed at 500, 600, 625, 650, 700, 750, 800 and 850 °C for 300 s.

Microstructure characterisation was undertaken via electron back-scattering diffraction (EBSD), conventional, high-resolution scanning and in-situ transmission electron microscopy (TEM). Mechanical behaviour was investigated using a combination of uniaxial tensile testing and digital image correlation on dog-bone samples after 42% cold rolling and annealing at 500, 625, 650, 700 and 800 °C.

The hot-rolled microstructure comprised coarse, polygonised γ grains with annealing twins and ε-martensite plates within γ grains and lenticular α′-martensite within ε-martensite plates that formed on quenching after annealing. Between 5 and 20% thickness reductions the formation of deformation-induced ε-martensite at γ stacking faults and α′-martensite at the intersection of ε-martensite plates took place. $\{10\bar{1}2\}\langle\bar{1}011\rangle_{\varepsilon}$ extension twins were also observed in ε-martensite. Between 42 and 88% thickness reductions, the microstructure consisted of predominantly α′-martensite with a small fraction of ε-martensite and a trace of γ.

For the 5 and 10% thickness reduction conditions, high-resolution scanning transmission electron microscopy showed that the growth of ε-martensite occurs via lateral coarsening and coalescence with neighbouring ε-martensite laths. This thesis provided first-hand experimental evidence of the deformation accommodation in ε-martensite by a combination of perfect and partial basal slip (I_1 and I_2 ε-ISFs), pyramidal slip, $\{10\bar{1}2\}\langle\bar{1}011\rangle_{\varepsilon}$ extension twinning and a change in ε-ISFs character from I_2 to I_1-types. With respect to the latter, the mechanism for the change in ε-ISF character type was proposed.

In-situ heating in TEM of the 42% cold-rolled sample to 900 °C showed no changes to the initial ε or α′-martensite grain shape on their transformation to γ or the motion of the ε-martensite/γ or α′-martensite/γ interfaces during reversion; all of which is indicative of displacive transformation. The subsequent recovery of γ grains previously reverted from ε-martensite resulted in the formation of fine twins.

The microstructure of 500 °C sample comprised α′-martensite and γ reverted from ε-martensite. Annealing at 600, 625 and 650 °C resulted in the reversion of α′-martensite and this process is concurrent with the recrystallisation and growth of previously reverted γ grains. The formation of new γ grains takes place at the boundaries of two reverted γ grains. The γ recrystallisation was completed after annealing at 700 °C. Annealing between 750 and 850 °C led to γ grain growth via grain boundary diffusion with an activation energy of 235.2 ± 17.6 kJ/mol. On quenching after

annealing between 700 and 850 °C, the formation of ε-martensite plates within γ grains and lenticular α′-martensite within ε-martensite plates took place.

Irrespective of the processing condition, γ orientations on the α-fibre ($\langle 110\rangle_{\gamma}||$ND) transform to ε-martensite orientations along the $\{hkil\}_{\varepsilon}$-fibre and α′-martensite orientations along the α-fibre ($\langle 110\rangle_{\alpha'}||$RD) via the Shoji-Nishiyama, Kurdjumov-Sachs and Burgers orientation relationships defined as $\{111\}_{\gamma} \;||\; \{0001\}_{\varepsilon} \;||\; \{110\}_{\alpha'}$ and $\langle 110\rangle_{\gamma} \;||\; \langle 11\bar{2}0\rangle_{\varepsilon} \;||\; \langle 111\rangle_{\alpha'}$, respectively. The above orientation relationships were observed by both EBSD and TEM.

For the 42% cold-rolled and 500 °C conditions, EBSD maps before and after uniaxial tension was similar and comprised elongated and fragmented α′-martensite as the dominant phase with remnant ε-martensite and a trace amount of untransformed γ. In the case of the 625 and 700 °C conditions, uniaxial tension resulted in the transformation of reverted and recrystallised γ into fine and coarse deformation-induced α′-martensite via ε-martensite. This process was associated with the observed strain localisation along the gauge length. The true stress-strain curves showed: (i) a linear increase in stress with strain for the 625 and 650 °C conditions and, (ii) a slowly rising stress region for the 700 and 800 °C conditions in addition to the initial linear rising stress regions. $\{10\bar{1}2\}\langle\bar{1}011\rangle_{\varepsilon}$ extension twinning was also observed in ε-martensite. The samples annealed at 625 and 650 °C exhibited the best mechanical properties with the yield stress of 810 and 732 MPa, the ultimate true tensile strengths of 1237 and 1259 MPa and uniform true elongation values of 0.23 and 0.26, respectively. The fracture surfaces showed a mixture of ductile and brittle fracture modes after 42% cold rolling and annealing at 500 °C and ductile fracture mode after annealing at 625 and 700 °C.

Acknowledgements

I would like to thank my supervisors, Prof. Elena V. Pereloma and Dr. Azdiar A. Gazder for teaching, helping and assisting me with my PhD work and for providing me with a PhD scholarship.

I acknowledge Dr. Azdiar A. Gazder for training me in all aspects of sample preparation for SEM and TEM work including the development of new electrolytes and polishing conditions; for providing training on the JEOL JSM-7001F FEG-SEM, the EBSD of bulk and thin cross-section samples which are techniques that he developed, and for teaching me EBSD data and texture analysis. Dr. Ahmed A. Saleh is acknowledged for his help in the analysis of the EBSD and mechanical properties data.

I acknowledge Drs. David R. G. Mitchell and Gilberto Casillas-Garcia for training me on the JEOL JEM-ARM 200F and JEOL JEM-2010 transmission electron microscopes and for their training and help in data analysis.

I acknowledge Dr. David R. G Mitchell and Prof. Elena V. Pereloma for carrying out the in-situ TEM heating experiments at the University of Sydney. The use of the JEOL JEM-2200FS and the scientific and technical assistance of Dr. Hongwei Liu of the Australian Microscopy & Microanalysis Research Facility at the ACMM, University of Sydney is acknowledged.

Dr. Bradley Davis is acknowledged for helping to carry out the digital image correlation experiments during tensile testing. Thanks to Dr. Liang Chen for conducting the Gleeble 3500 thermomechanical simulator experiments. I am also grateful to Prof. D.B. Santos of the Universidade Federal de Minas Gerais, Brazil for providing the material for this research.

I am very grateful to Dr. Azdiar A. Gazder for re-writing the three journal papers and one conference paper that were submitted for publication review and form the major sections of three chapters of this thesis (Refs. 1-3 and 5 in the list of publications arising from this thesis). I thank Prof. Elena V. Pereloma and Dr. David R.G. Mitchell for re-writing the fourth paper which also forms a chapter in this thesis (Ref. 4 in the list of publications arising from this thesis). Furthermore, I thank Prof. Elena V. Pereloma, Dr. Azdiar Gazder and Dr. Ahmed A. Saleh for making further revisions by re-writing sub-sections in all papers upon review as well as proof reading the final accepted version of all papers before publication. I am also very grateful to Prof. Pereloma for all support and advice provided in writing and revising this thesis.

This research was supported by the Australian Research Council-Discovery Project grant DP130101882. The use of JEOL JEM-2010, JEOL JEM-ARM200F and JEOL JSM-7001F is acknowledged that were purchased from funds by Australian Research Council-Linkage, Infrastructure, Equipment and Facilities grants LE0237478, LE120100104 and LE0882613, respectively.

List of Figures

and 2 in Fig. 4.2d are magnified views of regions highlighted by white dashed rectangle 1 and 2, correspondingly.

Figure 4.3: Superimposed band contrast and phase maps after thickness reduction to (a) 20%, (b) 42%, (c) 66% and (d) 88%. Red = γ, green = ε-martensite, blue = α′-martensite, white = unindexed areas, silver = low-angle grain boundaries, black = high-angle grain boundaries, yellow = γ twin boundaries. Rolling direction (RD) = horizontal. Insets 1-3 in Figs. 4.2e are magnified views of regions highlighted by white dashed rectangle 1-3, correspondingly.

Figure 4.4: Misorientation angle distributions of (a) γ, (b) ε-martensite and (c) α′-martensite with thickness reduction up to 88%.

Figure 4.5: Representative bright-field transmission electron micrographs after (a) hot rolling and thickness reduction to (b) 10%, (c, d) 15% and (e) 20%. The inset diffraction patterns in Figs. 4.5a-4.5d are from the regions demarcated by yellow/white/blue circles or the complete area of interest. The top left and right diffraction patterns are from the yellow and white circular regions, respectively, in Fig. 4.5d. Zone axes are $[101]_\gamma$, $[11\bar{2}0]_\varepsilon$ in Figs. 4.5a-4.5e.

Figure 4.6: Representative (a, b, d) bright-field, (c, e) dark-field transmission electron micrographs after thickness reduction to (a) 42%, (b, c) 66% and (d, e) 88%. The inset diffraction patterns in Figs. 4.6a, 4.6b and 4.6d are from the regions demarcated by yellow circles or the complete area of interest. Zone axes are $[1\bar{1}\bar{1}]_{\alpha'}$, $[11\bar{2}0]_\varepsilon$ in Fig. 4.6a.

Figure 4.7: Representative (a) bright-field, (b) dark-field transmission electron micrographs and (c, d) HAADF STEM images after 5% thickness reduction. Figs. 4.7c, 4.7d are from regions (1) and (2) in Fig. 4.7b, respectively. In Figs. 4.7c and 4.7d, blue solid lines denote fault planes in γ. The inset diffraction pattern in Fig. 4.7a is from the region demarcated by a yellow circle. The zone axes are $[101]_\gamma$ and $[11\bar{2}0]_\varepsilon$.

Figure 4.8: Schematic of coarsening by coalescence of ε-martensite laths. The red and green circles represent fcc and hcp stacking sequences, respectively. Shockley partial dislocations are given by the symbol “⊥”.

Figure 4.9: Representative (a, b) bright-field STEM micrographs and (c-e) HAADF STEM images after 10% thickness reduction. Fig. 4.9b is a magnified view of the region denoted by red dashed square in Fig. 4.9a. Figs. 4.9c-4.9e are from the regions (1) to (3) in Fig. 4.9b, respectively. In Figs. 4.9c-4.9e, blue solid/dashed lines denote the γ/ε-martensite interface while Shockley partial dislocations are given by the symbol “┘”.

Figure 4.10: (a, c, e) Dark-field micrographs and (b, d) HAADF STEM micrographs after (a, b) hot rolling, thickness reduction to (c, d) 5% and (e) 15%. The inset diffraction patterns in Fig. 4.10c are from regions demarcated by a red square. Fig. 4.10e is observed under two beam conditions using $g = [1\bar{1}1]_\gamma$. Zone axes are $[101]_\gamma$, $[11\bar{2}0]_\varepsilon$ in Fig. 4.10c.

Figure 4.11: ε-martensite bright-field micrograph for the sample after 15% thickness reduction taken from zone axis $[01\bar{1}1]_{\varepsilon}$.

Figure 4.12: (a) Bright-field micrograph, (b, e) dark-field micrographs, (c, d, f) HAADF STEM micrographs after thickness reduction to (a-d) 10%, (e) 15% and (f) 42%. Shockley partial dislocations are shown by the symbol "┘" in Fig. 4.12f. The inset diffraction patterns in Figs. 4.12a and 4.12e are from the regions demarcated by yellow circles/whole micrograph. Fig. 4.12e is taken under two beam conditions using g = $[01\bar{1}1]_{\varepsilon}$. Zone axes are $[101]_{\gamma}$, $[11\bar{2}0]_{\varepsilon}$ in Fig. 4.12a.

Figure 4.13: Schematic of phase transformation from γ to ε-martensite followed by a transition in stacking fault character from I_2 to I_1 –type ε-ISFs. The red and green circles represent fcc and hcp stacking sequences, respectively. Shockley partial dislocations are given by the symbol "⊥".

Figure 4.14: Schematic of deformation and transformation behaviour of high Mn steel with increasing thickness reduction up to 88%. Red = γ, green = ε-martensite, blue = α′-martensite. γ intrinsic stacking faults are shown in purple while I_2 and I_1 faults in ε-martensite are shown in orange and brown, respectively. Annealing twins in γ and $\{10\bar{1}2\}\langle\bar{1}011\rangle_{\varepsilon}$ extension twins in ε-martensite are shown in yellow and fuchsia, respectively.

Figure 4.15: $\phi_2 = 0°$, 45° and 65° ODF sections of γ showing (a) the ideal orientations and after (b) hot rolling, thickness reduction to (c) 5, (d) 10, (e) 15, (f) 20 and (g) 42%. Contour = 0.5×

Figure 4.16: ϕ_2 = 0° and 30° ε-martensite ODF sections showing (a) ideal ε-martensite orientations, after (b) hot rolling and thickness reduction to (c) 5, (d) 10, (e) 15, (f) 20, (g) 42, (h) 66%. In Fig. 4.16a, some γ orientation are provided for the S-N orientation relationship. Contour = 0.5×

Figure 4.17: α′-martensite ϕ_2 = 0° and 45° ODF sections showing (a) ideal orientations, after (b) hot rolling, cold deformation to (c) 5, (d) 10, (e) 15, (f) 20, (g) 42, (h) 66 and (i) 88% thickness reduction. In Fig. 4.17a, some γ and ε-martensite orientations are provided for the K-S and Burgers orientation relationships. Contour = 0.5×

Figure 5.1: Bright-field transmission electron micrographs showing (a, b, c, d) ε-martensite and (e, f) γ at (a, b) at 28 °C (room temperature) and after in-situ annealing to temperatures of (c) 240 °C, (d) 390 °C, (e) 410 °C, (f) 650 °C. Fig. 5.1b is the magnified view of the white dashed rectangle in Fig. 5.1a. The inset diffraction patterns were obtained from the solid circles in Figs. 5.1a, 5.1e for zone axis $[\bar{2}4\bar{2}3]_{\varepsilon}$, $[\bar{1}22]_{\gamma}$, respectively. White arrows in Fig. 5.1f indicates remnant dislocations.

Figure 5.2: (a) Simulated diffraction pattern of γ/ε-martensite based on S-N orientation relationship for the $[\bar{2}4\bar{2}3]_{\varepsilon}$ zone axis and (b) evolution of reciprocal distance of γ/ε-martensite reflections with temperature. Red and blue spots in Fig. 5.2a are for γ and ε-martensite, respectively.

Figure 7.12: γ, ε and α'-martensite pole figures of the (a, b) cold-rolled and annealed at (c, d) 500 °C, (e, f) 625 °C and (g, h) 700 °C samples, (a, c, e, g) before and (b, d, f, h) after tension. In Fig. 7.12a, the ideal fcc orientations on (111) pole figure is superimposed on ε, α'-martensite and $(100)_\gamma$, $(111)_\gamma$ pole figure of γ. Key: ◆ $G_\gamma = \{110\}\langle001\rangle_\gamma$, ◇ $C_\gamma = \{001\}\langle100\rangle_\gamma$, □ $Cu_\gamma = \{112\}\langle111\rangle_\gamma$, ■ $A_\gamma = \{110\}\langle111\rangle_\gamma$, ● $Br_\gamma = \{110\}\langle112\rangle_\gamma$, ▲ Rt-$G_\gamma = \{011\}\langle011\rangle_\gamma$ In Figs. 7.12b, 7.12d, 7.12f, 7.12h, RD || tensile axis = vertical. Contours levels = 0.5×

Figure 7.13: Fractography of the fractured tensile samples after (a, b) cold rolling and annealing at (c, d) 500 °C. Figs. 7.13b, 7.13d, are zoomed-in views of regions highlighted by red dashed rectangles from Figs. 7.13a, 7.13c, respectively.

Figure 7.14: Fractography of the fractured tensile samples after annealing at (a, b) 625 °C and (c, d) 700 °C. Figs. 7.14b and 7.14d are the zoomed-in views of regions highlighted by red dashed rectangles in Figs. 7.14a and 7.14c, respectively.

Figure: A.1 Representative (a) weak beam dark-field micrograph and (b) the distribution of the measured width of the Shockley partial dislocations with respect to the angle between the Burgers vector and the dislocation line vector for γ in the sample after 5% thickness reduction. The inset diffraction patterns in Fig. A.1a is from the regions demarcated by a white dashed rectangle in Fig. A.1a using $g = [20\bar{2}]_\gamma$. The red and blue arrows in Fig. A.1a show the perfect and Shockley partial dislocations.

Figure A.2: Representative (a) bright-field image, (b, c) weak beam dark-field images and (d) the distribution of the measured width of the Shockley partial dislocations with respect to the angle between the Burgers vector and the dislocation line vector for ε-martensite after 5% thickness reduction. The inset diffraction patterns in Figs. A.2b, A.2c are from the regions demarcated by red dashed rectangles/squares in Figs. A.2a, A.2c, respectively. The inset diffraction patterns in Figs. A.2b, A.2c use $g = [10\bar{1}0]_\varepsilon$ and $g = [0002]_\varepsilon$.

List of Tables

List of abbreviations

AC: air cooling

AHSS: advanced high strength steels

Al: aluminium

bcc: body-centred cubic

bct: body-centred tetragonal

BF: bright-field

C: carbon

CP: complex phase

CRSS: critical resolved shear stress

DF: dark-field

DIC: digital image correlation

DP: dual phase

EBSD: electron back-scattering diffraction

EDS: energy dispersive spectroscopy

ESF: extrinsic stacking fault

fcc: face-centred cubic

HAADF STEM: High angle annular dark-field scanning transmission electron microscopy

hcp: hexagonal closed packed

HAGBs: high-angle grain boundaries

HR: hot rolling

HT: solution heat treatment

ISF: intrinsic stacking fault

K-S OR: Kurdjumov-Sachs orientation relationship

LAGBs: low-angle grain boundaries

LNQ: liquid nitrogen quenching

LT: loading temperature

Mn: manganese

Ni: nickel

ND: normal direction

ODF: orientation distribution function

OR: orientation relationship

Q-P: quenched and partition

PTMC: phenomenological theory of martensite crystallography

RD: rolling direction

RT: room temperature

SFE: stacking fault energy

SEM: scanning electron microscopy

Si: silicon

STEM: scanning transmission electron microscopy

S-N OR: Shoji-Nishiyama orientation relationship

TD: transverse direction

TEM: transmission electron microscopy

TKD: transmission Kikuchi diffraction

TRIP: transformation-induced plasticity

TWIP: twinning-induced plasticity

UTS: ultimate tensile strengths

WBDF: weak beam dark-field imaging

WQ: water quenching

XRD: X-ray diffraction

YS: yield stress

Publications arising from the thesis

(1) S. Pramanik, A.A Saleh, D.B. Santos, E.V. Pereloma, A. A. Gazder, Microstructure evolution during isochronal annealing of a 42% cold rolled TRIP-TWIP steel, IOP Conference Series: Materials Science and Engineering, Volume 89, 2015.

(2) S. Pramanik, A.A. Saleh, A.A. Gazder, E.V. Pereloma, Nucleation, coarsening and deformation accommodation mechanisms of ε-martensite in a high manganese steel, Materials Science and Engineering A, 2018, 731, 506-519.

(3) S. Pramanik, A.A. Gazder, A.A. Saleh, D.B. Santos, E.V. Pereloma, Effect of uniaxial tension on the microstructure and texture of high Mn steel, Advanced Engineering Materials, 2018, doi: 10.1002/adem.201800258.

(4) S. Pramanik, D.R.G. Mitchell, A.A. Saleh, A.A. Gazder, E.V. Pereloma, Evolution of microstructure during the in-situ heating of 42% cold-rolled high Mn steel, Metallurgical and Materials Transactions A, 2018 (under review).

(5) S. Pramanik, A.A. Gazder, A.A. Saleh, E.V. Pereloma, Effect of annealing temperature on the evolution of microstructure, texture and mechanical properties for a 42% cold-rolled high Mn steel, Materials Characterization, 2018, 144, 66-76.

CHAPTER 1 INTRODUCTION

1.1 General background

In recent years, there is a considerable amount of effort to reduce the weight of car bodies to minimise fuel consumption and the consequent emission of greenhouse gases. The above targets can be achieved by developing new advanced high strength materials. Steels are the ideal candidate material in the above criteria due to their high strength and ductility. Also, they are relatively cheaper than other metals and alloys [1]. This has led to the development of advanced high strength steels (AHSS). AHSS can be divided into three categories based on their strength and elongation into (i) first generation, (ii) second generation and (iii) third generation [2]. First generation AHSS contains mostly body centred cubic ferrite (α)/α′-martensite (bcc) in their microstructure. This group comprises dual phase (DP) steel, low Mn (1.5-2 wt.%) Transformation-Induced Plasticity (TRIP) steels, Complex Phase (CP) steel, quenched and partition (Q-P) steels and martensitic steels. Second generation AHSS contains mostly metastable face-centred cubic austenite (γ) in their microstructure. These include high Mn-based Transformation-Induced Plasticity (TRIP) steels and Twinning-Induced Plasticity (TWIP) steels. The first and second generation AHSS was reported to produce ultimate tensile strengths (UTS) of 500-1600 MPa and 900-1600 MPa, respectively [3]. The total elongation of the first and second generation AHSS was noted to be, correspondingly, 5-30% and 45-70%. The third generation of AHSS contains a mixture of α and metastable γ with UTS between 500-1600 MPa and total elongation between 25-50%. The medium Mn steels containing 5-7 wt.% Mn belong to the third generation of AHSS [3, 4]. The location of AHSS with other steels on the UTS vs. total elongation plot is shown in Fig. 1.1.

The high Mn-based TRIP and TWIP steels belong to a broad category of high Mn steels. They contain Mn content greater than 15 wt.% along with the minor additions of Aluminium (Al), Silicon (Si) and Carbon (C). Due to the high Mn content in these steels γ is the primary phase. These steels can also contain secondary phases, such as hexagonal closed packed (hcp) ε-martensite and α′-martensite in their microstructure. The ε and α′-martensite can form by quenching after annealing and during any processing involving deformation. The composition of high Mn steels defines the martensite formation start temperature (M_s) [5, 6]. When M_s is above the room temperature, then martensite forms on quenching. The addition of a large amount of Mn lowers the γ stacking fault energy (γ-SFE) of these steels (γ-SFE less than 20 mJ/m^2), which in turn leads to the formation of deformation-induced ε and α′-martensites accompanied by partial dislocation slip [7, 8]. Deformation-induced γ-twinning along with deformation-induced ε and α′-martensite formation was also observed in some high Mn steels [8-11]. The formation of ε and α′-martensite and deformation twinning during straining in these high Mn steels give rise to a high rate of strain hardening resulting in a combination of high strength and ductility [9]. This combination makes them perfect candidates for high-performance automotive materials where passenger safety is an important issue. However, due to the addition of a large amount of Mn, segregation in the hot-rolled plates is a major issue in the production of high-Mn based AHSS. Also, high amounts of total alloying additions (greater than 15 wt.%) lead to an increase in the cost of production [12]. Another hurdle in the production and use of AHSS is their poor surface quality [12]. The presence of surface defects originating from steel refining and continuous casting hinders the application of these steels for automotive components.

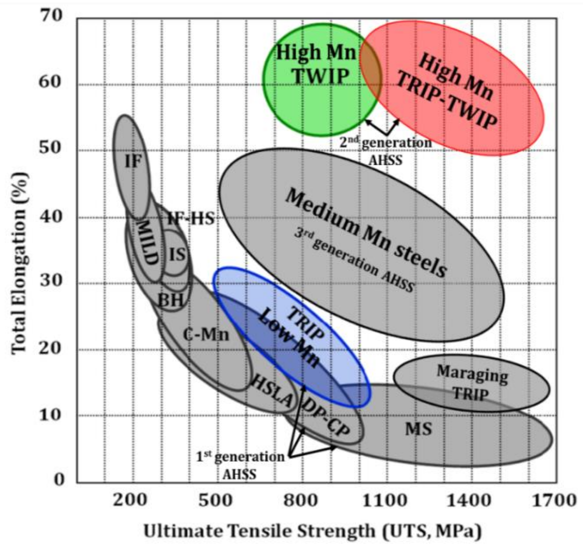

Figure 1.1: Ultimate tensile strength vs. total elongation plot of steels showing the strength and elongation values of advanced high strength steels (medium Mn, high Mn transformation-induced plasticity-twinning induced plasticity steels, twinning-induced plasticity steels, complex phase steels, dual phase steels and martensitic steels) along with other conventionally used steels (interstitial free, mild steel and high strength low alloy steels) [13].

1.2 Thesis objectives

High Mn steels are used in cold-rolled and annealed conditions. The enhanced understanding of the microstructural changes taking place during the stages of processing is important to achieve the best combination of strength-elongation in these steels.

During cold rolling, the formation of deformation-induced ε and α′-martensite occurs. There are limited studies on the nucleation and growth mechanism of ε-martensite [14, 15]. Fujita and Ueda [15] reported that the frequency of overlapping of stacking faults is increased by the passing of dislocations on the slip planes near the stacking fault planes upon tensile testing. The overlapping regions are the nucleus of thin ε-martensite plates. Also, ε-martensite formation takes place by the motion of Shockley partial dislocations or stacking faults on every alternate $(111)_\gamma$ planes [16, 17]. The growth of ε-martensite was reported [14] by the clustering of thin (1-2 nm) ε-martensite plates to form thicker plates. The role of stacking faults in the proposed ε-martensite nucleation and growth models based on the overlapping of stacking faults and their subsequent clustering [14, 15] was not studied using aberration-corrected transmission electron microscopy. The deformation accommodation mechanisms of γ, such as partial dislocation slip and martensite formation, were reported in details in the existing literature [8, 18-21]. However, the deformation mechanism of ε-martensite was addressed only in a few previous studies [22-24]. The X-ray diffraction (XRD) analysis showed the formation of ε-martensite intrinsic stacking faults (ε-ISFs) upon tension for an Fe-17Mn-0.02C high Mn steel [22]. Kim *et al.* [25] observed dislocations with a ⟨c⟩ component in ε-martensite which dissociate into Shockley partial dislocations in the basal plane to accommodate deformation during tensile testing of an Fe-17Mn steel to 0.05 engineering strain. In-situ neutron diffraction studies by Saleh *et al.* [24] showed ε-martensite to accommodate compressive deformation upon cyclic loading of an Fe-17Mn-3Al-2Si-1Ni-0.06C steel. However, in spite of the previous investigations, the detailed microstructural investigations regarding the deformation mechanisms operating during deformation of ε-martensite using high-resolution scanning transmission electron microscopy (STEM) technique was not undertaken. *Thus, this study attempts to investigate the nucleation, coarsening and deformation accommodation mechanisms of ε-martensite upon plane strain compression/cold rolling.*

Upon annealing after cold rolling, the reversion of deformation-induced ε and α′-martensite takes place. Several previous ex-situ studies [8, 10, 26-28] have investigated the ε and α′-martensite reversion mechanisms during annealing of cold-rolled metastable austenitic steels. As these studies [7, 8, 29] employed post-mortem microstructural analysis they do not directly observe the microstructural changes occurring during ε and α′-martensite reversion. Some in-situ annealing studies were also undertaken using TEM [30-34]. In this regard, the reversion mechanism of ε-martensite was reported via the shrinkage of stacking faults by in-situ annealing for an Fe-Mn-Si based shape memory alloy [34]. Also, the reversion mechanism of α′-martensite was investigated for metastable austenitic steels via in-situ annealing studies showing the motion of ledges across the γ/α′-martensite interface [31]. This reversion mechanism of ε-martensite has not been studied by in-situ annealing for high Mn steels. The reverted γ was reported [10, 35] to shows fine γ-twins. However, the mechanism of γ-twin formation is not explained in the literature. *Thus, this study plans to investigate the mechanisms of ε and α′-martensite reversion and subsequent γ-twin formation using in-situ TEM annealing experiments.*

The previous studies [8, 10] on the annealing of cold-rolled high Mn steels did not extensively investigate the relationships between reverted γ orientations and the ε and α′-martensite orientations. Following reversion, the recrystallisation of reverted γ takes place. Previous studies

[8, 10] on recrystallisation of reverted γ have not explained the mechanism of nucleation and texture evolution. *This study thus aims to address the texture evolution of γ upon reversion and recrystallisation via in-house developed γ grain segmentation technique.*

Uniaxial tension tests were performed in nearly all studies on high Mn steels [9, 36-40]. However, very few studies [41, 42] was carried out on uniaxial tensile testing on high Mn steels along with digital image correlation (DIC). These previous DIC based studies [41, 42] were performed on only fully recrystallised samples, thus missing the DIC observations during phase transformation of γ in samples initially comprising unrecrystallised γ or recrystallised γ, ε and α′-martensite formed upon quenching after annealing. *Thus, this study aims to investigate the DIC response in high Mn steel samples subjected to tension with different initial microstructures.*

1.3 Thesis outline

The thesis consists of eight chapters which are as follows:

Chapter 1 includes a general introduction and aims of the thesis.

Chapter 2 comprises the literature review on the effects of plane strain deformation and annealing on the microstructure, texture and tensile properties. The deformation accommodation mechanisms and the deformation-induced ε and α′-martensite reversion mechanisms presented in the literature for the previously studied high Mn steel is recapitulated in details. The evolution of texture during the plane strain deformation and annealing of high Mn steels in the literature is also summarised. Finally, the information on the tensile properties of high Mn steels displaying transformation-induced plasticity was collected from the literature and presented in chapter 2.

Chapter 3 addresses the composition of the studied high Mn steel, the experimental and analytical techniques. All the experimental details regarding plane strain compression/cold rolling, annealing and further tensile testing of the cold-rolled and annealed microstructures are outlined. Sample preparation via electropolishing for both electron back-scattering diffraction (EBSD) and TEM are also described. The experimental details regarding EBSD mapping and TEM imaging are presented. EBSD based analytical procedures related to γ grain segmentation and determination of γ grain size in the microstructures containing ε and α′-martensite are also described.

Chapter 4 comprises the effect of plane strain compression and cold rolling on the microstructure and texture of γ, ε and α′-martensite. The nucleation and growth mechanism of ε-martensite is explored. Subsequently, the deformation accommodation mechanisms in γ, ε and α′-martensite are also presented. In particular, the ε-martensite deformation accommodation mechanism via ε-ISFs is studied in details. The correlation of deformation-induced ε and α′-martensite orientations obtained from γ orientations upon phase transformation via the Shoji-Nishiyama (($\{111\}_{\gamma}||\{0001\}_{\varepsilon}$,$\langle 011\rangle_{\gamma}||\langle 11\bar{2}0\rangle_{\varepsilon}$) and Kurdjumov-Sachs ($\{111\}_{\gamma}||\{011\}_{\alpha'}$, $\langle\bar{1}01\rangle_{\gamma}||\langle 1\bar{1}1\rangle_{\alpha'}$) orientation relationships is also carried out.

Chapter 5 observes the changes in the microstructure during the reversion of deformation-induced ε and α′-martensite upon in-situ TEM annealing. Also, the recovery-induced twining in reverted γ is observed and its mechanism of formation is explained.

Chapter 6 describes the effect of isochronal annealing on the changes in microstructure and texture of the steel cold-rolled to 42% thickness reduction. The γ microstructure evolution during reversion, recrystallisation and grain growth was investigated using EBSD and TEM. The correlation of γ orientations formed upon the reversion with those of ε and α′-martensite orientations was carried out.

Chapter 7 presents the effect of microstructures formed after cold rolling and annealing on the tensile properties of high Mn steel studied via DIC. The changes in the microstructure and texture upon tension was investigated and discussed. The effect of initial microstructure on the fracture mechanisms is also addressed.

Chapter 8 gives the general conclusions and describes the contributions made in this work to the existing body of knowledge on the deformation and annealing of high Mn steels. Also, some suggestions regarding the future directions of research are included.

CHAPTER 2 LITERATURE REVIEW

This chapter is a summary of the information available in the literature on the mechanisms of deformation accommodation and annealing of high Mn steels. The effects of deformation and annealing on the evolution of microstructure, mechanical properties and texture are also recapitulated in this chapter. In addition, the basic concepts about stacking faults and twin formation in γ and ε-martensite were also introduced in this chapter.

2.1 Classification of high Mn steels based on chemical composition

Based on the chemical composition, high Mn steels can be classified into two categories. Both types of these steels are produced by casting, hot rolling followed by cold rolling and annealing.

2.1.1 Fe-Mn-C

The Fe-Mn-C based high Mn steels contain C content equal to or less than 0.6 wt.% along with the addition of Mn in the range of 15-22 wt.% [8, 43-47]. In these steels, γ deforms via deformation twinning or transformation to ε-martensite or α′-martensite in addition to partial slip. Mn stabilises γ and also reduces the γ-SFE. The addition of C below 0.6 wt.% leads to the reduction of γ-SFE and it also stabilises γ. The amount of Mn varies depending on the concentration of C.

2.1.2 Fe-Mn-Al-Si

The Fe-Mn-Al-Si based high Mn steels contain relatively low C content of ~0.06 wt.%. These steels comprise a higher range of Mn concentration between 15-30 wt.% [7, 10, 11, 48-52]. Depending on the Mn content, these steels may contain Al between 2-3 wt.% and Si between 2 and 6 wt.%. Due to the low C content these steels may or may not show deformation-induced twinning depending on their exact composition. However, these steels show the transformation of γ to ε and α′-martensite along with partial slip.

2.2 Role of alloying elements

(i) As the major alloying element, Mn stabilises γ. The Mn content below ≈15 wt.% leads to the formation of α′-martensite, while above 30 wt.% results in the formation of deformation twins/brittle β-Mn phase. The formation of brittle β-Mn phase deteriorates formability [53]. Below a critical concentration of Mn, the γ-SFE decreases whereas above a critical content γ-SFE increases (Fig. 2.1) [54]. With increasing Mn concentration the martensite start temperature (M_s) for the formation of ε-martensite decreases, thus increasing the stability of γ [55]. So, the appropriate Mn content required to obtain γ at room temperature is about ≈15-30 wt.%.

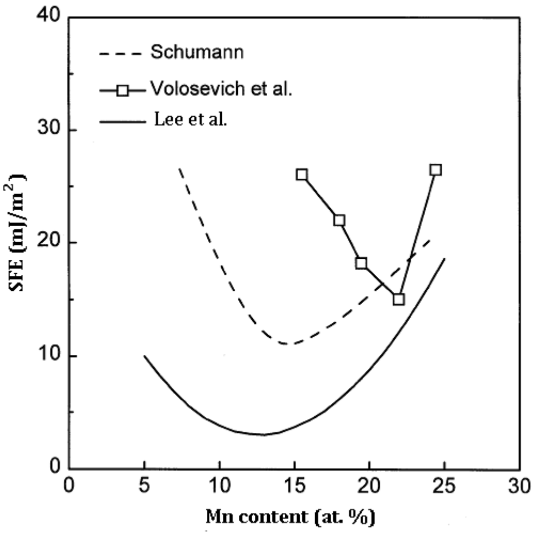

Figure 2.1: Effect of Mn content on the γ-SFE for Fe-Mn alloys [54, 56].

(ii) Al addition increases the γ-SFE (Fig. 2.2), thus suppressing the γ to ε-martensite transformation [54]. It also leads to the facilitation of deformation twinning [5, 57] and also prevents the formation of cementite (Fe_3C) [58]. The increase in strength by solid solution strengthening and improved corrosion resistance of γ are also beneficial outcomes of Al addition [57]. However, a large amount of Al decreases the strain hardening rate of high Mn steels [57]. The segregation of Al at grain boundaries during the casting of these steels can lead to the formation of a low melting compound Fe_2Al_5 which can cause cracking during further processing [59, 60].

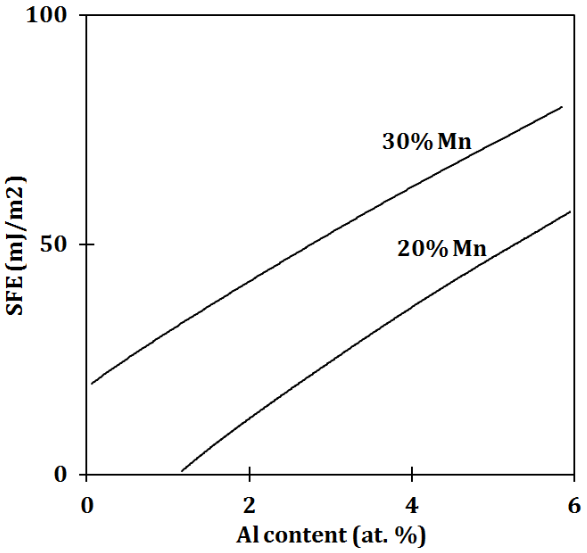

Figure 2.2: The variation of γ-SFE with Al addition for Fe-Mn alloys at 22 °C [23].

(iii) Si decreases the γ-SFE and enhances the γ to ε-martensite transformation during cooling and deformation [61-65]. It refines the ε-martensite plates, thus increasing the fracture strength. Si in solid solution imparts good machinability and strengthening [66]. Si addition was also reported to prevent the formation of cementite (Fe_3C).

(iv) The effect of C addition on the γ-SFE is not straight forward. The C addition below 0.5 wt.% leads to the decrease in γ-SFE whereas addition above 0.5 wt.% increases γ-SFE (Fig. 2.3), thus preventing ε-martensite formation [67]. It imparts solid solution strengthening and also increases γ stability. For an Fe-22Mn steel, the γ-SFE decreases from 30 to 22 mJ/m^2 by the addition of 1 wt.% C [57].

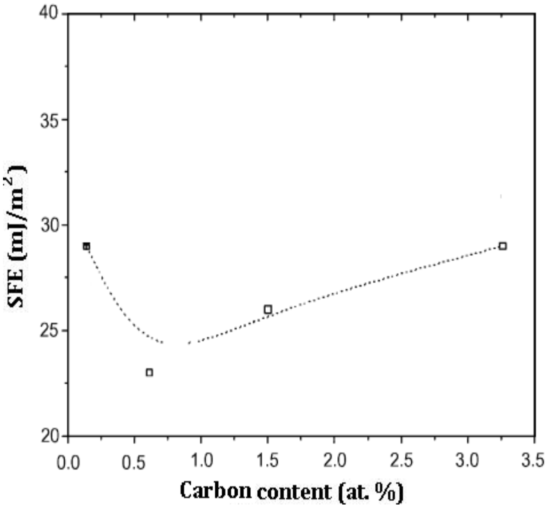

Figure 2.3: Influence of carbon content on the γ-SFE for an Fe-22Mn-C steel [67].

(v) Nickel (Ni) increases the γ-SFE, thus preventing the formation of ε and α′-martensite and also enhancing the corrosion resistance [68]. The hot ductility of high Mn steels alloyed with Al can be improved by the small additions of Boron, Titanium and Zirconium [69]. Nitrogen addition produces the strengthening of γ along with an increase in γ-SFE [57]. It was reported [70] that the addition of Nitrogen to an Fe-16.5Mn steel leads to a decrease in the volume fraction of ε-martensite due to the decrease in the M_s.

The γ-SFE of high Mn steels in literature is presented in Table 2.1. In general, it can be observed that steels containing relatively higher Mn concentration show higher γ-SFE. It can be observed that with increasing the Al content an increase in γ-SFE is observed for the same concentration of Mn and C. However, the addition of Si is observed to significantly reduce the γ-SFE.

Table 2.1 γ-stacking fault energy in high Mn steels in literature.

Composition					**γ-SFE**	**γ-SFE temperature**	**γ-SFE calculation method**	**Deformation mode**	**Deformation temperature**	**Strain rate $\dot{\varepsilon}$ (s^{-1})**	**Microstructural constituents**		**Ref.**
Mn	**Al**	**Si**	**Ni**	**C**							**Before**	**After**	
12				0.6	11.8	RT	Thermodynamic model	Tensile testing	RT	10^{-3}	γ, ε and α′-martensite	γ twins, ε and α′-martensite	[43]
12	1.5			0.6	25.5	RT	Thermodynamic model	Tensile testing	RT	10^{-3}	-	γ twins	[43]
12	2			0.6	29.9	RT	Thermodynamic model	Tensile testing	RT	10^{-3}	-	-	[43]
15				0.6	12.4	RT	Thermodynamic model	Tensile testing	RT	10^{-3}	γ	γ twins and ε-martensite	[43]
15	1.5			0.6	25.8	RT	Thermodynamic model	Tensile testing	RT	10^{-3}	-	γ twins	[43]
15	2			0.6	30.1	RT	Thermodynamic model	Tensile testing	RT	10^{-3}	-	-	[43]
17	3	2	1	0.06	14.5	RT	Thermodynamic model	Cold rolling	RT	-	γ, ε and α′-martensite	γ, ε and α′-martensite	[71]*
18				0.6	14.3	RT	Thermodynamic model	Tensile testing	RT	10^{-3}	-	γ twins	[43]
18				0.6	13 ± 3	RT	WBDF	Tensile testing	RT	-	γ	-	[72]
18				0.6	16	RT	Thermodynamic model	Tensile testing	RT	5×10^{-3}	γ	γ twins	[73]
18				0.6	19.3	RT	XRD analysis	Tensile testing	RT	10^{-4}	γ	γ twins	[74]
18		1.5		0.6	13.8	RT	XRD analysis	Tensile testing	RT	10^{-4}	γ	γ twins	[74]
18		1.5		0.6	29.1	RT	XRD analysis	Tensile testing	RT	10^{-4}	γ	γ twins	[74]
18		1.5		0.6	30 ± 10	RT	WBDF	Tensile testing	RT	-	γ	-	[72]
18		1.5		0.6	27.6	RT	Thermodynamic model	Tensile testing	RT	10^{-3}	-	γ twins	[43]
18	2.5			0.6	38	RT	Thermodynamic model	Tensile testing	RT	5×10^{-3}	γ	γ twins	[73]
18	3			0.6	40	RT	Thermodynamic model	Tensile testing	RT	10^{-3}	-	-	[43]
20				1.2	15	RT	WBDF	Tensile testing	RT	-	γ	γ twins	[75]
22	3	3			15 ± 3	RT	WBDF	Tensile testing	RT	4×10^{-4}	γ	γ, ε and α′-martensite	[76]
24.7	2.66	2.92			16 ± 4	RT	WBDF	Tensile testing	RT	4×10^{-4}	γ	γ twins and ε-martensite	[76]
25	3	3			21±3	RT	WBDF	Tensile testing	-25 °C	4×10^{-4}	γ	γ, ε and α′-martensite	[76]
28	3	3			40 ± 5	RT	WBDF	Tensile testing	-100 °C	4×10^{-4}	γ	γ and ε -martensite	[76]
31		0.25		0.8	17.4	RT	XRD analysis	Tensile testing	RT	2×10^{-3}	γ	-	[77]
31		2		0.8	14.7	RT	XRD analysis	Tensile testing	RT	2×10^{-3}	γ	-	[77]
31		5.3		0.8	10.5	RT	XRD analysis	Tensile testing	RT	2×10^{-3}	γ	γ and ε-martensite	[77]
31		8.7		0.8	6.3	RT	XRD analysis	Tensile testing	RT	2×10^{-3}	γ	γ and ε-martensite	[77]

Legend: RT= room temperature, WBDF = weak beam dark-field imaging, Thermodynamic model [78]: Eq. 2.4, * = present steel composition.

2.3 Determination of γ stacking faults energy

The γ-SFE can be determined using two methods: (a) theoretical ab-initio calculations and (b) experimentally using weak beam dark-field imaging (WBDF).

The theoretical calculation of γ-SFE was done by applying density functional theory using the Vienna ab inito simulation package. In the first step shearing a block of atoms with fcc lattice is performed to generate a suitable type of stacking fault. A block of 12 atomic layers in the $\langle 111 \rangle_\gamma$ the direction was created and sheared by $\frac{a}{6}\langle 112 \rangle_\gamma$ to generate a γ-ISF [79]. The next step involves determining the change in internal energy of the sheared crystal with respect to the undeformed crystal. Using this method the stacking fault energies of Fe-Cr-Ni -based metastable austenitic steels were calculated [80]. For the Fe-13Cr-12Ni and Fe-18Cr-12Ni steels, the γ-SFE was determined to be 36 and 30 mJ/m^2, respectively. However, this method was not applied to calculate the γ-SFE of high Mn steels.

In the experimental method, the dislocation cores of γ are imaged in TEM by WBDF technique. If the dissociation of a $\frac{a}{2}[110]_\gamma$ perfect dislocation is observed in two $\frac{a}{6}[112]_\gamma$ Shockley partial dislocations, then the separation of the dislocations in γ can be related to the γ-SFE using the equation [76, 81, 82]:

$$\gamma = \frac{\mu b^2}{8\pi d}\left(\frac{2-\nu}{1-\nu}\right)\left(1 - \frac{2\nu\cos 2\alpha}{2-\nu}\right) \tag{2.1}$$

where γ is the SFE (mJ/m^2), μ is the shear modulus on the $(111)_\gamma$ fault plane, b is the Burgers vector of the partial dislocations, d is the separation between the dislocations, ν is the Poisson's ratio, α is the angle between Burgers vector and the dislocation line vector. μ, ν are calculated using the equation:

$$\mu = \left(C_{44}\frac{(C_{11}-C_{12})}{2}\right)^{0.5} \tag{2.2}$$

$$\frac{1}{1-\nu} = \frac{1}{3\mu}\left(\left[\frac{1}{2}C_{11}(C_{11} + C_{12} + 2C_{44})\right]^{0.5} + C_{12}\right)\left[\frac{C_{44}(C-C_{12})}{C_{11}(C+C_{12}+2C_{44})}\right]^{0.5}\left(1 + 2\frac{C_{11}}{\left[\frac{1}{2}C_{11}(C_{11}+C_{12}+2C_{44})\right]^{0.5}}\right) \tag{2.3}$$

The distance between the separated two partial dislocations is proportional to the attractive force by the fault and the repulsive force between the partials. In this method, the determination of γ-SFE is based on the anisotropic theory of elasticity. Using the WBDF technique, Pierce *et al.* [76] have determined the γ-SFE for the Fe-22Mn, Fe-25Mn and Fe-28Mn steels to be 14 ± 3, 19 ± 3 and 35 ± 5 mJ/m^2, respectively.

Another popular method used for the determination of γ-SFE is based on the use of empirical equation developed from thermodynamics. The γ-SFE can be analysed by using the equation [78]

$$\Gamma = 2\rho\Delta G^{\gamma\rightarrow\varepsilon} + 2\sigma \tag{2.4}$$

In Eq. 2.4, ρ represents the molar surface density of the $\{111\}_\gamma$, $\Delta G^{\gamma\rightarrow\varepsilon}$ represents the Gibbs free energy change due to the γ to ε-martensite transformation and σ represents the surface energy of {111} interface between γ and ε-martensite. The Eq. 2.4 is valid for γ-SFE calculation at room temperature (25 °C).

The γ-SFE can also be calculated via XRD peak analysis method using the equation [69]

$$\gamma = \frac{K_{111}\omega G_{111} a A^{-0.37}}{\pi\sqrt{3}} \frac{\langle\varepsilon\rangle_{111}^{2}}{\alpha} \tag{2.5}$$

where $K_{111}\omega$ is proportional constant with a value of 6.6, G_{111} is the shear modulus on $\{111\}_\gamma$, a is the lattice parameter, A is the Zener anisotropy parameter with a value of 3.43, $\langle\varepsilon\rangle_{111}^{2}$is the mean square micro-strain and α is the stacking fault probability.

The γ-SFE determined using the theoretical ab-inito calculations showed a large deviation from the experimentally derived γ-SFE [80]. On the other hand, Eq. 2.4 assumes the surface energy of {111} interface between γ/ε-martensite to be a value that was not experimentally determined. This can lead to the introduction of errors in the calculation of γ-SFE. For an Fe-18Mn-0.6C steel, the thermodynamic model gives different values depending on the assumed surface energy of {111} interface values between γ/ε-martensite. It can be noted that the γ-SFE calculated from the XRD peak analysis method is close to that determined via WBDF method for an Fe-18Mn-1.5Si-0.6C steel. Thus, γ-SFE can be determined using both the WBDF and XRD peak analysis methods. Table 2.1 summaries the γ-SFE of high Mn steels present in literature.

2.4 Deformation mechanisms in high Mn steel

The plastic deformation of polycrystalline materials can be accommodated via a combination of three processes: (i) slip via dislocation glide, (ii) mechanical twinning and (iii) martensite formation. The occurrence of these processes depends on the SFE of the material [83]. With increasing γ-SFE, the deformation mechanism changes from the transformation of γ to ε-martensite to α′-martensite to mechanical twinning in γ to dislocation glide. The effect of γ-SFE and the deformation temperature is summarised in Table 2.2. Increasing the temperature during deformation results in increasing the γ-SFE which returns a similar trend in the deformation mechanism [83].

The γ-SFE values between 15-20 mJ/m^2 show the occurrence of both twinning and martensite transformation (Table. 2.2). For a γ and α′-martensite, dual-phase Fe-19.7Mn-3.1Al-2.9Si steel, it was reported [84] that deformation takes place by ε-martensite formation assisted by deformation twinning at temperatures below 86 °C, whereas exclusively by deformation twinning at temperatures greater than 160 °C.

Table 2.2 Effect of γ-SFE/deformation temperature on the deformation mechanisms of γ [83].

SFE (mJ/m^2)	**Temperature (°C)**	**Active deformation mechanisms of γ**
<15	<5	martensite transformation, Shockley partial dislocation glide
15-20	5-50	martensite transformation, twinning, Shockley partial dislocation glide
20-30	50-120	twinning, Shockley partial dislocation glide
30-40	120-400	twinning, dislocation glide
>40	>400	dislocation glide

2.4.1 Partial slip via dislocation glide

The deformation by slip occurs by the motion of multiple dislocations along a slip plane in the slip direction. Slip results in the formation of steps on the surface of the crystal. The glide of individual dislocations is restricted to the plane containing both the dislocation line vector and Burgers vector. The slip planes are normally the planes with the highest density of atoms and the direction of slip is the direction in the slip plane corresponding to the shortest lattice translation vector (the directions where atoms are most closely spaced) [85]. For fcc crystals, the slip plane is $\{111\}_\gamma$ and the slip direction is $\langle 110\rangle_\gamma$ [85].

2.4.2 Formation of γ stacking faults

The stacking faults are planar defects created by the disruption of the local atomic sequence. Slip in γ occurs in $\{111\}_\gamma$ plane and along the $\langle 110\rangle_\gamma$ direction. As a unit translation along the $\langle 110\rangle_\gamma$ direction leaves the stacking sequence unchanged, the dislocations having a Burgers vector of $\frac{a}{2}\langle 110\rangle_\gamma$ are considered to be perfect dislocations. Stacking faults are created by the dissociation of a perfect dislocation into two Shockley partial dislocations having a Burgers vector of $\frac{a}{6}\langle 112\rangle_\gamma$. The region bounded by the two Shockley partial dislocations represents a stacking fault as shown in Fig. 2.4.

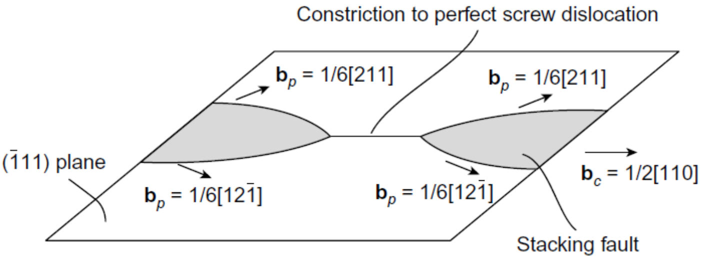

Figure 2.4: Dissociation of screw dislocation into two Shockley partial dislocations [85].

Outside the partial dislocations the stacking sequence of the $\{111\}_\gamma$ planes will be perfect ABCABC… whereas the region bounded by partial dislocations will have a stacking fault of ABCACABC... The formation of γ stacking faults can occur at two places: (i) at γ grain boundaries and annealing twins and (ii) at the intersection of a different family of slip planes.

There can be two types of stacking faults in γ lattice.

(i) Intrinsic stacking faults (ISFs): For γ stacking sequence ABCABC… the removal of an atomic plane creates ABCAB|ABC… stacking called as intrinsic stacking fault (ISF). In ISF, there is a creation of a local layer of hcp stacking sequence ACAC… as shown in Fig. 2.5. ISFs in fcc crystals are created by the dislocation reaction given by

$$\frac{a}{2}\langle\bar{1}10\rangle_\gamma \rightarrow \frac{a}{6}\langle\bar{2}11\rangle_\gamma + \frac{a}{6}\langle\bar{1}2\bar{1}\rangle_\gamma \qquad (2.6)$$

where a is the lattice parameter of fcc crystal.

ISFs are bounded by two Shockley partials dislocations of Burgers vectors $\frac{a}{6}\langle\bar{2}11\rangle_\gamma$ and $\frac{a}{6}\langle\bar{1}2\bar{1}\rangle_\gamma$. Physically, the formation of γ-ISFs occurs by the condensation of vacancies on an octahedral $\{111\}_\gamma$ plane.

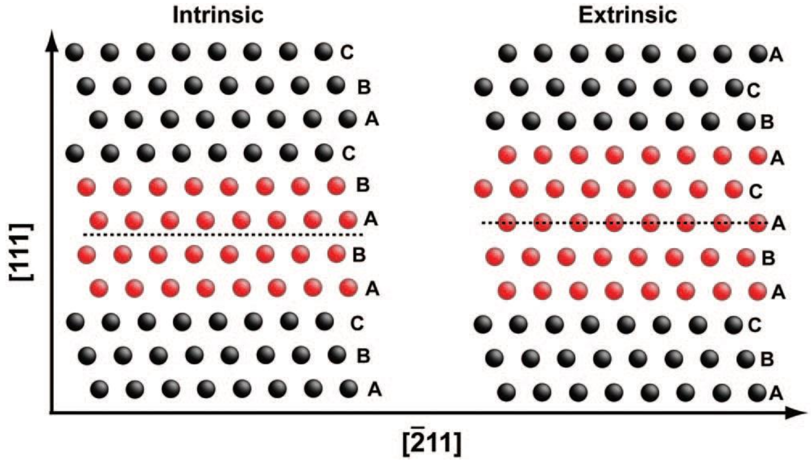

Figure 2.5: Atomic configurations for stacking faults in fcc. The dashed line indicates ISFs or ESFs. The X and Y-axis show the directions in a fcc crystal [86].

The formation of Shockley partial dislocations can be explained via the pole mechanism. This mechanism was proposed by Hoshino *et al.* [41]. In this mechanism the multiplication of Shockley partial dislocations on every second $(111)_\gamma$ plane takes place around an immobile pole dislocation leading to the formation of ε-martensite. The formation of a pole dislocation takes place by the dissociation of a perfect dislocation into Frank and Shockley partial dislocations.

$$\frac{a}{2}[1\bar{1}0]_\gamma + \frac{a}{2}[011]_\gamma + \frac{a}{2}[0\bar{1}1]_\gamma \rightarrow \frac{2a}{3}[1\bar{1}1]_\gamma + \frac{a}{6}[\bar{1}12]_\gamma \qquad (2.7)$$

where $\frac{2a}{3}[1\bar{1}1]_{\gamma}$ is the pole dislocation. It can be noted that the total dislocation energy remains the same from the above reaction if dislocation energy is taken to be proportional to the square of the Burgers vector.

(ii) Extrinsic stacking faults (ESFs): When an extra layer of atoms is inserted creating a stacking sequence of ABCAB|ACABC… it leads to the formation of extrinsic stacking fault (ESF) [87]. The ESFs (Fig. 2.5) could be formed by the precipitation of interstitial atoms on the octahedral $\{111\}_{\gamma}$ planes. Therefore, the energy of ESFs is slightly greater than that of ISFs. Due to its lower energy, the formation of ISFs is more favoured than that of ESFs. As ESF formation is closely related to γ twin nucleation, it was described in Section 2.1.2, Chapter 2. It has to be noted that Weertman convention [88] is followed throughout the text by which an ISF is defined with the stacking sequence of ABCAB|ABC… or ABAB|**C**BCBCB…., whereas ESF is defined with a stacking sequence of ABCAB|ACABC… or ABAB|**C**|ABAB for both γ and ε-martensite.

2.4.3 γ twinning

Twinning is a phenomenon where a parent crystal undergoes a homogeneous shear deformation to produce a crystal of new orientation as illustrated in Fig. 2.6. The parent and daughter crystal are mirror images of each other. Twins can form during γ deformation as well as recrystallisation. Deformation twins are finer having a lenticular shape whereas annealing twins are coarser with two parallel straight facets. Twinning in γ occurs in the $\{111\}_{\gamma}$ plane along the $\langle 11\bar{2}\rangle_{\gamma}$ direction [89]. Twins are formed by the passage of Shockley partial dislocations on every $\{111\}_{\gamma}$ plane. The shear strain associated with twinning in fcc metals is $\frac{1}{\sqrt{2}}$ which manifest itself in the deformation of the crystal.

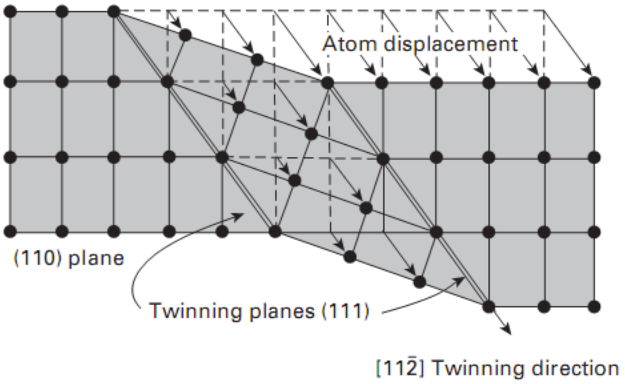

Figure 2.6: Schematic diagram showing the twinning mechanism in fcc crystal [90].

The twinning mechanism proposed by Mahajan and Chin [91] leads to the glide of coplanar Shockley partial dislocations on the adjacent $\{111\}_\gamma$ planes following the reaction.

$$\frac{a}{2}[\bar{1}10]_\gamma + \frac{a}{2}[01\bar{1}]_\gamma \rightarrow \frac{3a}{6}[\bar{1}2\bar{1}]_\gamma \tag{2.8}$$

The dislocation reaction forms an ESF-ISF pair that thickens by the glide of Shockley partial dislocations on adjacent $\{111\}_\gamma$ planes. As more Shockley partial dislocations glide past each other, a microscopic twin is formed. The γ-ISFs and twins form predominantly in the $\langle 110\rangle_\gamma$ orientated grains. Alternatively, twins and γ-ESFs form in $\langle 100\rangle_\gamma$ || tensile direction γ oriented grains at higher strains in TWIP steel [92]. ESFs was shown [92, 93] to help in the growth of γ-twins at higher strain in $\langle 100\rangle_\gamma$ || tensile axis oriented grains. The above reaction is repulsive in nature but can occur in high-stress concentration areas.

Another mechanism for twin formation is the pole mechanism proposed by Venables [94]. The mechanism consists of the dissociation of perfect dislocation into Shockley and Frank dislocations such that Shockley partial dislocation revolves around the Frank partial dislocation generating a microscopic twin. The observation of this mechanism was also reported [93, 95]. Twin nucleation by the synchronized activation of Shockley partial dislocations is also active in the $\langle 100\rangle_\gamma$ || tensile axis oriented γ grains in TWIP steel [92, 93]. Twin nucleation in $\langle 111\rangle_\gamma$ || tensile axis oriented γ grains is accompanied by the formation of ISFs.

Karaman *et al.* [96] also proposed the formation of Lomer-Cottrell locks by the interaction of two different Shockley partial dislocations gliding on different $\{111\}_\gamma$ type planes acting as the high-stress concentration region. Due to the high-stress concentration, the trailing Shockley partial dislocation undergoes cross slips into the $(\bar{1}1\bar{1})_\gamma$ plane. After further dissociation into the $(1\bar{1}\bar{1})_\gamma$ plane it forms an ESF. Due to the pinning of the trailing dislocation in the ESF by the other dislocations, the leading partial creates a dislocation loop. The leading partial then cross slips into the parallel $(1\bar{1}\bar{1})_\gamma$ plane. The overlapping of faults on the $(1\bar{1}\bar{1})_\gamma$ plane forms the micro twin.

2.4.4 ε-martensite formation

The formation of ε-martensite from γ takes place by the motion of Shockley partial dislocations on alternate $\{111\}_\gamma$ planes (Fig. 2.7). A sequence of Shockley partial dislocations between every alternate $\{111\}_\gamma$ plane will create a glissile interface separating γ and ε-martensite. The Burgers vector of these dislocations lies in the glide plane forming a continuous interface at a macroscopic interfacial plane as represented in Fig. 2.7. The gliding of this dislocation network brings the transformation of γ to ε-martensite, whereas the transformation of ε-martensite to γ takes place by the reverse motion. As the interfacial plane lies at an angle to $\{111\}_\gamma$ or $(0001)_\varepsilon$ plane, it is not irrational.

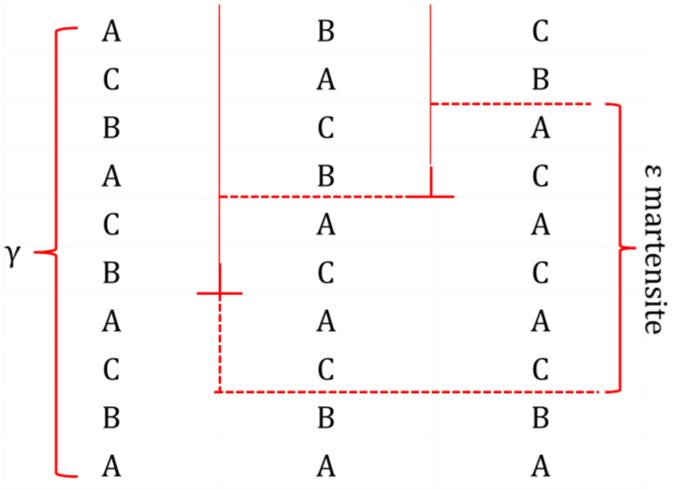

Figure 2.7: The mechanism of ε-martensite formation by the motion of an array of Shockley partial dislocations [97].

At a microscopic level, the interface consists of stepped planar coherent facets parallel to $\{111\}_{\gamma}$ or $(0001)_{\varepsilon}$ planes with the height of a step of two atomic closed packed planes (Fig. 2.7) [97]. The transformation of γ to ε-martensite leads to volume contraction. The amount of contraction depends on the total number of ε-martensite variants formed. Due to self-accommodation of transformation strain between ε-martensite variants, the formation of four ε-martensite variants leads to a volume contraction of 0.29% contrary to 1.16% when only one ε-martensite variant is realised [98].

The ε-martensite formation was explained by invoking the stacking fault mechanism (i.e., the extension and overlapping of stacking faults). Based on the formation of ε-martensite in 18/8 stainless steel, Fujita *et al.* [99] described the three stages of this process: (i) the formation of wide stacking faults, (ii) irregular overlapping of stacking faults and (iii) regular overlapping of stacking faults.

In γ crystal, all four $\{111\}_{\gamma}$ type planes are the shear planes, each containing $\langle 112\rangle_{\gamma}$ type shear direction. There are a total of four distinct variants of ε-martensite crystals that can form from one γ grain [100]. Since there are three different $\langle 112\rangle_{\gamma}$ directions, two types of stacking of ε-martensite variants can be obtained.

(i) Self-accommodated stacking: As shown in Fig. 2.8a self-accommodated stacking consists of an arrangement of three $\langle 112\rangle_{\gamma}$ type shear directions within a $\{111\}_{\gamma}$ plane such that the shear strains associated with each ε-martensite variant nullify each other leading to a zero macroscopic shape change [101].

(ii) Mono partial stacking: In this kind of stacking the ε-martensite variants are arranged in a manner producing the highest lattice shape change. This also represents a homogeneous lattice shear of 35.3% at an angle of 19.47° (Fig. 2.8b) [101].

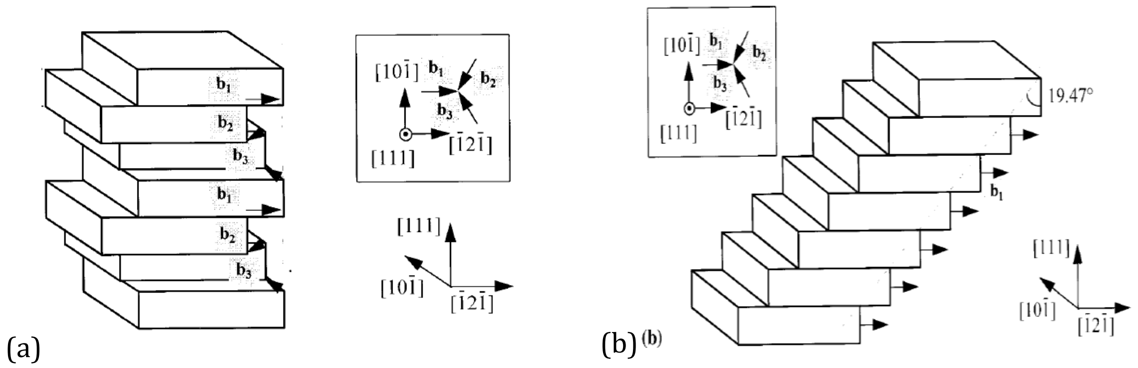

Figure 2.8: The stacking of ε-martensite variants for (a) self-accommodated and (b) mono partial stacking [101].

2.4.4.1 *Athermal and deformation-induced ε-martensite*

The formation of ε-martensite takes place upon quenching after annealing and also on deformation. The ε-martensite formed by these two ways can be distinguished by three methods:

(i) High-resolution transmission electron microscopy (HR TEM) imaging: The previous studies have revealed that the quenched ε-martensite forms in the self-accommodated stacking form (Fig. 2.8a), whereas the stress-induced ε-martensite appears in the mono partial stacking sequence as depicted in Fig. 2.8b. Therefore, imaging the interface between γ and ε-martensite can be used to separate the ε-martensite formed by the two processes. In the case of ε-martensite formed upon quenching after annealing, the γ/ε-martensite interface is expected to be atomically smooth, whereas in the case of deformation-induced ε-martensite the interface is expected to contain ledges [101].

(ii) Optical microscopy: It was reported that the colour etchant with a composition of 1.2% $K_2S_2O_5$ + 0.5% NH_4HF_2 with distilled water can be used to distinguish between the two types of ε-martensite. The etchant delineates the ε-martensite formed upon quenching after annealing as white (Fig. 2.9a) whereas the deformation-induced ε-martensite is black (Fig. 2.9b). The γ and α′-martensite appear as brown and blue colours, respectively.

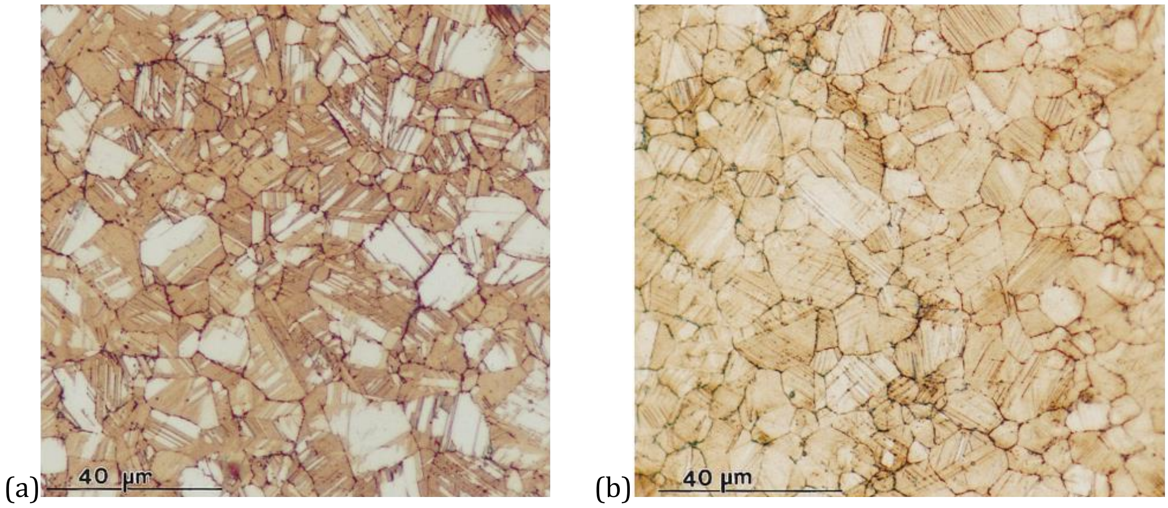

Figure 2.9: Microstructure of ε-martensite after colour etching (a) athermal martensite (in white) and (b) stress-induced martensite (in dark striations) [101].

(iii) Atomic force microscopy: During the formation of quenched in ε-martensite, there is an increase in the local γ surface elevation (Fig. 2.10a) whereas, for deformation-induced martensite, there is a decrease in the γ surface elevation as shown in Fig. 2.10b. Thus, measuring the surface height by using an atomic force microscope, the martensite formed in the two processes could be distinguished [101].

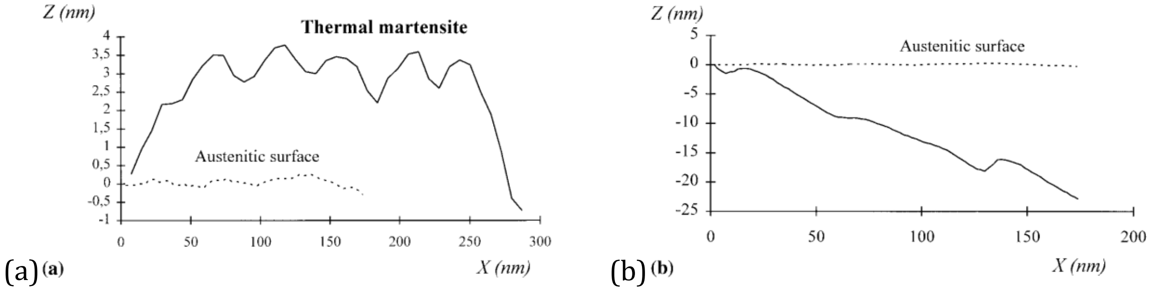

Figure 2.10: Surface topographies created by martensitic transformation by (a) thermal ε-martensite and (b) stress-induced ε-martensite [101].

2.4.4.2 *Stacking faults in ε-martensite*

In ε-martensite, three types of faults namely ISFs, ESFs and twin faults are formed. The formation of a partial dislocation in ε-martensite takes place by the splitting of a perfect dislocation $\frac{a}{3}[2\bar{1}\bar{1}0]_{\varepsilon}$ (lattice parameter a) gliding on the $(0001)_{\varepsilon}$ basal plane of an hcp crystal into two Shockley partial dislocations by the reaction:

$$\frac{a}{3}[2\bar{1}\bar{1}0]_{\varepsilon} \rightarrow \frac{a}{3}[10\bar{1}0]_{\varepsilon} + \frac{a}{3}[1\bar{1}00]_{\varepsilon} \qquad (2.9)$$

(i) ISF: ISFs created by the motion of Shockley partial dislocations in ε-martensite can be of two types I_1 and I_2. I_1 type ISF depicted in Fig. 2.11a can be presented by the dislocation reaction where a Shockley partial dislocation reacts with a Frank dislocation with Burgers vector $\frac{a}{2}[0001]$ to produce a Frank-Shockley composite dislocation [53]. The dislocation reaction is given as:

$$\frac{a}{3}[10\bar{1}0]_{\varepsilon} + \frac{a}{2}[0001]_{\varepsilon} \rightarrow \frac{a}{6}[20\bar{2}3]_{\varepsilon} \qquad (2.10)$$

Due to the composite nature (Frank-Shockley dislocation), the resultant fault is sessile. Another possible way to visualise I_1 type faults is by the removal of one layer of basal plane atoms followed by the slip of the crystal by $\frac{a}{3}[10\bar{1}0]_{\varepsilon}$. The intermediate stage in the above process produces a fault with a very high energy due to the overlapping of the same layer of stacking. The process can be described as:

ABABABABABAB.... → ABA**BB**ABABAB.... → ABAB|**C**BCBCB.....

The formation of sessile ISFs of type I_2 is described as ABABABABAB…→ABAB|**C**|ACACA… and its dislocation reaction is identical to Eq. 2.6 and facilitated by the motion of $\frac{a}{3}[10\bar{1}0]_{\varepsilon}$ Shockley partial dislocations.

(ii) ESF: The formation of ESFs is due to the glide of two Shockley partial dislocations with Burgers vector $\frac{a}{3}[10\bar{1}0]_{\varepsilon}$ of opposite sign, on the top and bottom adjoining basal planes resulting in the insertion or removal of multiple layers of basal stacking from the lattice [53]. This dislocation motion occurs on the basal plane creating a stacking sequence of ABAB|**C**|ABAB… (presented in Fig. 2.11b) without altering the nearest-neighbour arrangement of the hcp stacking sequence. The dislocation reaction for the formation of ESF can be represented by the equation [53]

$$\frac{a}{2}[0001]_{\varepsilon} + \frac{a}{3}[10\bar{1}0]_{\varepsilon} + \frac{a}{3}[\bar{1}010]_{\varepsilon} \rightarrow \frac{a}{2}[0001]_{\varepsilon} \qquad (2.11)$$

The stacking sequence changes from:

ABABABAB… → ABAB|**C**ABAB… or BABABABA… → BABA|**C**BCB…

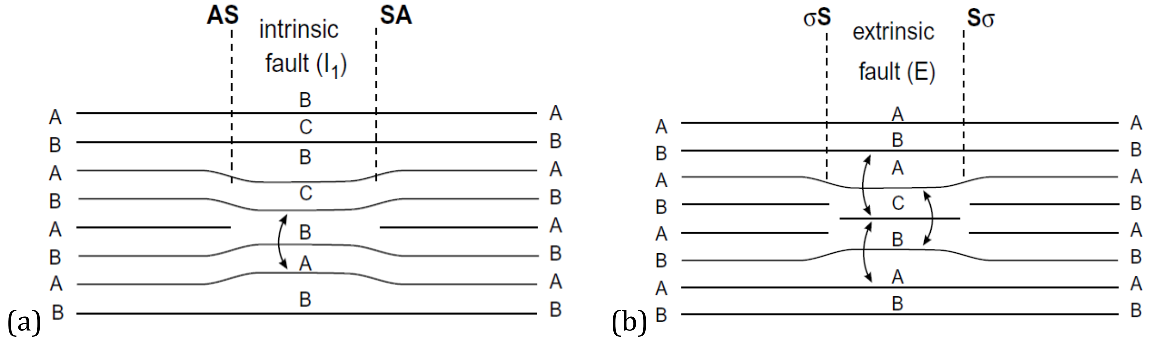

Figure 2.11: Stacking sequence in ε-martensite for (a) intrinsic (type I_1) and (b) extrinsic faults [85]. In Figs. 2.11a, 2.11b AS/SA and σS/Sσ are dislocations with Burgers vector $\frac{1}{6}[\bar{2}203]_{\varepsilon}$ and $\frac{1}{2}[0001]_{\varepsilon}$, respectively.

(iii) Twin fault: Another type of fault, which is uncommon, is twin fault because of its mirror symmetry about the basal plane. The formation of twin faults was described by the shearing of subsequent basal planes by dislocations with Burger vector $\frac{a}{3}[10\bar{1}0]_{\varepsilon}$ [102]. The atomic stacking of these faults can be visualised by ABABABABAB…→ AB**AB|C|**BABAB… Twin faults are not twins despite the occurrence of a mirror symmetry [103]. A homogenous shear is required to produce a twin fault whereas a homogeneous shear cannot produce a twin.

In the basal faults, the appearance of the local fcc-like environment (highlighted in bold fonts) takes place in the above stacking arrangement. In ISFs, ESFs and twin faults there are one, three and two fcc-like environments occurring, respectively. Therefore, the energy of the faults follows $E(ESF)\approx\frac{3}{2}E(Twin)\approx 3E(ISF)$ [104]. Thus, it is expected for ε-martensite to contain more ISF than ESF or twin faults.

2.4.5 α′-martensite formation

Martensitic transformation occurs by the shearing of the lattice, with the atoms moving only a fraction of the interatomic distance. There is no compositional change associated with martensitic transformation. Based on the phenomenological theory of martensite crystallography (PTMC), for the accomplishment of martensitic transformation, the presence of an invariant line (for the glissile interface) and invariant plane (observed experimentally) is required. The two conditions are met by the combination of the following processes:

(i) Bain strain: This is a homogenous pure distortion which converts γ lattice into the α′-martensite lattice by expansion and contraction of the three axes of γ crystal with the minimum atomic displacement (Figs. 2.12a, 2.12b). Fig. 2.12b shows that a body-centred tetragonal cell (bct) can be visualized between two γ unit cells. A bct lattice can be considered as a bcc with c/a ≈1.4. So, the bct lattice (between two fcc lattices) can be converted into bcc lattice by a compression parallel to the b3 axis (Fig. 2.12b) and extension parallel to b1 and b2 axis (Fig. 2.12b). Therefore, the application of Bain strain leads to the increase in volume upon γ to α′-martensite transformation. The Bain strain can be expressed mathematically as

$$\text{Bain strain}=\begin{pmatrix}\eta_1 & 0 & 0\\ 0 & \eta_2 & 0\\ 0 & 0 & \eta_3\end{pmatrix} \qquad (2.12)$$

where η_1, η_2 and η_3 are the strains in the three principal directions.

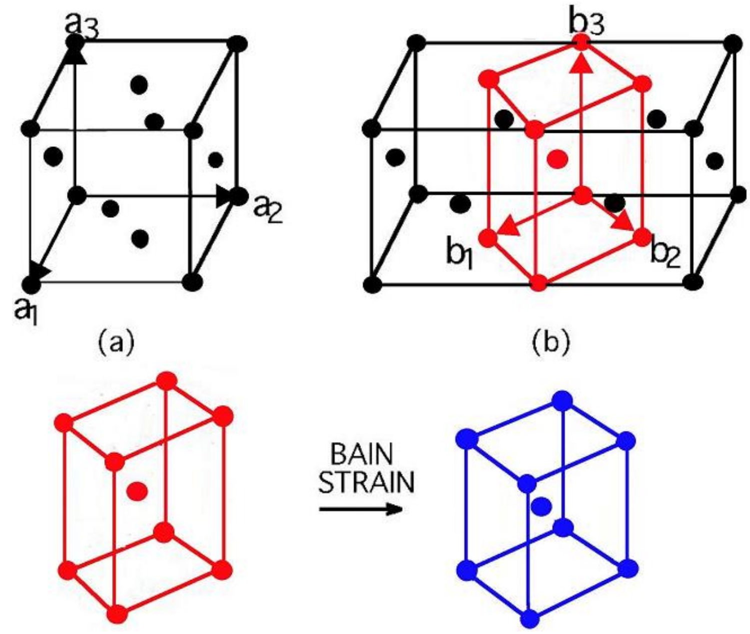

Figure 2.12: (a) Bct unit cell within fcc lattice and (b) Bain strain along the b1, b2 and b3 axis returning the transformation of an fcc/bct to bcc lattice [105]. In Figs. 2.12a and 2.12b a1, a2, a3 and b1, b2, b3 are the principal axis of the fcc and bct/bcc lattice, respectively.

(ii) Rigid body rotation: As there is no undistorted line associated with Bain strain, thus the invariant line strain associated with martensitic transformations cannot be explained by Bain strain alone. This leads to the requirement of a rigid body rotation along with Bain strain which leaves a line both undeformed and unrotated (invariant line strain). The Bain strain along with rigid body rotation is not a pure strain as the principal axes are rotated. The combination of Bain strain and rigid body rotation is called a lattice transformation strain. This strain is an invariant plane strain (IPS) which acts on the habit plane (p) and along the shear direction (d) to return the shape change observed during the γ to α'-martensite transformation. Mathematically shape deformation can be expressed as

$$\mathrm{IPS}=\mathrm{I}+\mathrm{m}^*[\mathrm{p}][\mathrm{d}] \tag{2.13}$$

$$\mathrm{I}=\begin{pmatrix}1 & 0 & 0\\ 0 & 1 & 0\\ 0 & 0 & 1\end{pmatrix} \tag{2.14}$$

where m is the magnitude of shape deformation, I is the identity matrix.

(iii) Shear deformation of γ/α'-martensite interface: The experimentally observed shape change during the γ to α'-martensite transformation is an invariant plane strain. The shear at the interface occurs by the heterogeneous invariant lattice deformation such as slip or twinning [105] without changing the crystal structure of α'-martensite.

2.4.5.1 *Mechanism of deformation-induced α′-martensite formation*

It is generally assumed that the formation of deformation-induced α′-martensite takes place at the intersection of two slip bands as described below. This is due to the favourable shear strain created at the intersection site by two intersecting slip bands. The α′-martensite is observed to grow in the form of plates and these plates will stop at γ high angle grain boundaries (HAGBs) or at other α′-martensite plates. The shear required for the transformation of γ lattice into α′-martensite can be divided into two invariant plane strains which can occur simultaneously or successively in accordance with the Bogers-Burgers model [103].

(i) The first invariant plane strain can be due to one-third of twinning shear in γ with a displacement $\frac{a}{18}\langle 112\rangle_{\gamma}$ and denoted by T/3. This shear can be achieved by the motion of an array of Shockley partial dislocations on every third $\{111\}_{\gamma}$ plane (Fig. 2.13).

(ii) The second invariant plane strain can be attained by the application of a second shear component corresponding to one-half of the twinning shear (displacement of $\frac{a}{12}\langle 112\rangle_{\gamma}$) in the γ lattice and is represented as T/2 in Fig. 2.13. The movement of Shockley partial dislocations on every second plane $\{111\}_{\gamma}$ plane can achieve this invariant plane strain.

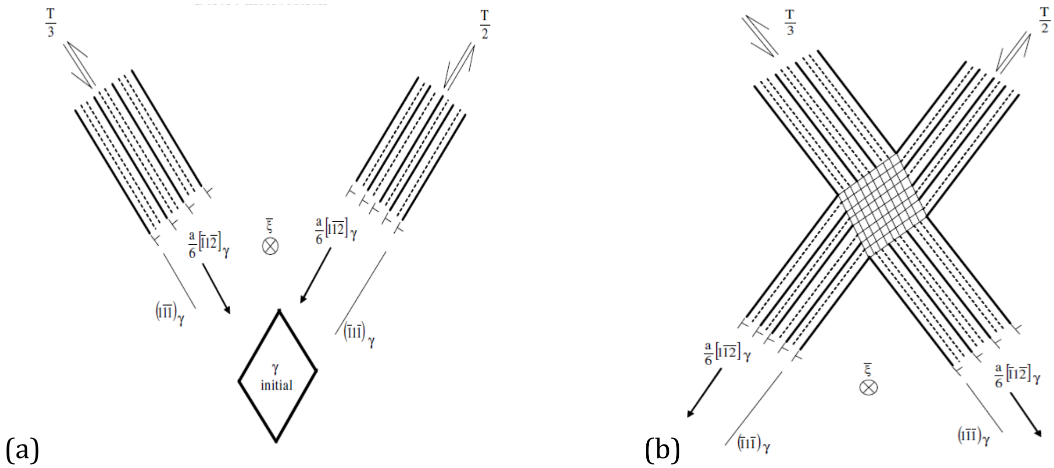

Figure 2.13: Schematic illustration of intersecting shears due to two arrays of $\frac{a}{6}\langle 112\rangle_{\gamma}$ partial dislocations in γ (a) before and (b) after the intersection of localised slip band. One array has partial dislocations on every third $\{111\}_{\gamma}$ plane and averages one-third of a twinning shear while another array has partial dislocations on every second $\{111\}_{\gamma}$ plane and averages one half of a twining shear. The resulting double-faulted intersection has an exact bcc structure [106].

2.4.5.2 *Stress and strain-induced α′-martensite*

Fig. 2.14a shows the thermodynamics involved in the transformation of γ to α′-martensite. $\Delta G^{\gamma-\alpha'}$ is the total free energy change/driving force for the γ to α′-martensite transformation which can be calculated as

$$\Delta G^{\gamma-\alpha'} = G^{\gamma} - G^{\alpha'} \tag{2.15}$$

where G^{γ} and $G^{\alpha'}$ are the free energy of γ and α′-martensite, respectively. At the M_s, the free energy change for γ to α′-martensite transformation is zero. At temperatures below M_s, the $\Delta G^{\gamma-\alpha'}$ is negative and at temperatures above M_s, the $\Delta G^{\gamma-\alpha'}$ is positive. This implies that at temperatures higher than M_s, $G^{\gamma} > G^{\alpha'}$ whereas below M_s $G^{\gamma} < G^{\alpha'}$. Near the M_s temperature, the $\Delta G^{\gamma-\alpha'}$ can be approximated as

$$\Delta G^{\gamma-\alpha'} = \Delta H^{\gamma-\alpha'} \frac{T-M_s}{M_s} \tag{2.16}$$

where $\Delta H^{\gamma-\alpha'}$ is the enthalpy change during γ to α′-martensite transformation and T is the temperature. The total free energy change due to α′-martensite transformation can be supplemented via plastic deformation. In Fig. 2.14a U is the free energy change/driving force associated with the plastic deformation. The formation of deformation-induced martensite can be categorised into two types: (i) stress-induced and (ii) strain-induced martensite.

(i) The nucleation of α′-martensite under the influence of elastic stress produces stress-induced α′-martensite. In this case, α′-martensite nucleates at stress levels below the yield stress of γ at pre-existing nucleation sites (Fig. 2.14b).

(ii) The nucleation of α′-martensite above the yield stress of γ is strain-induced. Plastic deformation above yielding leads to the formation of new potent nucleation sites [103]. Fig. 2.14 shows the temperature range between M_S and M_S^{σ} where yielding under the applied stress is initiated by the onset of α′-martensite formation and above which yielding is initiated by regular slip processes in γ. In Fig. 2.14 M_s is the martensite start temperature, M_S^{σ} is the temperature where stress required to initiate stress-induced α′-martensite is equal to the yield stress of γ and M_d is the temperature above which plastic deformation cannot produce α′-martensite.

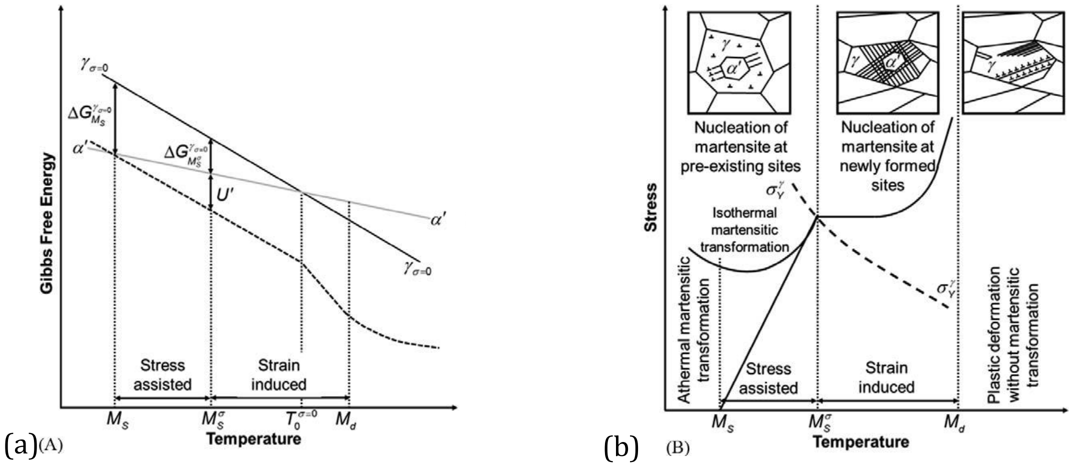

Figure 2.14: Schematic representation of (a) change in Gibbs free energy with temperature and (b) deformation mechanism as a function of temperature. $\mathrm{M_S}$ is the martensite start temperature. $\mathrm{M_S^\sigma}$ is the temperature at which the stress required for the onset of martensite is greater than the yield stress of γ. $\mathrm{M_d}$ is the temperature above which no martensite formation is possible [107].

The γ-stacking faults produced by the deformation of γ are one of the potent nucleation sites for ε-martensite. Thus, ε-martensite can be considered to be strain-induced. The formation of α′-martensite at the intersection of two ε-martensite plates or by the intersection of the ε-martensite plate with a twin or at γ grain boundary in deformed 304 austenitic stainless steel are cases where a nucleating site was created by plastic straining. Thus, in such cases, the α′-martensite generation may be construed as a strain-induced process. However, the α′-martensite formation can also be stress-induced. With the use of DIC technique, Eskandari *et al.* [41] detected the formation of stress-induced martensite before yielding. Thus, in metastable austenitic steel, the occurrence of both stress and strain-induced martensite was reported in the literature.

2.5 Crystallography of γ/ε-martensite and γ/α′-martensite transformations

Four ε-martensite variants form from a single γ grain following the Shoji-Nishiyama (S-N) orientation relationship ($\{111\}_\gamma||\{0001\}_\varepsilon$,$\langle 011\rangle_\gamma||\langle 11\bar{2}0\rangle_\varepsilon$) as shown in Table 2.3 [105].

Table 2.3 Four ε-martensite variants generated during the phase transformation of γ to ε-martensite via S-N orientation relationship [100].

ε-martensite variant	Plane-Direction in γ	Plane-Direction in ε-martensite
V1	$(111)[10\bar{1}]_\gamma$	$(0002)[2\bar{1}\bar{1}0]_\varepsilon$
V2	$(\bar{1}11)[01\bar{1}]_\gamma$	$(0002)[2\bar{1}\bar{1}0]_\varepsilon$
V3	$(\bar{1}\bar{1}1)[\bar{1}0\bar{1}]_\gamma$	$(0002)[2\bar{1}\bar{1}0]_\varepsilon$
V4	$(1\bar{1}1)[0\bar{1}\bar{1}]_\gamma$	$(0002)[2\bar{1}\bar{1}0]_\varepsilon$

Similarly, the formation of α′-martensite from ε-martensite was described to follow the Burgers orientation relationship ($\{110\}_{\alpha'}||\{0001\}_{\varepsilon}$,$\langle 111\rangle_{\alpha'}||\langle 11\bar{2}0\rangle_{\varepsilon}$) [108]. Due to the α′-martensite bcc crystal symmetry, during the hcp to bcc transformation, six variants of α′-martensite can be obtained from one ε-martensite crystal upon phase transformation via the Burgers orientation relationship. The six variants of α′-martensite are listed in Table 2.4.

Table 2.4 Six variants of α′-martensite generated during the phase transformation of ε to α′-martensite via the Burgers orientation relationship [100].

α′-martensite variant	**Plane-Direction in ε-martensite**	**Plane-Direction in α′-martensite**
V1	$(0002)[2\bar{1}\bar{1}0]_{\varepsilon}$	$(011)[11\bar{1}]_{\alpha'}$
V2	$(0002)[11\bar{2}0]_{\varepsilon}$	$(011)[11\bar{1}]_{\alpha'}$
V3	$(0002)[\bar{1}2\bar{1}0]_{\varepsilon}$	$(011)[11\bar{1}]_{\alpha'}$
V4	$(0002)[\bar{2}110]_{\varepsilon}$	$(011)[11\bar{1}]_{\alpha'}$
V5	$(0002)[\bar{1}\bar{1}20]_{\varepsilon}$	$(011)[11\bar{1}]_{\alpha'}$
V6	$(0002)[1\bar{2}10]_{\varepsilon}$	$(011)[11\bar{1}]_{\alpha'}$

The misorientation angle-axis pairs obtained from a single ε-martensite grain upon phase transformation to α′-martensite grains with different variants are presented in Table 2.5.

Table 2.5 Misorientation angle-axis pairs between α′-martensite variants obtained from a single ε-martensite grain upon phase transformation via the Burgers orientation relationship [109].

Misorientation angle	**Misorientation axis**
10. 5°	$[110]_{\alpha'}$
49.5°	$[110]_{\alpha'}$
60.0°	$[110]_{\alpha'}$
60.0°	$[111]_{\alpha'}$

The fcc crystal can transform to a bcc crystal by the observation of Kurdjumov-Sachs (K-S) orientation relationship $\{111\}_{\gamma}||\{011\}_{\alpha'}$, $\langle\bar{1}01\rangle_{\gamma}||\langle 1\bar{1}1\rangle_{\alpha'}$ [53] or Nishiyama-Wassermann (N-W) orientation relationship $\{111\}_{\gamma}||\{011\}_{\alpha'}$, $\langle 1\bar{1}0\rangle||\langle 001\rangle_{\alpha'}$ [105]. However, during the γ to α′-martensite transformation in high Mn steels, the occurrence of K-S orientation relationship was reported most commonly. The formation of twenty-four variants of α′-martensite takes place via the K-S orientation relationship, which is listed in Table 2.6.

Table 2.6 Twenty four α′-martensite variants generated during the phase transformation of γ to α′-martensite via the K-S orientation relationship [110].

α′-martensite variant	**Plane-Direction in γ**	**Plane-Direction in α′-martensite**
V1	$(111)[\bar{1}01]_{\gamma}$	$(011)[\bar{1}\bar{1}1]_{\alpha'}$
V2	$(111)[\bar{1}01]_{\gamma}$	$(011)[\bar{1}1\bar{1}]_{\alpha'}$
V3	$(111)[01\bar{1}]_{\gamma}$	$(011)[\bar{1}\bar{1}1]_{\alpha'}$
V4	$(111)[01\bar{1}]_{\gamma}$	$(011)[\bar{1}1\bar{1}]_{\alpha'}$
V5	$(111)[1\bar{1}0]_{\gamma}$	$(011)[\bar{1}\bar{1}1]_{\alpha'}$
V6	$(111)[1\bar{1}0]_{\gamma}$	$(011)[\bar{1}1\bar{1}]_{\alpha'}$
V7	$(1\bar{1}1)[10\bar{1}]$	$(011)[\bar{1}\bar{1}1]_{\alpha'}$
V8	$(1\bar{1}1)[10\bar{1}]$	$(011)[\bar{1}1\bar{1}]_{\alpha'}$
V9	$(1\bar{1}1)[\bar{1}01]_{\gamma}$	$(011)[\bar{1}\bar{1}1]_{\alpha'}$
V10	$(1\bar{1}1)[\bar{1}01]_{\gamma}$	$(011)[\bar{1}1\bar{1}]_{\alpha'}$
V11	$(1\bar{1}1)[011]_{\gamma}$	$(011)[\bar{1}\bar{1}1]_{\alpha'}$
V12	$(1\bar{1}1)[011]_{\gamma}$	$(011)[\bar{1}1\bar{1}]_{\alpha'}$
V13	$(\bar{1}11)[0\bar{1}1]_{\gamma}$	$(011)[\bar{1}\bar{1}1]_{\alpha'}$
V14	$(\bar{1}11)[0\bar{1}1]_{\gamma}$	$(011)[\bar{1}1\bar{1}]_{\alpha'}$
V15	$(\bar{1}11)[\bar{1}0\bar{1}]_{\gamma}$	$(011)[\bar{1}\bar{1}1]_{\alpha'}$
V16	$(\bar{1}11)[\bar{1}0\bar{1}]_{\gamma}$	$(011)[\bar{1}1\bar{1}]_{\alpha'}$
V17	$(\bar{1}11)[110]_{\gamma}$	$(011)[\bar{1}\bar{1}1]_{\alpha'}$
V18	$(\bar{1}11)[110]_{\gamma}$	$(011)[\bar{1}1\bar{1}]_{\alpha'}$
V19	$(11\bar{1})[\bar{1}10]_{\gamma}$	$(011)[\bar{1}\bar{1}1]_{\alpha'}$
V20	$(11\bar{1})[\bar{1}10]_{\gamma}$	$(011)[\bar{1}1\bar{1}]_{\alpha'}$
V21	$(11\bar{1})[0\bar{1}\bar{1}]_{\gamma}$	$(011)[\bar{1}\bar{1}1]_{\alpha'}$
V22	$(11\bar{1})[0\bar{1}\bar{1}]_{\gamma}$	$(011)[\bar{1}1\bar{1}]_{\alpha'}$
V23	$(11\bar{1})[101]_{\gamma}$	$(011)[\bar{1}\bar{1}1]_{\alpha'}$
V24	$(11\bar{1})[101]_{\gamma}$	$(011)[\bar{1}1\bar{1}]_{\alpha'}$

The Fig. 2.15 shows the hierarchical structure of lath α′-martensite formed with changing C content. In low C steels containing 0-0.4 wt.% C [110, 111], inside a prior γ grain, the α′-martensite laths are organized into crystallographic packets, blocks and laths (Fig. 2.15a). Each packet is divided into blocks which contain laths of the same or similar orientations. Inside a crystallographic packet, all the α′-martensite laths contain the same habit plane and are arranged in a parallel morphology. A twinning relationship may exist between different blocks within a packet. A prior γ grain can transform into four kinds of crystallographic packets containing α′-martensite variants: (i) V1-V6, (ii) V7-V12, (iii) V13-V18 and (iv) V19-V24 (Table 2.4). In low C steels (0-0.4 wt.%) the blocks within a packet are parallel. With an increase in the C content from ~0-0.6 wt.% the block and packet sizes decrease [110]. The blocks are much finer in high C steel (in micron size) compared to lower C steels. Each block in a high C steel with 0.6 wt.% C contains six crystallographic packets with each packet containing laths of a single α′-martensite variant. In medium C steels containing 0.75 wt.% C, the α′-martensite laths are not arranged in blocks of similar orientations as shown in Fig. 2.15b. However, each crystallographic packet contains two twin related variants of lath α′-martensite.

For high C steels containing 1.8 wt.% C the α′-martensite morphology changes to plates as shown in Fig. 2.15c [112]. However, in the plate morphology, the sizes of the plates vary considerably along with their non-parallel arrangement. Plate α′-martensite contains a distinct midrib which is parallel to the growth direction. The width of the plate α′-martensite is restricted by the formation of α′-martensite plates of different orientations near the side of a growing α′-martensite plate. Further on small α′-martensite plates form between two large α′-martensite plates. This is due to the restricted growth of these smaller plates by the presence of large plates. A large fraction of retained γ is observed in high C steels. With increasing the C content to 1.8% the tendency for formation of α′-martensite variant having the same habit plane within a group of plates decreases. The higher C content leads to the formation of lath α′-martensite having twin relation to each other [112].

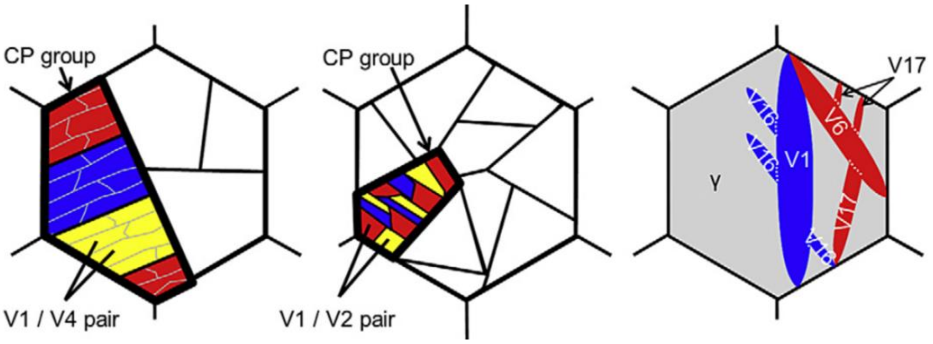

(a) (b) (c)

Figure 2.15: Schematic showing the change in the microstructure of α′-martensite with C content (a) ~0, (b) 0.75 and (c) 1.8 wt.% C [112]. Each colour represents laths with similar α′-martensite orientations/variants. CP: crystallographic packet.

In metastable austenitic stainless steel containing low C ≈0.017 wt.%, the formation of deformation-induced lath and dislocation cell type α'-martensite was observed [99] on cold rolling to 45% thickness reduction [99]. The dislocation cell type α'-martensite is formed upon the subsequent deformation of lath α'-martensite. The diffraction pattern of lath α'-martensite displays a standard pattern similar to that of a single crystal lattice whereas the diffraction pattern from a dislocation cell α'-martensite exhibits ring pattern due to the misorientation between multiple subgrains/cells present within the lath.

2.6 Effect of deformation on the α'-martensite variant selection

Bowles and Mackenzie [113] proposed that change in shape during the formation of an α'-martensite plate can be described by an invariant plane strain along with a small dilatation. It was observed that the atomic displacements involved in α'-martensite formation cannot be achieved via a homogenous strain as the homogenous strain does not convert the initial structure to the final observed structure of α'-martensite. Thus, the simultaneous action of two strains was proposed. The first strain changes the shape of the γ to α'-martensite whereas the second strain changes the crystal structure of γ to α'-martensite. It was proposed that the shape change strain comprises a shear (s) and dilatation (δ) strain components, leaving the habit plane undistorted and unrotated. The second strain that converts the crystal lattice was assumed to be a simple shear via slip or twinning on the slip/twinning planes in the slip/twinning direction. Both the shape and lattice strains were assumed to be an invariant plane strain.

For the formation of α'-martensite, the values of $s \sim 0.22$-0.26 and $\delta \sim 0.03$ are observed which are much larger than the elastic strains. Due to the involvement of deformation, the externally applied stress can influence the total driving force accompanying the transformation. To explain the influence of external stress, Patel and Cohen [114] have proposed the equation

$$U = \sigma_N \delta + \tau s \tag{2.17}$$

where σ_N and τ are the normal and shear stress, respectively, on the habit plane, whereas δ and s are the dilatation and shear components, correspondingly. Therefore, it is expected that during the formation of deformation-induced α'-martensite one or more out of 24 variants will be favoured. During the uniaxial tensile testing, those α'-martensite variants with their habit plane inclined at 45° to the stress axis are favoured [100].

2.7 Kinetics of deformation-induced α′-martensite formation

There are two widely used equations to model the transformation kinetics of γ to deformation-induced α′-martensite.

(i) Guimares *et al.* [25] suggested the following equation

$$f = 1 - \exp(-k\varepsilon^{z}) \qquad (2.18)$$

where f is the volume fraction of deformation-induced α′-martensite, ε is the strain and k, z are constants. In this model, the rate of increase of volume fraction of deformation-induced α′-martensite was observed to change from a linear behaviour to a sigmoidal behaviour with an increase in strain.

(ii) Olson and Cohen [103] introduced the following equation

$$f = 1 - \exp(-\beta(1 - \exp(-\alpha\varepsilon))^{n}) \qquad (2.19)$$

where f is the volume fraction of deformation-induced α′-martensite, ε is the strain, α, β, n are constants. α is the rate of formation of shear bands with strain. β represents the probability of α′-martensite nucleation at the shear band intersection. Both the terms α, β are sensitive to temperature. This model is based on the mechanism of strain-induced α′-martensite nucleation at the intersection of shear bands and hence is more realistic to apply in the present case as shown in Fig. 2.16. It can be noted that the experimentally measured α′-martensite volume fraction matches very closely to that predicted with Eq. 2.9.

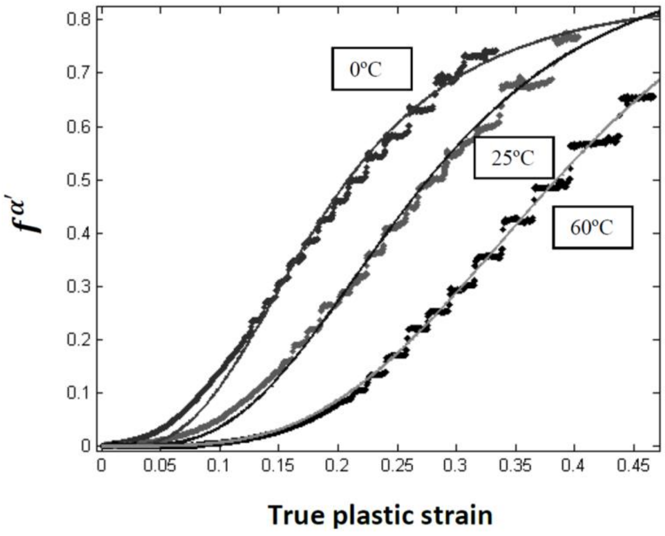

Figure 2.16: Variation in the volume fraction of deformation-induced α′-martensite with a plastic strain in a 304 stainless steel at various deformation temperatures. The solid line and broken line are the predicted (Eq. 2.19) and the experimentally measured α′-martensite volume fraction, respectively [115].

2.8 Effect of cold rolling on the microstructure of high-Mn steels

Lü *et al.* [8, 46] reported the microstructure and texture evolution during cold rolling between 20 and 50% thickness reductions of an Fe-22Mn-0.38C steel. On cold rolling, the γ transforms to ε-martensite with a maximum volume fraction of 28% at 50% thickness reductions. The deformation mechanisms observed during cold rolling were (i) partial slip, (ii) twinning and (iii) γ to ε-martensite transformation. The formation of shear bands was also observed to take place after 43% thickness reduction. Shear bands are regions of localised deformation that takes place when the material hardening rate decreases during the later stages of cold rolling. It was stated that γ to ε-martensite transformation contributed to less than 10% of the total plastic strain whereas partial dislocation slip and twinning were the dominant deformation mechanism. On cold rolling, Lü *et al.* [8] also observed lamellar lines which were ascribed to either slip, twins or ε-martensite. On increasing the thickness reduction to 50%, the lamellar lines were observed to be bent. Haase *et al.* [116] described the formation of deformation twins and slip bands during the deformation of an Fe-28Mn-0.28C steel to 30% thickness reduction.

Fig. 2.17 shows the microstructure evolution with increasing cold rolling thickness reduction of an Fe-26Mn-3Si-3Al steel. During the cold rolling of an Fe-26Mn-3Si-3Al steel to 10% thickness reduction (Fig. 2.17a), Kowalska *et al.* [11] observed the onset of γ to ε and α′-martensite transformation. Further cold rolling to 30% thickness reduction (Fig. 2.17b) led to the formation of deformation twins, more ε and α′-martensite with the presence of γ containing high dislocation density [10]. The twin intersection was observed to be the preferred nucleation site for ε-martensite.

Upon further deformation to 57% thickness reduction (Fig. 2.17c), the microstructure comprised lath α′-martensite with a trace amount of ε-martensite. Gazder *et al.* [7] also revealed that during 66% cold rolling of an Fe-17Mn-2Si-3Al-1Ni-0.06C steel the transformation of γ to (i) ε and (ii) α′-martensite takes place. The cold-rolled microstructure consisted of blocky ε-martensite along with elongated α′-martensite grains and a small amount of remnant γ. The presence of stacking faults in ε-martensite indicating its deformation was also stated in Ref. [7].

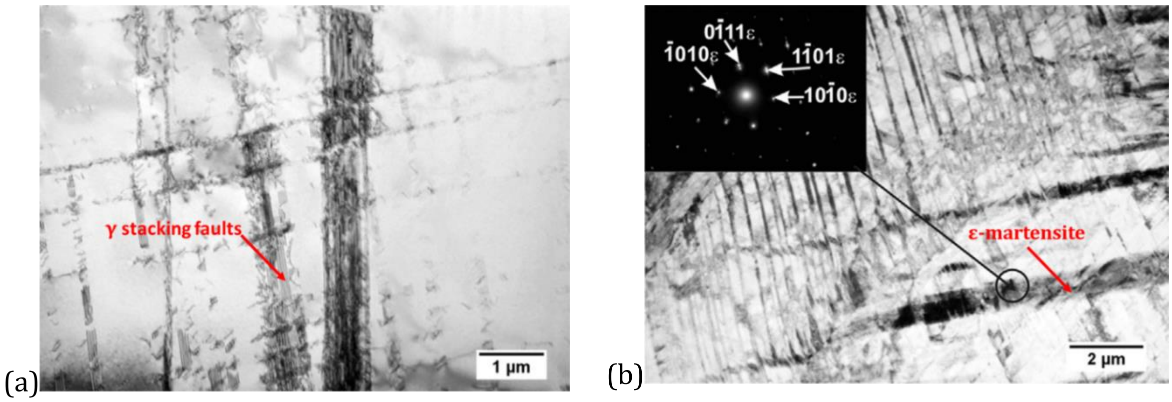

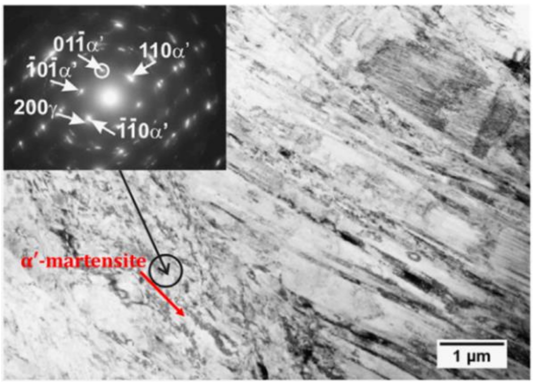

(c)

Figure 2.17: Bright-field transmission electron micrographs showing the microstructure evolution with increasing cold rolling thickness reductions to (a) 10%, (b) 30% and (c) 57% for an Fe-26Mn-3Si-3Al steel [11].

A study conducted by Lü *et al.* [8] by measuring the hardness of ε-martensite for different cold-rolled samples showed the value to remain constant (≈10.5 GPa). The ε-martensite basal $(0001)_\varepsilon$ poles were observed to remain at a constant separation of ~20° deviated from the ND without any $(0001)_\varepsilon$ pole rotation. On the basis of the above observations, Lü *et al.* [8] described ε-martensite to be a hard phase without undergoing any deformation during cold rolling.

Contrary to the above studies, Wenk *et al.* [117] have observed the rotation of the basal $(0001)_\varepsilon$ poles during the compression of hcp ε-iron to 200 GPa pressure. By the application of ViscoPlastic Self-Consistent modelling [117], the above authors suggested that basal slip might be an active deformation mechanism causing the $(0001)_\varepsilon$ pole rotation. The observation of dislocations with a ⟨c⟩ component and deformation bands in ε-martensite during the tensile testing of an Fe-17Mn steel also pointed out to the occurrence of dislocation activity on the $(0001)_\varepsilon$ basal plane [47]. Saleh *et al.* [24] showed ε-martensite to accommodate compressive load during cyclic in-situ neutron diffraction. Using XRD peak analysis of an Fe-17Mn-0.02C steel, an earlier study suggested that ε-ISFs are responsible for the reverse transformation of ε-martensite back to the γ phase during tensile deformation [22].

In the literature [8, 24, 47, 117] there are two opposing views regarding the deformation accommodation by ε-martensite. Lü *et al.* [8] by measuring the hardness of ε-martensite for the cold-rolled samples in addition to measuring the separation of the basal $(0001)_\varepsilon$ poles proposed ε-martensite to be a hard phase without accommodating any deformation during cold rolling. On the other hand, Wenk *et al.* [117] observed the rotation of the basal $(0001)_\varepsilon$ poles during compression of hcp ε-iron. Also, Saleh *et al.* [24] and Gazder *et al.* [7, 48] showed ε-martensite to accommodate compressive stress by cyclic in-situ neutron diffraction and transmission Kikuchi diffraction (TKD)/TEM, respectively. Therefore, a detailed investigation needs to be undertaken to reveal the micro-mechanisms operating during the deformation accommodation in ε-martensite via aberration-corrected transmission electron microscopy.

2.9 Effect of tensile testing on the microstructure of high Mn steels

Ding *et al.* [118] defined four stages of strain hardening during the tensile testing ($\dot{\varepsilon} = 10^{-3}s^{-1}$) of an Fe-18.8Mn-3Al-3Si steel at room temperature as shown in Fig. 2.18a.

(i) Stage 1 (ε = 0 - 0.06)

Elastic region and the onset of yielding in the sample.

(ii) Stage 2 (ε = 0.06 - 0.14), γ to ε-martensite to α′-martensite transformation

The volume percentage of ε and α′-martensite increases in this strain range. The width of the stacking faults increases and the overlapping of the stacking faults is found at the intersection of active slip planes. The formation of ε-martensite takes place through the overlapping of stacking faults. The nucleation of α′-martensite takes place at the intersection of two ε-martensite plates. The further growth of α′-martensite grains takes place by coalescence.

(iii) Stage 3 (ε = 0.14 - 0.35), γ twinning

The volume fraction of γ, ε and α′-martensite remains unchanged but the true stress sharply increases due to the deformation twinning, which was observed in the microstructure. This can be explained by the increase in strain hardening rate as deformation twin boundaries hinder the dislocation motion by acting as obstacles (Fig. 2.18b).

(iv) Stage 4 (ε = 0.35-0.45), γ to α′-martensite transformation

During the loading between 0.35 to 0.45 strains, the volume fraction of (i) α′-martensite increases and (ii) of ε-martensite decreases. This indicates the dominance of (i) γ to α′-martensite and (ii) ε-martensite to α′-martensite transformation. At this stage, nucleation of α′-martensite was also noticed directly in γ at the high-stress concentration regions such as twin/twin, shear-band/shear-band and twin/shear-band intersections [119]. Also, thickening of the existing deformation twins takes place. The α′-martensite formation leads to volume expansion which creates dislocation pile-ups at the interfaces, reducing the interfacial energy (γ/α′-martensite). As the α′-martensite starts to deform, the interface separates easily leading to micro-cracking. The above processes result in the decrease in work hardening rate and eventually failure.

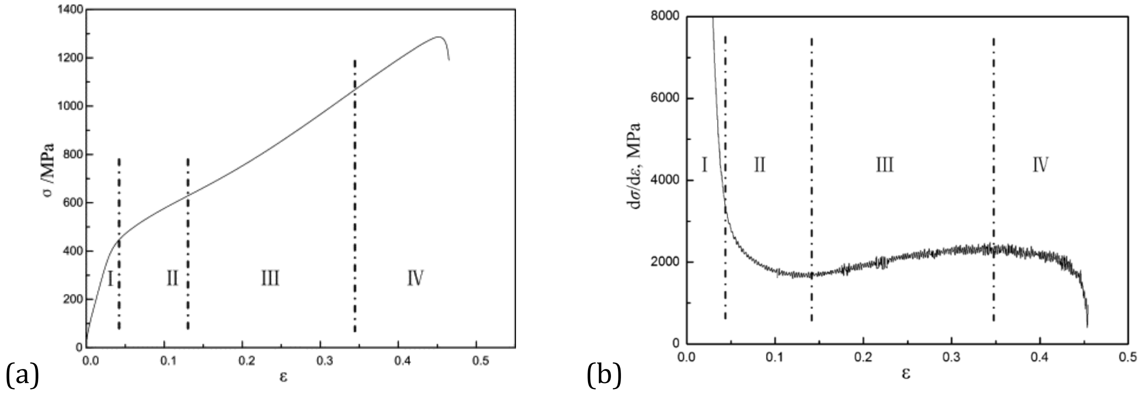

Figure 2.18: (a) Engineering stress-strain curve (b) strain hardening curve for an Fe-18.8Mn-3Al-3Si steel [118].

During a recent study by Chen *et al.* [52], tensile testing of an Fe-15Mn steel having an initial microstructure containing γ and ε-martensite formed upon quenching after annealing led to γ to ε-martensite transformation at lower engineering strains than 0.1 whereas ε to α′-martensite transition was the main deformation mechanism along with slip and tensile twining in ε-martensite at higher engineering strains between 0.1-0.3. The nucleation of α′-martensite was observed at the intersection of two ε-martensite plates. All the α′-martensite grains were found inside ε-martensite grains. Due to ε and α′-martensite transformation the steel showed an excellent combination of UTS of 772 MPa and ductility of 0.42.

Grassel *et al.* [120] stated that during the tensile testing of an Fe-20Mn-3Si-2Al TRIP-TWIP steel the volume fraction of γ decreases and of α′-martensite increases whereas that of ε-martensite remains constant. This indicates the direct transformation of γ to α′-martensite. During the tensile testing ($\dot{\varepsilon} = 4 \times 10^{-4}\,s^{-1}$) of an Fe-15.5Cr-6.1Mn-6.1Ni steel at temperatures between -60 to 200 °C two stages were observed: (a) deformation banding in γ, ε and α′-martensite formation between -60 to 40 °C, (b) ε-martensite formation between 40 and 100 °C and (c) deformation twinning between 100 and 200 °C [121]. The deformation bands were also observed in γ at low temperatures (less than 20 °C) and shown to consist of multiple stacking faults which overlap with increasing amount of deformation. The tensile testing of an Fe-24Mn steel containing coarse γ grains and athermal ε-martensite was also done at (i) 20 °C and (ii) -196 °C [122]. Tensile testing at both 20 and -196 °C leads to the formation of ε-martensite laths, however testing at -196 °C leads to a slight increase in the volume fraction of ε-martensite. The dislocation motion was observed to be planar and localised with the formation of deformation bands with high dislocation densities in γ was also observed during tensile testing at 20 °C. The inhomogeneous dislocation structures also developed within ε-martensite similar to those observed in γ upon tensile testing at 20 °C.

Lee *et al.* [123] studied the tensile deformation behaviour of an Fe-12Mn-0.6C steel. It was reported that the main deformation mechanism changed from ε-martensite formation to deformation-induced twinning with increasing strain rate above 10^{-2} s^{-1}. This resulted in the enhanced work hardening and increased total elongation. This was due to the increase in the critical resolved shear stress (CRSS) for the onset of ε-martensite transformation with increasing strain rate. With increasing strain rate the CRSS of ε-martensite formation became higher than the CRSS of γ twinning leading to the occurrence of deformation twinning in preference to the ε-martensite formation.

2.10 Annealing of cold-rolled high Mn steels

Annealing treatment is an important stage in the industrial production of metals and alloys as it increases ductility by removal of prior defect structure and controls the final microstructure (grain shape and size) and crystallographic texture [124]. Thus, the final mechanical properties of metallic metals and alloys depend on annealing parameters such as temperature, time and heating rate.

During the annealing of high Mn steels, a number of events take place. These include ε and α′-martensite recovery and subsequent reversion, γ recovery, recrystallisation and grain growth. The ε-martensite reversion was shown to occur at a lower temperature (100-250 °C) for the Fe-17Mn-3Al-2Si-1Ni-0.6C steel [40]. The reversion of α′-martensite to γ starts at ~500 °C [40]. At this temperature, the simultaneous occurrence of recovery of the (i) reverted γ from ε-martensite and (ii) retained γ during cold rolling takes place. Annealing at 600 °C leads to the onset of recrystallisation of the retained/reverted γ along with the reversion of α′-martensite. The grain growth of recrystallised γ is also observed to take place. The γ recrystallisation is completed at 700 °C.

2.10.1 Reversion of deformation-induced ε and α′-martensite

Before the onset of the displacive ε-martensite reversion the shrinkage of ε-martensite stacking faults takes place. The ε-martensite reverts to γ via a displacive mechanism in which the reverted γ grain inherits the same shape as the parent ε-martensite grain. The reversion starts within and outside of the parent ε-martensite grain leading to the formation of a thin γ/ε-martensite lamellar structure [34]. Also during the displacive ε-martensite reversion, the transformation start temperature is found to be independent of the heating rate during annealing [8].

There are two possible mechanisms of α′-martensite reversion: (i) displacive and (ii) diffusional. (i) In displacive reversion, the α′-martensite revert to γ via shear without any significant change in the microstructure (grain shape and size) as shown in Fig. 2.19. The reverted γ contains a high density of dislocations which were introduced by the shear reversion [27]. The validation of the K-S orientation relationship between γ/α'-martensite is observed during displacive reversion.

(ii) In diffusional reversion, the reverted γ grains bounded by HAGBs nucleate within α'-martensite grains (Fig. 2.19) and grow by consuming the surrounding α'-martensite grains. The K-S orientation relationship is observed between γ and α'-martensite during diffusional reversion.

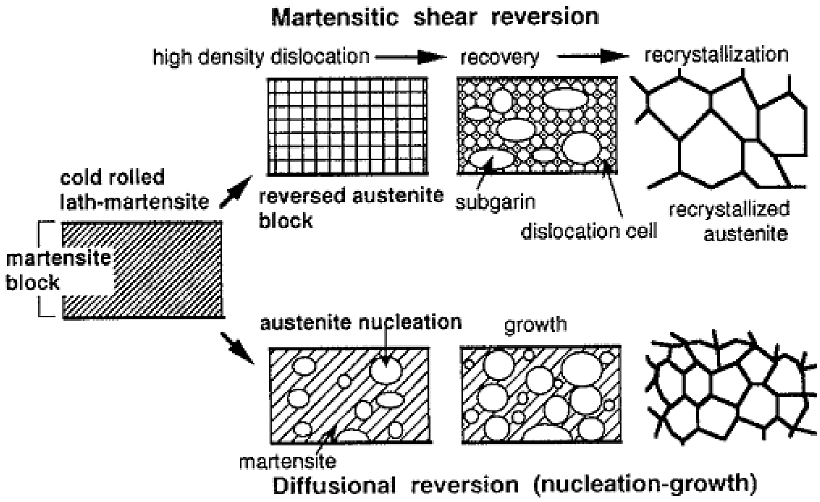

Figure 2.19: Illustration of the two α'-martensite reversion mechanisms [27].

The occurrence of displacive and diffusional α'-martensite reversion mechanisms depends on factors such as (i) heating rate [29], (ii) annealing temperature/change in free energy and (iii) α'-martensite morphology [125]. Heating rates higher than 10 °Cs^{-1} was reported [29, 126] to favour displacive transformation due to less available time for diffusion of different elements. For displacive α'-martensite reversion, the reversion temperature is independent of the heating rate. The free energy required for displacive reversion is higher than that for diffusional reversion [97]. So, annealing at high temperatures, favours the displacive α'-martensite reversion mechanism. The higher ratios of γ/α stabilisers were shown to increase the free energy change, thus reducing the critical temperature for displacive α'-martensite reversion [27]. Lath α'-martensite with randomly arranged dislocations was reported to transform via displacive transformation [125, 127], whereas the one with dislocation cell structure has undergone diffusional transformation [125] during annealing.

During the operation of diffusional α'-martensite reversion, a wide range of γ grain sizes is observed [128]. This is due to the dependence of reverted γ grain nucleation on the α'-martensite morphology. The presence of both types of α'-martensite within the same sample can be ascribed to 90% thickness reduction during cold rolling in which some of the already formed lath type α'-

martensite transforms to dislocation cell type α′-martensite by an increase in dislocation density to accommodate deformation. Thus, for a fixed annealing time, the γ nucleates and grows preferentially earlier in dislocation cell α′-martensite containing a density of dislocation and slip bands compared to lath α′-martensite leading to a wide range of γ grain sizes.

Escobar *et al.* [40] studied the reversion of ε and α′-martensites occurring in an Fe-17Mn-3Al-2Si-1Ni-0.06C steel using dilatometry and indicated the reversion temperature range of ε and α′-martensites to be 100-250 °C and 500-700 °C, respectively. The reversion temperature range of α′-martensite is the same as the recrystallisation of reverted γ (600-700 °C) during isochronal heating.

The reversion temperature range of ε-martensite was measured to be 200-375 °C and 100-250 °C for 57% cold-rolled Fe-22Mn-0.38C and 45% cold-rolled Fe-17Mn-3Al-2Si-1Ni-0.06C steels, respectively. The reversion temperatures were determined by dilatometry heating experiments with a heating rate of $1 °Cs^{-1}$. The reversion temperatures of ε and α′-martensite remained unchanged when the cold rolling thickness reductions increased from 35% to 81% [129] indicating the transformation to occur by the displacive mechanism. Gazder *et al.* [7] described the incomplete reversion of α′-martensite to γ during the isochronal annealing of 66% cold-rolled Fe-17Mn-3Al-2Si-1Ni-0.06C steel at 625 °C for 300 s. The annealed microstructure consisted of predominantly γ along with α′-martensite. The presence of a trace amount of ε-martensite was also observed along the γ grain boundaries. During the annealing of 66% cold-rolled Fe-17Mn-3Al-2Si-1Ni-0.06C steel at 625 °C for 5 min, the reverted γ was found to be encircled by α′-martensite grains [7]. The displacive reversion of α′-martensite was also observed in a 73.5% cold-rolled Fe-16Cr-10Ni-0.008C stainless steel annealed at 900 °C for 1 s [130] and in a 90% cold-rolled Fe-18Cr-9Ni steel (with C content less than 0.005 wt.%) annealed at 750 °C for 10 s [27].

During the annealing of 98 % cold-rolled Fe-33.5Ni alloy initially containing γ and α′-martensite the formation of γ-twins was witnessed [35]. In that study, the formation of fine γ-twins was observed after heating to 50 °C above the α′-martensite reversion finish temperature. Furthermore, γ-twin was observed during the in-situ TEM annealing of an Fe-5Mn-0.2C steel at 650 °C [33]. Kowalska *et al.* [10] noted the formation of deformation-induced α′-martensite after 57% thickness reduction. Upon annealing at 500 °C for 30 min, the α′-martensite transformed to reverted γ containing fine twins as shown in Fig. 2.20. The formation of fine twins was also reported during the early stages of annealing of other cold-rolled low SFE fcc materials, such as brass [131, 132] and Co-Cr-Mo alloy [133]. However, in all the previous studies [33, 35, 131-133] the mechanism of formation of these fine twins was not clearly stated which needs to be explored.

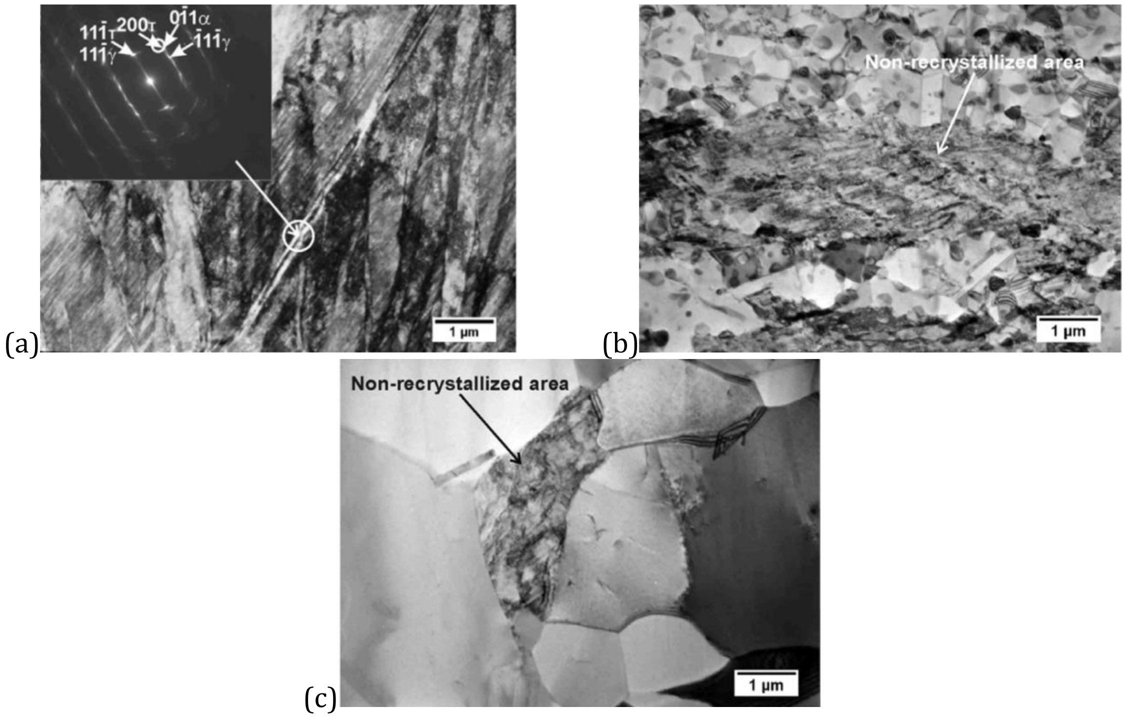

Figure 2.20: Bright-field transmission electron micrographs of an Fe-26Mn-3Al-3Si steel showing the microstructure evolution after cold rolling to 57% thickness reduction and isochronal annealing for 30 min at (a) 500 °C, (b) 650 °C and (c) 750 °C, respectively [10].

In-situ annealing studies of ε and α′-martensite were also undertaken using TEM [30-32, 34]. They showed that the reversion of ε-martensite also occurred via a displacive mechanism. The key features of this included the formation of γ/ε-martensite lamellar structure due to the onset of reversion within and outside of the ε-martensite grains during in-situ annealing of an Fe-24Mn-6Si shape memory alloy [34]. The reverted γ was observed to contain dislocations in which the cross slip of dislocations was noted. An in-situ TEM isothermal annealing study of an Fe-20Ni-5.4Mn alloy at 560 °C for holding duration of 0, 30 and 135 s containing lath α′-martensite showed that the γ/lath α′-martensite interface migrates by the fast motion in a direction normal to the γ/α′-martensite interface and by a slow lateral motion of the ledges (Fig. 2.21) [30]. The dislocations were also observed to move along the ledge and normal to the γ/α′-martensite interface.

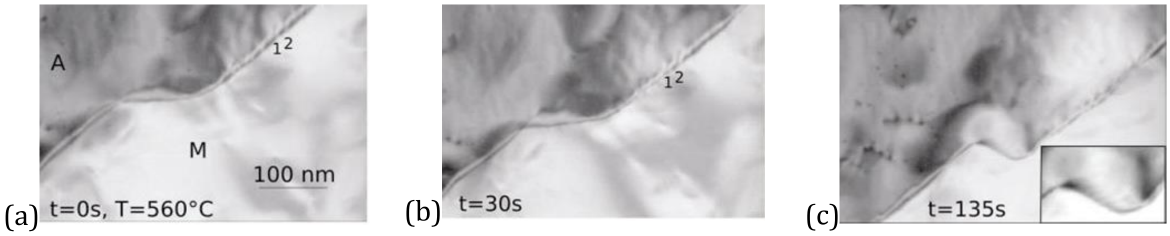

Figure 2.21: Bright-field transmission electron micrographs showing the motion of γ/α′-martensite interface during the isothermal in-situ annealing at 560 °C for (a) 0 s, (b) 30 s and (c) 135 s [30].

For an Fe-5Mn-0.2C steel processed by annealing at 1200 °C for 1800 s followed by quenching to produce α′-martensite, in-situ annealing at 650 °C showed the reversion of α′-martensite to occur via the nucleation and growth at the α′-martensite lath boundaries [33]. The ex-situ annealing at 700 °C on the Fe-17Mn-3Al-2Si-1Ni-0.06C steel showed the reversion of ε and α′-martensite to γ [134]. However, the ε and α′-martensite reversion mechanisms was not explored in details. It was reported [125, 135, 136] that the ε and α′-martensite reversion mechanisms change with the chemical composition of metastable austenitic steels. Thus, it is important to study the reversion mechanism in high Mn steels. To the best of our knowledge, the literature does not contain any in-situ TEM based annealing study of ε and α′-martensite reversion in high Mn steels. Therefore, the study of the evolution of the microstructure to determine the ε and α′-martensite reversion mechanisms during the in-situ annealing of high Mn steel is essential.

2.10.2 Recovery, recrystallisation and grain growth of reverted γ

On annealing, the recovery of reverted γ takes place. Recovery is the process by which the γ grains reduce their internal stored energy by the annihilation of excess defects and the rearrangement of dislocations resulting in the formation of dislocation cell structure, which is bounded by low-angle grain boundaries (LAGBs). LAGBs are defined as boundaries that have a misorientation angle between 2° and 15°. No long-range migration of HAGBs with misorientation angle greater than 15° takes place during recovery. Recovery is followed by γ recrystallisation. Recovery proceeds spontaneously, whereas recrystallisation requires an incubation period to develop a nucleus. In low SFE materials recovery is very limited due to the large separation between the Shockley partial dislocations hindering the rearrangement of dislocations. The driving force for recrystallisation is the stored energy of cold deformation. In a fully recovered/polygonised microstructure, the stored energy is assumed to be in the dislocations present in the cell walls.

The mechanisms of static recrystallisation can be of two types:

(i) In continuous recrystallisation, there is no long-range migration of HAGBs. Continuous recrystallisation occurs by coarsening of subgrains as shown in Fig. 2.22 [137]. The dislocation cells developed during recovery, coarsen leading to the formation of subgrains. As more dislocation merging takes place at subgrain walls, the LAGBs transform to HAGBs [124]. This process is characterised by a gradual buildup of the grain boundary misorientation.

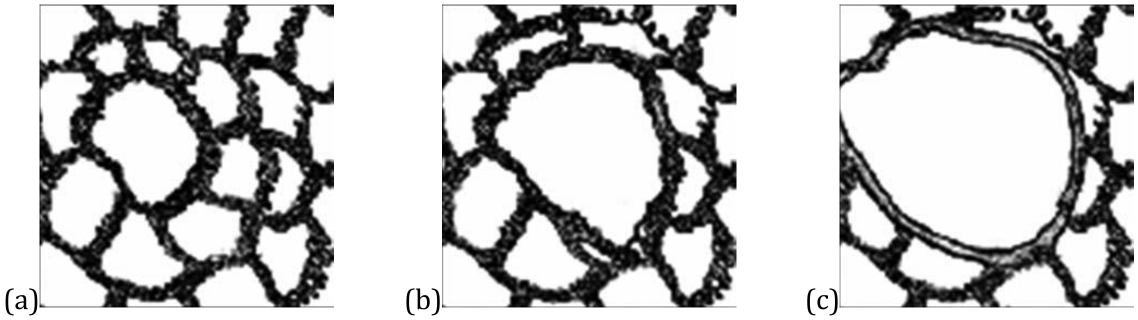

Figure 2.22: Schematic showing the evolution of microstructure during continuous recrystallisation for (a) initial subgrain structure, (b) the middle subgrain growth over the smaller ones and (c) boundary of the middle subgrain free from defects [137].

(ii) Discontinuous recrystallisation occurs by the nucleation of new strain-free grains by grain boundary bulging, which consumes the deformed elongated grains to produce the recrystallised grain structure. The boundary of the recrystallised nucleus moves into the deformed grain to form a strain-free region which leads to the decrease in the number of deformed grains [138, 139]. The various stages of discontinuous recrystallisation is shown in Fig. 2.23.

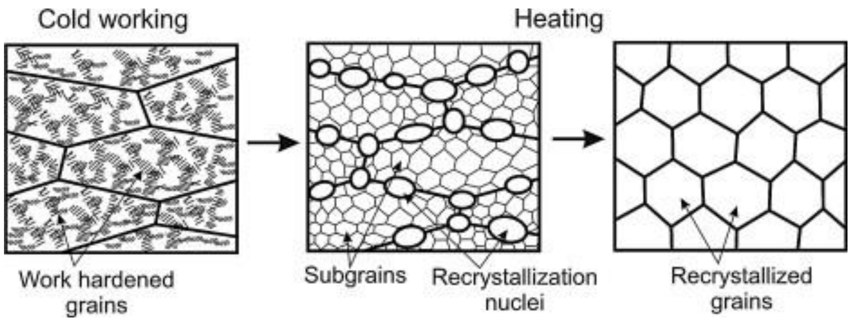

Figure 2.23: Schematic showing the discontinuous static recrystallisation of cold-rolled metals [140].

The conditions required for a potential nucleus to grow are the possession of HAGBs due to their high mobility, a minimum size for growth and the presence of a non-uniform distribution of dislocations around the newly formed nuclei [124]. Generally, during recrystallisation, the formation of nuclei with HAGBs takes place [25, 124, 140]. Due to the difficulty in the simultaneous attainment of the above three conditions, the nuclei are observed to form in regions of high local strain. Some of the most common nucleation sites are HAGBs, transition band, highly misoriented deformation zones around particles and misoriented regions within shear bands.

To date, there are no publications on the exclusive study of the recovery of reverted γ. Lü *et al.* [46] reported that on isothermal annealing of an Fe-21.6Mn-0.38C steel at 560 °C for 600 and 1800 s, the nucleation of new strain-free γ grains takes place at shear bands and grain boundary triple junctions. The nucleation near the vicinity of (i) deformation twins and (ii) at the intersection of twins and shear bands were also observed. The growth rate of the nucleus was not constant and decreased with increasing annealing time during isothermal annealing. This was attributed to the decrease in the driving force. Site saturated nucleation was reported during the isothermal annealing at both 560 and 700 °C by observing optical microstructures from relatively large areas (670 × 540 μm^2). The partial reversion together with the onset of recrystallisation during the isochronal annealing of a 66% cold-rolled Fe-17Mn-2Si-3Al-1Ni-0.06C steel at 625 °C, 300 s was observed [7]. Kowalska *et al.* [10] observed the onset of γ recrystallisation after annealing for 30 min at 650 °C of an Fe-26Mn-3Al-3Si steel cold-rolled to 57% thickness reduction. However, after annealing at 750 °C for 30 min the completion of recrystallisation was not observed.

Haase *et al.* [141] observed the nucleation of γ grain in the vicinity of prior HAGBs and triple junctions during the annealing at 700 °C for a 30% cold-rolled Fe-28Mn-0.28C steel. Relatively fewer nucleation sites were detected inside the γ grains such as the intersection of slip bands and deformation twin bundles. The γ nucleus is observed to develop from γ subgrains or dislocation cells containing HAGBs with the neighbouring deformed γ grain. Subsequently, the nuclei grew by local grain boundary bulging into the neighbouring deformed γ grain.

After the completion of recrystallisation, the grain growth of γ grains takes place. The driving force for grain growth is to reduce the surface energy associated with grain boundary. The grains grow in size with their number and grain boundary area decreases, thus the total surface energy is reduced. During γ grain growth, the curvature-driven grain boundary migration, i.e. the motion of the grain boundaries towards the centre of their curvature, takes place (Fig. 2.24). During γ grain growth random HAGBs are observed to grow at a higher rate as compared to the LAGBs [124]. In particular, HAGBs having a misorientation of 40° across the ⟨111⟩ axis was observed to possess a very high mobility. For LAGBs, vacancy diffusion between dislocations is the mobility determining factor, whereas for a HAGB the jump of atoms from the shrinking to growing grain is the mobility determining factor.

However, if all the grain boundaries are assumed to have the same energy then, the equilibrium orientation of the boundaries shall be obtained when the boundaries meet each other at 120° (Fig. 2.24).

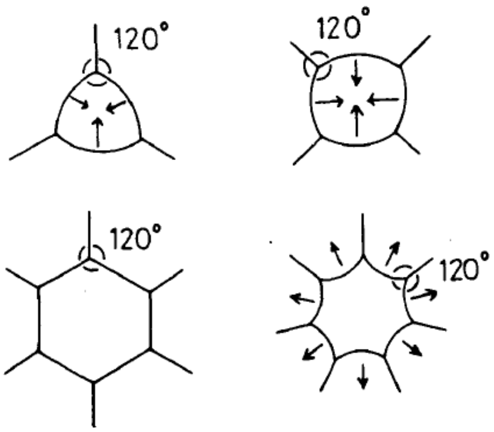

Figure 2.24: Effect of grain boundary curvature on grain growth [97].

The driving force for grain growth can be quantified as

$$\Delta G = \frac{2\gamma V_m}{D} \tag{2.20}$$

where ΔG is the driving force created due to grain boundary curvature, V_m is the molar volume, γ is the surface energy, D is the grain size. Thus, fine-grained γ is more susceptible to grain growth [142].

The grain growth during isothermal annealing is usually quantified by the equation

$$d_t - d_0 = \left(A\exp\left(-\frac{Q}{RT}\right)\right) * t \tag{2.21}$$

where d_t is the grain size after time t, d_0 is the initial grain size (at t = 0), Q is the activation energy of grain growth, T is the temperature, t is the time and A is a constant. Due to the presence of ε and α′-martensite that formed during the quenching from high temperature after annealing, it is difficult to determine accurately the γ grain size. This may lead to the inaccurate determination of γ grain growth activation energy.

The studies of γ grain growth in an Fe-22Mn steel have shown a sluggish grain growth at temperatures below 1000 °C, thus yielding a high activation energy value of 363 ± 60 kJ/mol [143]. The grain growth in an Fe-22Mn steel resulted in the increase from 14 to 40% in the annealing twin area percentage [143]. The γ grain growth studies during the isothermal annealing of an Fe-29.2Mn-5.2Al steel at 1000 °C between 300 and 1800 s demonstrated a fast grain growth, which yielded a lower activation energy of 208 kJ/mol [144]. During the γ grain growth in high Mn steels, the formation of Σ3 boundaries (annealing twins) with misorientation $60°\langle 111\rangle_\gamma$ and Σ9 (secondary twins) boundaries with misorientation $38.9°\langle 101\rangle_\gamma$ are commonly observed as shown in the misorientation angle distribution in Fig. 2.25. The Σ9 boundaries can form by the impingement of two Σ3 boundaries at a triple junction [145]:

$$\Sigma 3 + \Sigma 3 \rightarrow \Sigma 9 \tag{2.22}$$

During the annealing of low SFE materials generally, a large fraction of Σ3 boundaries and low fraction of Σ9 boundaries are obtained.

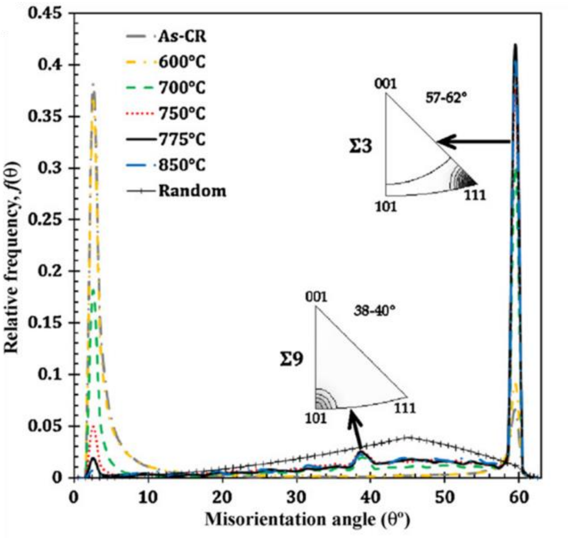

Figure 2.25: Misorientation angle distribution showing the occurrence of Σ3 and Σ9 boundaries [146].

2.11 Tensile properties of high Mn steels

Table 2.7 is a literature-based summary of the tensile properties according to the steel processed via (i) solution treatment and hot rolling followed by air cooling/water quenching or, (ii) solution treatment, hot rolling, cold rolling and annealing.

In the case of the first processing route (i) high Mn steels typically containing ≈19-24 Mn wt.% and the initially single-phase γ which transforms to α′+ ε-martensite during tensile testing, return 600-1020 MPa UTS and 0.66-0.86 total elongation [23, 147, 148]. Initially, dual-phase γ + ε-martensite containing high Mn steels (≈15-20 Mn wt.%) transform to α′ + ε-martensite during tension with 574-1234 MPa UTS. The latter range of UTS values for dual-phase steels is higher than that for single-phase γ containing steels [21, 26, 28, 37-39, 52]. In case of Ref. [37], an initially dual-phase γ + ε-martensite microstructure obtained after solution treatment, water quenching and hot rolling transformed to ε-martensite during tension and returned a UTS of 842 MPa. Alternatively, when the same steel was processed by solution treatment, liquid nitrogen quenching and hot rolling, the same dual-phase microstructure transformed to α′ + ε-martensite on tension and recorded a higher UTS of 924 MPa [38]. Initially multiphase high Mn steels with γ + ε + α′-martensite and/or α phases are composed of ≈9-19Mn, 2.4-3Al, ≈3Si and transform to α′ + ε-martensite during tension with 728-1437 MPa UTS. The latter value is higher than those of steels containing initially single or dual-phase microstructures [21, 118, 149-151].

In the case of further processing via cold rolling and annealing, initially single-phase γ steels containing ≈12-24Mn and 0.12-0.32C transform to α′ and/or ε-martensite during tension with 698-822 MPa UTS [9, 36, 81, 152]. Initially dual-phase γ + ε-martensite/α steels with ≈23-5Mn and 0.08-0.32C transform to α′ + ε-martensite after tension with 696-1547 MPa UTS [9, 36, 153-158]. Multiphase high Mn steels containing ≈4-17 Mn with initially γ + ε + α′-martensite microstructures transform to α′+ ε-martensite during tension with 856-1378 MPa UTS, which is higher than the UTS for similarly processed single and dual-phase high Mn steels [159-161]. Alternatively, other metastable multiphase steels with γ + ε + α′-martensite initial phases and carbides/carbonitrides within γ are composed of ≈9-10 Mn and record even higher 1193-1360 MPa UTS. The higher UTS values are ascribed to precipitation hardening [149, 155]. Frommeyer *et al.* [21] studied the uniaxial tensile behaviour of an Fe-20Mn-3Al-3Si steel and stated high UTS (1100 MPa) and total elongation of ≈0.55 values as due to γ to ε and α′-martensite. Similar transformation behaviour of γ to ε-martensite to α′-martensite, γ to α′-martensite was described upon the tension of Fe-23.8Mn steel [148]. During the tension of the Fe-15Mn-3Al-3Si and Fe-20Mn-3Al-3Si steels, extensive γ-twinning and γ to ε-martensite transformation were reported [162] leading to a high strain hardening rate.

Table 2.7 clearly shows that for high Mn steels that have only been processed by solution treatment and hot rolling, further processing by cold rolling and annealing leads to higher UTS and total elongations on account of grain refinement in the latter case. Furthermore, an initially dual-phase Fe-23.4Mn-0.03Al-0.06Si-0.08C steel with approximately equal area fractions of reverted/recrystallised γ and ε-martensite returns a UTS of 844-875 MPa [9]. On the other hand, the same steel comprising an initially fully recrystallised γ microstructure returns UTS of only 792 MPa. It follows that the reverted microstructures possess higher UTS than their fully recrystallised counterparts.

Table 2.7 Tensile properties of metastable Mn steels in literature.

Composition										**Solution HT**			**HR**		**Other**	**CR**	**Annealing**			**Other**	**Phases**		**LT(°C)**	**Speed(mm/min)**	**$\dot{\varepsilon}$($s^{-1} \times 10^{-3}$)**	**YS(MPa)**	**UTS(MPa)**	**e_u**	**e_f**	**Ref**
Mn	Al	Si	Ni	Mo	Cr	V	Nb	C	N	T(°C)	t (h)	Med	T(°C)	R (%)		R(%)	T(°C)	t (h)	Med		Before	After								
23.8	2.7	3						0.6		1100	1	WQ		-							γ	α′+γ	RT	1.5	1	339	666	≈0.67	≈0.8	[148]
23.3	1.9	2.1					0.017		0.008	1230	1		1150								γ	α′+ε+γ	-75	-	1	220	800	0.72	0.86	[147]
19.1	1.8				4.4			0.07		1200	0.5		1200	88			1000	1	WQ		γ	γ+ε+α′	-273	0.42	0.14	195	1020	-	0.68	[23]
19.1	1.8				4.4			0.07		1200	0.5		1200	88			1000	1	WQ		γ	α′+ε+γ	RT	0.42	0.14	160	600	-	0.66	[23]
20.1	2.9	2.8													S(77%)		1000	2	WQ		γ+ε	α′+γ+ε	RT	-	0.1	289	764/1365‡	0.58	-	[21]
20	3	3								1000	2				S(77%)						γ+ε	α′+γ+ε	100	-	1	184	574	0.68	0.78	[26]
20	3	3								1000	2				S(77%)						γ+ε	α′+γ+ε	22	-	1	268	≈600	0.73	0.85	[26]
20	3	3								1000	2				S(77%)						γ+ε	α′+γ+ε	-200	-	1	393	1234	0.45	0.5	[26]
17.8		5.2						0.35		1100	0.67				F						γ+ε	γ+ε+α′		2	0.667	425	918/1111‡	0.21/0.19‡	-	[28]
17								0.3		1000	1	WQ	1000								γ+ε	ε+γ	100	-	0.170	259	842	0.71	-	[37]
17								0.3		1000	1	WQ	1000								γ+ε	ε+γ	RT	-	0.170	180	730	0.11	-	[37]
17								0.3		1000	1	WQ	1000								γ+ε	ε+γ	0	-	0.170	197	720	0.06	-	[37]
17								0.3		1000	1	LNQ	1000								γ+ε	α′+ε+γ	100	-	0.170	381	924	-	0.21	[38]
17								0.3		1000	1	LNQ	1000								γ+ε	α′+ε+γ	RT	-	0.170	236	752	-	0.13	[38]
17								0.02		1150	2		1150	55							γ+ε	ε+γ+α′	-273	0.8	1	558	1073	0.65	0.75	[39]
17								0.02		1150	2		1150	55							γ+ε	ε+γ+α′	RT	0.8	1	343	691	0.25	0.26	[39]
15		0.02						0.005		1200	2		1150				900	5	WQ		γ+ε	α′+γ+ε	RT	3	1.25	≈450	≈773	0.35	0.39	[52]
18.8	2.9	2.9						0.04		1150	2		1150	91	F		1100	1	WQ		γ+α′+ε	α′+γ+ε	RT	-	1	420	829/1300‡	0.57/0.45‡	-	[118]
15.3	2.4	2.9						0.07	0.002	1100	2	AC	900	80			900	0.167	WQ		ε+γ+α′	α′	RT	0.6	0.2	332	1165	0.33	0.35	[150]
12													1100	83							γ+ε+α′	α′+ε+γ	RT	7.5	10	309	943/1032‡	0.09/0.09‡	0.21	[93]
12													1100	83							γ+ε+α′	α′+ε+γ	-150	7.5	10	548	1237/1395‡	0.13/0.12‡	0.22	[93]
12													1100	83							γ+ε+α′	α′+ε+γ	-196	7.5	10	676	1437/1704‡	0.19/0.17‡	0.25	[93]
19.6	3.1	2.9								1100	24		1200	70			900	1			γ+α+α′	α+α′+γ+ε	RT	-	-	397	781/1177‡	0.5/0.41‡	-	[151]
19.6	3.1	2.9								1100	24		1200	70			1000	1			γ+α+α′	α+α′+γ+ε	RT	-	-	336	728/1166‡	0.6/0.47‡	-	[151]
16	3	2.8								1100	24		1200	70			900	1			γ+α+α′	α+α′+γ+ε	RT	-	-	595	994/1303‡	0.31/0.27‡	-	[151]
16	3	2.8								1100	24		1200	70			1000	1			γ+α+α′	α+α′+γ+ε	RT	-	-	558	963/1301‡	0.35/0.3‡	-	[151]
9								0.05		1200	2		900				620	0.167			γ+α+Fe_3C	γ+α+α′+Fe_3C	RT	0.15	1	830	1034	≈0.18	0.27	[149]
15.8	3	2.9													S(77%)		1000	2	WQ		γ+α+α′+ε	α+α′+ γ+ε	RT	-	0.1	406	1073/1585‡	0.48/0.39‡	-	[21]
24.1					0.008			0.12	0.02	1200	24		1150			33	1000	0.5	AC		γ	γ+ε	42	0.9	1	168	772/1175‡	0.42‡	-	[152]
22	3	3											1100			50	900	0.5			γ	γ+ε	-	-	0.4	290	698/1199‡	0.54‡	-	[81]
16.8	1.5	0.03						0.32		1150	5		1150	96		50	600	0.033			γ	-	RT	1.8	1	434	822	0.48	0.54	[9]
12	3							0.3					-			50	750	0.167			γ	γ+α′	RT	1.5	1	429	785	0.28	-	[36]
23.4	0.3	0.06						0.08		1150	5		1150	96		50	350	0.033		5%†	γ+ε	-	RT	1.8	1	254	844	0.276	0.28	[9]
23.4	0.3	0.06						0.08		1150	5		1150	96		50	550	0.083		5%†	γ+ε	-	RT	1.8	1	220	875	0.326	0.33	[9]
23.4	0.3	0.06						0.08		1150	5		1150	96		50	800	1			γ+ε	-	RT	1.8	1	279	792	0.205	0.21	[9]
23.4	0.3	0.06						0.08		1150	5		1150	96		50	800	1		5%†	γ+ε	-	RT	1.8	1	496	869	0.22	0.22	[9]
16.8	1.5	0.03						0.32		1150	5		1150	96		50					γ+ε	-	RT	1.8	1	1278	1547	0.014	0.03	[9]
16.8	1.5	0.03						0.32		1150	5		1150	96		50	350	0.033			γ+ε	-	RT	1.8	1	1249	1541	0.014	0.03	[9]

16.8	1.5	0.03						0.32		1150	5		1150	96		50	550	0.033			γ+ε	-	RT	1.8	1	1140	1331	0.022	0.07	[9]
16					4			0.1								20	700	0.0028			γ+ε	-	RT	1.5	1	780	1190	-	0.42	[153]
16					4			0.1								35	700	0.28			γ+ε	-	RT	1.5	1	890	1340	-	0.41	[153]
16					4			0.1								50	700	0.28			γ+ε	-	RT	1.5	1	970	1380	-	0.37	[153]
15.9					3.9			0.09					900			17	700	0.283	LNQ		γ+ε	α′+γ+ε	-	-	1	543	1222/1700‡	0.33‡	-	[154]
10.6		0.36		0.28				0.08	0.003	1200	1		1200			50	610	0.133	WQ		γ+α	α′+ε+γ+α		1.5	1	1080	1390	-	0.27	[163]
10	3	2						0.3					1200			50	800				γ+α	α′+α+γ	-	-	1	862	1128	0.63	0.64	[156]
6.1	2.2	1.6				0.23		0.29		-							810	0.167	WQ		γ+α	α′+α+γ		-	1	711	1530	0.19	0.2	[157]
5								0.1					-			70	650	18	AC		γ+α	α′+α+γ	RT	-	0.250	410	696	-	~0.4	[158]
10.6		0.36		0.28				0.08		1200	1		1200			50	550	2	WQ		γ+α+ $V_4(C,N)_3$	α′+ε+ γ+α +$V_4(C,N)_3$	-	1.5	1	1240	1360	-	0.09	[163]
9	0.08	0.3						0.05		1200	2		900			60	620	0.167			γ+α+Fe_3C	α′+α+γ+Fe_3C	RT	0.15	0.1	1060	1193	≈0.23	≈0.3	[149]
17	3	2	1					0.06		1100	2		1070	50		45					α′+ε+γ	-	RT	-	1	1200	-	0.01	0.02	[159]
17	3	2	1					0.06		1100	2		1070	50		45	700	0.083			γ+ε+α′	-	RT	-	1	650	920	0.35	0.42	[159]
17	3	2	1					0.06		1100	2		1100	52		42					γ+ε+α′	γ+ε+α′	RT	2.1	1	1080	1135/1157‡	0.02/0.02‡	0.05	*
17	3	2	1					0.06		1100	2		1100	52		42	500	0.083			γ+α′	γ+α′	RT	2.1	1	1075	1150/1173‡	0.02/0.02‡	0.42	*
17	3	2	1					0.06		1100	2		1100	52		42	625	0.083			γ+ε+α′	α′+ε+γ	RT	2.1	1	810	1006/1237‡	0.26/0.23‡	0.02	*
17	3	2	1					0.06		1100	2		1100	52		42	700	0.083			γ+ε+α′	α′+ε+γ	RT	2.1	1	465	856/1121‡	0.36/0.31‡	0.25	*
13								0.1					-			67	580	0.167			γ+ε+α′	-	-	2	-	1231	1257	0.17	0.33	[160]
13								0.1					-			67	600	0.167			γ+ε+α′	-	-	2	-	1007	1296	0.2	0.21	[160]
13								0.1					-			67	620	0.167			γ+ε+α′	-	-	2	-	561	1321	0.24	0.3	[160]
13								0.1					-			67	640	0.167			γ+ε+α′	-	-	2	-	484	1378	0.23	0.26	[160]
4.6		0.003						0.092					1200			70	670	1	AC		α+γ+α′	α+α′+γ	-	24	8	-	950	≈0.16	0.18	[161]
4.6		0.003						0.092					1200			70	670	2	AC		α+γ+α′	α+α′+γ	-	24	8	-	951	≈0.18	0.21	[161]
4.6		0.003						0.092					1200			70	670	4	AC		α+γ+α′	α+α′+γ	-	24	8	-	933	≈0.16	0.19	[161]
4.6		0.003						0.092					1200			70	670	5	AC		α+γ+α′	α+α′+γ	-	24	8	-	959	≈0.16	≈0.2	[161]
4.6		0.003						0.092					1200			70	670	7	AC		α+γ+α′	α+α′+γ	-	24	8	-	868	0.21	≈0.3	[161]
4.6		0.003						0.092					1200			70	670	8	AC		α+γ+α′	α+α′+γ	-	24	8	-	977	0.13	0.14	[161]
4.6		0.003						0.092					1200			70	670	9	AC		α+γ+α′	α+α′+γ	-	24	8	-	961	0.14	0.16	[161]
4.6		0.003						0.092					1200			70	670	10	AC		α+γ+α′	α+α′+γ	-	24	8	-	950	0.13	0.14	[161]

Legend: HT = heat treatment, T = temperature, Med= medium, AC= air cooling, WQ= water quenching, LNQ= liquid nitrogen quenching, HR =hot rolling, CR =cold rolling, R = reduction, γ = austenite, ε = epsilon martensite, α′ = alpha martensite, LT = loading temperature, $\dot{\varepsilon}$ = initial strain rate, YS = yield stress , UTS = ultimate tensile strength (engg), e_u = uniform elongation, e_f = total elongation, ‡ = true stress/strain, * = present work, † = tension. The order of phases are in their decreasing amount of volume fraction.

2.11.1 Digital image correlation studies of metastable austenitic steels

Tension complemented with DIC is a viable tool to investigate the deformation accommodation and/or phase transformation behaviour in high Mn steels [164, 165]. In this regard, several authors [166-170] have used microscopic-DIC (μ-DIC) technique to measure the strain distribution in the microstructure upon tension. The difference between conventional DIC and μ-DIC is that the former is done on optical images whereas the latter is done on in-situ scanning electron microscopy (SEM) images of the sample surface upon tension. The μ-DIC provides higher resolution imaging of the phase and defect structure associated with the microstructure. However, the field of view of μ-DIC is restricted compared to conventional DIC. For conventional DIC, the tensile sample is sprayed upon with black and white paint to create a speckle pattern. However, in μ-DIC, the electropolished sample surface is coated with a ≈50 nm thick layer of gold [171, 172]. The sample is then heated at 350 °C for 90 min in a humid atmosphere. This leads to the redistribution of the gold particles creating a speckle pattern. The strain distribution was calculated by the geometric changes in the speckle pattern upon tension. As heating to 350°C will result in the reverse transformation of ε-martensite, the μ-DIC is not suitable to study the mechanical behaviour of steels containing ε-martensite in the initial microstructure.

The DIC study on the metastable austenitic stainless steel comprising γ showed the development of regions of high axial and shear strains along the gauge length corresponding to localised areas undergone a phase transformation to α′-martensite [170]. DIC investigation on an Fe-10.3Mn-2.9Al-0.2C steel comprising an α+γ starting microstructure showed the localised transformation of γ to α′-martensite during the propagation of PLC bands [173]. Similar observations were also reported for a dual-phase α+γ Fe-5Mn-2.5Al-0.2C steel [174]. The μ-DIC studies on α/α′-martensite dual-phase steels showed strain localisation in an α grain constrained between two α′-martensite grains. During further loading strong strain heterogeneity develops in the microstructure. The μ-DIC investigation also showed the nucleation of micro-cracks at the α grain boundaries orientated at ≈45° to the loading direction and also at α/α′-martensite interphase boundaries [167-169]. In that study, the damage resistance of α/α′-martensite boundaries was observed to increase with the decrease in the α′-martensite thickness. The DIC studies on TRIP-aided multiphase steel showed strain partitioning effects in the softer α phase compared to the harder bainitic α and α′-martensite phases [175]. The DIC studies on an Fe-25Mn-12.1Cr-0.42N-0.33C TWIP steel showed homogenous strain distribution across the gauge length until UTS [176]. However, strain localisation due to shear banding at ~54° to the tension axis was noted after UTS. The strain localisation associated with the initiation and propagation of Portevin-Le Chatelier (PLC) bands was also observed in high Mn TWIP steels [177-180].

For high Mn TRIP-TWIP steels, Eskandari *et al.* [41] used a combination of EBSD and DIC to characterise an Fe-21Mn-2.5Si-1.6Al-0.11C steel subjected to room temperature tension at 0.001 s^{-1} strain rate. At the onset of micro-yielding (∼0.02 true strain), the single-phase γ microstructure began transforming to deformation-induced ε-martensite (Fig. 2.26a). Higher tensile strains resulted in the further phase transformation to α′-martensite (Figs. 2.26b and 2.26c); along with a concomitant increase in strain inhomogeneity across the gauge length. Thereafter, the fracture was ascribed to the nucleation and coalescence of cracks at the intersection of α′-martensite plates (Fig. 2.26d).

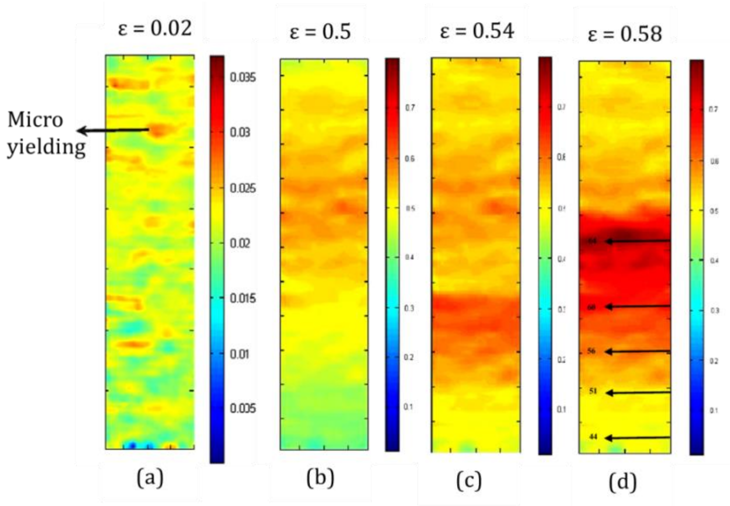

Figure 2.26: The DIC axial strain distribution for engineering strains (a) 0.02, (b) 0.2, (c) 0.54 and (d) 0.58. The black arrows in Fig. 2.26d indicate the volume fraction of α′-martensite [41].

Tensile testing at 0.003 s^{-1} strain rate resulted in a greater strain localisation and was attributed to more phase transformation to ε-martensite compared to tension at 0.001 s^{-1} strain rate [42]. Furthermore, tension at 180 and 300 °C, 0.001 s^{-1} strain rate revealed the preference for γ-twinning over phase transformation to ε and α′-martensite [42] along with the early onset of strain localisation in axial strain along the gauge length.

2.12 Texture of high Mn steels

The texture is the prefered crystallographic orientation of several crystals in the microstructure. The crystallographic orientation of a particular crystal with respect to an external frame of reference can be described by several methods:

(1) Miller indices: By the application of two sets of Miller indices, the crystal orientation (notation {hkl}⟨uvw⟩) can be defined as the crystal plane normal parallel to the normal direction (ND) and the crystal direction parallel to the rolling direction (RD). The Miller indices are easy to use for the

description of the ideal orientations of fcc, bcc and hcp metals as shown in Tables 2.8, 2.9 and 2.10, respectively.

(2) Euler angles: It is convenient to use Miller indices for the description of the ideal orientation of crystals however, it is difficult to describe the orientations of crystals that are slightly rotated from the ideal orientations. By the use of a set of three Euler angles the above problem is solved. The three Euler angles (ϕ_1, Φ, ϕ_2) signify the three rotations that are needed to be given to each crystal in the crystal reference frame in order to bring its crystallographic axes (⟨100⟩, ⟨010⟩, ⟨001⟩) into coincidence with the specimen reference frame comprising the ND, RD and transverse direction (TD). The Euler angles for the ideal orientations of the fcc, bcc and hcp metals are shown in Tables 2.8, 2.9 and 2.10, respectively. In Table 2.9, the $[10\bar{1}0]_\varepsilon$ || RD and $[0002]_\varepsilon$ || ND convention was used for representing the ideal hcp orientations.

Table 2.8 Ideal orientations for fcc metals [146].

Fcc orientations	**Miller indices ({hkl}⟨uvw⟩)**	**Euler angles (ϕ_1, Φ, ϕ_2)**
Cube (C_γ)	$\{001\}\langle100\rangle_\gamma$	(0, 0, 0)
Goss (G_γ)	$\{110\}\langle100\rangle_\gamma$	(90, 90, 45)
Goss/Brass (G_γ/Br_γ)	$\{110\}\langle115\rangle_\gamma$	(74, 90, 45)
Brass (Br_γ)	$\{110\}\langle112\rangle_\gamma$	(35, 45, 0)
A_γ	$\{110\}\langle111\rangle_\gamma$	(35, 90, 45)
Rotated Goss (Rt-G_γ)	$\{011\}\langle011\rangle_\gamma$	(0, 90, 45)
Rotated Cube (Rt-C_γ)	$\{001\}\langle110\rangle_\gamma$	(0, 0, 45)
Goss Twin (G-T_γ)	$\{113\}\langle332\rangle_\gamma$	(90, 25, 45)
Copper (Cu_γ)	$\{112\}\langle111\rangle_\gamma$	(90, 35, 45)
Copper twin (CuT_γ)	$\{552\}\langle115\rangle_\gamma$	(90, 74, 45)
Rotated Copper (Rt-Cu_γ)	$\{112\}\langle011\rangle_\gamma$	(0, 35, 45)
S_γ	$\{123\}\langle634\rangle_\gamma$	(59, 37, 63)
E_γ	$\{111\}\langle011\rangle_\gamma$	(0, 55, 45)
F_γ	$\{111\}\langle112\rangle_\gamma$	(30, 55, 45)

Table 2.9 Ideal orientations for bcc metals [181].

Miller indices ($(\mathbf{hkl})[\mathbf{uvw}]_{\alpha'}$)	**Euler angles (ϕ_1, Φ, ϕ_2)**
$(001)[0\bar{1}0]_{\alpha'}$	(45, 0, 45)
$(001)[1\bar{1}0]_{\alpha'}$	(0, 0, 45)
$(111)[1\bar{1}0]_{\alpha'}$	(0/60, 55, 45)
$(111)[\bar{1}\bar{1}2]_{\alpha'}$	(30/90, 55, 45)
$(114)[\bar{1}10]_{\alpha'}$	(0, 20, 45)
$(112)[\bar{1}10]_{\alpha'}$	(0, 30, 45)
$(223)[\bar{1}10]_{\alpha'}$	(0, 40, 45)
$(110)[001]_{\alpha'}$	(90, 90 ,45)
$(110)[1\bar{1}0]_{\alpha'}$	(90, 90 ,45)

Table 2.10 Ideal orientations for hcp metals [182].

hcp orientations/fibres	**Miller indices $\{\mathbf{hkil}\}\langle\mathbf{uvtw}\rangle_{\varepsilon}$**	**Euler angles (ϕ_1, Φ, ϕ_2)**
Basal fibre	$\{0001\}\langle uvtw\rangle_{\varepsilon}$	(0-90, 0, 0-60)
$\{hkil\}_{\varepsilon}$-fibre	$\{hkil\}\langle uvtw\rangle_{\varepsilon}$	(0-90, 15-25, 0-90)
	$\{0001\}\langle 10\bar{1}0\rangle_{\varepsilon}$	(30, 0, 0)
	$\{0001\}\langle 11\bar{2}0\rangle_{\varepsilon}$	(0, 0, 0)
$\{10\bar{1}0\}_{\varepsilon}$-fibre	$\{10\bar{1}0\}\langle uvtw\rangle_{\varepsilon}$	(0-90, 90, 30)
	$\{10\bar{1}0\}\langle 0001\rangle_{\varepsilon}$	(90, 90, 30)
	$\{10\bar{1}0\}\langle 11\bar{2}0\rangle_{\varepsilon}$	(0, 90, 30)
$\{11\bar{2}0\}_{\varepsilon}$-fibre	$\{11\bar{2}0\}\langle uvtw\rangle_{\varepsilon}$	(0-90, 90, 0/60)
	$\{11\bar{2}0\}\langle 0001\rangle_{\varepsilon}$	(90, 90, 0/60)
	$\{11\bar{2}0\}\langle 10\bar{1}0\rangle_{\varepsilon}$	(0, 90, 0/60)

The representation of orientations can be done via the following methods:

(1) Pole figures: Pole figures are two-dimensional stereographic projections in which the positions and intensities of orientations are plotted in relation to the specimen reference frame (RD, ND and TD). Stereographic projections are angle true projections such that the angular relationships between different directions and planes can be obtained [183].

(2) Orientation distribution function (ODF): In ODF the three Euler angles (ϕ_1, Φ, ϕ_2) are used to describe the orientation of a crystal and can be calculated from the measured pole figures. ODF

presents the probability density of an orientation to occur in the Euler space. Most commonly, the ODFs are presented in sections of a constant ϕ_2 values. Due to the presence of sample symmetry of most cold rolling textures for cubic metals the ODF sections are plotted in the range of $0°\leq\phi_1\leq90°$, $0°\leq\Phi\leq90°$ and $0°\leq\phi_2\leq90°$. During cold rolling and annealing of hcp metals, the ODF sections are plotted in the range of $0°\leq\phi_1\leq90°$, $0°\leq\Phi\leq90°$ and $0°\leq\phi_2\leq30°$. The ideal orientations produced during cold rolling and annealing of fcc metals appear in the ϕ_2 = 0°, 45° and 65° ODF sections and are represented in the Euler space as shown in Fig. 2.27.

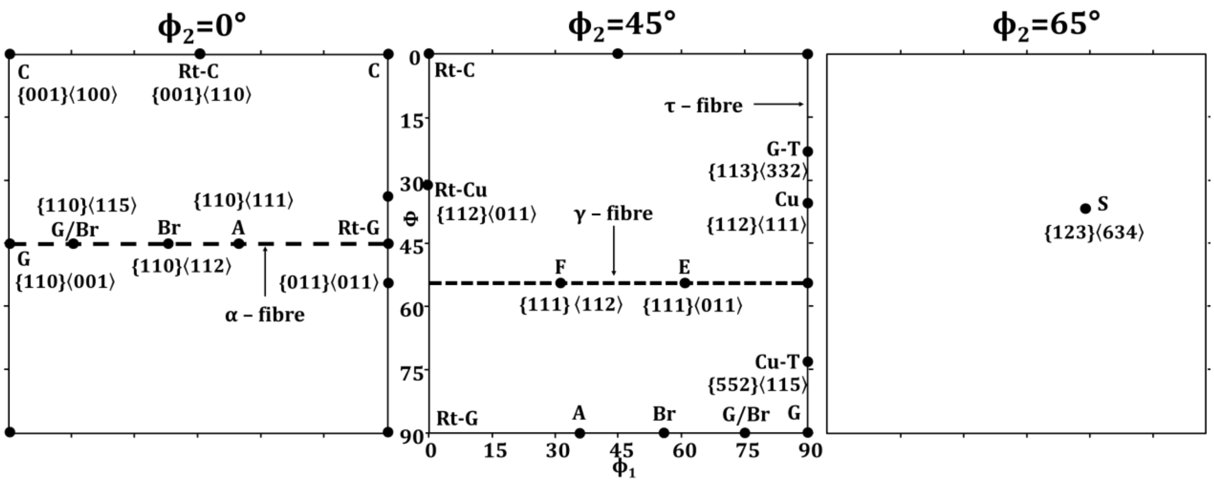

Figure 2.27: ϕ_2 = 0°, 45° and 65° ODF sections representing the ideal fcc orientations [7].

Fig. 2.28 shows the position of the ideal orientations produced during the cold rolling and annealing of bcc metals in the ϕ_2 = 0° and 45° ODF sections.

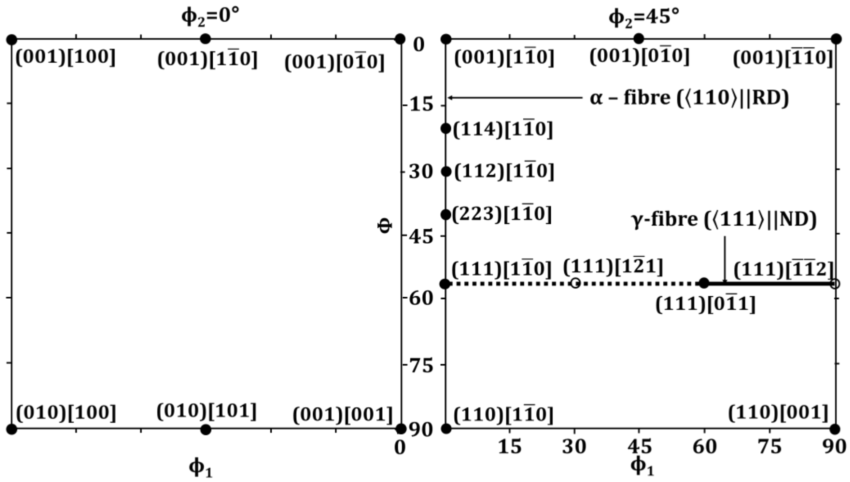

Figure 2.28: ϕ_2 = 0 and 45° ODF sections representing the ideal bcc orientations [7].

The ideal orientations of hcp metals represented in the ϕ_2 = 0° and 30° ODF sections are shown in Fig. 2.29.

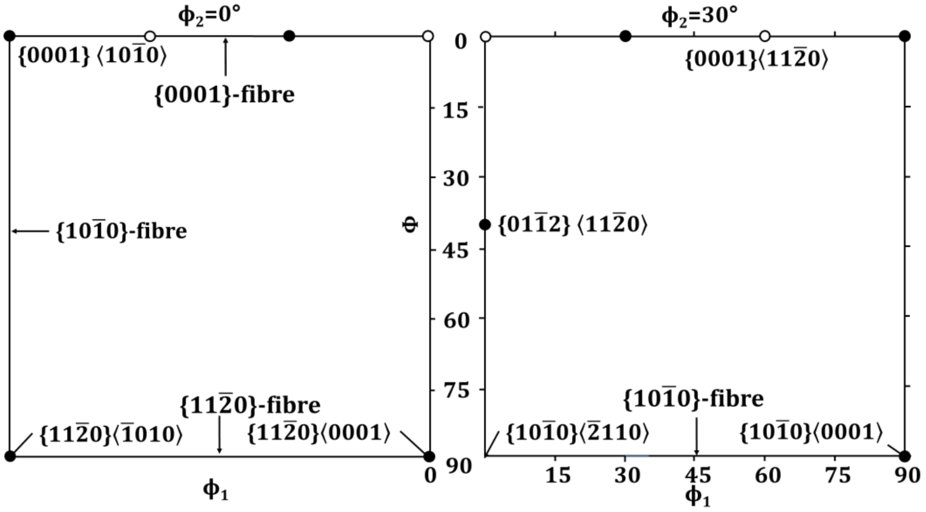

Figure 2.29: ϕ_2 = 0° and 30° ODF sections representing the ideal hcp orientations [7].

(3) Inverse pole figures (IPF): In IPF the distribution of a certain selected sample direction (RD, ND and TD) in relation to the crystal directions ((100), (010), (001)) is depicted. The representation in the IPF is exactly inverse of the pole figure. The projection plane for an IPF is a standard projection of the crystal where the unit stereographic triangle is shown [183]. For cubic crystal symmetry, as the twenty-four crystallographic triangles are crystallographically equivalent, therefore one of the unit triangles is used as shown in Fig. 2.30.

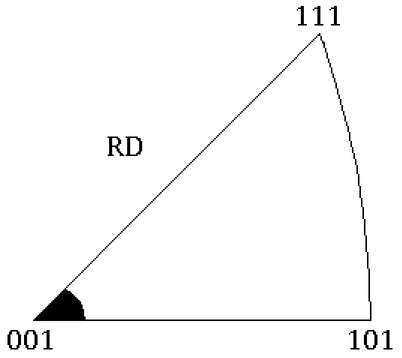

Figure 2.30: Schematic inverse pole figure representation for direction ⟨001⟩||RD for cubic crystal [13].

2.12.1 Deformation texture in high Mn steels

2.12.1.1 *γ texture after plane strain compression/cold rolling*

After cold rolling, the fcc metals with medium/high SFE develops Cu$_{\gamma}$-type texture whereas low SFE metals develop Br$_{\gamma}$-type texture. The Cu$_{\gamma}$-type texture consists of orientations: Cu$_{\gamma}$, Br$_{\gamma}$ and S$_{\gamma}$ whereas Br$_{\gamma}$-type texture consists of orientations: Br$_{\gamma}$ and G$_{\gamma}$ with a negligible fraction of Cu$_{\gamma}$. Initially, it was proposed that the tendency of easy cross slip in high SFE metals lead to Cu$_{\gamma}$-type texture [184]. Later it was suggested that the evolution of Br$_{\gamma}$-type texture in low SFE materials is related to deformation twinning [185]. However, it was experimentally observed that the propensity of twinning decreases at intermediate levels of cold rolling and also the volume fraction of twins is very low to have a direct effect on the texture evolution. Therefore, it was proposed that deformation twinning leads to the formation of shear bands at higher strains and dislocation glide within shear bands leads to the formation of Br$_{\gamma}$ orientation [186].

Lü *et al.* [8] reported the evolution of Br$_{\gamma}$ orientation with a spread towards G$_{\gamma}$ orientation in an Fe-21.6Mn-0.38C steel during cold rolling to 50% thickness reduction. With increasing thickness reduction upon cold rolling the volume fraction of C$_{\gamma}$ orientation decreased and the orientation completely disappeared after thickness reduction higher than 20%. After thickness reduction to 30%, a decrease in the intensity of Cu$_{\gamma}$ and S$_{\gamma}$ orientations was noted. This was ascribed to the phase transformation of these γ grain orientations to ε-martensite orientations. The Fe-26Mn-3Si-3Al steel in the initial state shows, the orientations with weak intensities along the α_{γ}-fibre ($\langle 110\rangle_{\gamma}||$RD) and with Cu$_{\gamma}$ orientation [11]. After cold rolling to 40% thickness reduction, the intensity of Br$_{\gamma}$ orientation along the α_{γ}-fibre is observed to increase. Upon cold rolling, to 56% thickness reduction the intensity of G$_{\gamma}$/Br$_{\gamma}$ and Cu$_{\gamma}$ orientations is observed to increase and decrease, respectively [10]. For an Fe-24Mn-3Al-2Si-1Ni-0.0C steel, after cold rolling to 42% thickness reduction shows strong intensities around the G$_{\gamma}$ and Br$_{\gamma}$ orientations [187]. The formation of similar orientations was noted during the cold rolling to 80% thickness reduction for the Fe-18Mn-0.6C and Fe-18Mn-1.5Al-0.06C steels [188].

2.12.1.2 *Deformation-induced ε-martensite texture*

The texture of hcp metals after cold rolling can be classified into three categories depending on the ideal c/a ratio (= 1.633) as shown in Fig. 2.31. The three classes are: (a) c/a ratio ≈ 1.633, (b) c/a greater than 1.633 and (c) c/a less than 1.633. The metals such as Mg (c/a ≈ 1.624) with c/a ratio ≈ 1.633 forms hcp orientations along the basal fibre; as slip predominantly occurs on the $(0001)_{\varepsilon}$basal plane after cold rolling (Fig. 2.31a). The metals such as Zn (c/a = 1.856) and Cd (c/a = 1.885) with c/a ration greater than 1.633 produce hcp orientations with the $(0001)_{\varepsilon}$ basal plane tilted ±15–25°

towards the RD along with the $(11\bar{2}0)_\varepsilon$ plane aligned along the RD (Fig. 2.31b). Such orientations are produced due to the operation of both basal slip and large-scale deformation-induced twinning. The metals such as Zr (c/a =1.589) and Ti (c/a = 1.587) with c/a less than 1.633, form hcp orientations with the $(0001)_\varepsilon$ basal plane tilted ± 20-40° away from the ND towards the TD and $(10\bar{1}0)_\varepsilon$ prismatic plane aligned towards RD (Fig. 2.31c) due to slip-on the $(10\bar{1}0)_\varepsilon$ prismatic plane.

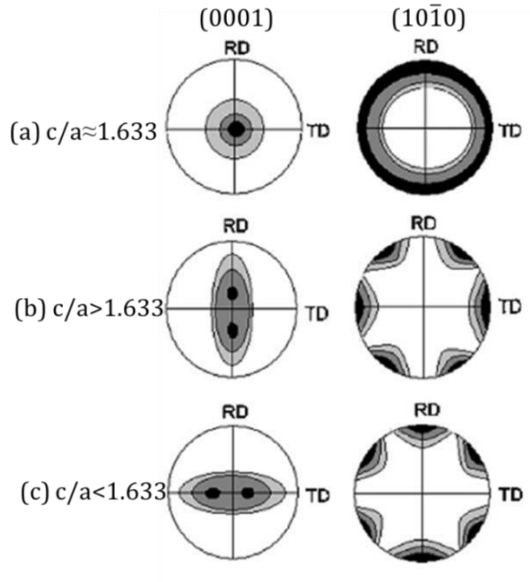

Figure 2.31: $(0001)_\varepsilon$ and $(10\bar{1}0)_\varepsilon$ pole figures showing cold rolling texture of hcp metals with c/a ratio (a) ≈1.633, (b) greater than 1.633, (c) less than 1.633 [182].

During the cold rolling to 66% thickness reduction of an Fe-17Mn-3Al-2Si-1Ni-0.06C steel, Gazder *et al.* [7] reported ε-martensite orientations comprising $(0001)_\varepsilon$ basal plane tilted 15° away toward the RD, the $(10\bar{1}0)_\varepsilon$ prismatic plane aligned towards the TD. In ϕ_2 = 0° and 30° ODF sections of ε-martensite, it is represented as $\{hkil\}_\varepsilon$-fibre which is offset from the ideal $(0001)_\varepsilon$ basal-fibre by angle of ≈15-25° towards the RD [7]. The c/a ratio of ε-martensite is 1.627 for the Fe-17Mn-3Al-2Si-1Ni-0.06C steel [24] but the experimentally observed texture corresponds to hcp metals with c/a ratio greater than 1.633. This was explained by the occurrence of two consequent processes: (i) γ to ε-martensite deformation-induced phase transformation and (ii) the deformation accommodation of ε-martensite [7]. With regards to (i), the ε-martensite forms from a pre-textured γ. The ε-martensite then deforms via mechanisms similar to hcp metals with c/a ratio less than 1.633 [7].

For an Fe-21Mn-3Si-3Al steel cold rolled to 18 and 29% thickness reductions, the deformation-induced ε-martensite $(0001)_\varepsilon$ basal poles were observed to be deviated by 32° and 26°, respectively, towards the RD [11]. Lü *et al.* [8, 46] showed the formation of $\{1129\}\langle 3362\rangle_\varepsilon$ orientation after cold rolling to 50% thickness reduction for an Fe-21.6Mn-0.4C steel. A decrease in the intensity of Cu_γ and S_γ orientations was observed due to the transformation of these orientations to $\{1129\}\langle 3362\rangle_\varepsilon$ orientation. During the deformation of high Mn steel, the ε-martensite orientations obtained from γ orientations were not correlated [8, 11]. Fig. 2.32 shows the superimposition of the schematic $(111)_\gamma$ pole figure containing the ideal γ orientations on the experimental $(0001)_\varepsilon$ pole figure. The ε-martensite orientations along the $\{hkil\}_\varepsilon$-fibre originated from the γ orientations between the G_γ and Br_γ along the α_γ-fibre and also from the Cu_γ orientation upon phase transformation via the S-N orientation relationship [7].

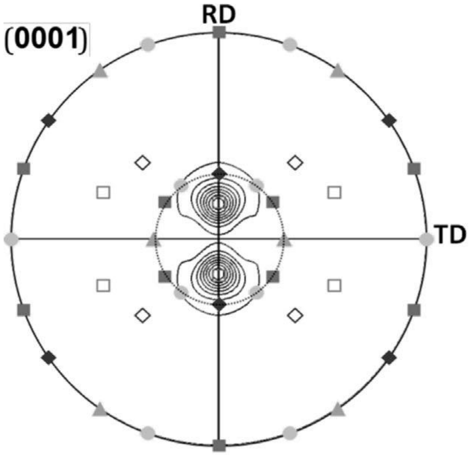

Figure 2.32: $(111)_\gamma$ pole figure superimposed on experimental $(0001)_\varepsilon$ pole figure. Legend: solid square A_γ $\{110\}\langle 111\rangle_\gamma$, hollow square Cu_γ $\{112\}\langle 111\rangle_\gamma$, solid diamond G_γ $\{110\}\langle 001\rangle_\gamma$, hollow diamond C_γ $\{001\}\langle 001\rangle_\gamma$, solid triangle Rt-$G_\gamma$ $\{110\}\langle 110\rangle_\gamma$ and solid circle Br_γ $\{110\}\langle 112\rangle_\gamma$ [7].

The orientations along the $\{hkil\}_\varepsilon$-fibre of ε-martensite remained stable upon increasing cold rolling thickness reduction to 50% [8]. This was explained as ε-martensite being a hard phase subsequently unable to accommodate deformation during cold rolling.

2.12.1.3 *Deformation-induced α′-martensite texture*

Gazder *et al.* [7] reported the formation of deformation-induced α′-martensite with strong intensities centred around the $(112)[\bar{1}10]_{\alpha'}$, $(223)[\bar{1}10]_{\alpha'}$ and $(111)[0\bar{1}1]_{\alpha'}$ orientations with weak intensities around the $(001)[100]_{\alpha'}$ orientation after cold rolling to 66% thickness reduction. After cold rolling the Fe-26Mn-3Al-3Si steel to 57% thickness reduction, strong intensity centred around the $(112)[\bar{1}10]_{\alpha'}$ orientation along the bcc-α fibre ($\langle 110\rangle_{\alpha'} \parallel$ RD) was witnessed [10]. The intensity of the deformation-induced α′-martensite orientations was relatively weaker than γ orientations after cold rolling [10]. The deformation-induced α′-martensite orientations were ascribed to the phase transformation from γ to α′-martensite with the subsequent deformation of α′-martensite. Fig. 2.33 shows the particular deformation-induced α′-martensite orientations (in black) produced from the γ orientations (in red) upon the phase transformation via the K-S orientation relationship [7, 189]. It can be observed that (i) $(112)[\bar{1}10]_{\alpha'}$, (ii) $(111)[0\bar{1}1]_{\alpha'}$ and (iii) $(001)[100]_{\alpha'}$ orientations originate from the (i) G_γ, Cu_γ, (ii) G_γ and (iii) G_γ orientations upon phase transformation via the K-S orientation relationship. There are presently no studies relating the ε-martensite to α′-martensite orientations produced upon phase transformation via the Burgers orientation relationship.

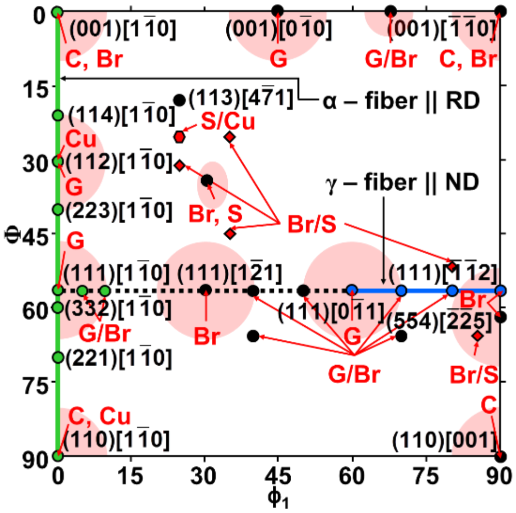

Figure 2.33: ϕ_2 = 45° ODF section showing the α′-martensite orientations (in black) generated from the γ orientations (in red) upon the phase transformation via the K-S orientation relationship [7, 189].

2.12.2 Annealing texture of high Mn steels

2.12.2.1 *Remnant α′-martensite texture*

For an Fe-26Mn-3Al-3Si steel cold-rolled to 57% thickness reduction, upon annealing at 500 °C for 30 min shows the intensity of α′-martensite orientations increased slightly due to α′-martensite recovery [10]. Upon further annealing at 650 °C for 30 min, the intensity of the α′-martensite orientations decreases due to the onset of α′-martensite reversion to γ. In that study, the formation of $(001)[110]_{\alpha'}$ orientation and weak intensities around the orientations along the $\gamma_{\alpha'}$-fibre ($\langle 111\rangle_{\alpha'}$|| ND) was observed during the annealing at 650 °C for 30 min. For an Fe-17Mn-3Al-2Si-1Ni-0.06C steel cold-rolled to 66% thickness reduction; on annealing at 625 °C for 5 min, the unreverted α′-martensite shows strong intensities around the $(001)[110]_{\alpha'}$ orientation with weak intensities around the $(111)[\bar{1}\bar{1}2]_{\alpha'}$ and $(554)[\bar{2}\bar{2}5]_{\alpha'}$ orientations [7].

2.12.2.2 *Reverted γ texture*

The reverted γ orientations are mainly derived from the ε and α′-martensite orientations following the S-N and K-S orientation relationships, respectively. For an Fe-26Mn-3Al-3Si steel cold-rolled to 57% thickness reduction upon the annealing at 500 °C, for 30 min showed the formation of strong intensities centred around the G_γ orientation and weak intensities around the Cu_γ orientation [10]. This was ascribed to ε and α′-martensite reversion and subsequent γ recovery. Upon further annealing at 650 and 750 °C for 30 min, the retention of the γ orientations was observed with the decrease in intensities due to recrystallisation. Lü *et al.* [8] during the annealing at 630 °C for 16 s of an Fe-21.64Mn-0.376C steel cold-rolled to 50% thickness reduction noted an increase in the intensities centred around the S_γ orientation due to the reversion from the $\{1129\}\langle 3362\rangle_\varepsilon$ orientations via the S-N orientation relationship [8]. For an Fe-17Mn-2Si-3Al-1Ni-0.06C steel cold-rolled to 66% thickness reduction, annealing at 625 °C for 300 s presented the formation of Br_γ orientation which was ascribed to the deformation-induced α′-martensite $(001)[110]_{\alpha'}$ and $(111)[\bar{1}\bar{1}2]_{\alpha'}$ orientations upon phase transformation via the K-S orientation relationship [7].

During cold rolling to 57% thickness reduction of an Fe-26Mn-3Al-3Si steel, strong intensity around the $(112)[\bar{1}10]_{\alpha'}$ orientation along the $\alpha_{\alpha'}$-fibre ($\langle 110\rangle_{\alpha'} \parallel$ RD) was witnessed [10]. The γ and ε-martensite orientations that resulted in the formation of the $\alpha_{\alpha'}$-fibre orientations were not explored. Kowalska *et al.* [10] did not correlate the γ orientations G_γ and Cu_γ obtained during the reversion from the ε and α′-martensite orientations during the annealing of an Fe-21Mn-3Al-3Si high Mn steel at 500 °C, for 30 min. During the annealing of high Mn steel at 630 °C for 16 s, Lü *et al.* [8] tracked the evolution of only one $\{1129\}\langle 3362\rangle_\varepsilon$ orientation upon reversion to γ. However, during the annealing of an Fe-17Mn-2Si-3Al-1Ni-0.06C steel, Gazder *et al.* [7] correlated the γ orientations obtained from the α′-martensite orientations upon reversion using the K-S orientation relationship. Therefore, a comprehensive study needs to be carried out to correlate the ε-martensite orientations obtained from the γ orientations and also the α′-martensite orientations obtained from the ε-martensite orientations upon cold rolling along with the γ orientations found from the ε and α′-martensite orientations upon reversion.

2.12.2.3 *γ recrystallisation and grain growth textures*

During γ recovery, the slight strengthening of the deformation texture orientations is observed which is due to the annihilation of defects by the short-range interaction between dislocations and subgrain boundaries. The recrystallisation of γ may result in three different kinds of texture: (i) with the retention of orientations produced upon deformation, (ii) formation of new orientation with strong intensities and (iii) formation of random orientations [190]. In some cases, annealing after cold rolling to lower thickness reduction leads to the retention of deformed γ orientations or the formation of random orientations. The formation of γ orientations with strong intensities after recrystallisation upon cold rolling to large thickness reduction can be explained by two theories: (i) oriented nucleation and (ii) oriented growth. In oriented nucleation theory, the γ grains of certain orientations nucleate more than other orientations which dominate the final recrystallisation texture. In oriented growth theory, the γ grains of the dominant orientations are produced by their (i) faster growth and/or (ii) coarse grain size. This can be achieved by the presence of special boundaries in fcc crystals having misorientations axis-angle of ⟨111⟩/40° in fcc crystal which has higher mobility.

The γ recrystallisation texture was stated to be similar to the reverted γ texture upon annealing of high Mn steels. Somani *et al.* [191] showed that after annealing at 800 and 1000 °C for 1 s of a 17/7 metastable austenitic stainless steel cold-rolled to 63% thickness reduction resulted in ε and α′-martensite reversion and γ recrystallisation, respectively. The γ have strong intensities around the Br_γ and G_γ orientations and weak intensities around the Cu_γ and S_γ orientations were observed to be present after recrystallisation. In that study [191], annealing at 800 °C for 1 s, at 900 °C for 1 s and 1000 s of a 301LN metastable austenitic stainless steel cold-rolled to 60% thickness reduction resulted in the reversion, recrystallisation and grain coarsening of γ, respectively, with the reverted G_γ, Br_γ, Cu_γ and S_γ orientations retained during γ recrystallisation. The intensities of G_γ and Br_γ orientations were stronger than Cu_γ and S_γ orientations. However, on γ grain growth, the weakening of intensity around the G_γ and Br_γ orientations were observed along with the disappearance of Cu_γ and S_γ orientations. Chowdhury *et al.* [192] reported the weakening of the reverted Br_γ, G_γ and S_γ orientations with the increase in spread around the Br_γ, G_γ and S_γ orientations upon recrystallisation after annealing at 800 °C for 1 h for a 304L metastable austenitic stainless steel cold-rolled to 95% thickness reduction.

2.13 Gaps in the existing body of knowledge

(1) The literature [8, 24, 47, 117] contains contrary views regarding the deformation accommodation of ε-martensite. However, the most prevalent view is the deformation accommodation of ε-martensite. In this regard, the mechanism of ε-martensite nucleation and subsequent deformation accommodation via the formation of stacking faults are also not explained in the existing literature and require further investigation.

(2) Lü *et al.* [8, 46] observed a displacive reversion of ε-martensite followed by the discontinuous recrystallisation of γ. However, the microstructural changes occurring during the displacive

reversion was not studied in details, as this requires direct observation via in-situ experiments. Thus, further in-situ experiments based study on ε and α′-martensite reversion upon annealing need to be undertaken.

(3) The formation of twins in the reverted γ was observed during the annealing of cold-rolled high Mn steel [10]. Currently, there is no explanation for the mechanism of γ-twin formation. Thus, it is important to gain insight into this phenomenon.

(4) There are also limited studies on the texture evolution during the cold rolling and annealing of high Mn steels. The evolution of orientations of three phases (γ, ε and α′-martensite) during the cold rolling and annealing of an Fe-21Mn-3Al-3Si high Mn steel was reported by Kowalska *et al.* [10, 11]. However, Refs. [10, 11] did not correlate the ε and α′-martensite orientations obtained during the transformation from the initial γ orientations during cold rolling and the γ orientations obtained during the reversion from ε and α′-martensite orientations during annealing. Lü *et al.* [8] tracked the evolution of $\{1129\}\langle 3362\rangle_{\varepsilon}$ orientation upon reversion to γ but such a study is limited to only one ε-martensite orientation. Thus, a comprehensive study needs to be carried out to correlate the ε-martensite orientations obtained during the transformation from γ and the α′-martensite orientations obtained by the transformation from ε-martensite.

CHAPTER 3 EXPERIMENTAL AND ANALYTICAL PROCEDURES

This chapter reviews the materials investigated and the experimental procedures used in this thesis. The sample preparation and the microstructural characterisation techniques are also introduced with their basic principles discussed.

3.1 Material

The composition of steel was selected based on the occurrence of both ε and α′-martensite formation during its deformation. The high Mn steel was supplied in the form of as-cast slabs from Universidade Federal de Minas Gerais, Brazil. The as-cast slab dimensions were: 245 (length) × 60 (width) × 20.6 (height) mm^3. The composition of the studied steel is given in Table 3.1.

Table 3.1 Nominal chemical composition of the studied steel (wt.%)

Mn	Al	Si	Ni	C	Fe
17.2	2.9	2.2	1.3	0.06	Balance

3.2 Processing

A schematic showing the processing stages of samples preparation along with their dimensions is shown in Fig. 3.1. The various processing steps involved are discussed in the following sections.

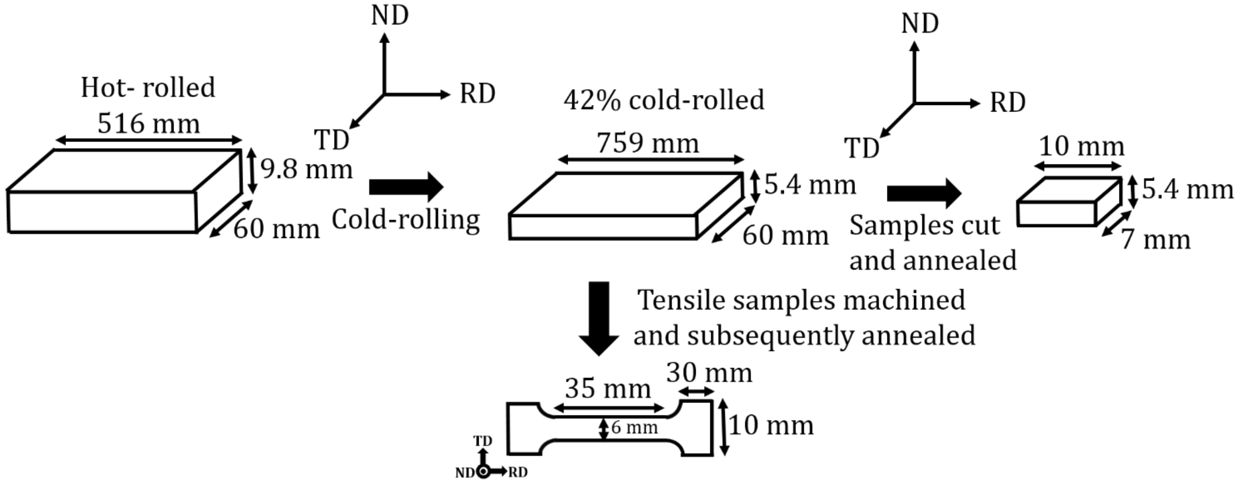

Figure 3.1: Schematic showing the processing of the samples.

3.2.1 Hot rolling

To break the as-cast structure the material was hot-rolled to 52% thickness reduction. The slabs were reheated to 1100 °C for 7200 s followed by hot rolling in 4 passes with 17% thickness reduction per pass on the laboratory 4-high rolling mill at Deakin University followed by water quenching. The hot-rolled plates were of dimensions: 516 (length) × 60 (width) × ≈9.8 (height) mm^3.

3.2.2 Plane strain compression by Gleeble 3500 thermomechanical simulator

Physical simulation of the plane strain deformation process can be successfully done using a Gleeble 3500 thermomechanical simulator. Another advantage associated with the Gleeble 3500 thermomechanical simulator over cold rolling is the use of a relatively small sample.

Thus, the Gleeble 3500 thermomechanical simulator was used in a hydra-wedge mode to simulate the plane strain compression until a maximum of 20% thickness reduction. For processing, samples of dimension 8 mm along the RD, 20 mm along the TD and 6 mm along the ND were cut from the hot-rolled plate as shown in Fig. 3.2a. Then the samples were plane strain compressed at room temperature to 5, 10, 15 and 20% thickness reductions using a strain rate of 1.7×10^{-2} s^{-1}. The maximum thickness reduction was governed by the maximum possible applied load of ≈10 kN in Gleeble 3500 thermomechanical simulator. The sample after plane strain compression is shown in Fig. 3.2b.

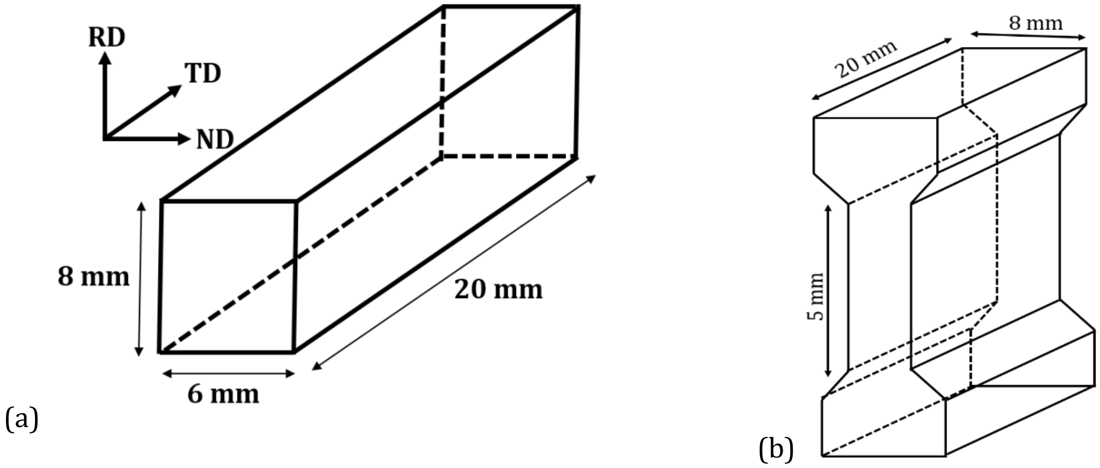

Figure 3.2: Schematic of the sample geometry (a) before and (b) after plane strain compression using Gleeble 3500 thermomechanical simulator.

The raw load-displacement data from the Gleeble 3500 thermomechanical simulator was converted to equivalent stress and strain values using the following equations [29]:

$$\varepsilon = \left(\frac{2}{\sqrt{3}}\right)\ln\left(\frac{t}{t_0}\right) \tag{3.1}$$

$$\sigma = \left(\frac{\sqrt{3}}{2}\right)\frac{F}{l_0 w_0} \tag{3.2}$$

where, $l_0 \times w_0 \times t_0 = 8 \times 20 \times 5\ \mathrm{mm}^3$ are the initial sample length, width and height that correspond to the RD, TD and ND of the hot-rolled plate, respectively. The symbols t and F denote the instantaneous sample height and load, respectively.

3.2.3 Plane strain compression by cold rolling

To keep the strain rate the same ($= 1.7 \times 10^{-2}\ \mathrm{s}^{-1}$) during cold rolling, the reduction per pass (r) was calculated using the diameter and the speed of the rolls according to the equations [193]:

$$\varepsilon = \dot{\varepsilon} t \tag{3.3}$$

$$r = \frac{h_0 - h_1}{h_0} \tag{3.4}$$

$$r = 1 - \frac{1}{e^{\varepsilon}} \tag{3.5}$$

$$t = \frac{60L}{2\pi NR} \tag{3.6}$$

$$L = \sqrt{2R(h_0 - h_1)} \tag{3.7}$$

where $\dot{\varepsilon}$ is the strain rate, ε is the strain per pass, h_0 is the initial height and h_1 is the final height of the sample after one pass, t is time required for the workpiece to pass, L is the effective roll contact length, N is the speed of the rolls, R is the roll radius. For the present schedule, the roll diameter and speed were 350 mm and 14.5 rpm, respectively. The cold rolling of the hot-rolled plates to three different thickness reductions of 42, 66 and 88% was done using the calculated value of 4.8% thickness reduction per pass. This corresponds to the equivalent strains of 0.63, 1.24 and 2.45, respectively, calculated using Eq. 3.1. After cold rolling the final thickness of the plates were ≈5.4 mm, ≈3.1 mm, ≈1.1 mm after 42, 66 and 88% thickness reductions, respectively.

3.2.4 Isochronal annealing

Samples were cut from the 42% cold-rolled plates into dimensions: 10 (RD) × 7 (TD) × 5 (ND) mm^3 and isochronally annealed in a muffle furnace in open atmosphere. The samples were annealed at 500, 600, 625, 650, 700, 750, 800 and 850 °C. After annealing the samples were immediately quenched in water. During annealing, the holding time at the selected temperature was 300 s and the total annealing time was 400 s for each annealing temperature. The heating rate was not constant for each annealing temperature during annealing. After fixing the annealing temperature, 100 s was the estimated time from the sample placement into the furnace to reaching of the selected temperature upon which the sample was held at the temperature for 300 s.

3.2.4.1 *Calculation of ε and α′-martensite formation start temperatures*

Based on the equation proposed by Yang *et al.* [5]:

$$\mathrm{M_s(K)} = 576 - 489(\mathrm{wt.\%\ C}) - 9.1(\mathrm{wt.\%\ Mn}) - 17.6(\mathrm{wt.\%\ Ni}) - 9.2(\mathrm{wt.\%\ Cr}) + 21.3(\mathrm{wt.\%\ Al}) + 4.1(\mathrm{wt.\%\ Si}) - 19.4(\mathrm{wt.\%\ Mo}) - 1(\mathrm{wt.\%\ Co}) - 41.3(\mathrm{wt.\%\ Cu}) - 50(\mathrm{wt.\%\ Nb}) - 86(\mathrm{wt.\%\ Ti}) - 4(\mathrm{wt.\%\ V}) - 13(\mathrm{wt.\%\ W}) \qquad (3.8)$$

the calculated ε-martensite transformation start temperature for the Fe-17Mn-3Al-2Si-1Ni-0.06C steel is 174 °C, which is above the room temperature. Thus, the formation of ε-martensite on quenching after annealing is expected in the steel. The calculated result is very close to the ε-martensite start temperature (177 °C) obtained by Tsuzuki *et al.* [6] using dilatometry for an Fe-16Mn-0.01Si-0.006C steel.

The α′-martensite transformation start temperature for the Fe-17Mn-3Al-2Si-1Ni-0.06C steel was also calculated from the empirical equation obtained for Mn steels [194]

$$\mathrm{M_s(°C)} = 539 - 423(\mathrm{wt.\%\ C}) - 30.4(\mathrm{wt.\%\ Mn}) - 7.5(\mathrm{wt.\%\ Si}) + 30(\mathrm{wt.\%\ Al}) \qquad (3.9)$$

Using the Eq. 3.9, the α′-martensite start temperature for the Fe-17Mn-3Al-2Si-1Ni-0.06C steel was calculated to be 72 °C. It can be observed that the α′-martensite formation start temperature is also higher than the room temperatures. Thus, the formation of α′-martensite upon quenching after annealing to room temperature is also expected.

3.3 Tensile testing using digital image correlation

Dog-bone-shaped ASTM-EM8-04 standard subsize tensile samples of dimensions: 35 mm gauge length, 6 mm width and 2 mm thickness were wire-cut from the centre of the 42% cold-rolled plate with the dimensions parallel to the RD, TD and ND, respectively, (Fig. 3.3) and isochronally annealed at 500, 625, 650, 700 and 800 °C for 300 s.

The uniaxial tensile tests were conducted on an Instron 1341 tensile testing machine with a 100 kN load cell at a strain rate of $10^{-3}\ \mathrm{s}^{-1}$. The initial crosshead speed of the grips was 0.035 mms^{-1}.

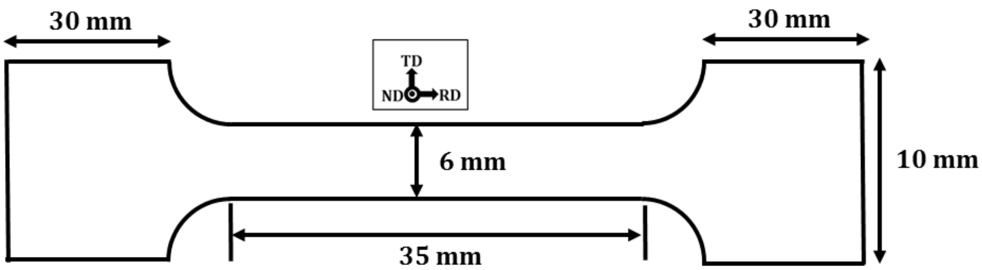

Figure 3.3: Schematic of the dog bone tensile sample.

The evolution of strain during the uniaxial tensile testing was recorded by DIC cameras (Fig. 3.4). To perform strain measurements via DIC, the sample was coated with a speckle pattern. In general, a stochastic pattern composed of two colours with large contrast with each other is used. The common colours are black and white. The distribution of the speckle pattern is dependent on the camera's proximity. Fig. 3.4 shows a schematic of the DIC system with the speckle pattern and two cameras.

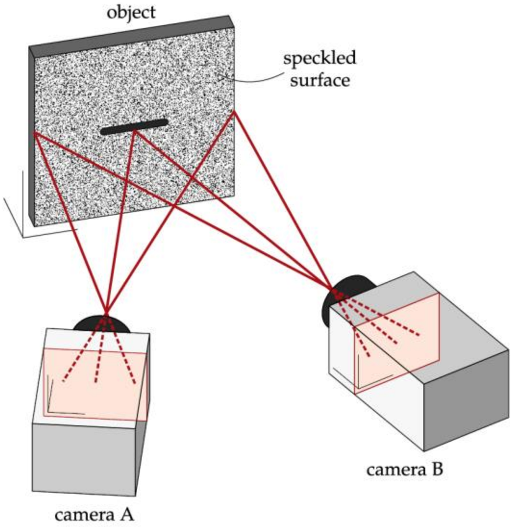

Figure 3.4: Schematic of the DIC camera configuration [195].

As the sample is lit up, the black regions absorb most of the incident light whereas the white regions reflect most of the light. The domain containing random white and black speckles forms a pattern containing grayscale values. The initial sample surface containing the grayscale values is discretised into a number of subset images allowing to track the strains and displacements as the sample surface deforms upon tension. In this procedure, a one to one correspondence is assumed between the initial and the deformed states. In theory, one camera can be used to capture the displacements in two-dimensional space. However, in the present experiment, two charge coupled device (CCD) cameras manufactured by Dantec Dynamics operating at 10 frames per second with an exposure time between 20-50 milliseconds and a resolution of 5 megapixels were used to increase the accuracy of the measurement. Also to increase the accuracy of the measurement, the strain was measured over the whole gauge section [41]. The post-processing of the DIC data was carried out using the Dantec Instra 4D software. During post-processing, the shear strain is defined as the strain in the XY (transverse-axial) plane.

3.4 Hardness testing

The hardness of the samples was measured by a Vickers micro-hardness tester (Struers Emco Test Durascan-70) using a 10 kgf load on the ND-RD plane. Ten measurements per sample were taken and the average hardness was reported with standard deviation. The load of 10 kgf was selected to minimise the effect of ε and α′-martensite on the hardness values; as with increasing load, the depth of indentation increases. The deformation-induced ε and α′-martensite forms on the surface during polishing. The distance between the two indentations was kept to five times the size of the indentation.

3.5 Sample preparation and microstructure characterisation techniques

The sample preparation for microstructural characterisation was undertaken by wire cutting the plane strain compressed, tensile deformed and annealed samples. Samples of dimensions: 10 (RD) × 7 (TD) × 5 (ND) mm^3 were machined from the plane strain deformed and annealed conditions. Rectangular samples of dimension: 15 (tension axis||RD) × 6 (TD) × 2 (ND) mm^3 was also machined from the parallel gauge section away from the fracture region for the 42% cold-rolled and 500, 625 and 700 °C samples after tensile testing.

Subsequent grinding of the samples was performed manually using silicon carbide abrasive paper of grit sizes: 400, 800, 1200, 2000 and 4000. The mechanical grinding operation can result in the transformation of metastable γ into deformation-induced ε and α′-martensite. To remove the deformation-induced ε and α′-martensite, if any formed during prior sample preparation, and improve the surface finish for EBSD characterisation, the samples were further electropolished using a solution of 330 ml methanol, 330 ml butoxyethanol and 40 ml perchloric acid in Struers LectroPol-5 operating at 50V and time period of 90 s.

Thin foils for TEM/STEM was prepared first by grinding the deformed and annealed samples to ≈70 μm thickness and then by punching out the 3 mm thin disks. The disks were twin jet electropolished using a solution of 90% methanol and 10% perchloric acid in a Struers Tenupol-5 operating at 30 V (≈150 mA) at -25 °C.

3.5.1 Scanning electron microscopy

SEM of the fracture surfaces for the 42% cold-rolled, 625 and 700 °C samples was conducted using a JEOL JSM-7001F field emission gun scanning electron microscope (FEG-SEM) operating at 15 kV with a working distance of 25 mm. Secondary electron detector was used for imaging the fracture surfaces using a probe current of ≈6.5 nA.

3.5.2 Electron back-scattering diffraction

EBSD is conducted by acquiring and subsequently indexing of electron back-scattering patterns known as Kikuchi patterns from a sample tilted at 70° from the horizontal stage position as shown in Fig. 3.5. The tilting of the sample is done to increase the number of back-scattering electrons exiting the sample. Fig. 3.5 shows the typical setup for the EBSD mapping consisting of EBSD detector, the sample and the FEG-SEM pole piece.

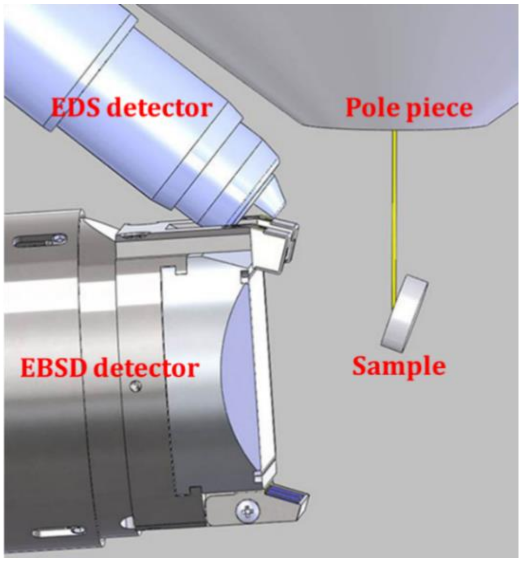

Figure 3.5: Setup for the electron back-scattering diffraction mapping in the scanning electron microscope chamber [196].

The back-scattering electrons escaping at Bragg angle diffract to form the Kikuchi patterns which are detected on the phosphor screen of the EBSD detector. The sample volume from which the back-scattering electrons are generated is dependent on the given step size. The Kikuchi patterns comprise bands which are indexed individually to return the unique crystal orientation. The EBSD mapping is conducted by focusing the electron beam onto the surface of the electropolished sample and scanning the beam in a grid across the sample to return grain orientation, morphology and boundaries. The shape of the gird depends on the specific EBSD system. For the acquired EBSD maps in this study, the beam scanned the sample in a square grid. During EBSD mapping, the simultaneous measurement of the chemical composition can be also done using the EDS detector.

The EBSD mapping was performed on a JEOL JSM-7001F FEG-SEM operating at 15 kV and ≈6.5 nA probe current, equipped with Nordlys-II detector interfacing the Oxford Instruments (OI) AZtec software suite.

The EBSD scans were executed with a step size of 1 μm for the hot-rolled sample, 5% plane strain compressed sample and 30 nm for the 10, 15, 20, 42, 66 and 88% plane strain compressed/cold-rolled samples. A step size of 30 nm was used for the 42% cold-rolled and 500, 600, 625 and 650 °C samples and 100 nm for the 700, 750, 800 and 850 °C samples. The EBSD scans were acquired at a working distance of 12 mm at the centre of the ND-RD sample cross-sections.

The EBSD maps for the cold-rolled and 500, 625 and 700 °C samples after tensile deformation was collected at 100 nm step size at a working distance of 15 mm on the transverse direction-tensile direction plane.

The EBSD scans were also conducted for the measurement of texture on the ND-RD sample plane with a coarse step size of 2 μm for the samples annealed at 700 and 750 °C, 2.5 μm for the hot-rolled, 800 and 850 °C samples, whereas 1 μm step size was used for the 5, 10, 15, 20, 42, 66 and 88% plane strain compressed/cold-rolled samples and 500, 600, 625 and 650 °C samples. For the measurement of texture at 15 mm working distance, the area of EBSD scans was 2.4×1.8 mm^2 for the hot-rolled, 700, 750, 800 and 850 °C samples, 1.2×0.9 mm^2 for the plane strain compressed/cold-rolled, 500 and 625 °C samples and 1×0.9 mm^2 for the 600 and 650 °C samples.

3.5.2.1 *Electron back-scattering diffraction data post-processing*

OI Channel-5 software package was utilised for post-processing of the EBSD maps using well-established procedures [197] by eliminating any potential wild orientation spikes. This was subsequently followed by the filling in of the zero solutions using cyclic extrapolation from 8 to 5 neighbours. The pixels with negative slopes generated by cyclic extrapolation were removed after each step, which rules out the introduction of any artificial grains.

The subgrain boundaries were defined by a minimum of three pixels, which was bounded by misorientations (θ) ≥ 2°. 2° ≤ θ < 15° are classified as LAGBs, whereas θ ≥ 15° denote HAGBs. For the EBSD maps acquired on the samples after tensile deformation, LAGBs was defined between 5° and

15°. The γ twin boundaries of the first order were defined as $\Sigma3 = 60°\langle 111\rangle_{\gamma}$ for a maximum deviation ($\Delta\theta$) of 6.03° following the Palumbo-Aust criterion ($\Delta\theta \leq 15° \ \Sigma^{-5/6}$) [198]. The $\{10\bar{1}2\}\langle\bar{1}011\rangle_{\varepsilon}$ extension twins in ε-martensite were defined as having a misorientation angle of ≈86° ± 5° about the $\langle 1\bar{2}10\rangle_{\varepsilon}$ axis [52]. The ODFs was plotted after exporting the orientation data from the OI Channel-5 software to JTEX software [199].

3.5.2.2 *Segmentation of the electron back-scattering diffraction maps*

The EBSD maps for the 600, 625 and 650 °C samples were segmented into the recrystallised and reverted/recovered γ grain fractions by the application of internal misorientation and subgrain aspect ratio threshold.

The procedure began with the creation of a subset containing only the γ grains using the OI Channel-5 software (Fig. 3.6a). A threshold based on the grain orientation spread (GOS) was applied to the γ grains subset to separate the reverted/recovered and recrystallised γ grains. GOS is an indicator of internal misorientation within a grain and is estimated by calculating the average misorientation between all the pixels within a grain/subgrain [200]. The GOS threshold (θ_c) used was determined based on noting where the change in slope of the normalised cumulative distribution vs. internal misorientation of the grains corresponds to 1 (Fig. 3.6b) [201]. The GOS thresholding resulted into two subsets of γ grains having misorientations: (a) less than $\theta_c = 0.95$ (Fig. 3.6c) and (b) greater than $\theta_c = 0.95$ (Fig. 3.6d). The γ grains with GOS values greater than θ_c was also found to be elongated and coarse. Thus, it could be assumed that these may be reverted γ grains. The γ grains with GOS values less than θ_c was observed to be fine but of varying different morphology. It could be speculated that some of these γ grains are recrystallised whereas the others (elongated) may be formed by the recovery of the reverted γ.

A second step was therefore applied using an aspect ratio (AR) threshold to the γ subset with GOS value less than θ_c to separate out the higher AR grains. The AR threshold used was determined in a similar manner to the GOS threshold by tracking the change of the slope of the normalised cumulative distribution vs. AR and accepting the value where the change of slope equals to 1 (Fig. 3.6e). The AR threshold was determined to be 2.65. The γ grains with AR lower than the critical value comprised the recrystallised γ grains (Fig. 3.6g). The γ grains with AR higher than the critical AR were observed to be fine and elongated (Fig. 3.6f) and considered to be the recovered γ grains. The above subset was merged with the subset of γ grains having GOS values above θ_c (Fig. 3.6d) to create a subset containing the reverted/recovered γ grains (Fig. 3.6h).

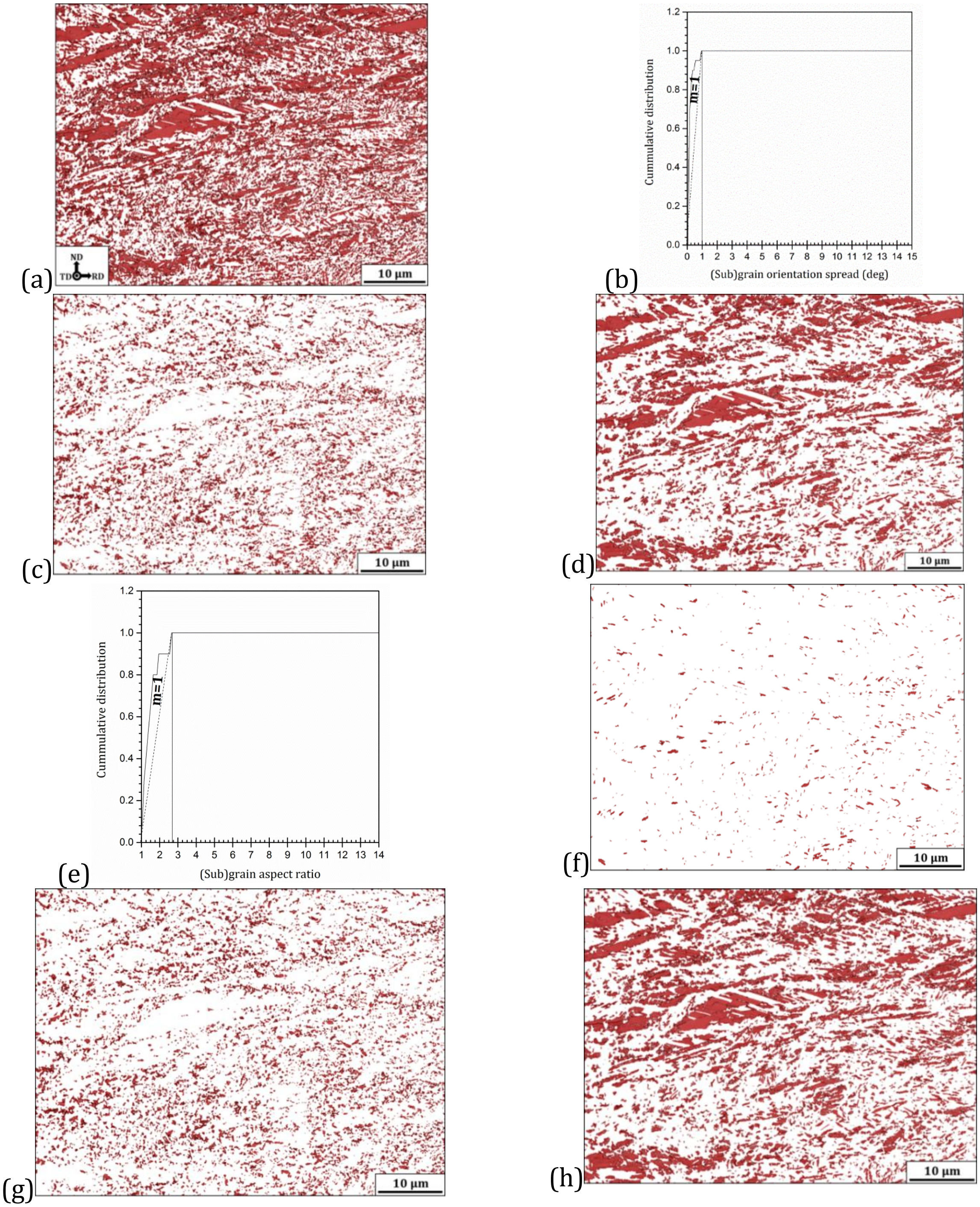

Figure 3.6: EBSD maps after annealing at 600 °C: (a) full γ grains map, (b) cumulative distribution of internal grain orientation spread indicating the threshold used for segmentation; (c) map of all the recrystallised and recovered γ grains, (d) map of reverted γ grains; (e) cumulative distribution of grain aspect ratio indicating the threshold used for segmentation; (f) map of the recovered γ grains; (g) map of all the recrystallised γ grains, (h) map of the reverted/recovered γ grains.

3.5.2.3 *Analytical procedure for delineation of γ-γ boundaries*

For the 700, 750, 800 and 850 °C samples due to the presence of ε and α′-martensite within the γ grain, it is difficult to determine the γ grain sizes accurately. Thus, a procedure was developed to identify the γ-γ grain boundaries and to calculate the γ grain sizes more precisely. The 850 °C sample is used to describe this procedure. The methodology uses image processing of the γ grain boundary maps and does not utilise any orientation data. The procedure started with the creation of a map (Fig. 3.7a) containing γ-γ HAGBs (in black), $60°\langle 111\rangle_\gamma$ γ twin boundaries (TB_γ, in red) and ε-γ, α′-γ interphase boundaries (in blue). The colour of the γ twin and interphase boundaries was re-assigned to white in order to yield an incomplete γ-γ grain boundary map (Fig. 3.7b).

The incomplete γ-γ boundary map was saved as a tagged image format file image and imported into the ImageJ software package [202]. A pixel-based image scale was defined. The image was then cropped to remove legend information. The cropped red green blue image was then converted to an 8-bit binary image and inverted such that the pixels comprising the incomplete γ-γ grain boundaries were white while the pixels denoting the γ grain interior were black (Fig. 3.7c).

The above procedure was necessary to reveal the incomplete γ-γ grain boundaries and to enable image thresholding into two distinct pixel sets comprising: 0 (or black) and 255 (or white) colour channels. Next, the watershed algorithm was applied to complete the γ-γ boundaries by connecting the end pixels of the incomplete γ-γ boundaries to their nearest neighbouring pixels by the shortest linear distance (Fig. 3.7d) [203]. Following this, Fig. 3.7d and Fig. 3.7b were visually compared in order to manually remove any artificially introduced boundaries (see the boundaries highlighted by red cross marks in Fig. 3.7d). Subsequently, the γ-γ grain boundary outlines were detected (Fig. 3.7e), the number of pixels within each outlined grain was quantified in order to determine the γ grain areas. The equivalent circle diameter (ECD) was calculated from the γ grain areas along with the average and standard deviation of the ECD distribution. It follows that the ECD value corresponds to that diameter of a circle whose area is equivalent to the area of a γ grain [202].

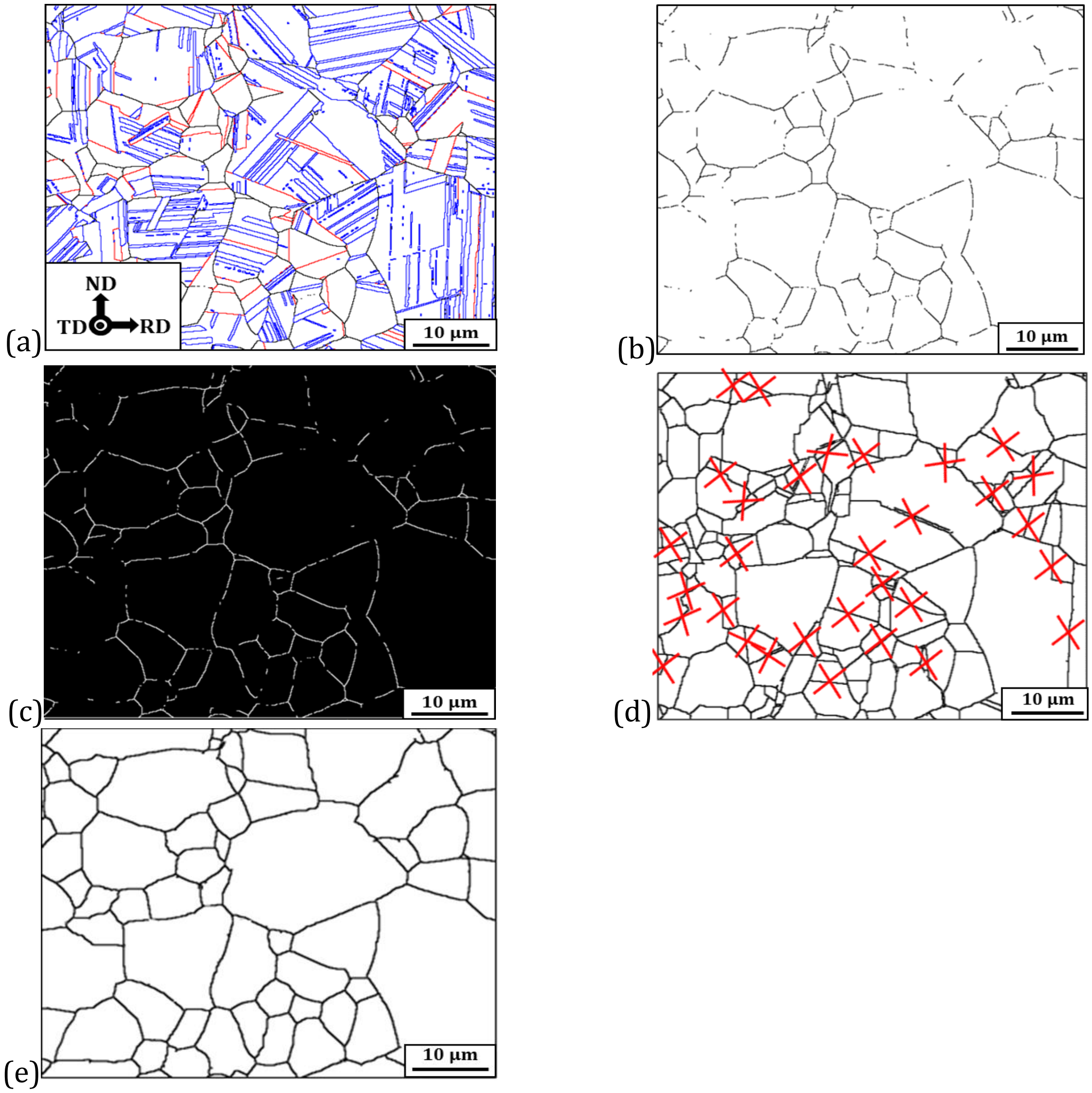

Figure 3.7: Representative boundary maps for the annealed sample showing (a) γ-γ (black), TB_{γ} (red), ε-martensite/γ and α′-martensite/γ interphase (blue) boundaries, (b) incomplete γ-γ boundaries, (c) 8 bit binary, inverted and thresholded incomplete γ/γ grain boundaries, (d) complete γ/γ boundaries after applying watershed algorithm (artificially introduced boundaries are shown by red "X") and (e) identifying individual γ grains to compute the equivalent circle diameter. RD = horizontal, TD = vertical.

3.5.3 Energy dispersive spectroscopy

Energy dispersive spectroscopy (EDS) was undertaken on the 625 °C sample to verify the distribution of elements: Mn, Al, Si and Ni. The EDS analysis was performed on JEOL JSM-7001F FEG-SEM operating at 15 kV at 10 mm working distance. Based on the EDS analysis shown in Fig. 3.8, it can be observed that the distribution of alloying elements is homogenous.

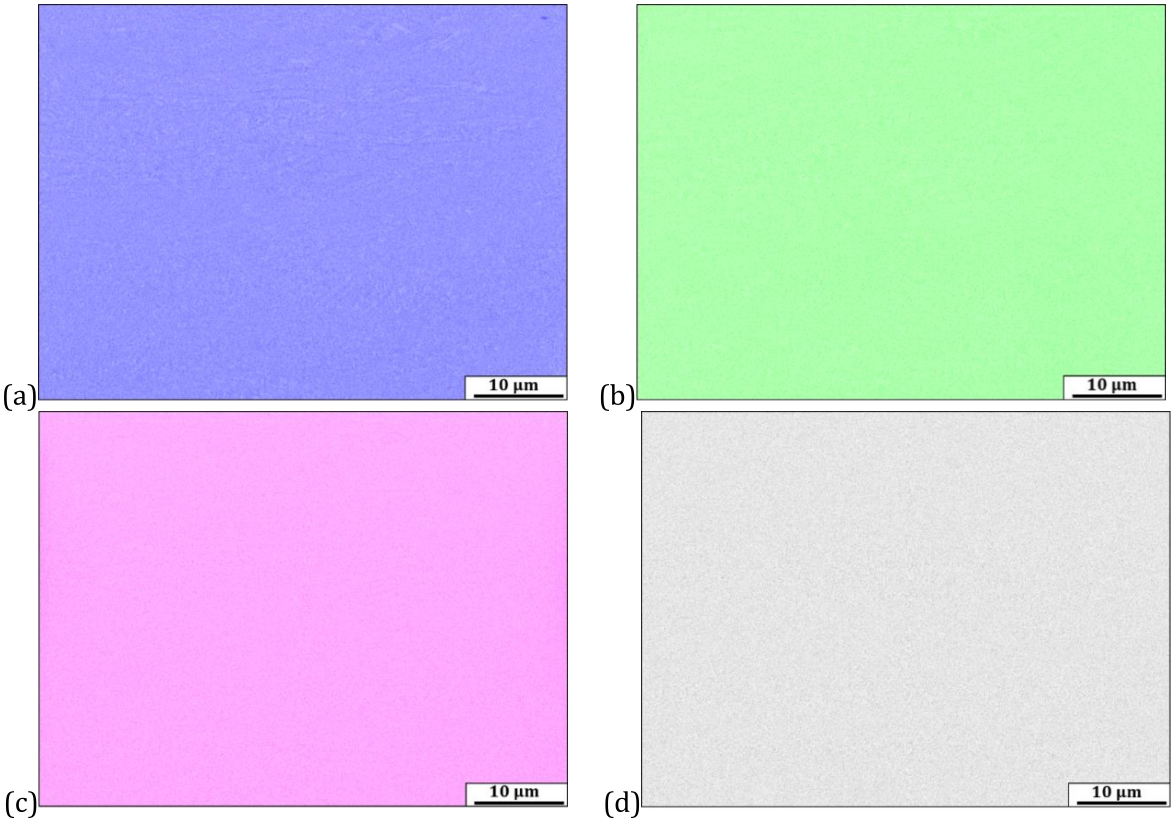

Figure 3.8: EDS maps showing the distribution of elements (a) Mn, (b) Al, (c) Si and (d) Ni.

3.5.4 Transmission electron microscopy

TEM studies were carried out using JEOL JEM-2010 LaB$_6$ TEM operated at 200kV and fitted with Gatan Orius CCD ≈4000 × 2000 camera. Bright-field (BF), selected area electron diffraction (SAED) and displaced aperture dark-field (DF) imaging were conducted on the samples during all the TEM imaging. Imagining of the Shockley partial dislocations in γ and ε-martensite was performed under WBDF condition. To attain WBDF condition in γ and ε martensite, the sample was tilted to $[111]_\gamma$ and $[2\bar{1}\bar{1}0]_\varepsilon$ zone axis, correspondingly. Then the samples were tilted along the $[20\bar{2}]_\gamma$, $[10\bar{1}0]_\varepsilon$, $[0002]_\varepsilon$ to form one line diffraction pattern, followed by sample tilting perpendicular to $[20\bar{2}]_\gamma$, $[10\bar{1}0]_\varepsilon$, $[0002]_\varepsilon$ to form a strong two beam condition with the g = $[20\bar{2}]_\gamma$, $g = [10\bar{1}0]_\varepsilon$, g = $[0002]_\varepsilon$. The beam was then tilted to bring g to the centre resulting in the desired g-3g condition. WBDF imaging was executed by using the g vector at the centre.

Further analysis of the local atomic structure of γ and ε-martensite was carried out using probe corrected STEM in JEOL JEM-ARM 200F which has a resolution of 0.8 nm at 200 kV. Double tilt holder with ± 35° tilting was used in JEOL JEM-ARM 200F equipped with a cold field emission gun. Atomic resolution high angle annular dark-field scanning transmission electron microscopy (HAADF STEM) micrographs were acquired using a hexagonal probe corrector in JEOL JEM-ARM200F with 68 and

180 mrad inner and outer collection angles, respectively, with a dwell time of 38 μs. The images were acquired with Gatan UltraScan 1000XP CCD camera and cleaned using the HRTEM filter tool in the Gatan DigitalMicrograph software suite [204].

The widths of ε-martensite plates/laths (w) was estimated using the measured widths (w_L) from the TEM micrographs via the following equation [205]:

$$w = \frac{2w_L}{\pi} \tag{3.10}$$

3.5.4.1 *In-situ heating in transmission electron microscope*

In-situ heating of the thin foils was carried out in a JEOL 2200FS TEM operating at 200 kV at the University of Sydney using a Gatan double tilt heating stage. The JEOL 2200FS was equipped with a thermal FEG and Gatan ultra scan 2000 × 2000 camera. Gatan 652 double tilt heating stage was used containing tantalum heating furnace with a maximum heating temperature of 1000 °C. The heating experiments were performed using a heating rate of 20 $°\mathrm{Cmm}^{-1}$ to the maximum temperature of 900 °C. The in-situ heating was interrupted at temperatures of every 50 or 100 °C to acquire diffraction patterns from the regions of interest to check for the reversion of ε, α′-martensite and γ twinning. The analysis of the diffraction patterns was carried out utilising the Digital Micrograph software [206]. The Java electron microscopy simulation software by Stadelmann *et al.* [207] was used for the simulation of the diffraction patterns.

CHAPTER 4 EFFECT OF PLANE STRAIN COMPRESSION AND COLD ROLLING ON THE MICROSTRUCTURE AND TEXTURE EVOLUTION IN HIGH MANGANESE STEEL

This chapter includes the characterisation of microstructure during the plane strain compression/cold rolling using EBSD and TEM in Section 4.2. The investigation of the nucleation and coarsening behaviour of ε-martensite with increasing plastic strain is presented in Section 4.3. The ε-martensite deformation accommodation mechanism via the formation of ε-ISF and change in the stacking fault character are elucidated by aberration-corrected TEM and discussed in Section 4.4. Finally, the evolution of texture in the γ, ε and α′-martensite phases with increasing thickness reduction is discussed in Section 4.5. The orientations of the deformation-induced ε and α′-martensite are correlated to the γ orientations by S-N and K-S orientation relationships, respectively.

4.1 Stress-strain and strain hardening curve upon plane strain compression

Fig. 4.1a shows the equivalent stress-strain curve for plane strain compression via Gleeble thermomechanical simulator up to 20% thickness reduction. The curve shows a linear increase followed by a slow rising stress region and an approximately linearly rising equivalent stress values. The start of the slow rising stress region is commonly ascribed to the onset of ε and α′-martensite transformation. The intersection point between the elastic modulus and the tangent to the end of the plateau region is defined as the triggering stress required for the onset of ε and α′-martensite transformation [208] and is calculated as 229 MPa. While the concept of triggering stress was mainly applied to phase transforming metastable β-Ti alloys, it was also used for CrNi metastable austenitic stainless steel subjected to tension [45].

The strain hardening curve is given in Fig. 4.1b shows three regions consisting of (i) sharp initial decrease, (ii) constant region of strain hardening followed by (iii) an increasing strain hardening rate. The Region 1 is due to the elasto-plastic transition [209, 210] and Region 2 is due to the onset of deformation-induced ε and α′-martensite formation (Fig. 4.1b). The increasing strain hardening rate in the Region 3 is due to further transformation of γ to ε and α′-martensite and ε to α′-martensite and the subsequent deformation accommodation by all three phases.

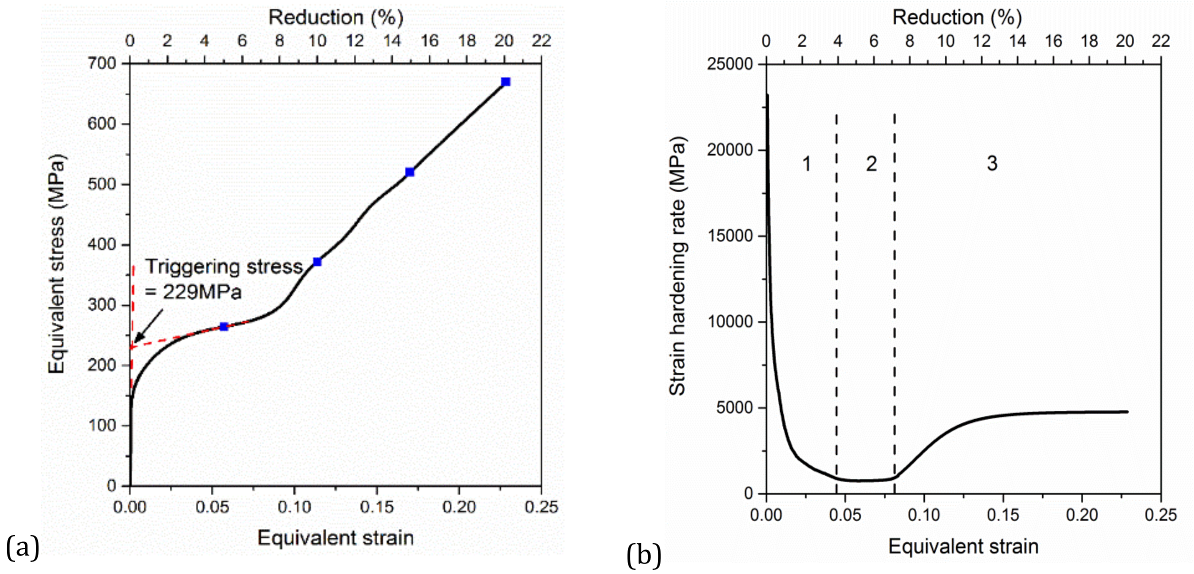

Figure 4.1: Equivalent (a) stress-strain and (b) strain hardening curves upon plane strain compression to 20% thickness reduction. In Fig. 4.1a the blue squares correspond to 5, 10, 15 and 20% thickness reductions. The red dashed lines are extrapolations of the elastic modulus and the tangent to the end of the plateau region for the calculation of the triggering stress.

4.2 Microstructural changes with increasing thickness reduction

Figs. 4.2 and 4.3 show the superimposed band contrast and phase maps after hot rolling and plane strain compression/cold rolling to 88% thickness reduction. The hot-rolled microstructure shows coarse γ grains (red) containing annealing twins (yellow) as well as ε (green) and α′-martensite (blue) formed upon quenching after hot rolling. As shown in Fig. 4.2a inset, the dark lines in γ grains showing no misorientation across their boundaries are probably due to γ stacking faults carried over from hot rolling [211]. The ε-martensite morphology consists of long thin laths or coarse plates running across γ grains. Inside the γ grains, parallel and intersecting ε-martensite plates are observed which belong to the same or different ε-martensite variants, respectively. Lenticular α′-martensite grains are present within thick ε-martensite plates. The formation of α′-martensite from ε-martensite was also observed in an Fe-15Mn-0.5C high Mn steel after solution treatment at 1000 °C for 1 h followed by water quenching [212].

Figs. 4.2b-4.2d and Figs. 4.3a-4.3d depict the microstructure evolution with increasing thickness reduction via plane strain compression and cold rolling. Coarse γ grains containing Σ3 annealing twins carried from the hot-rolled microstructure are observed to 20% thickness reduction (Figs. 4.2b-4.2d and Fig. 4.3a). Inside γ grains, the formation of fine deformation-induced ε-martensite laths occurs at γ stacking faults, which were determined to be of intrinsic type by TEM [50] (dark band contrast regions) shown in the top right inset in Fig. 4.2b or at pre-existing γ Σ3 annealing twin boundaries (top right inset (1) in Fig. 4.2d). The presence of a coarse γ grain can be observed in the sample after 5% thickness reduction (Fig. 4.2b). It can be seen that a higher fraction of ε and α′-martensite is associated with the coarse γ grains due to a higher surface area available for nucleation and subsequent growth. The formation of $\{10\bar{1}2\}\langle\bar{1}011\rangle_{\varepsilon}$ extension twins with ~86° misorientation in ε-martensite grains are denoted in fuchsia (bottom left inset (2) in Fig. 4.2d).

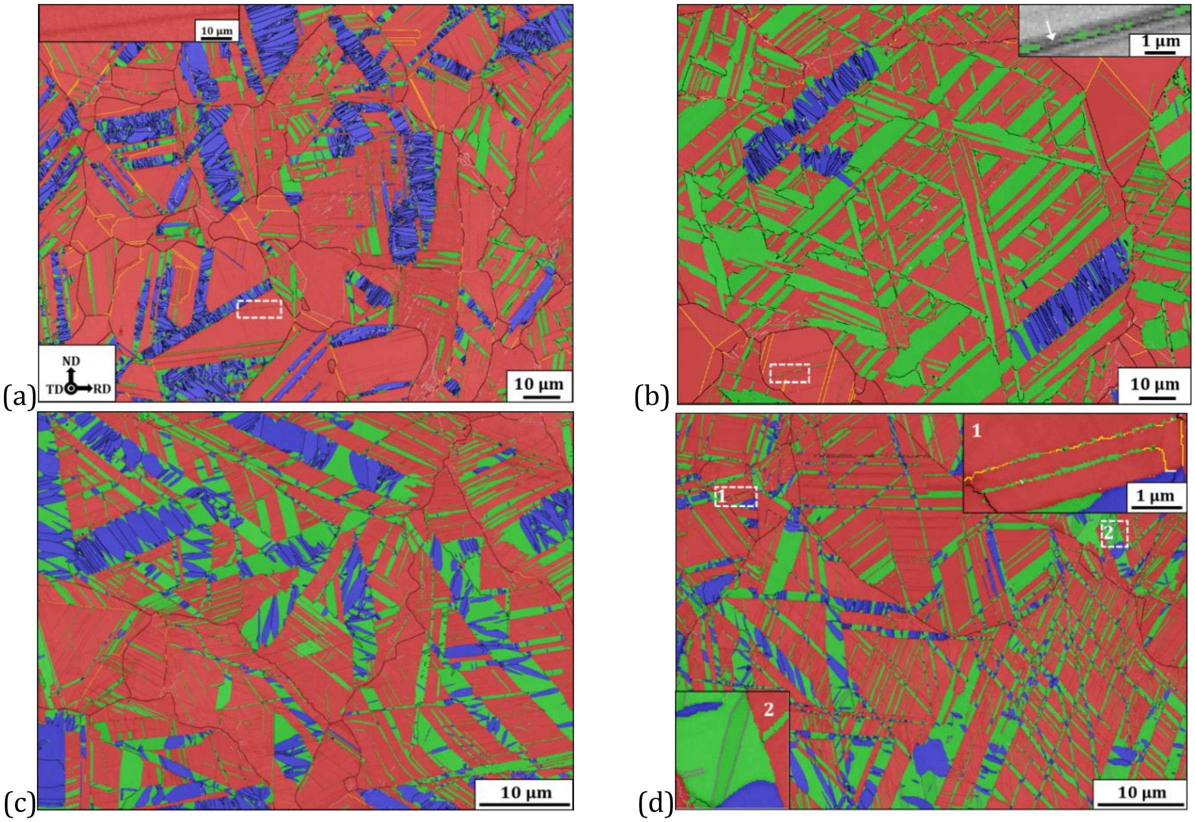

Figure 4.2: Superimposed band contrast and phase maps after (a) hot rolling and room temperature thickness reduction to (b) 5%, (c) 10% and (d) 15%. Red = γ, green = ε-martensite, blue = α′-martensite, white = unindexed areas, silver = low-angle grain boundaries, black = high-angle grain boundaries, yellow = γ twin boundaries. Rolling direction (RD) = horizontal. Insets 1 and 2 in Fig. 4.2d are magnified views of regions highlighted by white dashed rectangle 1 and 2, correspondingly.

The formation of deformation-induced α′-martensite with a lenticular morphology in thick ε-martensite plates carried over from quenching after hot rolling or by phase transformation from ε-martensite (Fig. 4.3a), or in a blocky morphology at the intersection of two ε-martensite laths (top left inset (1) in Fig. 4.3a) and at γ grain boundaries (bottom left inset (2) in Fig. 4.3a) is observed. Due to the sub-division of the ε-martensite plates carried from quenching and also during deformation after hot rolling by colonies of deformation-induced α′-martensite, the remnant ε-martensite has a blocky morphology as shown in the bottom left inset (2) and top right inset (3) in Fig. 4.3a by white arrows.

After 42% thickness reduction, the microstructure showed a majority of α′-martensite area fraction, minor ε-martensite area fraction and a trace amount of untransformed γ as shown in Fig. 4.3b. The pockets of ε-martensite in the cold-rolled sample (Fig. 4.3b) is the remnant ε-martensite formed due to the subdivision of a thick ε-martensite plate by lenticular α′-martensite [81]. The remnant γ which is localised in the 42% cold-rolled sample are less favourably oriented for phase transformation to ε and α′-martensite.

Upon 66% thickness reduction, further transformation of ε-martensite takes place to α′-martensite producing trace areas of ε-martensite and untransformed γ (refer to the arrows in Fig. 4.3c). The ε-martensite undergoes a change in morphology from blocky to elongated grains after 42% and 66% thickness reduction, respectively, indicating deformation accommodation while undergoing transformation to α′-martensite. During the thickness reduction from 42% to 88%, the α′-martensite widths, which were measured via the linear intercept method along the ND, decreased from 0.26 ± 0.1 to 0.15 ± 0.12 µm. In Fig. 4.3d, the white areas denote unindexed regions as well as regions of highly localised strain such as macroscopic shear bands.

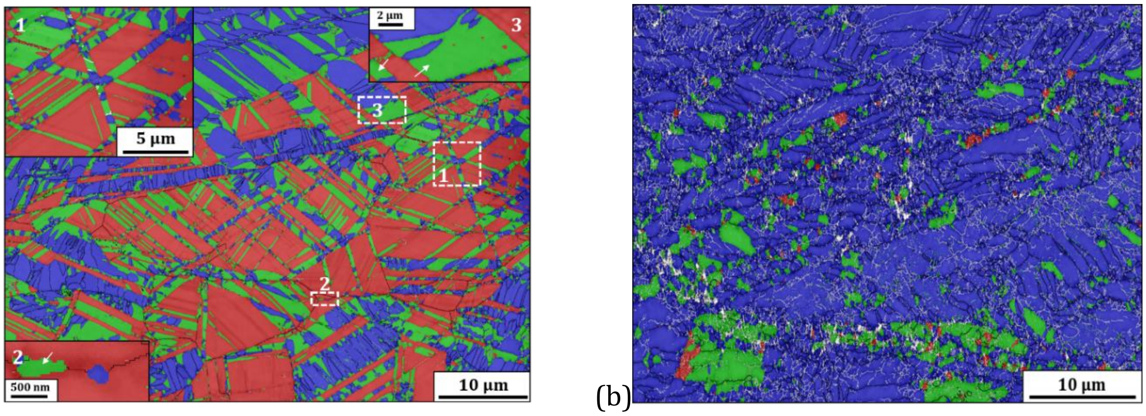

(a) (b)

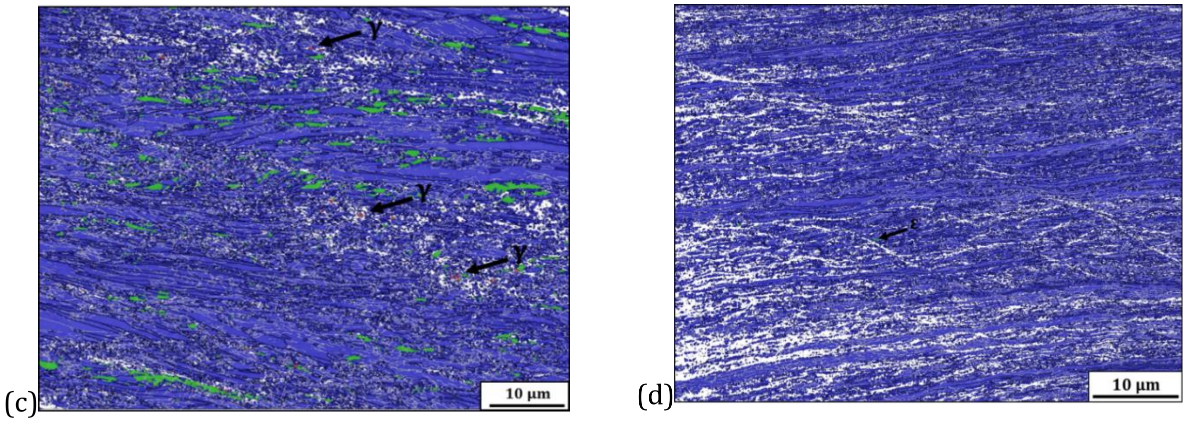

Figure 4.3: Superimposed band contrast and phase maps after thickness reduction to (a) 20%, (b) 42%, (c) 66% and (d) 88%. Red = γ, green = ε-martensite, blue = α′-martensite, white = unindexed areas, silver = low-angle grain boundaries, black = high-angle grain boundaries, yellow = γ twin boundaries. Rolling direction (RD) = horizontal. Insets 1-3 in Fig. 4.3a are the magnified views of regions highlighted by white dashed rectangle 1-3, correspondingly.

Figs. 4.4a-4.4c show the misorientation angle distributions of all the three phases after plane strain compression and cold rolling. With increasing thickness reduction, the γ shows an increase in LAGBs fraction from ≈0.14 to 0.97 and a decreasing fraction of Σ3 twin boundaries (Fig. 4.4a). The decrease in the twin boundary fraction is due to the accumulation of dislocations at twin boundaries [213] during deformation leading to the deviation away from the Palumbo-Aust criterion [198] as well as the nucleation of ε-martensite at twin boundaries.

The inter-variant boundary population in Figs. 4.4a-4.4c shows the occurrence of S-N orientation relationship between γ and ε-martensite [105], K-S orientation relationship between γ and α′-martensite [53] and Burgers orientation relationship between ε and α′-martensite [108].

In Fig. 4.4b, ε-martensite shows a high fraction of LAGBs and grain boundaries having misorientation angle/axis of $70°/\langle 11\bar{2}0\rangle_{\varepsilon}$ which is due to inter-variant boundaries between ε-martensite plates/laths [109, 214]. The fraction of inter-variant boundaries decreases with increasing thickness reduction due to the transformation to α′-martensite. Smaller fractions of HAGBs are also observed at 86° and 90° misorientation angles with $\langle 11\bar{2}0\rangle_{\varepsilon}$ misorientation axis due to $\{10\bar{1}2\}\langle\bar{1}011\rangle_{\varepsilon}$ twinning. The $\{10\bar{1}2\}\langle\bar{1}011\rangle_{\varepsilon}$ extension twins also deviate away from their ideal misorientation angle/axis with increasing thickness reduction. The ε-martensite LAGBs population is seen to increase with thickness reduction.

In Fig. 4.4c, the α′-martensite shows high fractions of $10°/\langle 110\rangle_{\alpha'}$, $50°/\langle 110\rangle_{\alpha'}$, $60°/\langle 110\rangle_{\alpha'}$ and $60°/\langle 111\rangle_{\alpha'}$ misorientation angle/axis boundaries; which correspond to inter-variant crystal pairs

[109]. The α′-martensite misorientation angle distribution matches with the misorientation angle distribution obtained in a titanium alloy as presented in Table 2.6 of Chapter 2. The bcc α′-martensite forms from the hcp ε-martensite via the operation of Burgers orientation relationship, which is also obeyed during the β (bcc) to α (hcp) phase transformation process in titanium alloys.

With increasing thickness reduction the LAGBs population is observed to increase. The α′-martensite inter-variant boundary fraction decreases due to the deviation away from the angle-axis criteria. This is due to the accumulation of dislocation at the α′-martensite inter-variant interface. With increasing thickness reduction the population of LAGBs in α′-martensite is noted to increase.

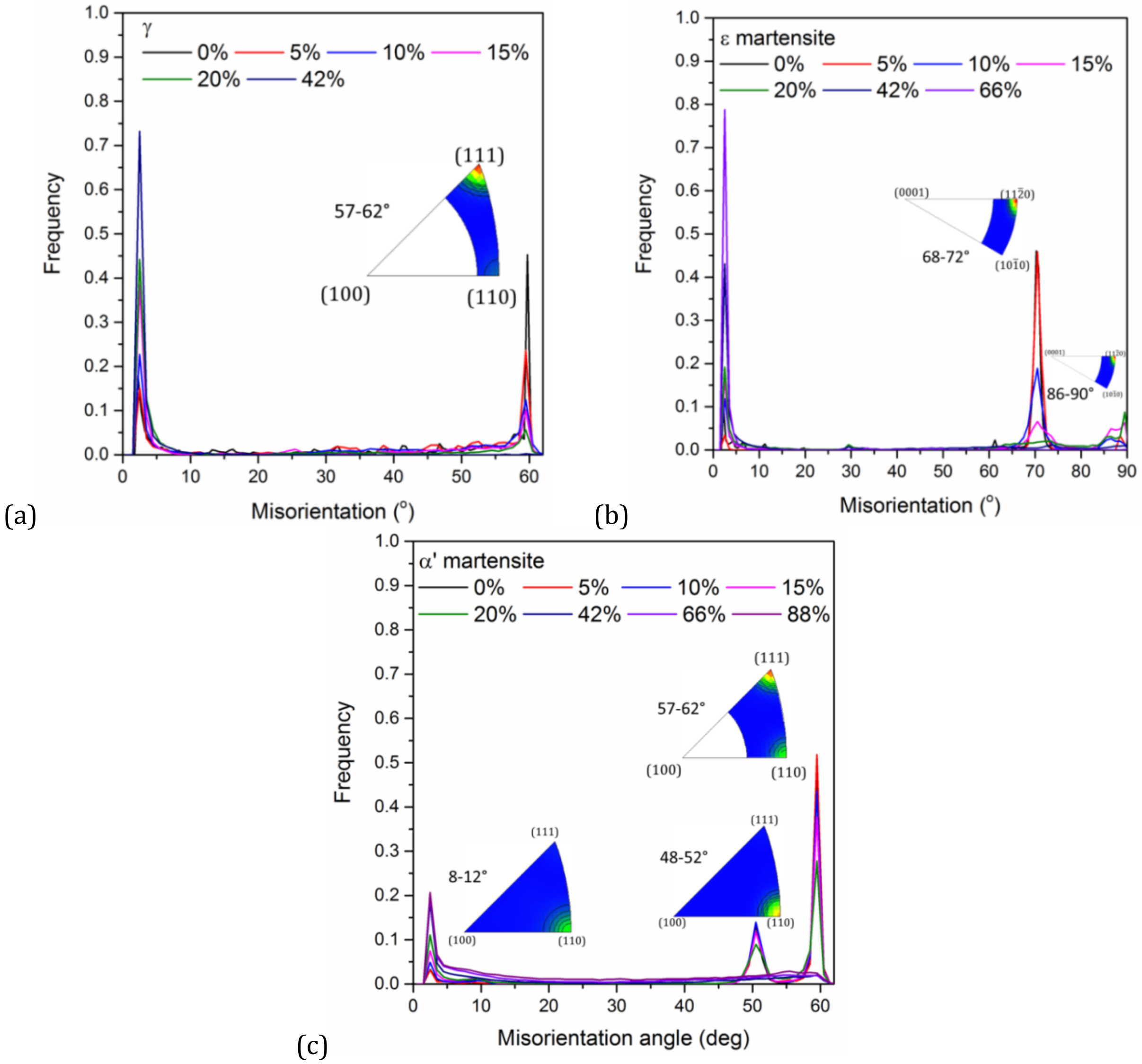

Figure 4.4: Misorientation angle distributions of (a) γ, (b) ε-martensite and (c) α′-martensite with thickness reduction up to 88%.

In Fig. 4.5, bright-field and dark-field TEM micrographs show the microstructure evolution with increasing thickness reduction to 20%. The coarse ε-martensite plates having S-N orientation relationship with their parent γ grains are present in the hot-rolled sample (Figs. 4.5a). Between 5 and 20% thickness reductions, the formation of deformation-induced ε and α′-martensite is seen in Figs. 4.5b-4.5e. The inset diffraction patterns in the Figs. 4.5b-4.5d shows the formation of deformation-induced ε-martensite to occur with S-N orientation relationship. The substructure of deformation-induced α′-martensite was detected to contain dislocations which are shown in Fig. 4.5d. Similar dislocation substructures in α′-martensite were witnessed in an Fe-17Mn-0.05C steel after tension to 15% engineering strain [212].

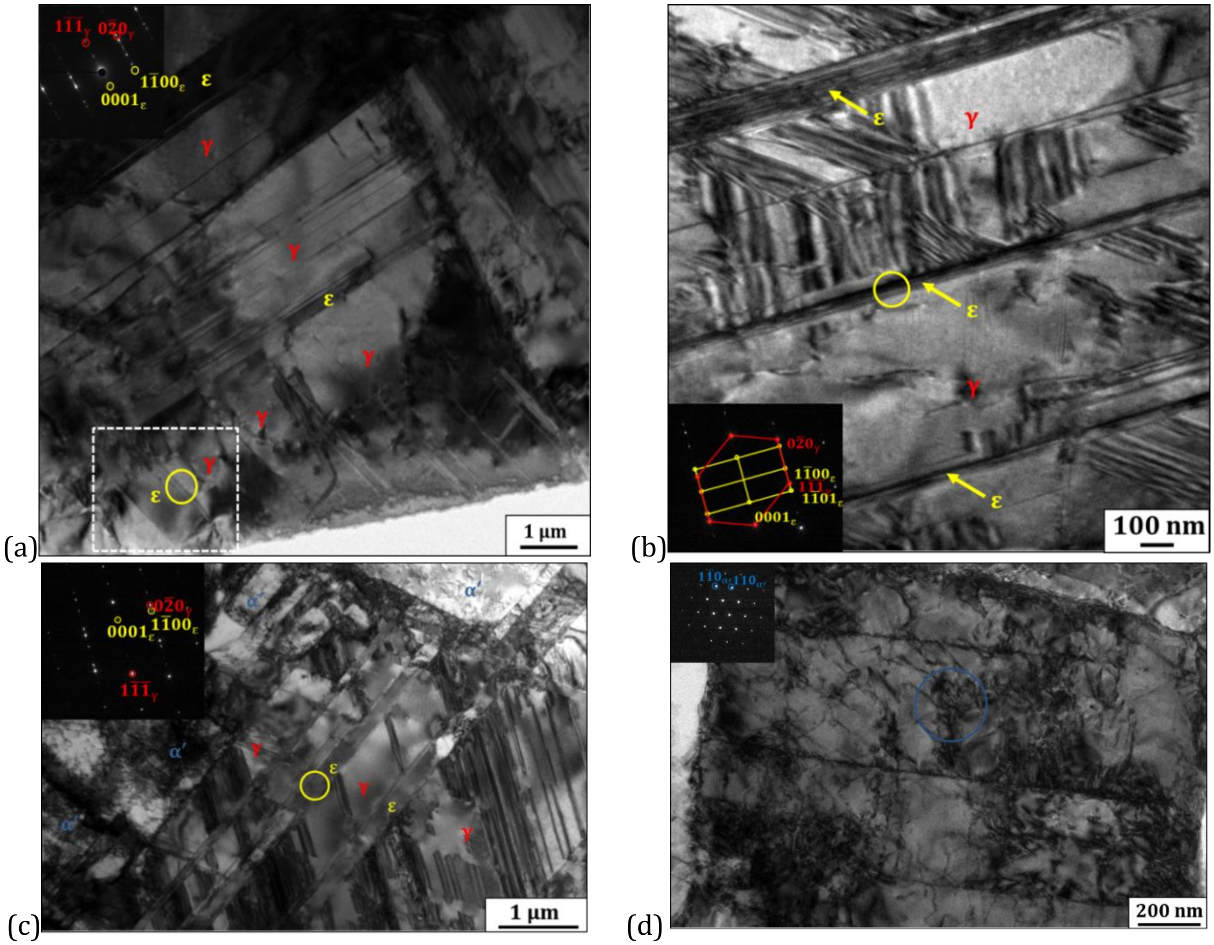

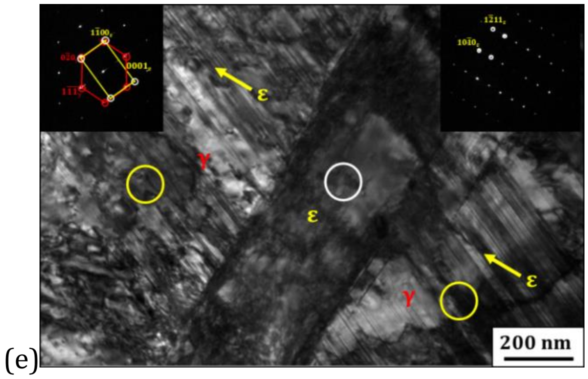

Figure 4.5: Representative bright-field transmission electron micrographs after (a) hot rolling and thickness reductions to (b) 10%, (c, d) 15% and (e) 20%. The inset diffraction patterns in Figs. 4.5a-4.5d are from the regions demarcated by yellow/white/blue circles or the complete area of interest. The top left and right diffraction patterns are from the yellow and white circular regions, respectively, in Fig. 4.5d. The zone axes are $[101]_{\gamma}$, $[11\bar{2}0]_{\varepsilon}$, $[\bar{1}11]_{\alpha'}$ in Figs. 4.5a-4.5e.

Thickness reduction to 42% shows the coarsening of the deformation-induced ε and α′-martensite (Fig. 4.6a). The TEM data confirms the same results obtained by EBSD. Thickness reductions to 66% and 88% (Figs. 4.6b-4.6e) produce elongated α′-martensite grains. The dark-field micrograph shows the remnants of ε-martensite along the α′-martensite boundaries (Figs. 4.6c and 4.6e).

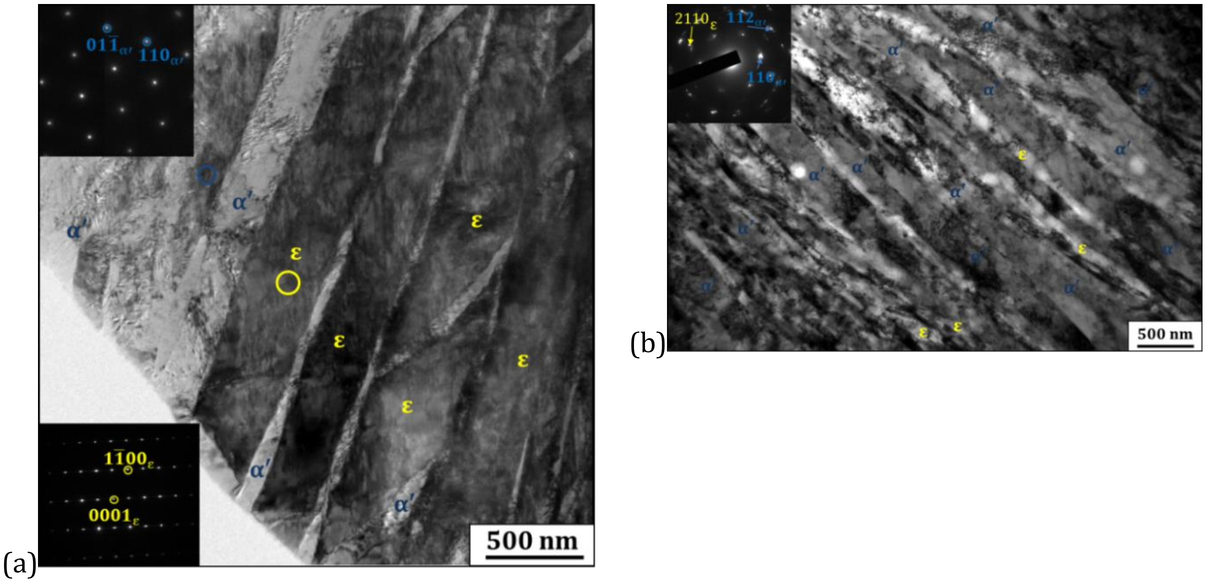

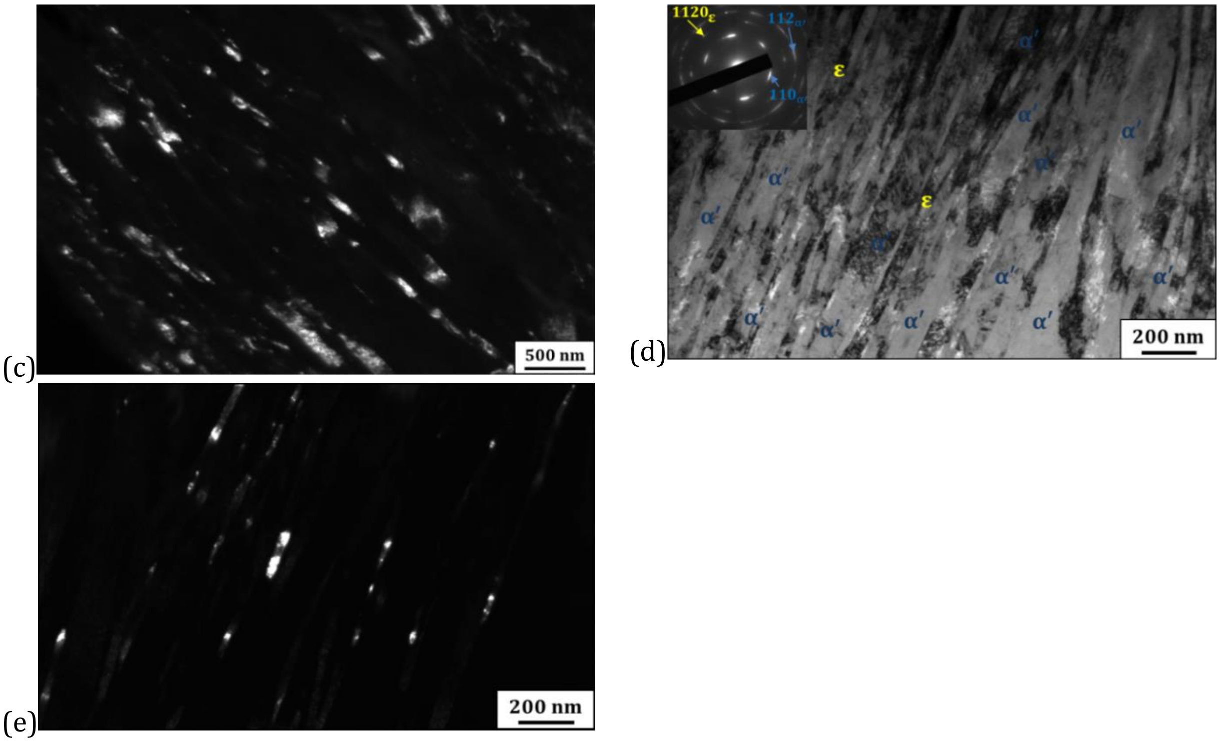

Figure 4.6: Representative (a, b, d) bright-field, (c, e) dark-field transmission electron micrographs after thickness reduction to (a) 42%, (b, c) 66% and (d, e) 88%. The inset diffraction patterns in Figs. 4.6a, 4.6b and 4.6d are from the regions demarcated by yellow circles or the complete area of interest. The zone axes are $[1\bar{1}\bar{1}]_{\alpha'}$, $[11\bar{2}0]_\varepsilon$ in Fig. 4.6a.

4.3 Nucleation of deformation-induced ε-martensite

Fig. 4.7a is a bright-field TEM micrograph obtained in the sample after 5% thickness reduction which shows the nucleation of fine, deformation-induced ε-martensite laths. The inset diffraction pattern shows the occurrence of S-N orientation relationship. The dark-field micrograph in Fig. 4.7b shows a deformation-induced ε-martensite of 3 ± 1 nm width along with 19 ± 3 nm lath which is expected to be carried over upon quenching after hot rolling. Along the 3 nm deformation-induced ε-martensite lath the intensity disappears.

HAADF STEM micrographs from regions: (1) along the edge, which is very close to the tip and (2) within the ε-martensite lath are given in Figs. 4.7c and 4.7d, respectively. The edge region near the tip shows γ containing ISFs with ABCA|CABC.. stacking along with a 4 layer nucleus of deformation-induced ε-martensite (Fig. 4.7c). Inside the deformation-induced ε-martensite lath, a thin layer of untransformed γ is also present (Fig. 4.7d). The interface between the γ and ε-martensite phases along the $[0002]_\varepsilon$ direction is smooth having a one-to-one congruence between the fcc and hcp atoms.

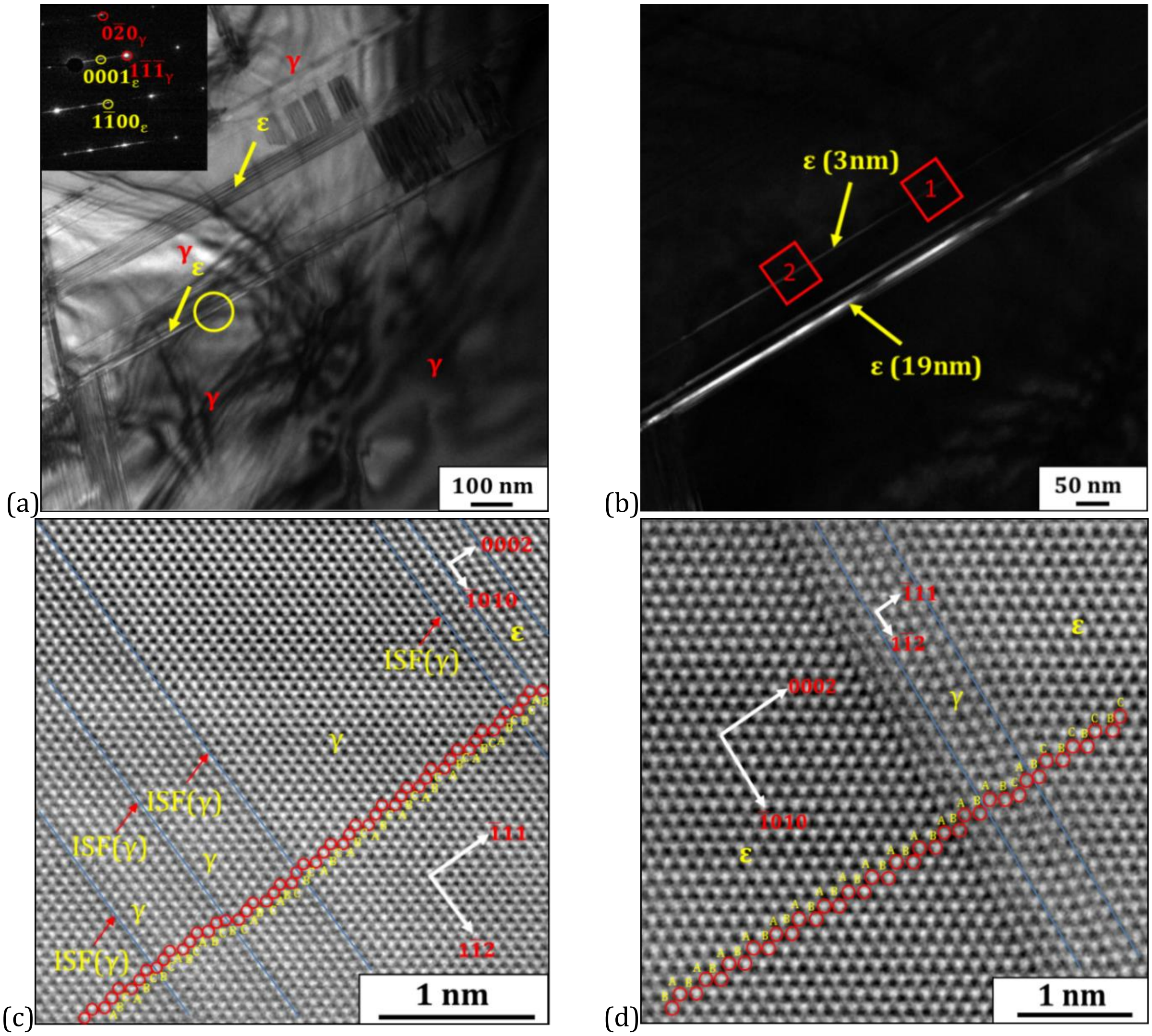

Figure 4.7: Representative (a) bright-field, (b) dark-field transmission electron micrographs and (c, d) HAADF STEM images after 5% thickness reduction. The Figs. 4.7c, 4.7d are from the regions (1) and (2) in Fig. 4.7b, respectively. In Figs. 4.7c and 4.7d, the blue solid lines denote fault planes in γ. The inset diffraction pattern in Fig. 4.7a is from the region demarcated by a yellow circle. The zone axes are $[101]_\gamma$ and $[11\bar{2}0]_\varepsilon$.

The nucleation of deformation-induced ε-martensite seen in Figs. 4.7c and 4.7d after 5% thickness reduction are in agreement with previous observations [15, 215-217], which report that γ-ISFs in γ nucleate ε-martensite and in turn coarsen laterally to form the fine deformation-induced laths. The occurrence of an untransformed γ region in Fig. 4.7d displays incomplete lateral coarsening. Pierce *et al.* [76, 82] also observed the formation of wide γ-ISFs on tension to 0.002 and 0.015 engineering strains, which resulted in the transformation of γ-ISFs to ε-martensite. This finding agrees with the present result. Also, Figs. 4.7c and 4.7d do not support the earlier suggestion of ε-martensite comprising a bundle of γ stacking faults [218].

A similar type of nucleation and coarsening mechanism was also reported by Kikuchi *et al.* [14], wherein 1-2 nm wide ε-martensite laths nucleated and coalesced with neighbouring ε-martensite plates; thereby increasing the thickness of the latter. Fujita and Ueda [15] also made a similar observation. In that study, it was proposed that stacking faults form irregularly on the $(111)_\gamma$ plane supported by the motion of Shockley partial dislocations emitted from the γ grain boundaries; which coarsen laterally to nucleate deformation-induced ε-martensite. The width of the stacking faults increases due to the activation of more faults in the nearby $(111)_\gamma$ planes which enhance the lateral coarsening as ε-martensite propagates within γ grains [15].

Fig. 4.8 is a schematic illustrating the coalescence of two fine, deformation-induced ε-martensite laths containing a thin region of untransformed γ. The coalescence occurs by the motion of Shockley partial dislocations on alternate "C" planes and ending in the "A" plane of γ. This mechanism is valid only when Shockley partial dislocations pass through the configuration in γ shown in Fig. 4.8. The passage of dislocations in a different configuration will lead to the occurrence of the same type of planes on top of each other, which is not energetically favourable.

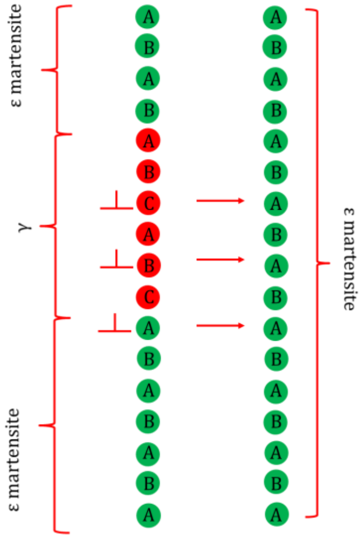

Figure 4.8: Schematic of coarsening by coalescence of ε-martensite laths. The red and green circles represent fcc and hcp stacking sequences, respectively. Shockley partial dislocations are given by the symbol "⊥".

Figs. 4.9a and 4.9b show bright-field STEM micrographs comprising deformation-induced ε-martensite laths in the sample after 10% thickness reduction. The HAADF STEM micrographs of the regions (1), (2) and (3) from Fig. 4.9b are presented in Figs. 4.9c, 4.9d and 4.9e, respectively, which illustrates the interfacial structure and the internal structure within the deformation-induced ε-martensite laths. In Fig. 4.9c, the interaction region represented using dashed blue lines depicts a distorted γ lattice. The shear associated with this region was calculated to be 0.09, which causes a localised distortion when moving from the fcc to hcp lattices along the $[10\bar{1}0]_\varepsilon$ direction. In Fig. 4.9d the interface between γ and ε-martensite is smooth and without ledges along the $[0002]_\varepsilon$ direction. Similar observations were reported in Ref. [101] where the deformation-induced ε-martensite was observed to have a smooth interface with γ. The tips of ε-martensite laths terminate in a Shockley partial dislocation (Fig. 4.9e).

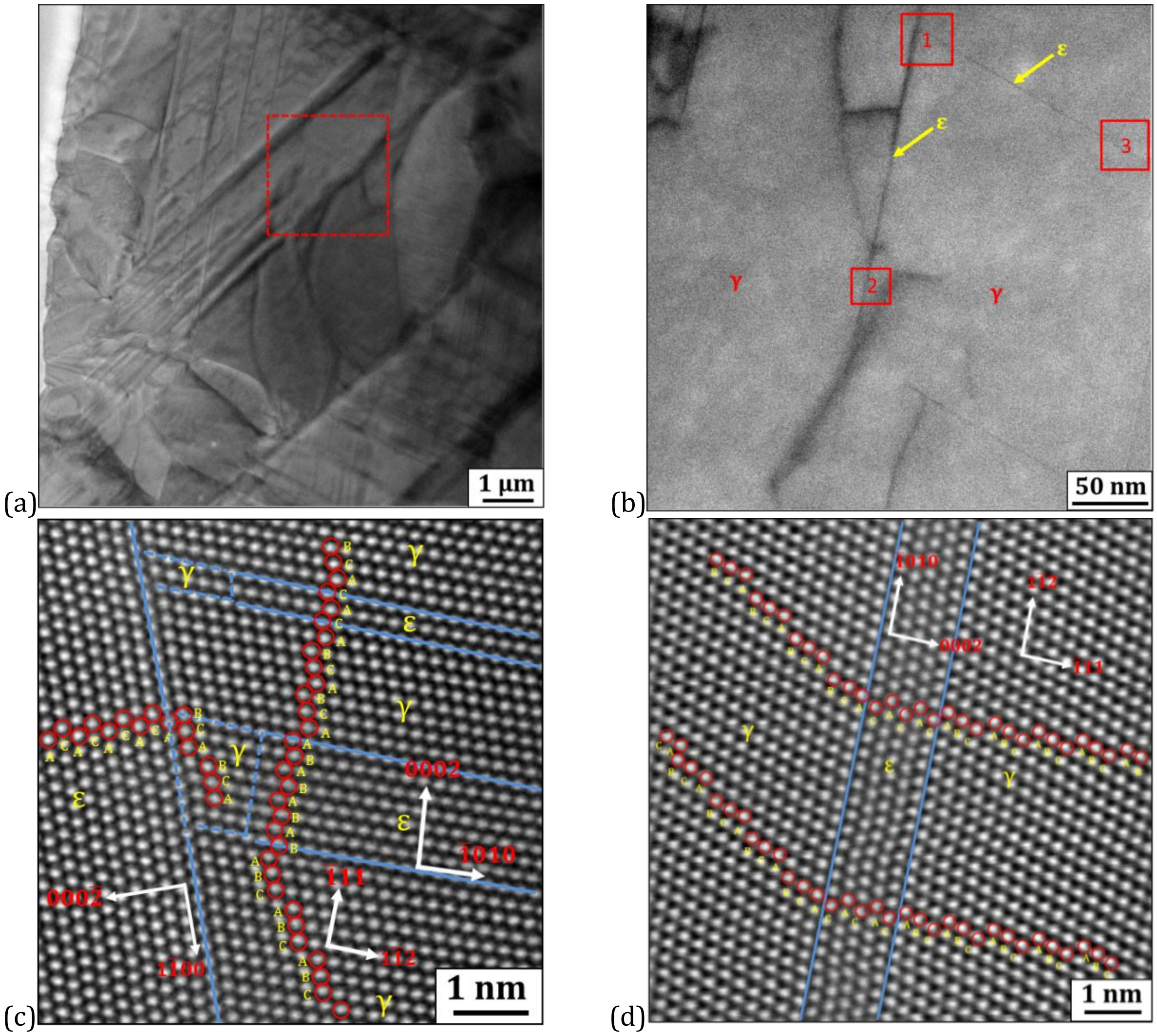

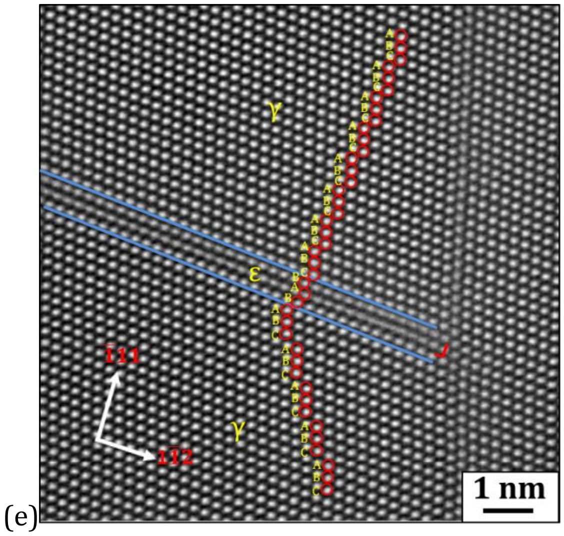

Figure 4.9: Representative (a, b) bright-field STEM micrographs and (c-e) HAADF STEM images after 10% thickness reduction. Fig. 4.9b is a magnified view of the region denoted by red dashed square in Fig. 4.9a. Figs. 4.9c-4.9e are from the regions (1) to (3) in Fig. 4.9b, respectively. In Figs. 4.9c-4.9e, the blue solid/dashed lines denote the γ/ε-martensite interface while Shockley partial dislocations are given by the symbol "┘".

4.4 Deformation accommodation mechanisms in γ and ε-martensite

Fig. 4.10a is a magnified, dark-field TEM micrograph of a ε-martensite plate from the hot-rolled sample. Fig. 4.10a is taken from the dashed white rectangular region shown in Fig. 4.5a. The interface between γ and ε-martensite is shown by HAADF STEM micrograph in Fig. 4.10b. The ε-martensite plate, formed on quenching after hot rolling, does not contain any faults. However, γ-ISFs are observed to be present. The dark-field TEM micrograph of the sample after 5% thickness reduction in Fig. 4.10c shows the distribution of relatively fine and coarse deformation-induced ε-martensite laths. The 65 nm wide ε-martensite lath in Fig. 4.10c returns I_1 -type ε-ISF in Fig. 4.10d. Fig. 4.10e shows the dark-field micrograph revealing γ-ISFs under two beam condition using the g = $[1\bar{1}1]_\gamma$ in the sample after 15% thickness reduction. This indicates the operation of partial basal slip.

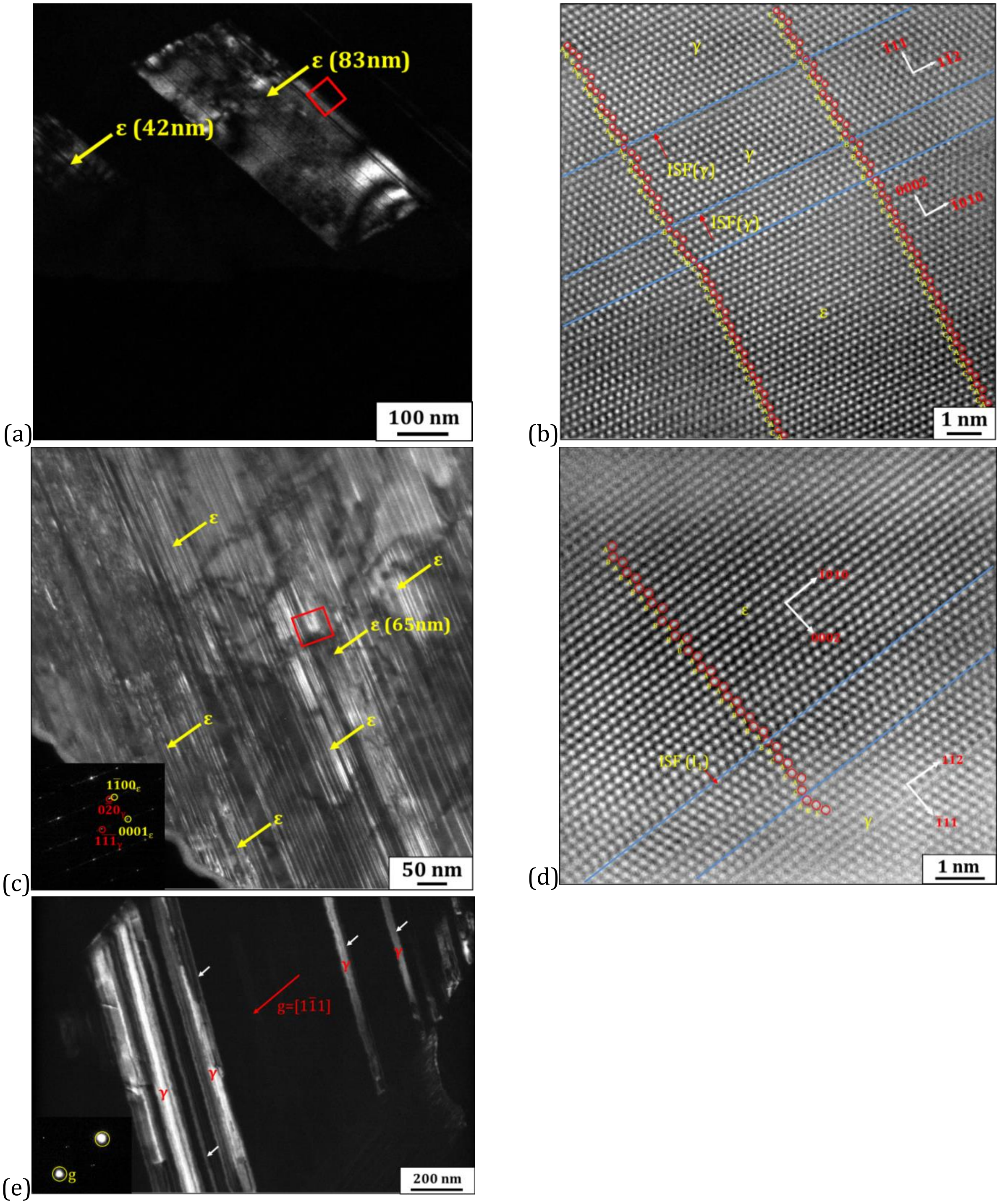

Figure 4.10: (a, c, e) Dark-field micrographs and (b, d) HAADF STEM micrographs after (a, b) hot rolling, thickness reduction to (c, d) 5% and (e) 15%. The inset diffraction patterns in Fig. 4.10c are from regions demarcated by a red square. Fig. 4.10e is observed under two beam conditions using g = [1$\bar{1}$1]$_\gamma$. The zone axes are [101]$_\gamma$, [11$\bar{2}$0]$_\varepsilon$ in Fig. 4.10c.

Fig. 4.11 shows dislocations in the pyramidal plane of ε-martensite in the sample after 15% thickness reduction. The formation of stacking faults (highlighted by black arrows) and dislocations tangles (highlighted by black arrows in inset) can also be observed. This indicates the occurrence of a pyramidal slip in ε-martensite. High activity of pyramidal dislocations was also observed in an Mg-3Y alloy after 3% plastic deformation [219]. The possibility of occurrence of $\{10\bar{1}1\}_\varepsilon$ pyramidal slip in Mg was also proposed by molecular dynamics simulations [220].

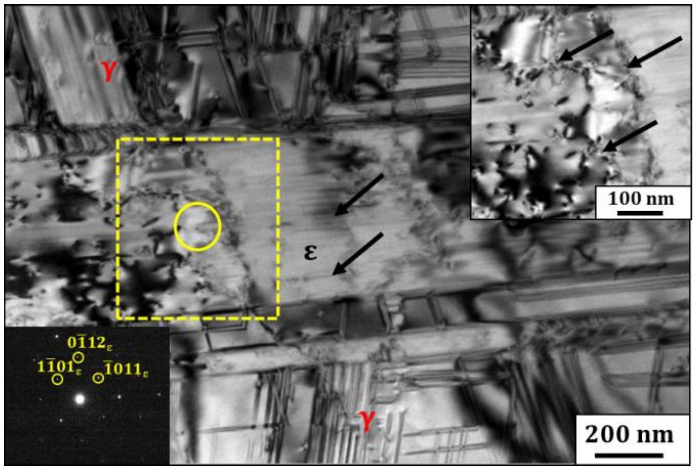

Figure 4.11: ε-martensite bright-field micrograph for the sample after 15% thickness reduction taken from the zone axis $[01\bar{1}1]_\varepsilon$.

Figs. 4.12a and 4.12b are bright and dark-field TEM micrographs, respectively, from ε-martensite plates in the sample after 10% thickness reduction. The HAADF STEM micrograph of the 20 nm wide ε-martensite lath shows an I_2 -type ε-ISF highlighted by blue lines in Fig. 4.12c. In Fig. 4.12d the presence of multiple I_1 -type ε-ISFs highlighted by blue lines on parallel $(0002)_\varepsilon$ planes within a 64 nm wide ε-martensite lath can be observed. ε-ISFs (Fig. 4.12e) was also identified in the samples after 15% thickness reduction in the dark-field images obtained under two beam condition using the g = $[01\bar{1}1]_\varepsilon$ [221] and by employing the procedures outlined in Ref. [222].

In ε-martensite, I_1 and I_2 -type ε-ISFs are created by the motion of Shockley partial dislocations that form by the dissociation of $\frac{a}{3}[2\bar{1}\bar{1}0]_\varepsilon$ perfect dislocations by the reaction:

$$\frac{a}{3}[2\bar{1}\bar{1}0]_\varepsilon \rightarrow \frac{a}{3}[10\bar{1}0]_\varepsilon + \frac{a}{3}[1\bar{1}00]_\varepsilon \tag{4.11}$$

The HAADF STEM micrograph of a 223 nm wide ε-martensite plate observed in the sample after 42% thickness reduction which is taken from the yellow circular region in Fig. 4.6a and shown in Fig. 4.12f shows I_1 -type ε-ISFs. The strain fields of the Shockley partial dislocations distort the atomic layers in the micrograph in Fig. 4.12f due to the obstruction of electron channelling along atomic columns. The presence of ε-ISFs was reported in deformation-induced ε-martensite formed in metastable austenitic steels [101].

Therefore, the present EBSD and TEM results show that deformation accommodation in ε-martensite upon plane strain compression/cold rolling takes place via a combination of perfect and partial basal slip, pyramidal slip along with $\{10\bar{1}2\}\langle\bar{1}011\rangle_{\varepsilon}$ extension twinning.

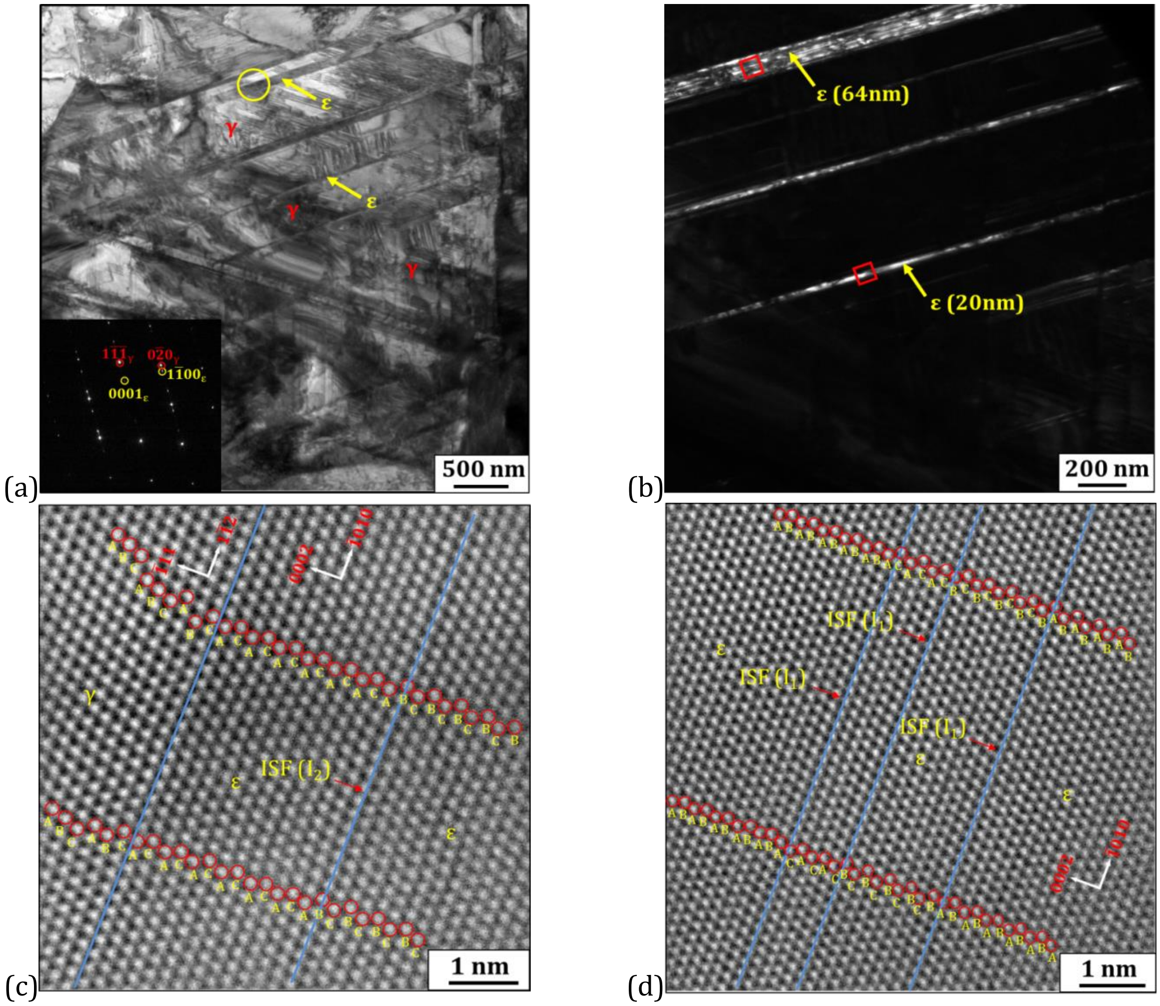

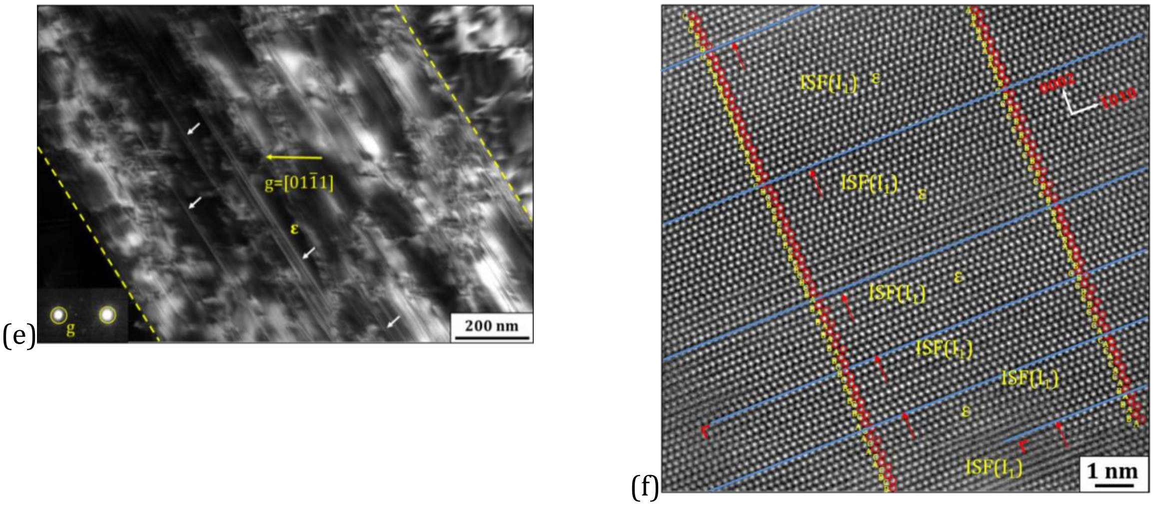

Figure 4.12: (a) Bright-field micrograph, (b, e) dark-field micrographs, (c, d, f) HAADF STEM micrographs after thickness reduction to (a-d) 10%, (e) 15% and (f) 42%. Shockley partial dislocations are shown by the symbol "┘" in Fig. 4.12f. The inset diffraction patterns in Figs. 4.12a and 4.12e are from the regions demarcated by yellow circles/whole micrograph. Fig. 4.12e is taken under two beam conditions using g = $[01\bar{1}1]_\varepsilon$. The zone axes are $[101]_\gamma$, $[11\bar{2}0]_\varepsilon$ in Fig. 4.12a.

A mechanism is proposed for the deformation of ε-martensite via the formation of ε-ISF as shown in Fig. 4.13. The schematic explains the formation mechanism of ε-martensite and subsequent deformation accommodation by ε-martensite through a change in ε-ISF character. In step 1, the motion of Shockley partial dislocations on every second plane leads to the transformation γ to ε-martensite. In step 2, the motion of Shockley partial dislocation via the "A" stacking sequence returns the formation of an I_2 -type ε-ISF. In step 3, the I_2 -type ε-ISF transforms to an I_1 -type ε-ISF via the motion of Shockley partial dislocations through every plane. Steps 2 and 3 show the formation of I_2 -type ε-ISFs and the change in stacking fault character results in the ε-martensite deformation accommodation. The formation of I_2 ε-ISF takes place first as it requires the motion of relatively less number of Shockley partials compared to I_1 ε-ISF.

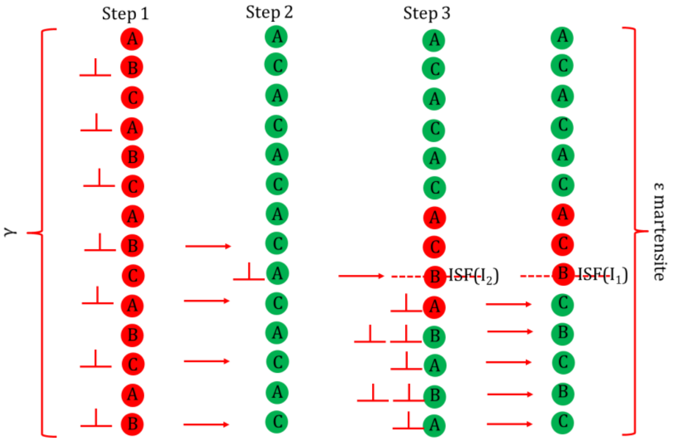

Figure 4.13: Schematic of the phase transformation from γ to ε-martensite followed by a transition in the stacking fault character from I_2 to I_1 -type ε-ISFs. The red and green circles represent fcc and hcp stacking sequences, respectively. Shockley partial dislocations are given by the symbol "⊥".

4.5 General overview of microstructure changes during plane strain compression and cold rolling

Based on the above results a schematic of the transformation and deformation accommodation behaviour with increasing thickness reduction is provided in Fig. 4.14. Upon quenching after hot rolling the microstructure consists of γ with stacking faults (in purple) and annealing twins (in yellow) as shown in Fig. 4.14, step 1. The parallel and intersecting ε-martensite plates and α′-martensite plates that form upon quenching are present within individual γ grains. However, this is not shown in the schematic in Fig. 4.14 as the discussion here is focused on the deformation and subsequent transformation behaviour of γ and does not include the deformation of ε and α′-martensite formed upon quenching after annealing.

In Fig. 4.14 step 2, after 10% thickness reduction, the γ deformation accommodation takes place by partial slip leading to the formation of γ-ISFs and also via the transformation to deformation-induced ε-martensite which appear either alongside ε-martensite plates or in isolation and at γ annealing twins. Concurrently, I_2 ε-ISFs (in orange) and I_1 ε-ISFs (in brown) form in fine ε-martensite laths.

In Fig. 4.14, up to ~20% thickness reduction (Fig. 4.14, step 3), the transition of I_2 -type ε-ISFs to I_1 -type ε-ISFs (in brown) occurs in ε-martensite. Concomitantly, the α′-martensite forms at the intersections of ε-martensite plates/laths, within ε-martensite plates/laths and also within the γ matrix. The formation of $\{10\bar{1}2\}\langle\bar{1}011\rangle_{\varepsilon}$ extension twins (in fuschia) also occurs in ε-martensite. The operation of partial slip leading to the formation of γ-ISFs also continues at this stage of deformation. However, the formation of ε and α′-martensite in γ is the dominant mechanism.

Thickness reduction up to ≈42% (Fig. 4.14, step 4) results in the blocky ε-martensite morphology and elongated, fragmented α′-martensite morphology whereas after thickness reduction to 66% (Fig. 4.14, step 5) the morphology of α′-martensite is pancaked. In the sample after 88% thickness reduction (Fig. 4.14, step 6), the microstructure predominantly contains α′-martensite with macroscopic shear bands and trace fractions of γ and ε-martensite. Therefore, α′-martensite accommodates deformation up to 88% thickness reduction via slip and macroscopic shear banding.

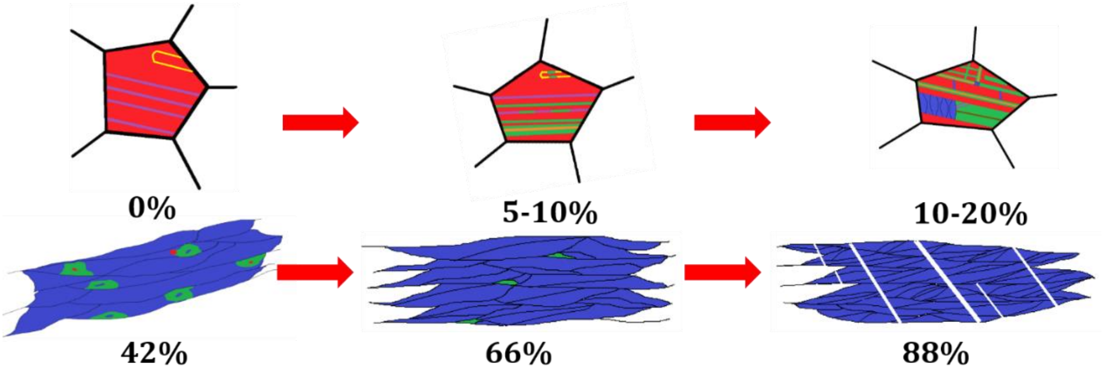

Figure 4.14: Schematic of deformation and transformation behaviour of high Mn steel with increasing thickness reduction up to 88%. Red = γ, green = ε-martensite, blue = α′-martensite. γ intrinsic stacking faults are shown in purple while I_2 and I_1 faults in ε-martensite are shown in orange and brown, respectively. Annealing twins in γ and $\{10\bar{1}2\}\langle\bar{1}011\rangle_{\varepsilon}$ extension twins in ε-martensite are shown in yellow and fuchsia, respectively.

4.6 Texture changes of γ, ε and α′-martensite with increasing thickness reduction

Fig. 4.15a shows the ideal γ orientations (in red) plotted in the ϕ_2 = 0°, 45° and 65° ODF sections. The γ orientations in the samples after hot rolling and plane strain compression/cold rolling to 42% thickness reduction are presented in Figs. 4.15b-4.15g. The ODF sections of γ were not plotted after thickness reduction to 66 and 88% due to its low area fraction.

The hot-rolled γ returns weak α_{γ}-fibre ($\langle 110\rangle_{\gamma}||$ND) $\{110\}\langle 223\rangle_{\gamma}$ (ϕ_1 = 42°, Φ = 90°, ϕ_2 = 45°) orientation, along with Copper (Cu_{γ}, $\{112\}\langle 111\rangle_{\gamma}$), S_{γ} ($\{123\}\langle 634\rangle_{\gamma}$) and Cube ($C_{\gamma}$, $\{100\}\langle 001\rangle_{\gamma}$) orientations (Fig. 4.15b). After thickness reductions to 5 and 10%, the γ shows orientations along the α_{γ}-fibre Goss (G_{γ}, $\{110\}\langle 001\rangle_{\gamma}$), $(011)[3\bar{1}\bar{1}]_{\gamma}$($\phi_1$ = 20°, Φ = 45°, ϕ_2 = 0°), Brass (Br_{γ}, $\{110\}\langle 112\rangle_{\gamma}$), Cu_{γ} and Br_{γ}, A_{γ}, S_{γ}, Cu_{γ} in Figs. 4.15c and 4.15d, respectively. Similar γ orientations were observed after thickness reduction to 15 and 20% (Figs. 4.15e and 4.15f). After thickness reduction to 42%, strong intensities around the Br_{γ} and S_{γ} orientations is noted along with the weak intensities around the C_γ and Rotated-Goss (Rt-G_γ, $\{011\}\langle 011\rangle_\gamma$) orientations (Figs. 4.15g). In summary, after thickness reduction to 42%, the strengthening of intensities around the Br_γ, S_γ and Cu_γ orientations (Fig. 4.15c-4.15f) occurs. The strengthening of intensities around the Br_γ orientation during the cold rolling of an Fe-22Mn-0.37C steel was also reported [8]. During the cold rolling of an Fe-22Mn-0.37C steel, Lü *et al*. [8] observed the formation of a strong Br_γ orientation along with a spread towards the G_γ orientation. In that study, weak intensities around the Cu_γ and S_γ orientations were also observed. Similar orientations were observed during the cold rolling of an Fe-26Mn-3Si-3Al steel to 56% thickness reduction [11].

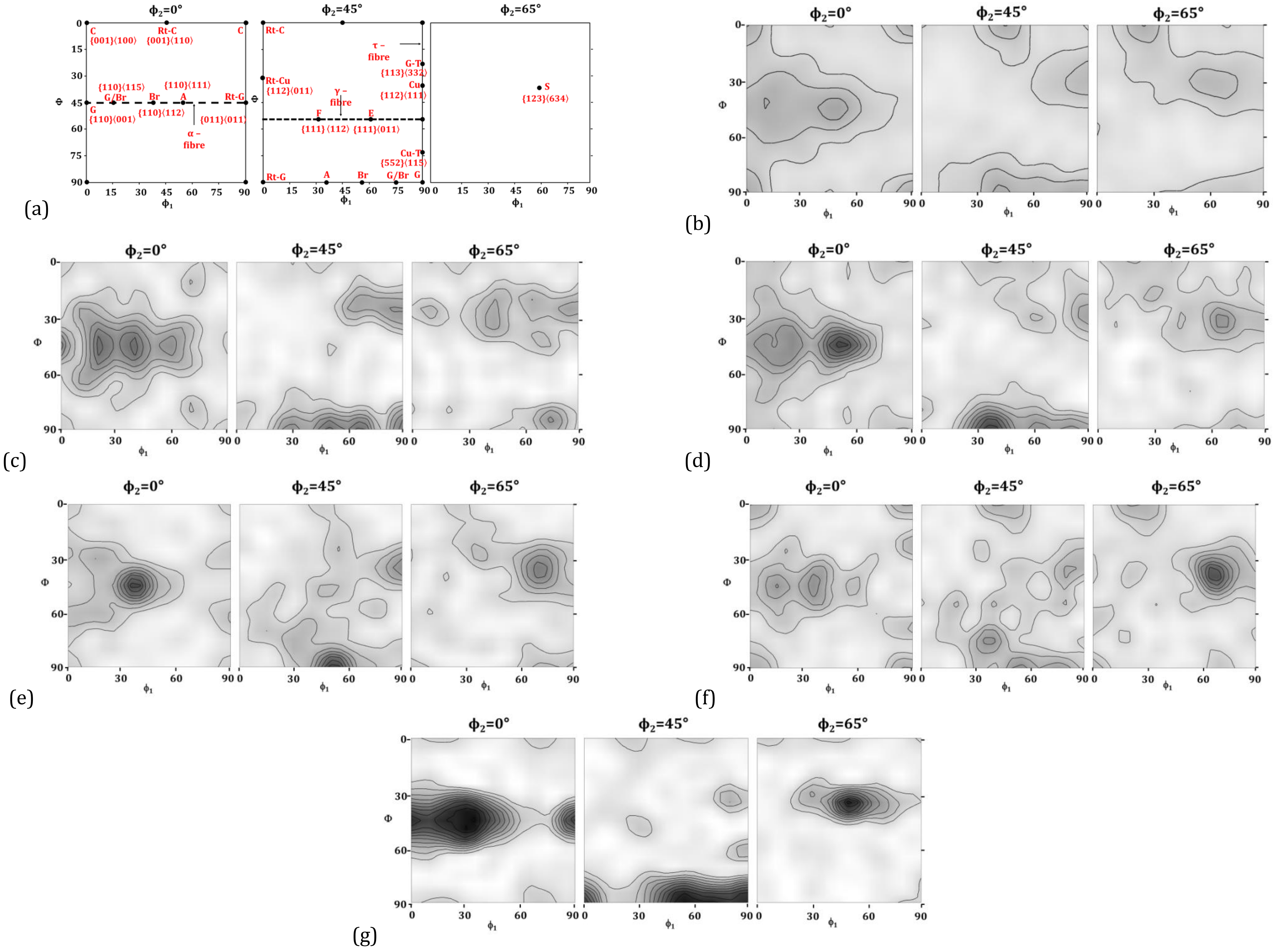

Figure 4.15: ϕ_2 = 0°, 45° and 65° ODF sections of γ showing (a) the ideal orientations and after (b) hot rolling, thickness reduction to (c) 5, (d) 10, (e) 15, (f) 20 and (g) 42%. Contour = 0.5×

The ideal ε-martensite orientations (in green) [182] are plotted in the ϕ_2 = 0° and 30° ODF sections (Fig. 4.16a) using the $[10\bar{1}0]_{\varepsilon}||$RD, $[0002]_{\varepsilon}||$ND convention on which particular γ orientations (in red) are superimposed. The ε-martensite orientations are formed from the γ orientations by phase transformation via the S-N orientation relationship upon plane strain compression/cold rolling.

Figs. 4.16b-4.16h shows the ε-martensite ϕ_2 = 0° and 30° ODF sections for the samples after hot rolling and thickness reduction to 66%. Due to the low volume fraction of ε-martensite in the sample after thickness reduction to 88% texture measurements were not taken.

As shown in Fig. 4.16b, the ε-martensite formed upon quenching after hot rolling shows weak intensity along the $\{hkil\}_{\varepsilon}$-fibre $\sim\{\bar{1}2\bar{1}5\}\langle 1\bar{2}13\rangle_{\varepsilon}$ (ϕ_1 = 90°, Φ = 24°, ϕ_2 = 0°) and $\sim\{01\bar{1}3\}\langle 0\bar{1}12\rangle_{\varepsilon}$ (ϕ_1 = 88°, Φ = 34°, ϕ_2 = 30°) orientations. After thickness reduction to 5 and 10% the formation of deformation-induced ε-martensite $\{hkil\}_{\varepsilon}$-fibre $\sim\{01\bar{1}3\}\langle 1\bar{2}13\rangle_{\varepsilon}$ (ϕ_1 = 72°, Φ = 34°, ϕ_2 = 30°) orientation takes place along with the formation of $\{11\bar{2}0\}\langle\bar{1}010\rangle_{\varepsilon}$ and $\{11\bar{2}0\}\langle 0001\rangle_{\varepsilon}$ orientations (Figs. 4.16c and 4.16d).

After 15 and 20% thickness reductions the deformation-induced ε-martensite $\{hkil\}_{\varepsilon}$-fibre comprise $\sim\{\bar{1}2\bar{1}5\}\langle 1\bar{2}13\rangle_{\varepsilon}$ (ϕ_1 = 90°, Φ = 32°, ϕ_2 = 0°) and $(01\bar{1}3)[0\bar{1}12]_{\varepsilon}$ (ϕ_1 = 90°, Φ = 34°, ϕ_2 = 30°) orientations, as shown in Figs. 4.16e and 4.16f. The $\{hkil\}_{\varepsilon}$-fibre orientations are deviated by ~30° along the RD after 20% thickness reduction.

After 42% thickness reduction the deformation-induced ε-martensite $\{hkil\}_{\varepsilon}$-fibre is deviated by ~25° towards the RD comprising $\sim\{\bar{1}2\bar{1}5\}\langle 1\bar{2}12\rangle_{\varepsilon}$ (ϕ_1 = 90°, Φ = 24°, ϕ_2 = 0°) and $\sim\{01\bar{1}4\}\langle 1\bar{3}23\rangle_{\varepsilon}$ (ϕ_1 = 72°, Φ = 23°, ϕ_2 = 30°) orientations (Fig. 4.16g). The presence of weak intensities around the deformation-induced ε-martensite $\{10\bar{1}0\}\langle 0001\rangle_{\varepsilon}$, $\{11\bar{2}0\}\langle 0001\rangle_{\varepsilon}$ and $\{\bar{1}2\bar{1}3\}\langle 10\bar{1}0\rangle_{\varepsilon}$ (ϕ_1 = 0°, Φ = 45°, ϕ_2 = 0°) orientations was also observed after 42% thickness reduction.

After thickness reduction to 66%, the $\{hkil\}_{\varepsilon}$-fibre [182] is observed to deviate by ~18° towards the RD. The strong intensities around the deformation-induced ε-martensite $\{0001\}\langle 1\bar{2}11\rangle_{\varepsilon}$ (ϕ_1 = 84°, Φ = 16°, ϕ_2 = 0°) and $\{0001\}\langle 0\bar{1}11\rangle_{\varepsilon}$ (ϕ_1 = 76°, Φ = 18°, ϕ_2 = 30°) orientations are seen in the sample after thickness reduction to 66% (Fig. 4.16h). The ε-martensite micro-texture of an Fe-17Mn-3Al-2Si-1Ni-0.06C steel cold-rolled to 66% thickness reduction showed $\sim\{011\bar{7}\}\langle 3\bar{6}21\rangle_{\varepsilon}$ and $\sim\{0001\}\langle\bar{2}\bar{2}31\rangle_{\varepsilon}$ orientations [7]. The decrease in deviation of the basal poles towards RD with increasing thickness reduction can be ascribed due to the deformation accommodation in ε-martensite. Similar results was presented during the compression of hcp ε-iron [117].

The formation of $\{hkil\}_{\varepsilon}$-fibre $\{\bar{1}2\bar{1}5\}\langle 1\bar{2}12\rangle_{\varepsilon}$ (ϕ_1 = 90°, Φ = 24°, ϕ_2 = 0°), $\sim\{01\bar{1}3\}\langle 0\bar{1}12\rangle_{\varepsilon}$ and $\sim\{01\bar{1}4\}\langle 1\bar{3}23\rangle_{\varepsilon}$ orientations takes from the $(213)[0\bar{2}1]_{\gamma}$ (ϕ_1 = 32°, Φ = 37°, ϕ_2 = 65°), G_{γ} and $(011)[3\bar{1}1]_{\gamma}$ orientations, respectively. The formation of $\{11\bar{2}0\}\langle\bar{1}010\rangle_{\varepsilon}$, $\{11\bar{2}0\}\langle 0001\rangle_{\varepsilon}$,

$\{10\bar{1}0\}\langle 0001\rangle_\varepsilon$ and $\{\bar{1}2\bar{1}3\}\langle 10\bar{1}0\rangle_\varepsilon$ orientations can be ascribed to the Br_γ, A_γ, Cu_γ and $\sim\mathrm{S}_\gamma$ orientations, correspondingly. The above ε-martensite orientations are formed from the γ orientations upon phase transformation via the S-N orientation relationship (Fig. 4.16a).

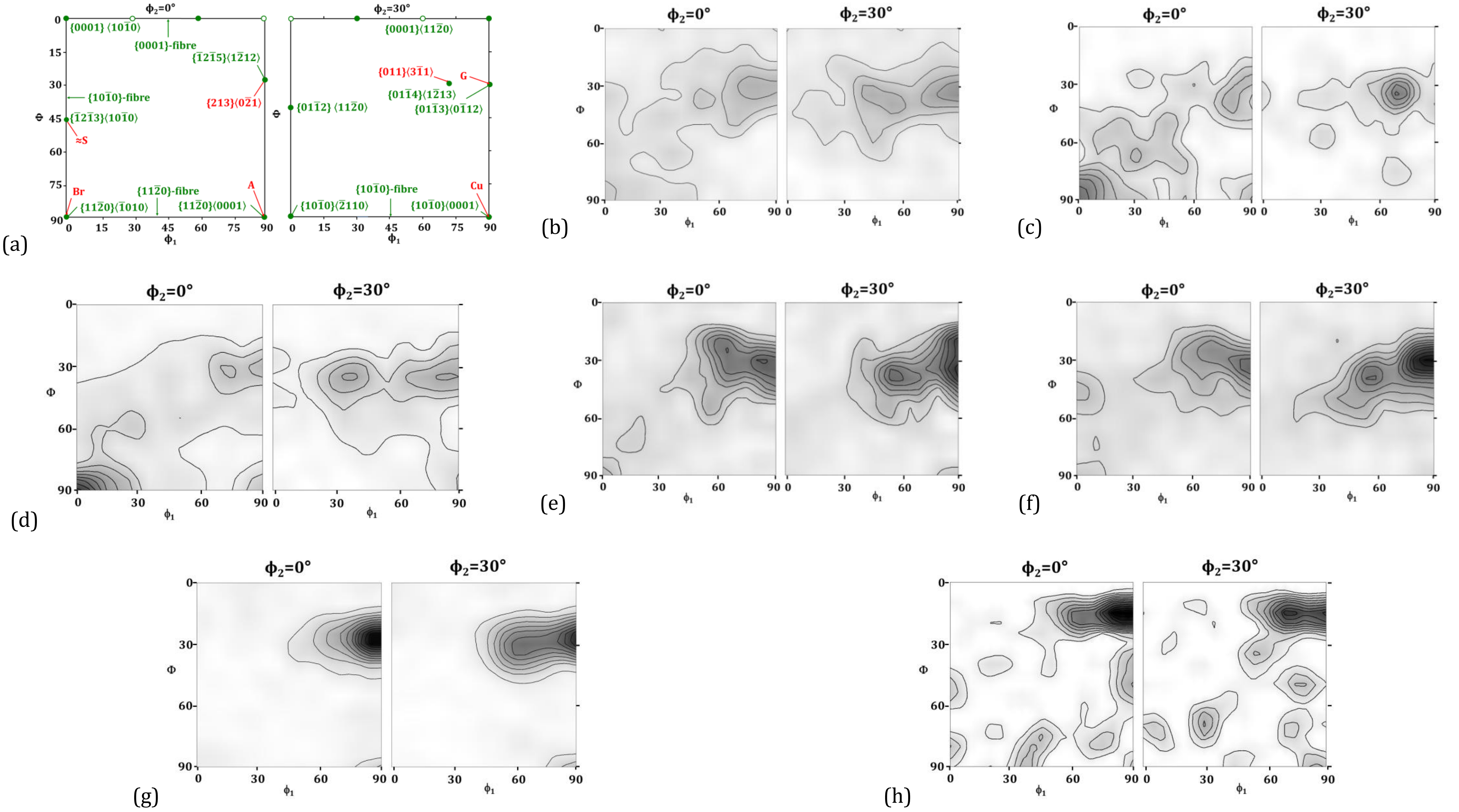

(a) (b) (c)

(d) (e) (f)

(g) (h)

Figure 4.16: ϕ_2 = 0° and 30° ε-martensite ODF sections showing (a) ideal ε-martensite orientations, after (b) hot rolling and thickness reduction to (c) 5, (d) 10, (e) 15, (f) 20, (g) 42, (h) 66%. In Fig. 4.16a, some γ orientation are provided for the S-N orientation relationship. Contour = 0.5×

The ideal α'-martensite orientations (in blue) are presented in the $\phi_2 = 0°$ and 45° ODF sections in Fig. 4.17a on which the γ (in red) and ε-martensite (in green) orientations are superimposed. The deformation-induced α'-martensite orientations are formed from the γ and ε-martensite by phase transformation via the K-S and Burgers orientation relationships, respectively.

The α'-martensite formed upon quenching after hot rolling returns $\alpha_{\alpha'}$-fibre ($\langle 110\rangle_{\alpha'}$||RD) $(001)[1\bar{1}0]_{\alpha'}$ orientation and weak intensities around the $\gamma_{\alpha'}$-fibre ($\langle 111\rangle_{\alpha'}$||ND) $(111)[\bar{1}\bar{1}2]_{\alpha'}$ orientation (Fig. 4.17b). After thickness reduction to 5 and 10%, the retention of $\alpha_{\alpha'}$ and $\gamma_{\alpha'}$-fibre $(001)[1\bar{1}0]_{\alpha'}$ and $(111)[\bar{1}\bar{1}2]_{\alpha'}$orientations, respectively, (Figs. 4.17c and 4.17d) with the formation of $(112)[1\bar{1}0]_{\alpha'}$ orientation. After thickness reduction to 15 and 20% the strengthening of intensities around the $(001)[1\bar{1}0]_{\alpha'}$ and $(111)[\bar{1}\bar{1}2]_{\alpha'}$ orientations are witnessed (Figs. 4.17e and 4.17f). Similar orientations were obtained during the formation and the subsequent deformation of α'-martensite in high Mn steels [49].

After cold rolling to 42% thickness reduction the formation of relatively strong intensities around the orientations along the $\alpha_{\alpha'}$-fibre $(001)[1\bar{1}0]_{\alpha'}$ and relatively weak intensities around the orientations along the $\gamma_{\alpha'}$-fibre ($\langle 111\rangle_{\alpha'}$||ND), $(111)[\bar{1}\bar{1}2]_{\alpha'}$, and $(554)[\bar{2}\bar{2}5]_{\alpha'}$ takes place (Fig. 4.17g). Strengthening of the $\alpha_{\alpha'}$-fibre $(001)[1\bar{1}0]_{\alpha'}$ orientation was also observed for the samples after 42, 66 and 88% thickness reductions (Figs. 4.17g-4.17i).

After cold rolling to 66 and 88% thickness reductions, the orientations $(001)[1\bar{1}0]_{\alpha'}$ and $(112)[1\bar{1}0]_{\alpha'}$ along the $\alpha_{\alpha'}$-fibre is observed (Figs. 4.17h and 4.17i). For the samples after 66 and 88% thickness reductions the α'-martensite orientations are retained from the sample after 42% thickness reduction. α'-martensite micro-texture measurements of an Fe-17Mn-3Al-2Si-1Ni-0.06C steel cold-rolled to 66% thickness reduction have shown the formation of $(001)[1\bar{1}0]_{\alpha'}$ and $(111)[\bar{1}\bar{1}2]_{\alpha'}$ orientations [7] which are similar to the observed α'-martensite orientations after 66% thickness reduction.

The formation of the (i) $(001)[1\bar{1}0]_{\alpha'}$, (ii) $(114)[1\bar{1}0]_{\alpha'}$, (iii) $(112)[1\bar{1}0]_{\alpha'}$, (iv) $(223)[1\bar{1}0]_{\alpha'}$, (v) $(111)[\bar{1}\bar{1}2]_{\alpha'}$ and (vi) $(554)[\bar{2}\bar{2}5]_{\alpha'}$ orientations can be attributed the (i) C_γ, Br_γ, (ii) Cu_γ, (iii, iv) Cu_γ, G_γ, (v) Br_γ and (vi) Br_γ orientations upon phase transformation via the K-S orientation relationship. Alternatively, these γ orientations can be ascribed to the (i) $\{11\bar{2}0\}\langle 0001\rangle_\varepsilon$, (ii), $\{10\bar{1}0\}\langle 0001\rangle_\varepsilon$ (iii, iv) $\{10\bar{1}0\}\langle 0001\rangle_\varepsilon$, $\{01\bar{1}4\}\langle 1\bar{3}23\rangle_\varepsilon$ ($\phi_1 = 72°$, $\Phi = 26°$, $\phi_2 = 30°$) and (v) $\{11\bar{2}0\}\langle\bar{1}010\rangle_\varepsilon$ orientations upon phase transformation via the Burgers orientation relationship (Fig. 4.17a).

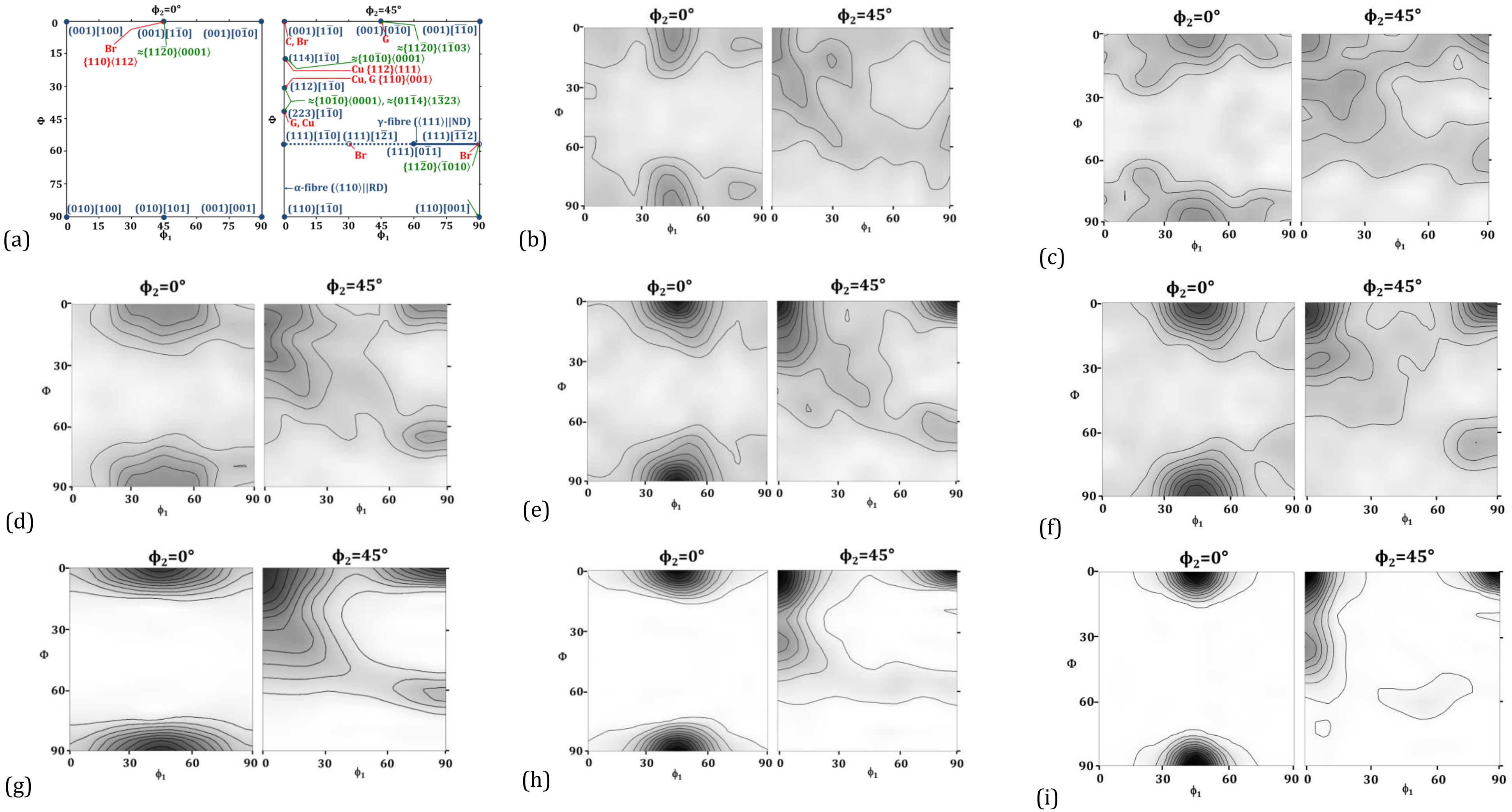

Figure 4.17: α′-martensite ϕ_2 = 0° and 45° ODF sections showing (a) ideal orientations, after (b) hot rolling, cold deformation to (c) 5, (d) 10, (e) 15, (f) 20, (g) 42, (h) 66 and (i) 88% thickness reduction. In Fig. 4.17a, some γ and ε-martensite orientations are provided for the K-S and Burgers orientation relationships. Contour = 0.5×

4.7 Conclusions

Characterisation via electron back-scattering diffraction and high-resolution transmission electron microscopy of the hot-rolled and plane strain compressed/cold-rolled samples led to the following conclusions:

(1) During plane strain compression/cold rolling, deformation-induced α′-martensite forms via two processes: (i) directly from γ and (ii) from γ via ε-martensite. The latter process was observed to be dominant during plane strain compression/cold rolling in the present study. Both the deformation-induced ε and α′-martensite were observed to nucleate with Shoji-Nishiyama and Kurdjumov-Sachs orientation relationships, respectively.

(2) During the plane strain compression and cold rolling of an Fe-17Mn-3Al-2Si-1Ni-0.06C steel, the γ deforms by partial slip, resulting in the formation of intrinsic stacking faults. Upon further plane strain compression/cold rolling, the nucleation of deformation-induced ε-martensite takes place at γ intrinsic stacking faults and pre-existing annealing γ twin boundaries. The growth of the deformation-induced ε-martensite takes place via lateral coarsening and coalescence with thick ε-martensite plates upon subsequent plane strain compression.

(3) ε-martensite accommodates deformation via perfect and partial basal slip, pyramidal slip and $\{10\bar{1}2\}\langle\bar{1}011\rangle_{\varepsilon}$ extension twinning. Upon deformation, the formation of ε-martensite stacking faults in the basal plane by the activation of partial basal slip is noted. A mechanism for ε-martensite deformation accommodation via a change in stacking fault character from I_2 to I_1 -type intrinsic stacking faults with increasing thickness reduction was proposed.

(4) The α′-martensite accommodates deformation with increasing thickness reduction via slip as evidenced by the increase in low angle grain boundary fractions and the formation of local macroscopic shear bands.

(5) After deformation, the γ shows the formation of Br_{γ}, S_{γ} and Cu_{γ} orientations. The analysis of texture development showed that the (i) $(001)[1\bar{1}0]_{\alpha'}$, (ii) $(112)[1\bar{1}0]_{\alpha'}$ and (iii) $(111)[\bar{1}\bar{1}2]_{\alpha'}$ orientations arise from the (i) C_{γ}, Br_{γ}, (ii) Cu_{γ}, G_{γ} and (iii) Br_{γ} orientations, respectively and alternatively from the (i) $\{11\bar{2}0\}\langle0001\rangle_{\varepsilon}$, (ii) $\{10\bar{1}0\}\langle0001\rangle_{\varepsilon}$, $\{01\bar{1}4\}\langle1\bar{3}23\rangle_{\varepsilon}$ and (iii) $\{11\bar{2}0\}\langle\bar{1}010\rangle_{\varepsilon}$ orientations upon phase transformation via the Kurdjumov-Sachs and Burgers orientation relationships, respectively.

(6) The analysis of texture components showed that the deformation-induced ε-martensite $\{hkil\}_{\varepsilon}$-fibre $\{\bar{1}2\bar{1}5\}\langle1\bar{2}12\rangle_{\varepsilon}$, $\{01\bar{1}3\}\langle0\bar{1}12\rangle_{\varepsilon}$ and $\{01\bar{1}4\}\langle1\bar{3}23\rangle_{\varepsilon}$ orientations form from the $(213)[0\bar{2}1]_{\gamma}$, G_{γ} and $(011)[3\bar{1}1]_{\gamma}$ orientations, respectively. The formation of $\{11\bar{2}0\}\langle\bar{1}010\rangle_{\varepsilon}$, $\{11\bar{2}0\}\langle0001\rangle_{\varepsilon}$,

$\{10\bar{1}0\}\langle 0001\rangle_\varepsilon$ and $\{\bar{1}2\bar{1}3\}\langle 10\bar{1}0\rangle_\varepsilon$ orientations can be ascribed to the Br_γ, A_γ, Cu_γ and $\sim\mathrm{S}_\gamma$ orientations, respectively, upon phase transformation via the Shoji-Nishiyama orientation relationship.

CHAPTER 5 EVOLUTION OF MICROSTRUCTURE DURING IN-SITU HEATING OF 42% COLD-ROLLED HIGH MANGANESE STEEL

This chapter studies the evolution of microstructure during in-situ transmission electron microscopy heating up to 900 °C of the 42% cold-rolled high Mn steel. The displacive mechanism of ε and α′-martensite reversion were noted upon in-situ transmission electron microscopy annealing. The formation of recovery twins in reverted γ was detected, for which a suitable mechanism of their formation was proposed.

5.1 ε-martensite reversion upon in-situ annealing

Fig. 5.1 shows the evolution of ε-martensite (with a representative diffraction pattern shown as an inset in Fig. 5.1a) during the in-situ annealing in TEM. In the magnified view in Fig. 5.1b, ε-martensite in the cold-rolled condition shows the presence of stacking faults (marked by white arrows) formed to accommodate deformation after cold rolling to 42% thickness reduction. The increase in the stacking fault spacing with increasing annealing temperature up to 390 °C is detected in Fig. 5.1d. Tomota *et al.* [34] also reported a reduction in the density of stacking faults in ε-martensite prior to the reverse transformation during in-situ annealing of an Fe-24Mn-6Si shape memory alloy. The superimposition of the micrographs after heating to 390 °C and 410 °C showed no change in shape and size of the parent ε-martensite grain (at 390 °C, Fig. 5.1d) and daughter reverted γ grain (at 410 °C, Fig. 5.1e). Also a jump of the foil was detected during our experiment due to the phase transformation of ε-martensite. Minor changes to the spacing between the reflections due to ε-martensite reversion are detected in the inset diffraction pattern in Fig. 5.1e. The remnant faults are present in the reverted γ after annealing at 410 °C. These remnant faults present at 410 °C disappeared after heating to 650 °C (Fig. 5.1f). However, the remnant dislocations (highlighted by white arrows) are revealed in γ. This is due to the low γ-SFE of 14.5 mJ/m^2 [71], which in turn, leads to limited recovery.

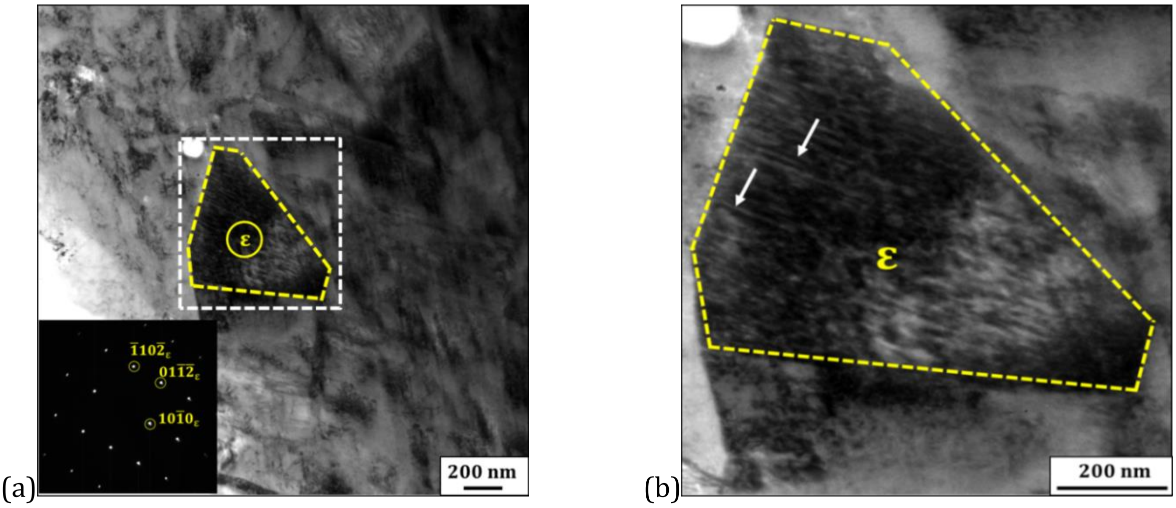

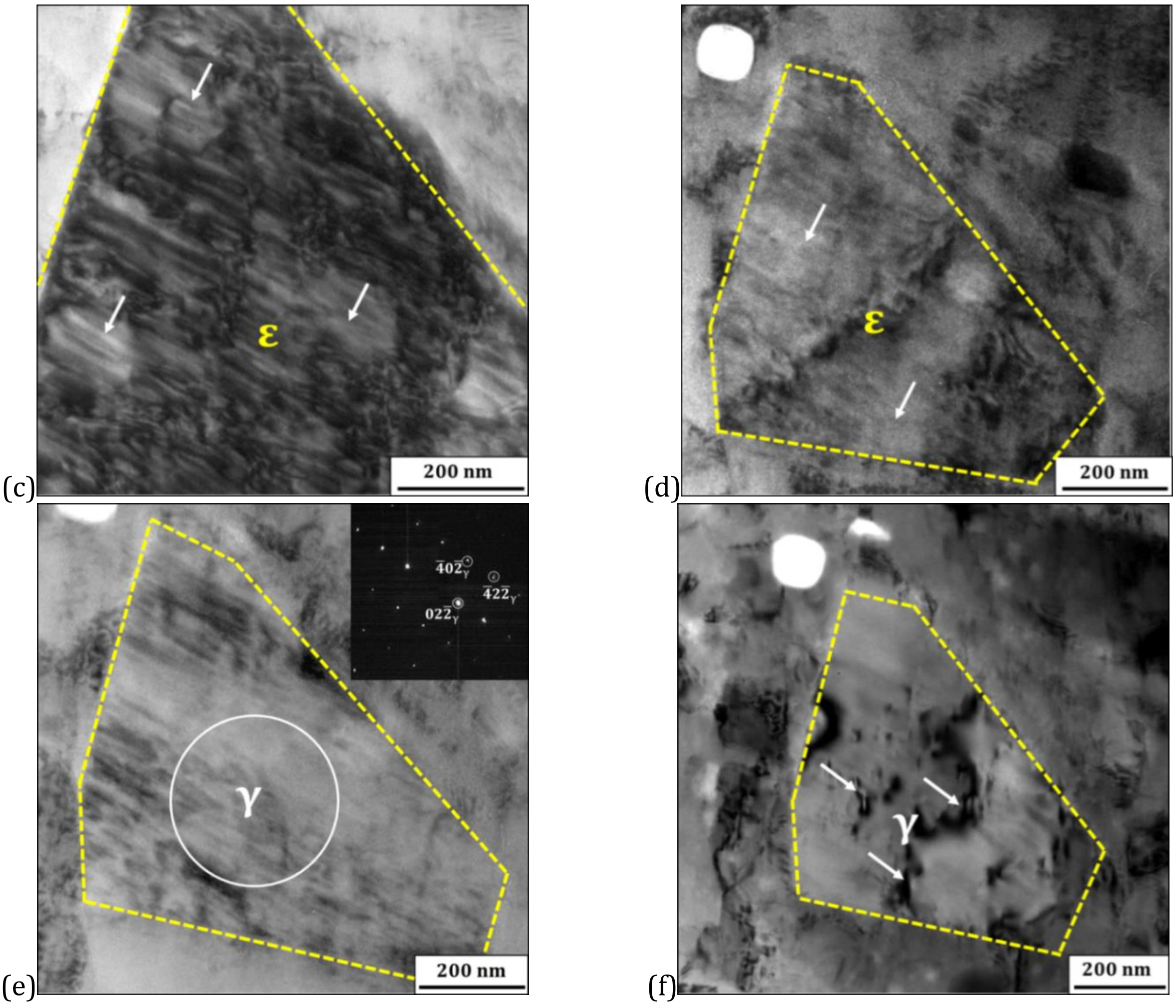

Figure 5.1: Bright-field transmission electron micrographs showing (a, b, c, d) ε-martensite and (e, f) γ at (a, b) 24 °C (room temperature) and after in-situ annealing to temperatures of (c) 240 °C, (d) 390 °C, (e) 410 °C and (f) 650 °C. Fig. 5.1b is the magnified view of the white dashed rectangle in Fig. 5.1a. The inset diffraction patterns were obtained from the solid circles in Figs. 5.1a and 5.1e for the zone axis $[\bar{2}4\bar{2}3]_\varepsilon$, $[\bar{1}22]_\gamma$, respectively. The white arrows in Figs. 5.1b-5.1d and Fig. 5.1f indicate ε-martensite stacking faults and remnant dislocations, respectively.

The γ diffraction pattern was simulated from the known $[\bar{2}4\bar{2}3]_\varepsilon$ ε-martensite zone axis using the S-N orientation relationship [105] which shows that the $(10\bar{1}0)_\varepsilon/(02\bar{2})_\gamma$, $(01\bar{1}\bar{2})_\varepsilon/(\bar{4}0\bar{2})_\gamma$ and $(11\bar{2}\bar{2})_\varepsilon/(\bar{4}2\bar{2})_\gamma$ spot pairs are very closely spaced (Fig. 5.2a). The spacing between the spots is measured with increasing annealing temperature which is shown in Fig. 5.2b. The decrease in the spot spacing of $(11\bar{2}\bar{2})_\varepsilon/(\bar{4}2\bar{2})_\gamma$ and $(01\bar{1}\bar{2})_\varepsilon/(\bar{4}0\bar{2})_\gamma$ at 410 °C indicates the reverse transformation of ε-martensite to γ.

During the ε-martensite to γ reversion, the $[1\bar{2}10]_\varepsilon$ zone axis was used to track the γ/ε-martensite interface as the interface is in the edge on condition. This is favourable for determining the exact position of the γ/ε-martensite interface [223]. The $[\bar{2}4\bar{2}3]_\varepsilon$ zone axis used here makes an angle of 24.7° with the $[1\bar{2}10]_\varepsilon$ zone axis. Although, the γ/ε-martensite interface is not in the edge on condition for the $[\bar{2}4\bar{2}3]_\varepsilon$ zone axis; the migration of the inclined γ/ε-martensite interface should be possible to detect.

However, this still was not observed in the present case. This indicates the displacive ε-martensite reversion.

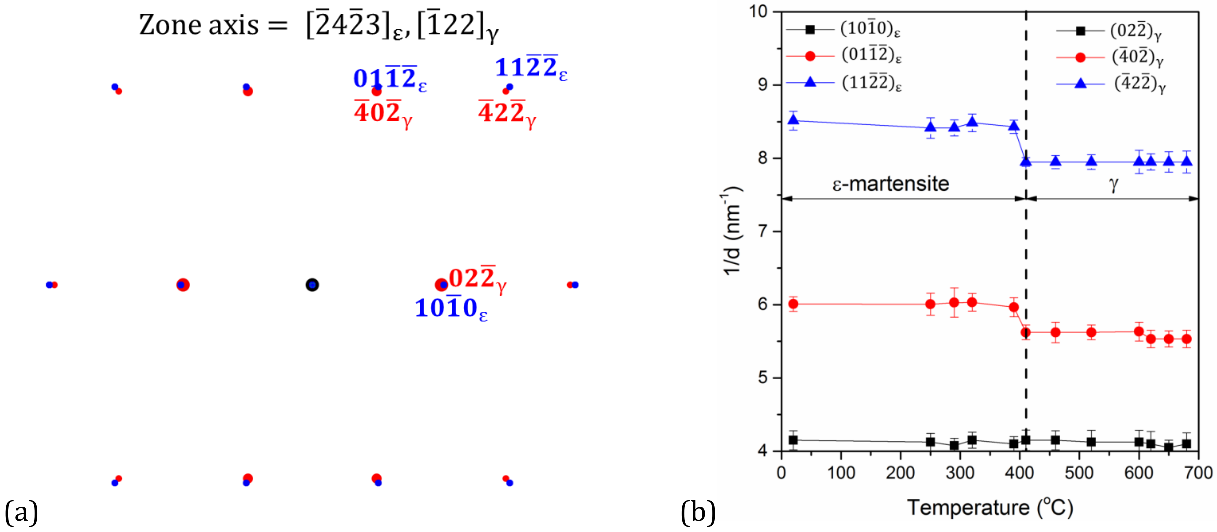

Figure 5.2: (a) Simulated diffraction pattern of γ/ε-martensite based on the S-N orientation relationship for the $[\bar{2}4\bar{2}3]_\varepsilon$ zone axis and (b) evolution of spot spacing of γ/ε-martensite reflections with temperature. The red and blue spots in Fig. 5.2a are for the γ and ε-martensite, respectively.

Another ε-martensite grain (Fig. 5.3) in another sample also shows the reduction in the density of stacking faults in the cold-rolled condition (Figs. 5.3a and 5.3b) upon heating to 400 °C (Fig. 5.3c). Further heating to 420 °C (Fig. 5.3d) does not show any change in the grain shape or the migration of the γ/ε-martensite interface. However, the recorded diffraction pattern in Fig. 5.3d, inset clearly indicates the reversion of ε-martensite to γ. The diffraction pattern of the reverted γ was simulated using the S-N orientation relationship (Fig. 5.3e) and the ε-martensite $[7\bar{2}\bar{5}3]_\varepsilon$ zone axis (inset Fig. 5.3a). The $[7\bar{2}\bar{5}3]_\varepsilon$ zone axis makes an angle of 19.8° with the $[1\bar{2}10]_\varepsilon$ zone axis. Similar to the previous case in Fig. 5.1 and despite the γ/ε-martensite interface not being in the edge on condition, the migration of the inclined γ/ε-martensite interface should be possible to detect, but still, it was not visible. The transformation occurred across the entire grain without any change in the grain shape and/or the motion of the γ/ε-martensite interface. Consequently, the above observations also indicate the operation of a displacive ε-martensite transformation in this grain.

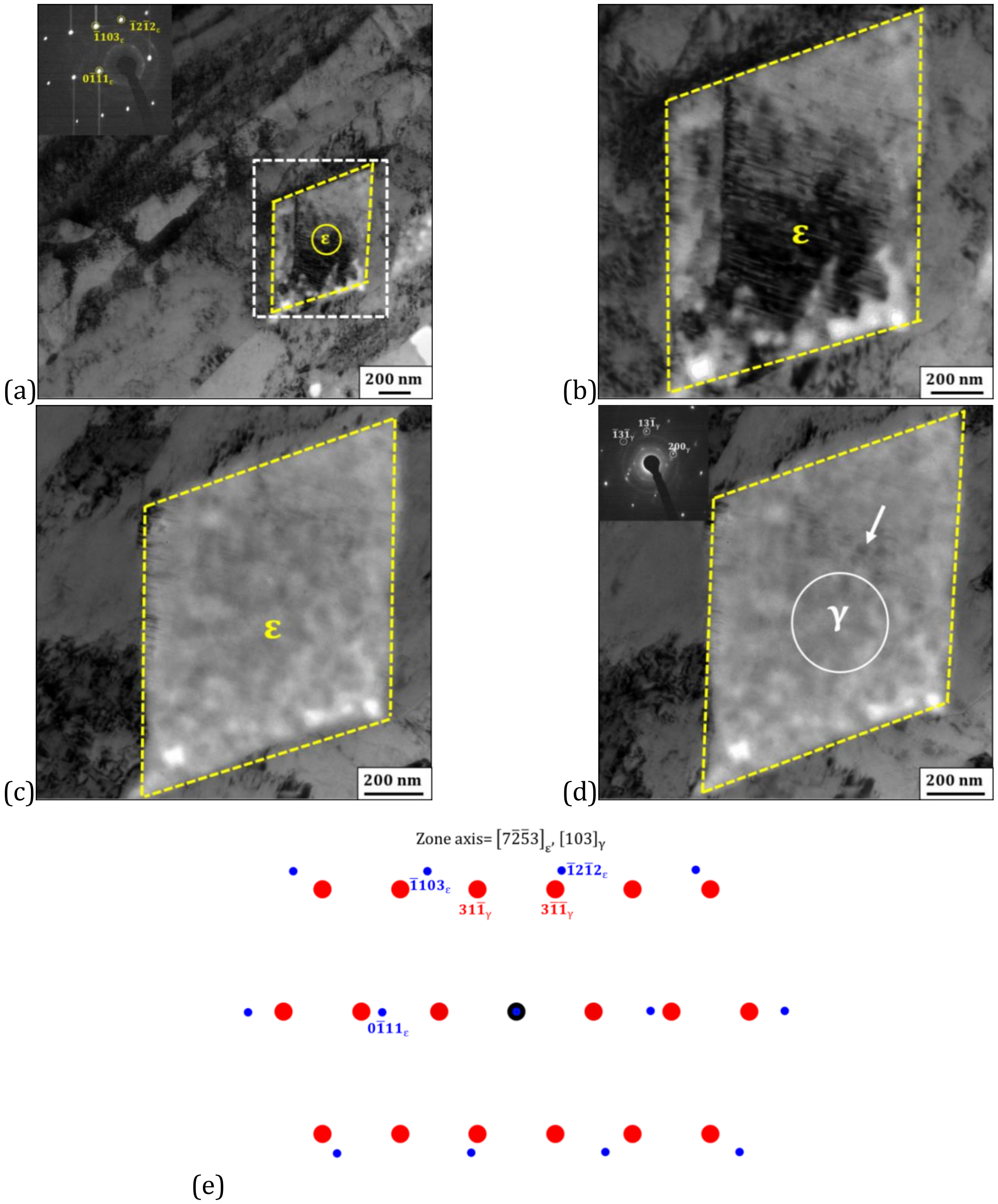

Figure 5.3: Bright-field transmission electron micrographs of (a, b, c) ε-martensite and (d) γ at (a, b) 24°C (room temperature) and after in-situ annealing to (c) 400 °C, (d) 420 °C and (e) simulated diffraction pattern of γ/ε-martensite by the Shoji-Nishiyama orientation relationship for the $[7\bar{2}\bar{5}3]_\varepsilon$ zone axis. The inset diffraction patterns were obtained from the circled regions in Figs. 5.3a and 5.3d for the zone axis $[7\bar{2}\bar{5}3]_\varepsilon$ and $[103]_\gamma$, respectively. In Fig. 5.3e, the red and blue spots are for γ and ε-martensite, respectively.

Tomota et al. [34] during the in-situ annealing of an Fe-24Mn shape memory alloy observed the displacive reversion of ε-martensite to γ. However, the formation of reverted γ reported by Tomota et al. [34] was different in comparison to the present investigation. Tomota et al. [34] observed the ε-martensite reverse transformation to start from inside and outside of the ε-martensite plates. This was due to the presence of γ and ε-martensite in the initial microstructure such that the pre-existing γ provides nucleation sites for reverted γ. The ε-martensite to γ reversion leads to the formation of a thin γ/ε-martensite lamellae [34]. In contrast, the present investigation does not show the formation of a thin γ/ε-martensite lamellae during ε-martensite reversion.

5.2 Twinning in reverted γ

After heating to 700 °C, the formation of twins (highlighted by white arrows in Fig. 5.4a) in the reverted γ grains is witnessed. The twin spacing (w) is calculated to be 7.6 ± 2.3 nm from the measured spacings (w_L) using the equation [205]:

$$w = \frac{2w_L}{\pi} \tag{5.1}$$

The diffraction pattern shows additional weak reflections/streaks in the inset diffraction pattern in Fig. 5.4a due to the oxidation of the foil at high temperature. The lower (bright) region of Fig. 5.4a depicts areas where the foil has oxidised whereas the other (darker) regions show mottled contrast which indicates that an oxide skin has formed on the surfaces of the foil.

The twin reflections are not clearly visible in the γ diffraction pattern (Fig. 5.4a, inset) due to the overlap between the twin and γ main spots. The simulated diffraction pattern in Fig. 5.4b returns the overlap between the $(1\bar{1}3)_\gamma$ twin and $(31\bar{1})_\gamma$ matrix spots.

Since the recrystallisation of γ was not detected after annealing at 700 °C (Fig. 5.4a), the twins are formed due to the recovery of γ. The formation of twins in reverted γ from α′-martensite was reported during the annealing of the 98% cold-rolled Fe-33.5Ni alloy initially containing γ and α′-martensite [35]. In that study, the fine twins were observed upon heating to 50 °C above the α′-martensite reversion temperature during the early stages of γ recovery. The similar formation of twins in reverted γ was reported during the in-situ TEM annealing of an Fe-5Mn-0.2C steel at 650 °C [33]. In that study, the reversion of γ from α′-martensite occurred via the nucleation and growth process at α′-martensite lath boundaries. The formation of fine twins during recovery was also reported during the annealing of other cold-rolled low SFE fcc materials such as brass [131, 132] and Co-Cr-Mo alloy [133].

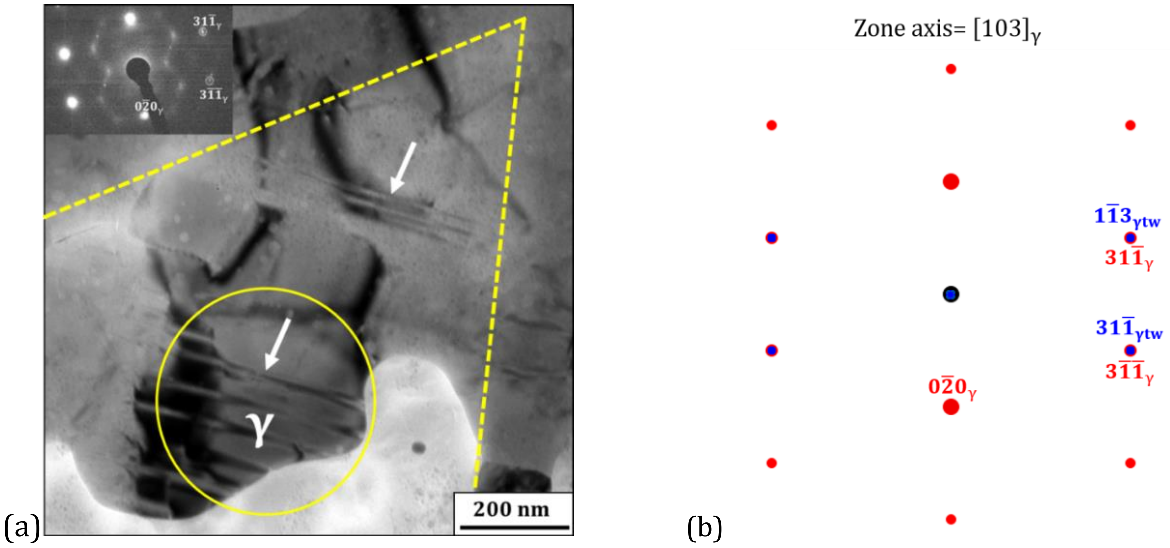

Figure 5.4: Bright-field transmission electron micrograph of (a) γ after in-situ annealing to 700 °C and (b) simulated diffraction pattern of γ/γ twin (γ_{tw}) for the $[103]_\gamma$ zone axis. The inset diffraction pattern was obtained from the circular region in Fig. 5.4a for the zone axis $[103]_\gamma$. In Fig. 5.4b, the red and blue spots are for γ and γ_{tw}, respectively.

The mechanism of ε-martensite reversion and the subsequent γ twin formation is shown in schematic Fig. 5.5. Earlier studies on the same steel by Saleh et al. [24] and Gazder et al. [7, 224] showed that ε-martensite can accommodate deformation via basal slip and the formation of stacking faults. In the follow-up study on the same investigated steel, the presence of ISFs of type I_1 in ε-martensite was noted after cold rolling to 42% thickness reduction (Section 4.5, Chapter 4). The reversion of the faulted ε-martensite upon annealing at 420 °C occurs by the motion of Shockley partial dislocations with Burgers vector $\frac{a}{3}[10\bar{1}0]_\varepsilon$ (where a is the lattice parameter of ε-martensite) on alternate planes. The net shear due to the propagation of the two Shockley partial dislocations below the plane of the ε-martensite ISF (I_1) is $\frac{2a}{3}[10\bar{1}0]_\varepsilon$. In addition, Shockley partial dislocations do not pass on the alternate planes of ε-martensite due to the presence of I_1-type ε-ISFs. The passing of $\frac{a}{3}[10\bar{1}0]_\varepsilon$ Shockley partial dislocations through I_1-type ε-ISFs leads to the transformation of I_1-type ε-martensite ISFs into a γ-ISF in the reverted γ lattice. In this regard, the white arrows in Fig. 5.3d indicates the presence of faint contrast due to faults in reverted γ. After annealing to 700 °C, the growth of these γ-ISFs occurs by the migration of Shockley partial dislocations $\frac{a}{6}[11\bar{2}]_\gamma$ (where a is the lattice parameter of γ) on the adjacent to the γ-ISF $(111)_\gamma$ planes. This leads to the change in the local stacking sequence to that of γ twins. A macroscopic twin then forms as more and more Shockley partial dislocations glide along with each other.

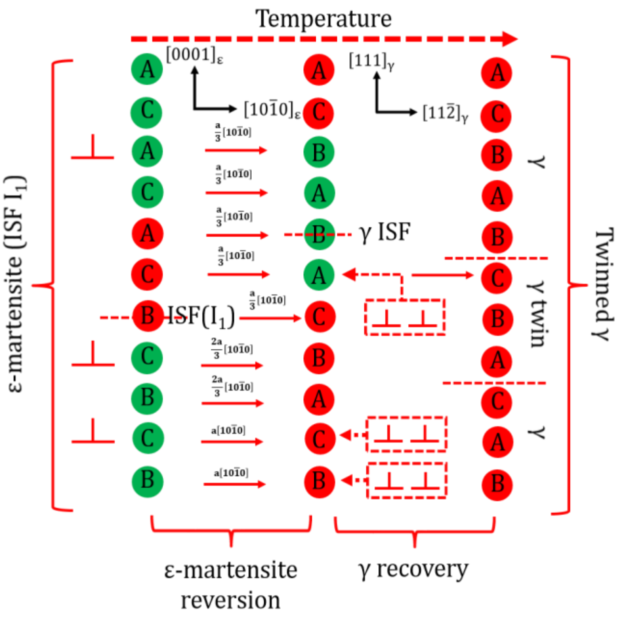

Figure 5.5: Schematic showing the reversion of faulted ε-martensite and twinning due to γ recovery with the red and green circles representing fcc and hcp stacking sequences, respectively, along with the Shockley partial dislocations which are shown by the symbol “⊥”.

5.3 α′-martensite reversion upon in-situ annealing

Fig. 5.6 presents the microstructural evolution during subsequent annealing up to 900 °C. The bright-field TEM micrograph at 800 °C shows elongated α′-martensite grains carried over from prior cold rolling. After holding at 800 °C for 10 min (Fig. 5.6b), no change in the grain shape or the migration of the γ/α′-martensite interface was noted. However, the recorded diffraction pattern (Fig. 5.6b, inset) clearly indicates the reversion of α′-martensite to γ. Upon holding for 20 min at 800 °C, (Fig. 5.6c), further heating to 850 °C (Fig. 5.6d) and 900 °C (Fig. 5.6e) the escape of dislocations from the foil surface is visible.

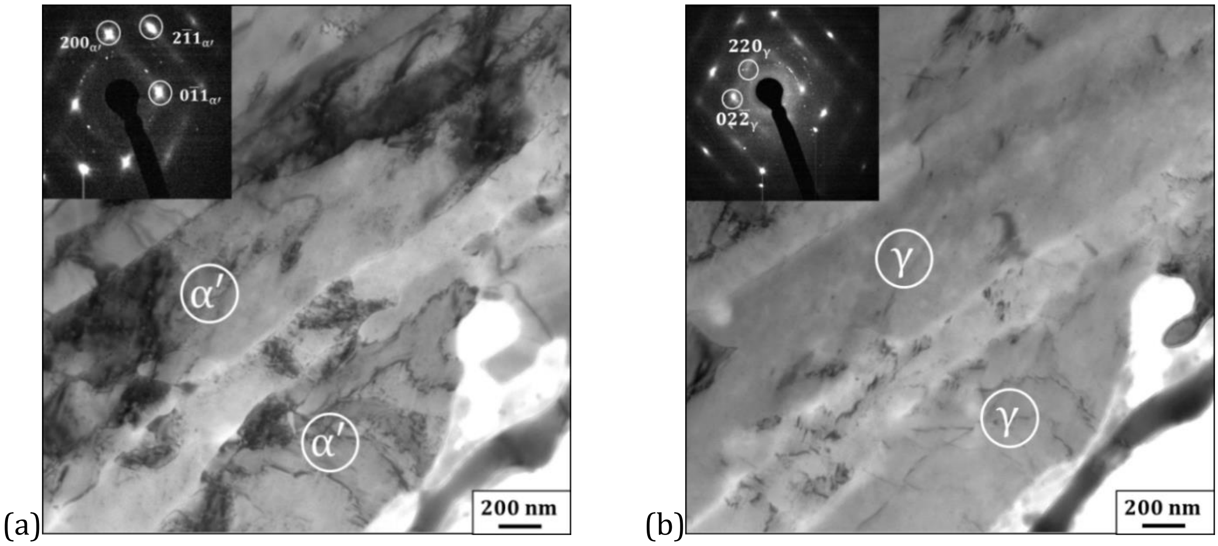

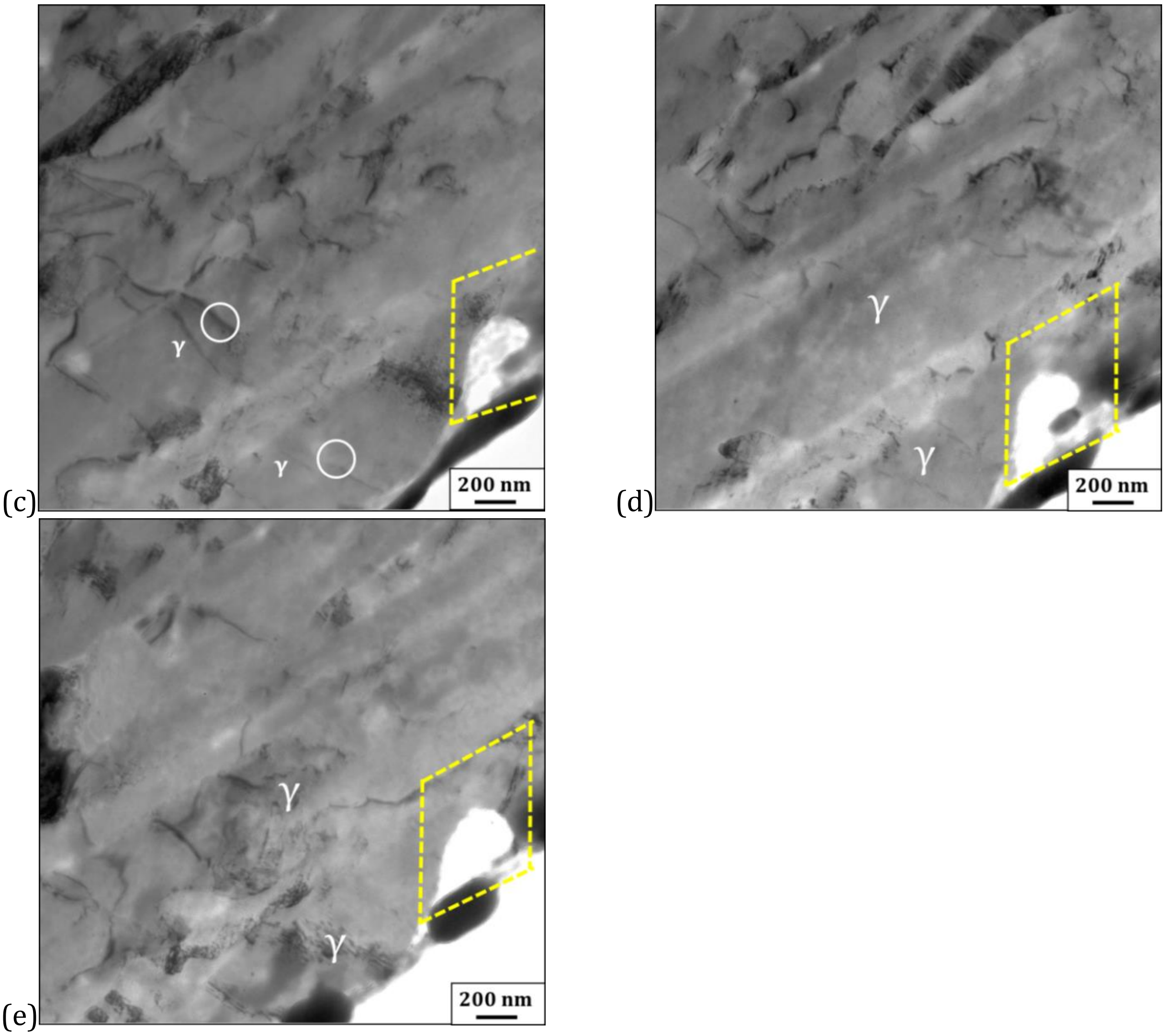

Figure 5.6: Bright-field transmission electron micrographs of (a) α'-martensite and (b) γ after (a) in-situ annealing to 800 °C, (b) holding at 800 °C for 10 min, and (c) simulated diffraction pattern of γ/α'-martensite by Kurdjumov-Sachs orientation relationship for $[011]_{\alpha'}$ zone axis. The inset diffraction patterns were obtained from the white circular regions in Figs. 5.6a and 5.6b for the zone axes $[011]_{\alpha'}$ and $[111]_{\gamma}$, respectively. In Fig. 5.6c, the red and blue spots are for γ and α'-martensite, respectively.

The γ diffraction pattern was simulated from the $[011]_{\alpha'}$ zone axis pattern (Fig. 5.6a, inset) using the K-S orientation relationship [53] and is shown in Fig. 5.7a. By comparing the experimental and simulated diffraction patterns the operation of K-S orientation relationship is confirmed.

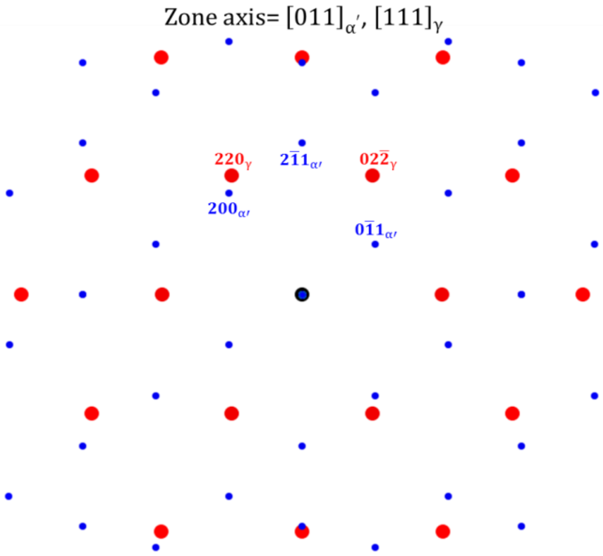

Figure 5.7: The simulated diffraction pattern of γ/α'-martensite by the K-S orientation relationship for $[011]_{\alpha'}$ zone axis. The red and blue spots are for γ and α'- martensite, respectively.

For the observation of the migrating γ/α'-martensite interface during the displacive transformation, as per the K-S OR the $[111]_{\alpha'}||\ [011]_{\gamma}$ zone axes were used as the $\{111\}_{\gamma}$ plane is on the edge during the in-situ annealing of an Fe-20.2Ni-5.5Mn steel [31]. The $[011]_{\alpha'}$ zone axis makes an angle of 35.3° with the $[111]_{\alpha'}$ zone axis. Although, the γ/α'-martensite interface is not in the edge on condition for the $[011]_{\alpha'}||\ [111]_{\gamma}$ zone axes; the migration of the inclined γ/α'-martensite interface should be possible to detect. However, this still was not observed in the present case. Thus, the reverse transformation occurred across the entire grain without any change in the grain shape or the motion of the γ/α'-martensite interface which shows displacive α'-martensite reversion mechanism.

In an Fe-9.6Ni-7Mn steel (subjected to solution treatment at 950 °C for 3600 s followed by quenching to 28 °C), the formation of reverted γ from α'-martensite was reported to occur by the diffusional and displacive transformations at relatively lower (540-585 °C) and higher annealing temperatures (585-640 °C), respectively [136]. During the annealing of an 92.5% cold-rolled Fe-12Cr-8.9Ni-4Mo-1.9Cu-1.4Ti steel to 750 °C with a heating rate of 10 $°Cs^{-1}$ the initial α'-martensite with lath morphology without a dislocation cell arrangement transformed by a displacive mechanism [125]. Thus, in the present investigation the relatively high annealing temperature (800 °C) and the presence of α'-martensite with lath morphology favours the displacive α'-martensite reversion.

However, due to the high annealing temperature of 800 °C along with the holding time of 600 s, it can be speculated that the diffusion of C may be involved during α'-martensite reversion. The C diffusion during the reversion of α'-martensite to γ by displacive transformation was also suggested in an Fe-5Mn-0.15C steel which was solution treated at 1000 °C for 1800 s followed by water quenching [225].

5.4 Feasibility of α'-martensite reversion via a displacive or diffusional mechanism

The probability of occurrence of displacive/diffusional α'-martensite reversion mechanisms was also evaluated by calculating the time required for the migration of Fe atoms in α'-martensite by diffusion. The atomic jump frequency during annealing at 800 °C, which is inversely proportional to the time required for the diffusional transformation, was calculated using the following equations [226]:

$$\mathrm{D} = \mathrm{D_o}\exp\left(\frac{-\mathrm{Q}}{\mathrm{RT}}\right) \tag{5.2}$$

$$1/\Gamma = \alpha^2/8\mathrm{D} \tag{5.3}$$

where D is the diffusion coefficient in paramagnetic α'-martensite at 800 °C, $\mathrm{D_o}$ is the frequency factor (= 1.92 $\mathrm{cm^2s^{-1}}$), Q is the activation energy, R is the universal gas constant (= 8.314 $\mathrm{Jmol^{-1}K^{-1}}$), T is the temperature (K), Γ is the jump frequency of an atom and α is the interatomic distance (= 2.48×10^{-8} cm) [226]. Using the activation energy of self-diffusion for bcc Fe (≈239 $\mathrm{kJmol^{-1}K^{-1}}$) [227], the mean time of stay ($\frac{1}{\Gamma}$) for Fe atoms at 800 °C (i.e., the time required for diffusional transformation) is calculated to be $\approx1.8\times10^{-5}$ s. The time required for the displacive transformation of γ to α'-martensite with lath morphology was reported to be $\approx10^{-5}$ s [228]. Assuming the reversion time of α'-martensite to γ to be the same ($\approx10^{-5}$ s), the required times for diffusional and displacive α'-martensite reversion during annealing at 800 °C are very similar. Consequently, either of the diffusional/displacive α'-martensite reversion mechanism could be operational.

5.5 Effect of thin foil surface on α'-martensite reversion mechanism

In addition to the factors listed in Section 2.10.1, Chapter 2, the occurrence of the displacive/diffusional α'-martensite reversion also depends on the availability of a constraint free sample surface present on a thin foil. Previous investigations [229-233] suggested a strong correlation between the presence of a sample surface and displacive α'-martensite transformation. In-situ observations using a laser scanning confocal microscope on an Fe-7.1Ni-2Mn-0.03C steel showed displacive α'-martensite formation mechanism on the sample surface at 452 °C, compared to 338 °C within the bulk [230]. This indicates a lower driving force is required on the sample surface. Here, the formation of α'-martensite on the sample surface reduces the stain energy (due to the shape change associated with the formation of α'-martensite) which in turn favours displacive transformation. Similarly, during the formation of α'-martensite in an single crystal of Fe-30Ni-0.04C alloy, the α'-martensite start temperature at the sample surface was found to be higher than in the bulk by 5-30 °C which indicates that a lower undercooling is required at the sample surface [229]. This was due to the availability of a free surface which assisted in the relief of shear strain caused by displacive α'-martensite transformation. For an Fe-6Mn-16Cr-3Ni-0.03C duplex stainless steel, the formation of a trench of width and depth of 1 μm was undertaken by focussed ion beam milling to create a free surface. In that study, the formation of a free surface, results in the transformation of neighboring retained γ grain to α'-martensite [231]. This was due to the lowering of the α'-martensite nucleation barrier as the strain energy is reduced which consequently favours displacive transformation. In this regard, the recovery of the α'-martensite surface relief (i.e., negative shape strain) was observed during reversion of α′-martensite to γ in an Fe-31Ni-0.4C alloy [234]. Thus the negative shape strain due to displacive α′-martensite reversion is also expected to be accommodated easily on the sample surface of thin foils compared to the bulk. Thus, it could be assumed that the availability of free surface due to thin foils, favours displacive α′-martensite reversion in the present investigation.

The α′-martensite reversion mechanism can differ when in-situ heating experiments are done on thin foils in comparison to postmortem observations on bulk samples. Thus, it has to be stated that more experimental work is required to draw a definite conclusion and to support the proposition of displacive α′-martensite reversion in this steel.

5.6 ε and α′-martensite reversion temperature of thin foils compared to bulk samples

The ε and α′-martensite reversion temperatures is higher during annealing of thin foils compared to the bulk samples. During the in-situ heating of thin foils the ε-martensite reversion was not observed on heating to 400 °C. However, during the heating of bulk samples by dilatometer, ε-martensite reversion was obtained between 100-250 °C.

During the heating of an Fe-24Mn-6Si alloy containing an initial microstructure of γ (70%) and ε-martensite (30%), the ε-martensite transformation in thin foils was observed at 227 °C which was higher in comparison to the bulk samples (183 °C) [34]. The differences in the composition and initial microstructures of the studied steel and the alloy in Ref. [34] are most likely responsible for the observed variation in the ε-martensite transformation temperatures.

The α′-martensite reversion was not observed on heating of thin foils between 600-800 °C whereas, during the heating of bulk samples by dilatometry it was noted between 500-700 °C [40]. For an Fe-20Ni-5Mn alloy the α′-martensite reversion was observed at 400 °C in bulk samples, however during the in-situ heating of thin foils reversion was noted at 550 °C [31].

The theoretical α′-martensite transformation temperature (T_o) at which the free energy of γ and α′-martensite is equal ($G^{\alpha} = G^{\gamma}$) was estimated by observing the change in the free energy for α′-martensite reversion ($\Delta G^{\alpha-\gamma}$, J/mol) for the Fe-17Mn-3Al-2Si-1Ni-0.06C steel using the following equations [27, 191, 235]:

$$\begin{aligned}\Delta G^{\alpha-\gamma} &= 10^{-2}\left(\Delta G_{\mathrm{Fe}}^{\alpha-\gamma}\right)\left(100-\mathrm{Cr_{eq}}-\mathrm{Ni_{eq}}\right)-\left(97.5\times\mathrm{Cr_{eq}}\right)+\left(2.02\mathrm{Cr_{eq}}\times\mathrm{Cr_{eq}}\right)-108.8\mathrm{Ni_{eq}}+\\&\left(0.52\mathrm{Ni_{eq}}\times\mathrm{Ni_{eq}}\right)-0.05\left(\mathrm{Cr_{eq}}\times\mathrm{Ni_{eq}}\right)+10^{-3}(73.3\times\mathrm{Cr_{eq}}-0.67\times\mathrm{Cr_{eq}}\times\mathrm{Cr_{eq}}+50.2\times\mathrm{Ni_{eq}}-\\&0.84\times\mathrm{Ni_{eq}}\times\mathrm{Ni_{eq}}-1.51\times\mathrm{Cr_{eq}}\times\mathrm{Ni_{eq}})\end{aligned}\tag{5.4}$$

$$\Delta G_{\mathrm{Fe}}^{\alpha-\gamma} = 6190.8 - 14.3\times10^{-2}T^{2} + 2\times10^{-6}T^{3} \tag{5.5}$$

$$\mathrm{Cr_{eq}} = \mathrm{Cr} + 4.5\times\mathrm{Mo} \tag{5.6}$$

$$\mathrm{Ni_{eq}} = \mathrm{Ni} + 0.6\times\mathrm{Mn} + 20\times\mathrm{C} + 4\times\mathrm{N} + 0.4\times\mathrm{Si} \tag{5.7}$$

where, $\Delta G_{\mathrm{Fe}}^{\alpha-\gamma}$ (J/mol) is the free energy of pure iron (Fe), T (K) is the temperature, $\mathrm{Ni_{eq}}$ and $\mathrm{Cr_{eq}}$ are the Ni and Cr equivalent (in wt.%), respectively, calculated using the present Mn, Si, Ni and C content (in wt.%). The variation in the free energy change with annealing temperature is shown in Fig. 5.8 along with the T_o at ~602 °C. Thus, the reversion of α′-martensite is expected to occur on heating above 602 °C. This calculated temperature is in agreement with the annealing of the bulk samples of the same steel where α′-martensite reversion was observed at 700 °C [40]. However, as mentioned above, α′-martensite reversion was not observed on heating of thin foils below 800 °C. This indicates that more driving force is required for α′-martensite reversion in thin foils compared to the bulk samples.

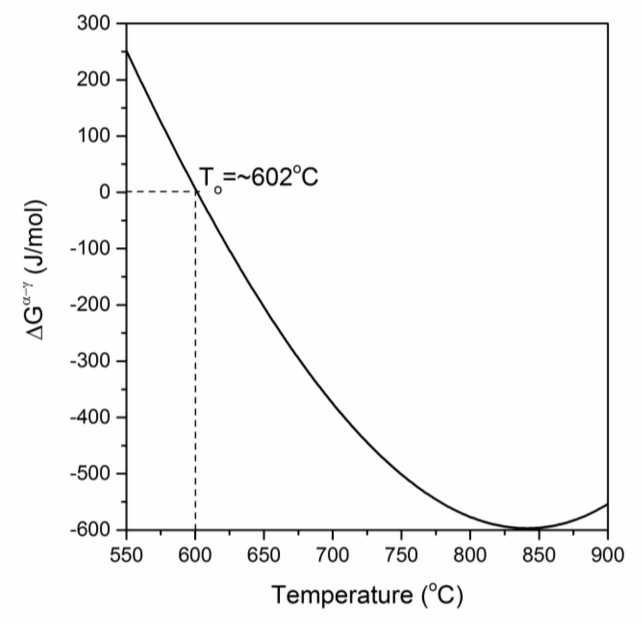

Figure 5.8: Free energy change for α′-martensite reversion to γ of high Mn steel as a function of annealing temperature.

During the electron back-scattering diffraction in-situ heating of an Fe-1.5Mn-1.5Si-0.2C steel (processed by annealing at 780 and 400 °C for 300 s), Tomota et al. [236] reported the decrease in the surface concentration of Mn and C measured using optical emission spectroscopy. The reduction in Mn and C concentration was due to the desorption of Mn atoms from the sample surface under high vacuum owing to its higher equilibrium vapour pressure along with decarburisation at the sample surface. The stability of γ in compared to α′-martensite is increased by both Mn and C. Thus, the decrease in their surface concentration leads to higher α′-martensite to γ reversion temperature [236]. Similar reasoning can be used for the increase in α′-martensite transformation temperature during our in-situ TEM heating experiment.

5.7 Conclusions

The microstructural characterisation by in-situ transmission electron microscopy heating of the 42% cold-rolled sample led to the following conclusions:

(1) The transformation on in-situ heating of thin foils resulted in the γ inheriting the shape of either ε or α′-martensite grains and exhibiting the S-N and K-S ORs, respectively. The ε and α′-martensite reversion occurred without any visible migration of the ε-martensite/γ and α′-martensite/γ interfaces

by displacive mechanism. For in-situ heating of thin foils, the transformation of ε and α′-martensite occurred at higher temperature compared to the bulk samples.

(2) The formation of fine twins in reverted γ during recovery can be explained based on the growth of γ-ISFs derived from the faulted ε-martensite using a mechanism of gliding Shockley partial dislocations.

CHAPTER 6 EFFECT OF ISOCHRONAL ANNEALING ON THE MICROSTRUCTURE, TEXTURE AND MECHANICAL PROPERTIES OF A COLD-ROLLED HIGH MANGANESE STEEL

This chapter studies the effect of isochronal annealing for 300 s on the microstructure and texture of high Mn steel cold-rolled to 42% thickness reduction with characterisation conducted using electron back-scattering diffraction and transmission electron microscopy. The segmentation of the reverted/recovered and recrystallised γ grains and the calculation of activation energy for γ grain growth was performed using the analytical procedures developed in Section 3.5.2.2, Chapter 3. The γ orientations obtained after reversion was correlated to the deformation-induced ε and α′-martensite orientations.

6.1 Hardness after cold rolling and annealing

The variation of hardness with annealing temperature is shown in Fig. 6.1. The softening fraction (X) was calculated from the hardness values using the equation [25]:

$$X = \frac{H_R - H_T}{H_R - H_0} \tag{6.1}$$

where H_R is the hardness of the cold-rolled sample, H_T is the hardness of the sample annealed at a particular temperature T and H_0 is the hardness of the sample annealed at 850 °C for 300 s.

The hardness curve can be divided into regions showing: (i) small reduction on annealing at 500 °C for 300 s due to the completion of ε-martensite reversion, recovery of the cold-rolled α′-martensite and the onset of α′-martensite reversion; (ii) large reduction after annealing for 300 s at temperatures between 600 and 650 °C due to α′-martensite reversion and subsequent γ recrystallisation; (iii) gradual decrease upon annealing for 300 s at temperatures between 700 and 850 °C arising from the completion of γ recrystallisation and subsequent grain coarsening.

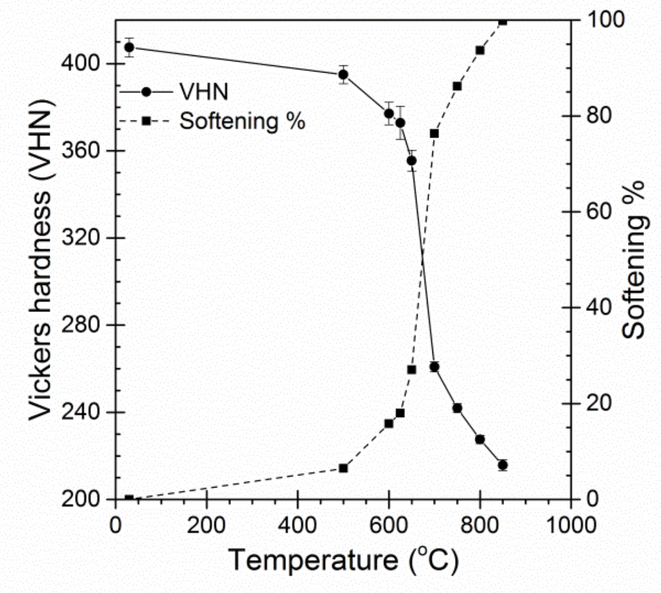

Figure 6.1: Variation in hardness and the softened fraction with annealing temperature.

6.2 Microstructure changes after cold rolling and annealing

The cold-rolled samples manifest microstructure containing elongated, fragmented α′-martensite as the dominant phase along with remnant ε-martensite and a trace amount of untransformed γ (Fig. 6.2a). Cold rolling of high Mn steels is reported [7, 48] to produce similar microstructures. After annealing to 500 °C the microstructure shows the completion of ε-martensite reversion and the onset of α′-martensite reversion to γ (Fig. 6.2b) along with twinning in the reverted/recovered γ grains (inset, Fig. 6.2b).

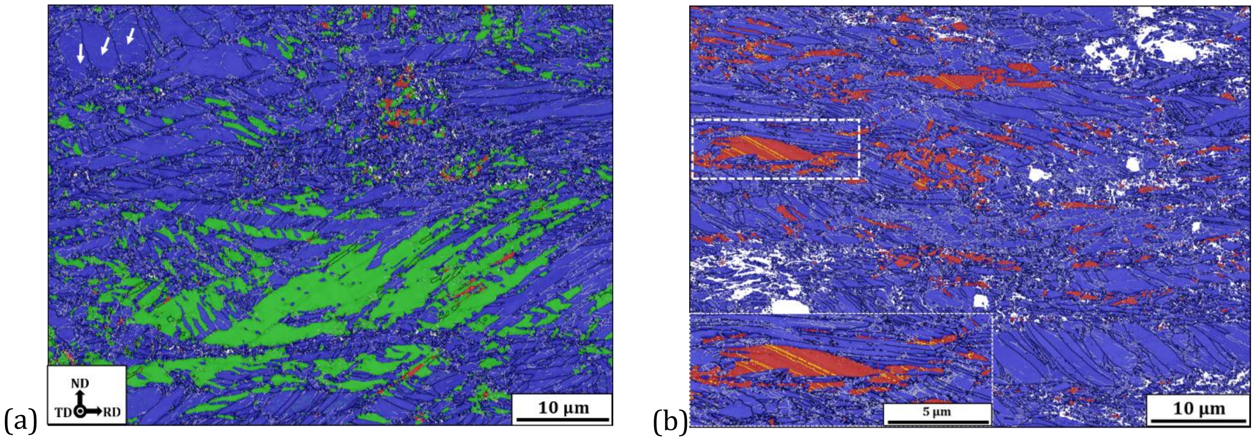

Figure 6.2: Superimposed band contrast and phase maps after (a) cold rolling and subsequent annealing at (b) 500 °C. Red = γ, green = ε-martensite, blue = α′-martensite, white = unindexed areas, silver = LAGBs, black = HAGBs, yellow = γ twin boundaries, rolling direction = horizontal. Inset in Fig. 6.2b shows twins in the reverted/recovered γ. White arrows in Fig. 6.2a shows the subdivision of the α′-martensite grains.

Upon annealing to 600 and 625 °C the microstructure consists of an approximately equal area fraction of α′-martensite, reverted/recovered and recrystallising γ (Figs. 6.3a and 6.3b). Annealing at 650 °C results in a microstructure comprising a mixture of recrystallised polygonised γ grains along with reverted/recovered γ and further reduced area fraction of α′-martensite (Fig. 6.3c). Annealing at 700 °C shows the completion of γ recrystallisation along with γ annealing twins (Fig. 6.3d).

Further annealing between 750 and 850 °C results in the γ grain coarsening (Figs. 6.3e-6.3g). The formation of plate-like ε-martensite and/or lenticular α′-martensite upon quenching after annealing is observed in the reverted/recovered/recrystallised γ grains (Figs. 6.3a, 6.3b and 6.3e-6.3g). The area fraction of ε and α′-martensite produced upon quenching after annealing increases with increasing annealing temperatures between 700 and 850 °C (Figs. 6.3d-6.3g). The increase in ε and α′-martensite area fraction is ascribed to the higher number of nucleation sites for their formation and the availability of a large γ grain area for growth. Also, the low γ-SFE (γ-SFE = 14.5 mJ/m^2 [71]) of the present high Mn steel favours the formation of ε and α′-martensite. A similar trend in the increase in ε and α′-martensite volume fractions with increasing γ grain size was observed [98].

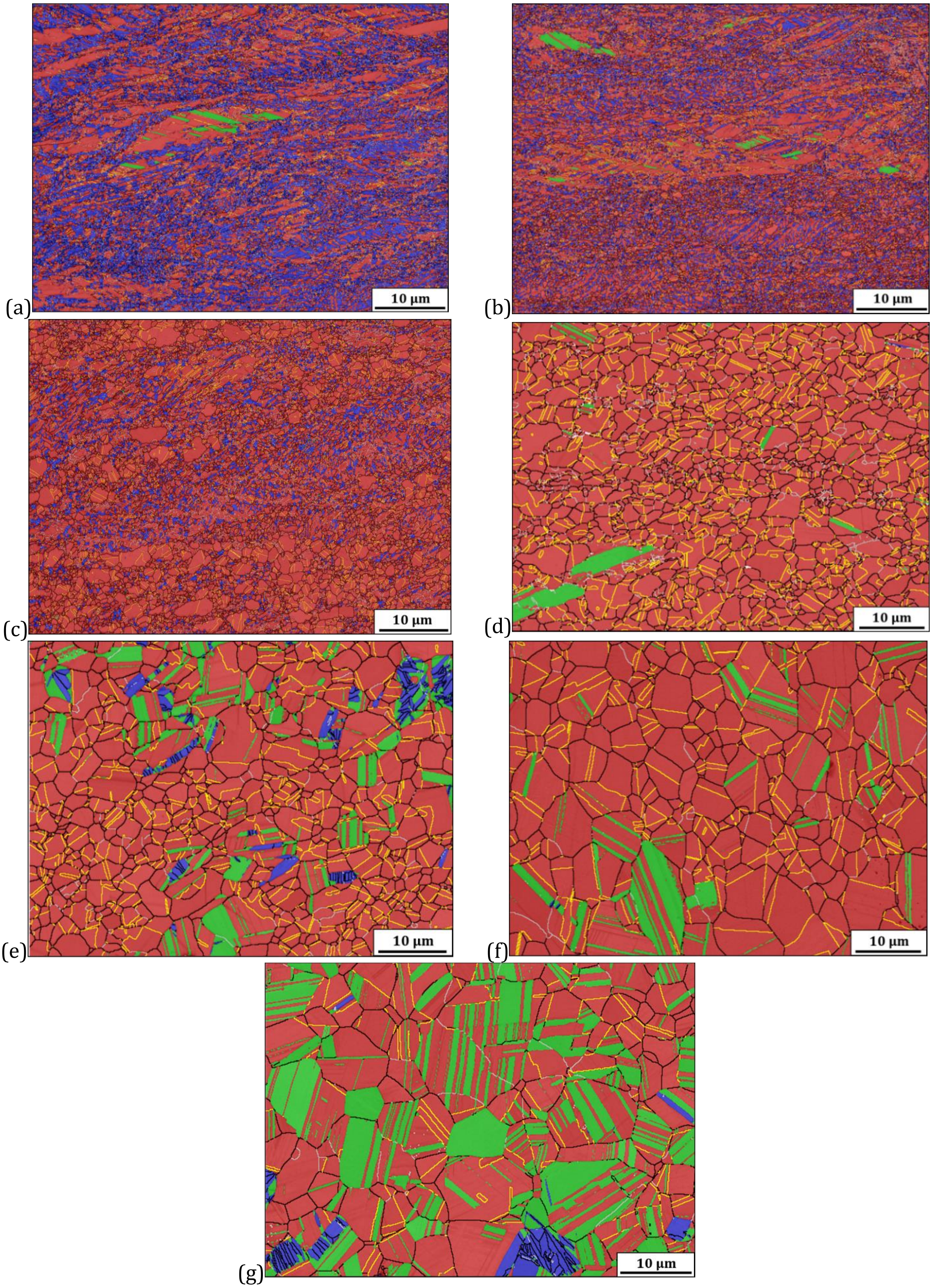

Figure 6.3: Superimposed band contrast and phase maps after annealing at (a) 600 °C, (b) 625 °C, (c) 650 °C, (d) 700 °C, (e) 750 °C, (f) 800 °C and (g) 850 °C. Red = γ, green = ε-martensite, blue = α′-martensite, white = unindexed areas, silver = LAGBs, black = HAGBs, yellow = γ twin boundaries, rolling direction = horizontal.

Figs. 6.4a-6.4c shows the γ grains segmented using the procedure illustrated in Section 3.5.2.3, Chapter 3 into the reverted/recovered (in green) and recrystallised (in fuchsia) grain fractions upon annealing at (a) 600 °C, (b) 625 °C and (c) 650 °C. The recrystallised γ grain size increased from 0.21 ± 0.1 μm to 0.23 ± 0.11 μm to 0.33 ± 0.25 μm with increasing annealing temperatures from 600 to 625 to 650 °C, respectively. The percentage of LAGBs decreased and HAGBs increased upon annealing between 600 and 650 °C for the reverted/recovered and recrystallised γ grains, correspondingly (Fig. 6.4d). It has to be stated that as one EBSD map was done per condition, error bars are missing in the segmented γ LAGBs and HAGBs fractions in Fig. 6.4d.

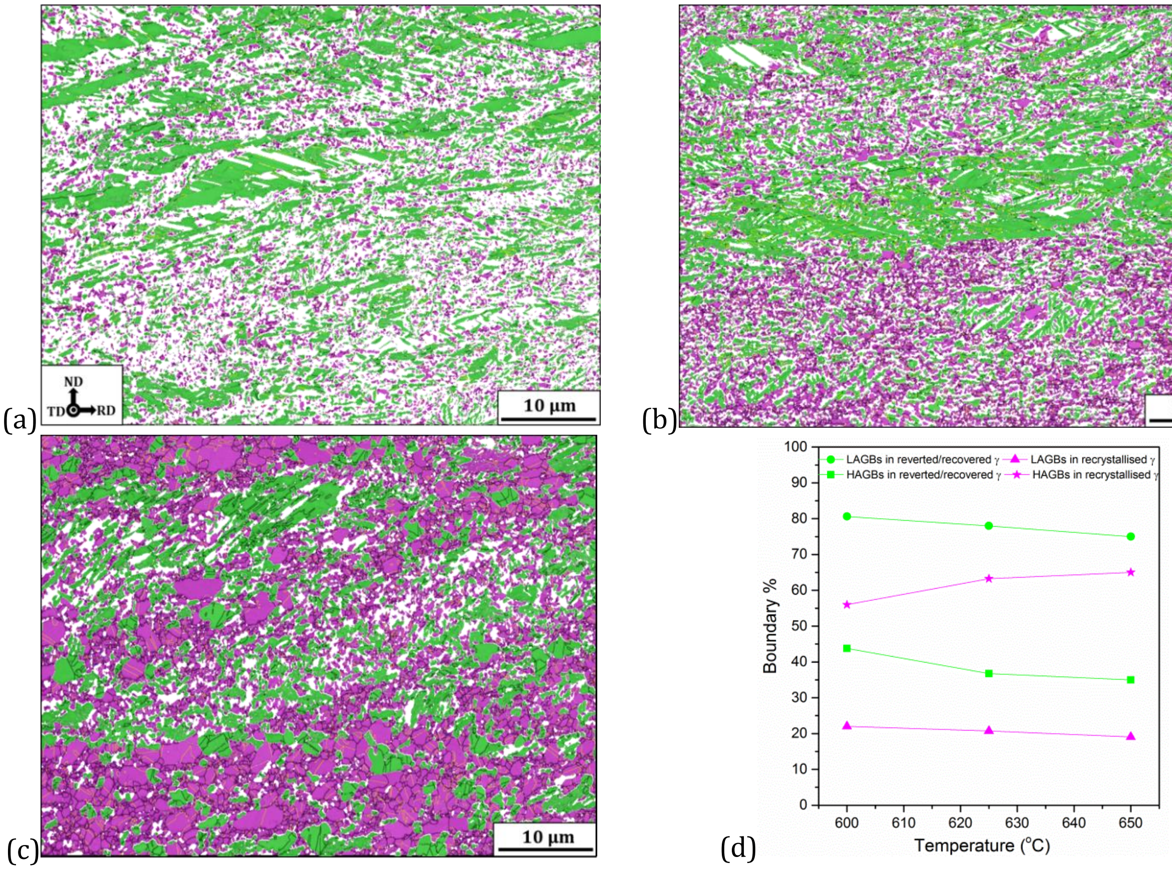

Figure 6.4: The γ grains segmented into reverted/recovered (in green), recrystallised (in fuchsia) fractions after annealing at (a) 600 °C, (b) 625 °C and (c) 650 °C, (d) the variation of γ low angle and high angle grain boundaries percentages with annealing temperature. The white regions in Figs. 6.4a-6.4c indicate ε and α′-martensite along with the unindexed areas.

The representative bright-field TEM micrographs in Fig. 6.5 shows the evolution of the microstructure after cold rolling and annealing at 500, 600, 625 and 650 °C. The micrographs of the cold-rolled sample (Figs. 6.5a and 6.5b) depict elongated α′-martensite grains and ε-martensite grains containing stacking faults (highlighted by green arrows, Fig. 6.5b) along with untransformed γ. Gazder *et al.* [7, 224] showed the formation of stacking faults in ε-martensite by TEM/TKD and suggested the deformation accommodation in ε-martensite. Using in-situ tensile testing accompanied by neutron diffraction, Saleh *et al.* [24] demonstrated ε-martensite to undertake compressive strains, which also indicates that ε-martensite accommodates deformation. During the plane strain compression of the present steel to 20% thickness reduction, the transformation of γ to deformation-induced ε and α′-martensite was observed without the formation of deformation-induced twins in γ.

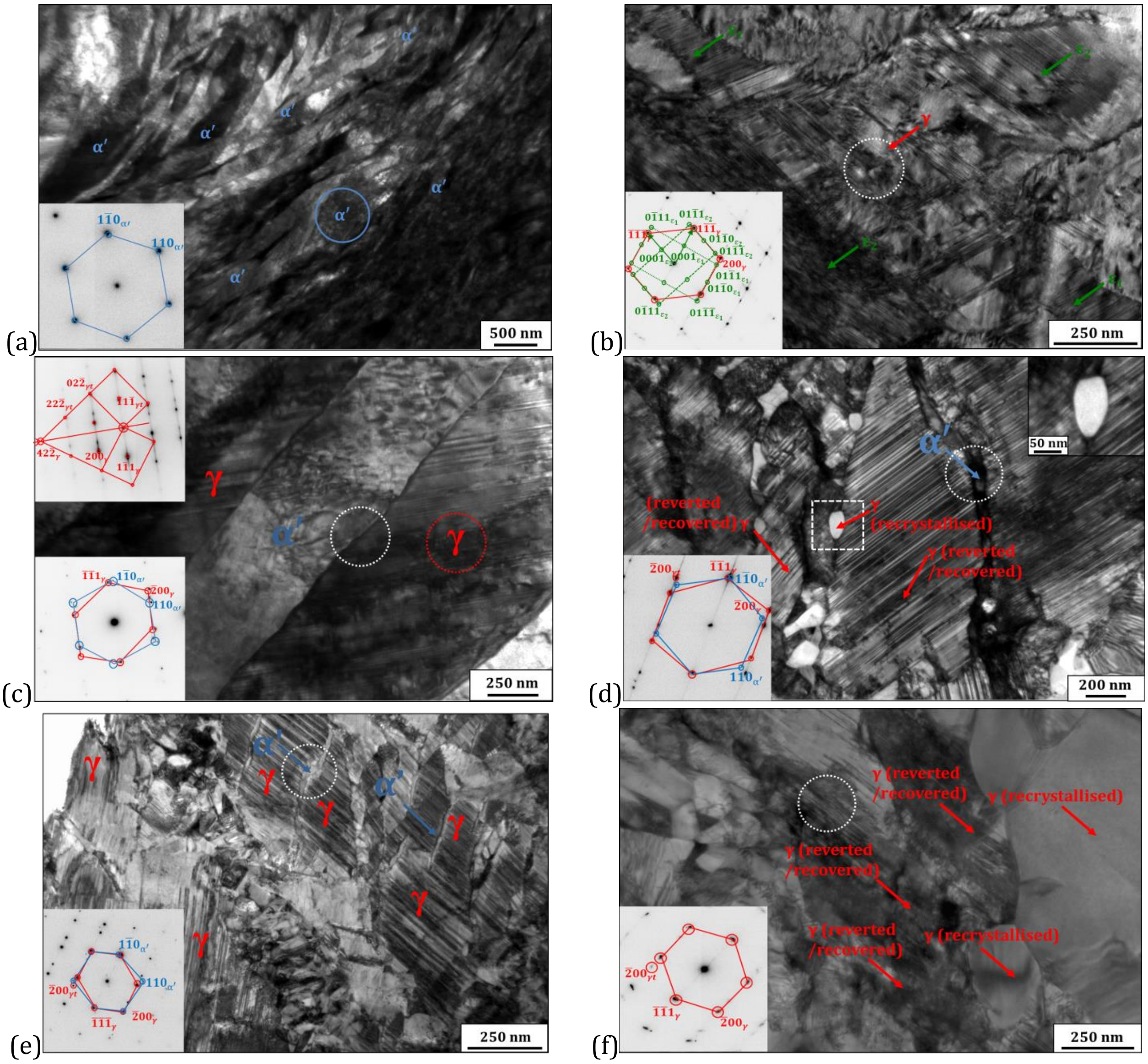

Figure 6.5: Representative (a-f) bright-field transmission electron micrographs after (a, b) cold rolling and annealing at (c) 500 °C, (d) 600 °C, (e) 625 °C and (f) 650 °C. The bottom left inset diffraction patterns in Figs. 6.5a-6.5f are from the regions delineated by white circles. The top left inset diffraction pattern in Fig. 6.5c is from the red circular region. The zone axes are $[111]_{\alpha'}$ in Fig. 6.5a, $[2\bar{1}\bar{1}0]_{\varepsilon}$, $[110]_{\gamma}$ in Fig. 6.5b, $[01\bar{1}]_{\gamma}$, $[11\bar{1}]_{\alpha'}$ in Figs. 6.5c-6.5e and $[110]_{\gamma}$ in Fig. 6.5f.

The formation of stacking faults in ε-martensite after cold rolling was discussed in Section 4.4, Chapter 4. In Chapter 4 a mechanism enabling the change in stacking fault character was proposed which involves the motion of Shockley partial dislocations on every plane below the stacking fault plane. The formation of fine twins in the reverted/recovered γ grains was observed upon annealing between 500 and 650 °C. In this regard, twinning in the reverted/recovered γ grains was also reported during the annealing at 500 °C for 30 min for an Fe-26Mn-3Si-3Al steel cold-rolled to 52% thickness reduction [10].

The actual thickness of the twins (w) was calculated from the measured thickness (w_L) using the equation [205]

$$w = (2w_L)/\pi \tag{6.2}$$

which returned ≈6.5 ± 4.2 nm for the samples annealed between 500 and 650 °C.

Twinning in reverted/recovered γ (verified by the top left inset diffraction pattern in Fig. 6.5c) was detected upon the in-situ TEM annealing after cold rolling to 42% thickness reduction and discussed in Section 5.2, Chapter 5. Twinning was attributed to the recovery of γ which reverted from the ε-martensite containing stacking faults. The recovery-induced twinning in γ which reverted from α′-martensite was witnessed during the annealing of an Fe-33.5Ni alloy [35].

The nucleation of recrystallised γ grain occurs at the boundary of two reverted/recovered γ grains is observed after annealing at 600 °C (Fig. 6.5d, top right inset). Similar nucleation events were depicted in the segmented EBSD map after annealing at 600 °C in Fig. 6.4a. The inset diffraction pattern shows the occurrence of S-N [105] and K-S [53] orientation relationships in Fig. 6.5b and Figs. 6.5c-6.5e, respectively.

6.2.1 Recrystallised γ grain growth

The γ grain sizes evaluated using the analytical procedure described in Section 3.5.2.3, Chapter 3 for the samples annealed between 700 and 850 °C are shown in Fig. 6.6. The γ grain size estimated excluding the ε and α′-martensite laths/plates present inside the γ grain is much larger than those directly estimated with the presence of ε and α′-martensite laths/plates. The difference between the γ grain sizes determined using the two techniques is higher at the annealing temperature of 850 °C due to the higher area fraction of ε and α′-martensite formed upon quenching from relatively higher annealing temperature. A similar trend in the increase in γ grain size with an order of magnitude faster kinetics was also observed in the Fe-18Mn [20] and Fe-18Mn-1.5Si-0.6C [26] steels annealed between 700 and 1100 °C.

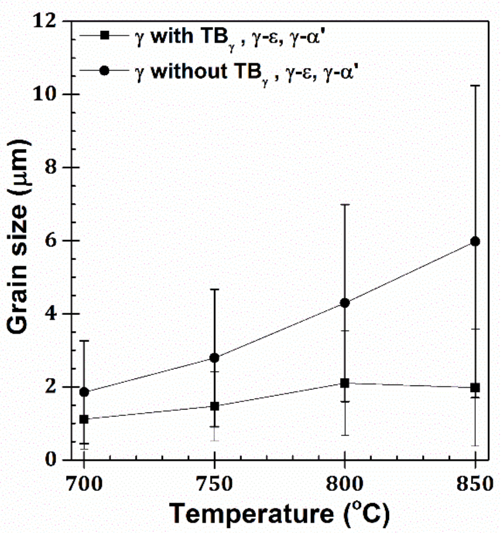

Figure 6.6: The variation of γ grain size with annealing temperature with and without considering γ twin boundaries ε and α′-martensite.

For the high Mn steel, the activation energy for γ grain growth was evaluated using the equation[144]:

$$d_T^{1/N} - d_0^{1/N} = K_0 t^n e^{(-Q/RT)} \tag{6.3}$$

where d_T is the γ grain size at a given temperature T, d_0 is the initial average γ grain size at 700 °C (1.85 ± 1.4 μm), N = 0.34 is the grain growth exponent, K_0 is a kinetic constant (equivalent to the y-intercept) t = 300 s is the holding time during annealing, n = 1 is a constant, Q is the computed activation energy for γ grain growth (J/mol), R = 8.314 J/molK is the universal gas constant and T is the annealing temperature (K).

Although isothermal annealing was not undertaken in the present work, the value of N from a similar isothermal annealing done on an Fe-29Mn-5Al-0.06C steel [144] was taken on the reasoning that the value of N does not change much with the composition for the same class of steels. The value of N changes from 0.36 (316L stainless steel) to 0.42 (301LN stainless steel) [144].

The assumptions of Eq. 6.3 are: no inclusions or chemical segregations are present at grain boundaries and the grain morphology is equiaxed with the microstructure containing uniform grain size [144]. Fig. 6.7 shows the determination of the activation energy (Q) from the slope of $\ln(d_T^{1/N} - d_0^{1/N})$ vs 1/T.

Using Eq. 6.3, the activation energy for γ grain growth was estimated with and without considering γ twins, ε and α′-martensite (Fig. 6.7). The obtained value of activation energy for γ grain growth without the presence of γ twins, ε and α′-martensite (solid circles, Fig. 6.7) is 235.2 ± 17.6 kJ/mol, whereas the value determined including γ twins, ε and α′-martensite (solid squares, Fig. 6.7) is 229.6 ± 88.7 kJ/mol. The activation energy taking into account γ twins, ε and α′-martensite is slightly lower than that obtained excluding γ twins, ε and α′-martensite.

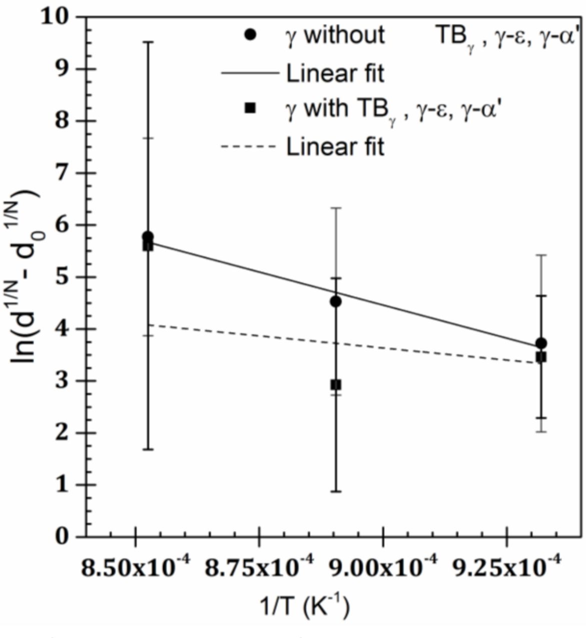

Figure 6.7: Fit for the calculation of γ grain growth activation energy.

The activation energy for γ grain growth was also determined using the γ grain size data for the two high Mn steels [156, 237]. The values of 253.8 ± 38.4 and 233.2 ± 74.5 kJ/mol were obtained for the Fe-18Mn and Fe-18Mn-1.5Si-0.6C steels, respectively. They are close to the determined value excluding γ twins, ε and α′-martensite. In addition, the activation energy of γ grain growth in an Fe-29Mn-0.06C high Mn steel during isothermal annealing at 1000 °C was reported as 208 kJ/mol [238]. In this regard, the activation energy for γ grain growth for the Fe-1.51Mn-0.03Si-0.17C, Fe-1.43Mn-0.03Si-0.12C and Fe-0.86Mn-0.03Si-0.11C plane C steels was reported as ≈262, 271 and 272 kJ/mol, respectively [93]. These values are slightly higher than the value for high Mn steel. For C-Mn-V, C-Mn-Ti, C-Mn-Nb based micro-alloyed low C steels the activation energy for γ grain growth was reported as 400, 437 and 435 kJ/mol, respectively [155]. These values are much higher compared to high Mn steels.

The γ grain growth activation energy with and without considering the presence of ε and α′-martensite formed upon quenching after annealing is lower than the activation energy for the self-diffusion of γ ($Q = 270$ kJ/mol) [46] indicating γ grain boundary diffusion as the main mechanism for γ grain growth compared to lattice self-diffusion. Higher errors are obtained for the activation energies when considering the ε and α′-martensite formed upon quenching after annealing due to an error in the accurate determination of γ grain size. For 316L austenitic stainless steel, Kashyap and Tangri [239] observed that γ grain growth at annealing temperatures lower than $0.85T_m$ (T_m is the melting temperature) occurs by grain boundary diffusion. At annealing temperatures higher than $0.85T_m$ γ grain growth takes place via lattice diffusion due to a higher concentration of vacancies. The annealing temperatures in the present condition between 700 and 850 °C for γ grain growth are below $0.85T_m$ (1150 °C, T_m greater than 1400 °C) [240] which favours γ grain boundary diffusion.

6.3 Changes in texture after cold rolling and annealing

Figs. 6.8-6.12 shows the α′, ε-martensite and γ orientation distribution function (ODF) sections in the cold-rolled and annealed samples. As α′ and ε-martensite are the major phases in the cold-rolled sample which transform to γ upon reversion their ODF sections are presented first. The ε-martensite ODF sections for the samples annealed between 500-650 °C are not plotted due to its low fraction.

Fig. 6.8 shows the $\phi_2 = 0°$ and 45° ODF sections of α′-martensite. Fig. 6.8a displays the ideal α′-martensite orientations (in blue) on which particular γ and ε-martensite orientations that form upon the phase transformation via the K-S and Burgers orientation relationships are shown in red and green, respectively. Similar bcc ODF sections correlating bcc and fcc orientations formed upon phase transformation by K-S orientation relationship was reported [241, 242]. TEM micrographs in Figs. 6.5c-6.5e showed the occurrence of K-S orientation relationship between the reverted/recovered γ and α′-martensite. Thus, only the K-S orientation relationship was chosen for texture analysis between γ and α′-martensite.

Figs. 6.8b-6.8f shows the ODF sections of the α′-martensite after cold rolling and annealing between 500-650 °C. The deformation-induced α′-martensite (Fig. 6.2a) and the remnant α′-martensite after annealing between 500-650 °C shows relatively stronger intensities along the ideal $\alpha_{\alpha'}$-fibre ($\langle 110\rangle_{\alpha'}$ || RD) centred around the $(001)[110]_{\alpha'}$ orientation and weaker intensities along the ideal $\gamma_{\alpha'}$-fibre ($\langle 111\rangle_{\alpha'}$ || ND) spread around the $(111)[\bar{1}\bar{1}2]_{\alpha'}$ and $(554)[\bar{2}\bar{2}5]_{\alpha'}$ orientations. Similar α′-martensite orientations were reported for an Fe-17Mn-3Al-2Si-1Ni-0.06C steel subjected to cold rolling up to 66% thickness reduction and subsequent annealing at 625 °C [7].

The α′-martensite $(001)[110]_{\alpha'}$ orientation forms upon the phase transformation of the ideal C_γ and Br_γ orientations via the K-S orientation relationship. Alternatively, it can also form from the transformation of $\{01\bar{1}2\}\langle 1\bar{1}01\rangle_\varepsilon$ orientation via the Burgers orientation relationship. The $(111)[\bar{1}\bar{1}2]_{\alpha'}$ and $(554)[\bar{2}\bar{2}5]_{\alpha'}$ orientations form upon the phase transformation of the ideal Br_γ or $\{11\bar{2}0\}\langle\bar{1}010\rangle_\varepsilon$ orientations via the K-S and Burgers orientations relationships, respectively.

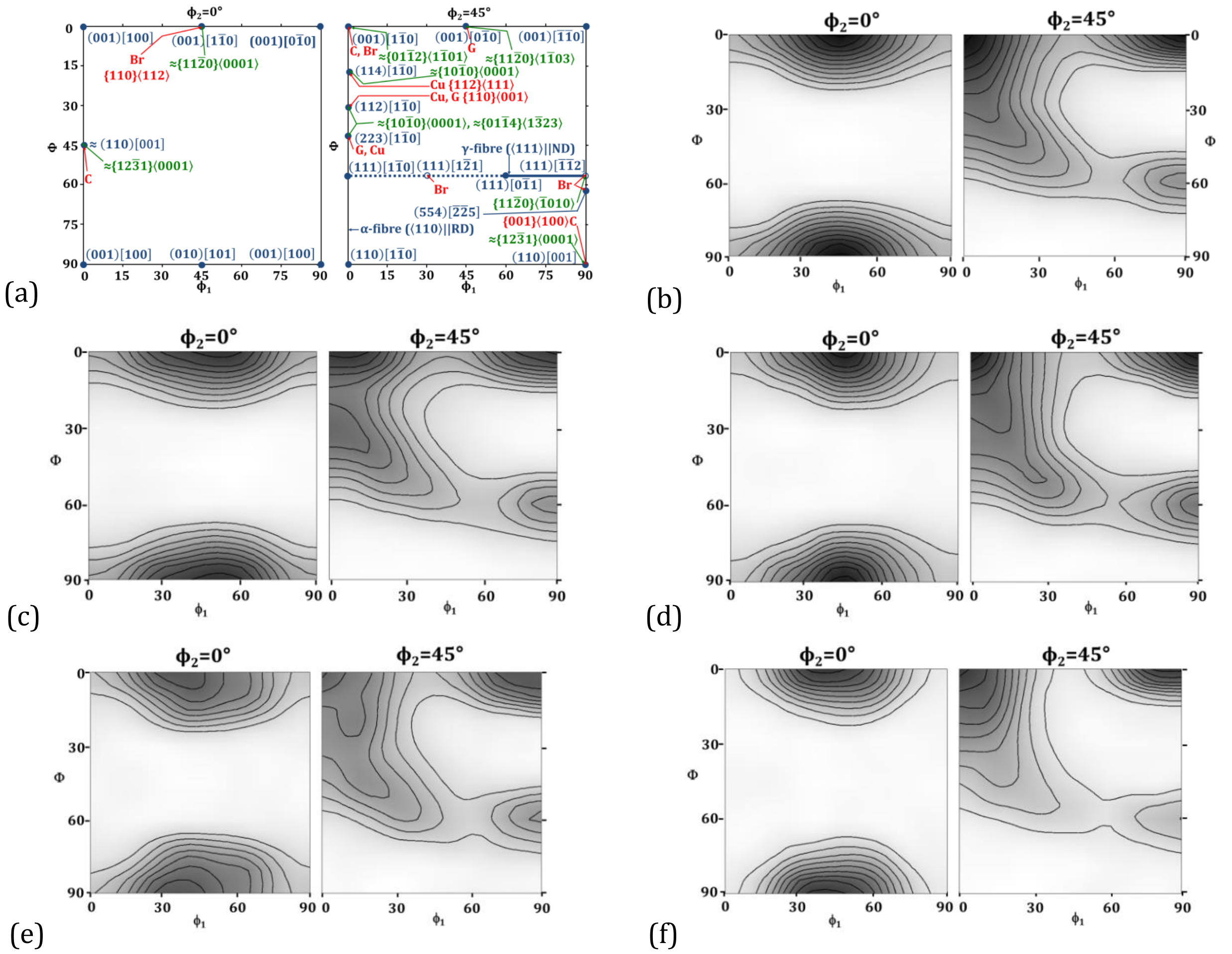

Figure 6.8: ϕ_2 = 0° and 45° orientation distribution function sections of α′-martensite showing the (a) ideal orientations (in blue), after (b) cold rolling and annealing at (c) 500 °C, (d) 600 °C, (e) 625 °C and (f) 650 °C. In Fig. 6.8a, the particular γ (in red) and ε-martensite (in green) orientations are provided for the K-S and Burgers orientation relationships, respectively. Contour levels = 0.5×.

Fig. 6.9 depicts the ϕ_2 = 0° and 45° ODF sections of α'-martensite formed upon quenching after annealing between 700-850 °C showing intensities centred around the $(001)[110]_{\alpha'}$ and $(110)[001]_{\alpha'}$ orientations. The $(110)[001]_{\alpha'}$ orientation forms on the phase transformation of the $\{12\bar{3}1\}\langle0001\rangle_{\varepsilon}$ orientation via the Burgers orientation relationship.

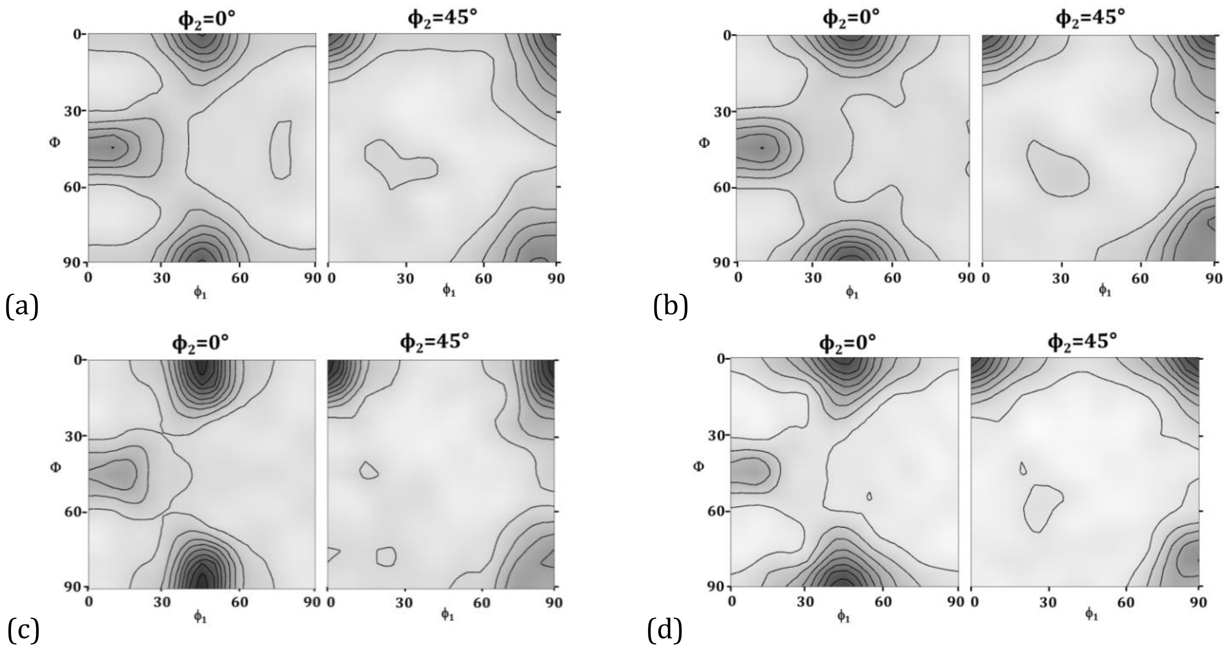

Figure 6.9: ϕ_2 = 0° and 45° orientation distribution function sections of α'-martensite after annealing at (a) 700 °C, (b) 750 °C, (c) 800 °C and (d) 850 °C. Contour levels = 0.5×.

Figs. 6.10 and 6.11 shows the ϕ_2 = 0° and 30° ODF sections of ε-martensite using the $[10\bar{1}0]_{\varepsilon}$ || RD and $[0002]_{\varepsilon}$ || ND convention. Fig. 6.10a is a schematic with the ideal ε-martensite orientations shown in green. The γ orientations that form upon the phase transformation from the particular ε-martensite orientations via the S-N orientation relationship are shown in red.

The ODF sections of deformation-induced ε-martensite are presented in Fig. 6.10b which depicts strong intensities centred around the $\{\bar{1}2\bar{1}5\}\langle1\bar{2}12\rangle_{\varepsilon}$ and $\{01\bar{1}4\}\langle1\bar{3}23\rangle_{\varepsilon}$ orientations along the $\{hkil\}_{\varepsilon}$-fibre. The $\{hkil\}_{\varepsilon}$-fibre have orientations with their $\{0001\}_{\varepsilon}$ poles deviated by ≈24°-26° towards the RD. The formation of $\{hkil\}_{\varepsilon}$-fibre was reported in the Fe-17Mn-3Al-2Si-1Ni-0.06C and Fe-21.6Mn-0.38C steels cold-rolled to 66% and 50% thickness reductions, respectively [7, 8]. The relatively weaker intensities around the $\{10\bar{1}0\}\langle0001\rangle_{\varepsilon}$, $\{11\bar{2}0\}\langle0001\rangle_{\varepsilon}$ and $\{\bar{1}2\bar{1}3\}\langle10\bar{1}0\rangle_{\varepsilon}$ orientations are also noted.

The deformation-induced ε-martensite orientations: $\{\bar{1}2\bar{1}5\}\langle1\bar{2}12\rangle_{\varepsilon}$, $\{01\bar{1}4\}\langle1\bar{3}23\rangle_{\varepsilon}$, $\{10\bar{1}0\}\langle0001\rangle_{\varepsilon}$, $\{11\bar{2}0\}\langle0001\rangle_{\varepsilon}$ and $\{\bar{1}2\bar{1}3\}\langle10\bar{1}0\rangle_{\varepsilon}$ are obtained upon the phase transformation from the γ orientations: $(213)[0\bar{2}1]_{\gamma}$, $(011)[3\bar{1}1]_{\gamma}$, Cu_{γ}, A_{γ} and $\approx S_{\gamma}$ via the S-N orientation relationship, respectively.

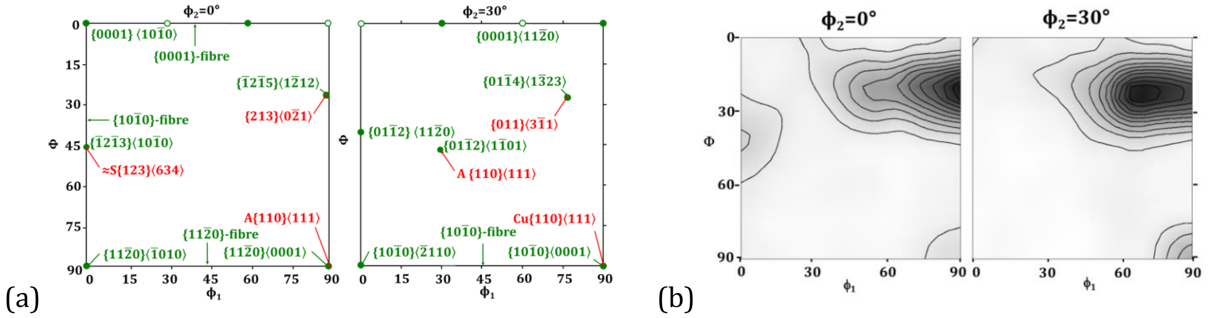

Figure 6.10: ε-martensite ϕ_2 = 0° and 30° orientation distribution function sections showing (a) the ideal orientations (in green) and (b) after cold rolling. In Fig. 6.10a, the particular γ orientations (in red) are provided for the S-N orientation relationship. Contour levels = 0.5×

Fig. 6.11 presents the ϕ_2 = 0° and 30° ODF sections of the plate-like ε-martensite formed upon quenching after annealing between 700 and 850 °C. The ε-martensite shows intensities around the $\{01\bar{1}2\}\langle 1\bar{1}01\rangle_\varepsilon$ and $\{\bar{1}2\bar{1}3\}\langle 10\bar{1}0\rangle_\varepsilon$ orientations. The $\{01\bar{1}2\}\langle 1\bar{1}01\rangle_\varepsilon$ and $\{\bar{1}2\bar{1}3\}\langle 10\bar{1}0\rangle_\varepsilon$ orientations form via the S-N orientation relationship upon the phase transformation of the A_γ and $\approx S_\gamma$ orientations, respectively.

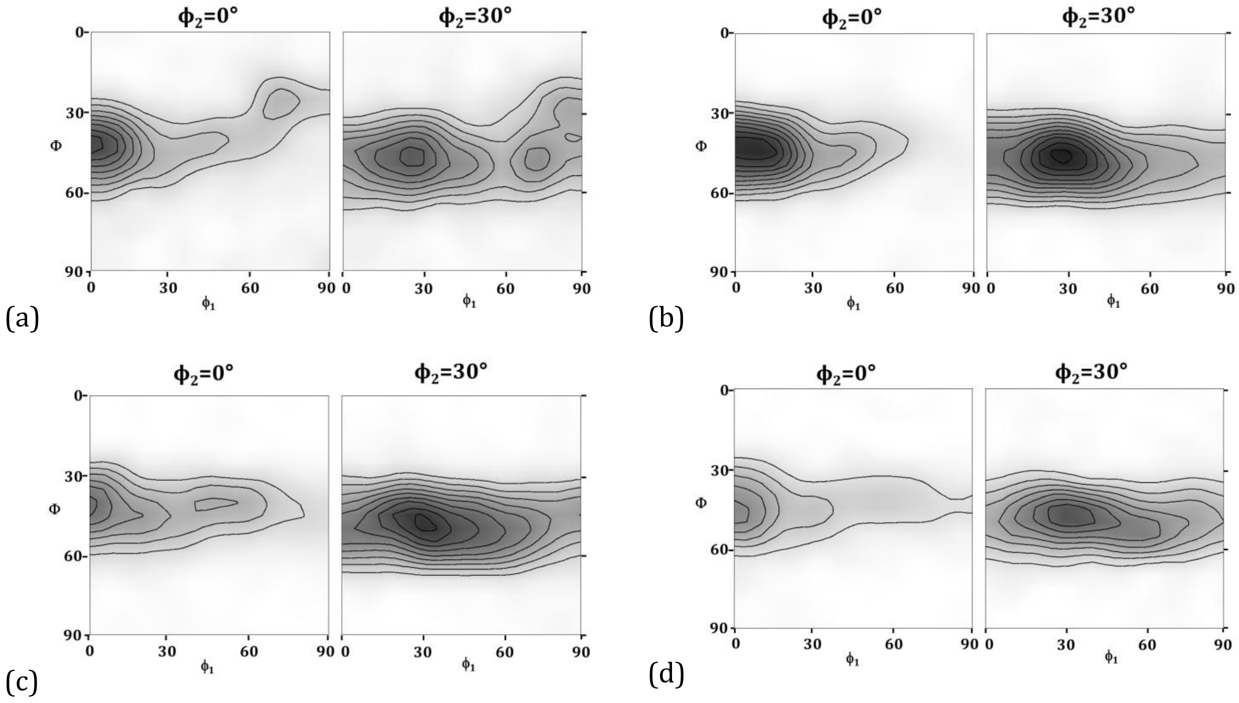

Figure 6.11: ϕ_2 = 0° and 30° orientation distribution function sections of ε-martensite after annealing at (a) 700 °C, (b) 750 °C, (c) 800 °C and (d) 850 °C. Contour levels = 0.5×

Fig. 6.12 shows the ϕ_2 = 0°, 45° and 65° ODF sections of γ. Fig. 6.12a is a schematic displaying the ideal γ orientations and fibres in red and also the γ orientations that form upon the phase transformation of the particular ε (green) and α′-martensite (blue) orientations via the S-N [105] and K-S [53] orientation relationships, respectively.

Figs. 6.12-6.14 shows the ODF sections of γ after cold rolling and annealing between 500 and 850 °C. The untransformed γ after cold rolling and the reverted, recovered and recrystallised γ after annealing between 500-650 °C show strong intensities along the ideal α_γ-fibre ($\langle 110\rangle_\gamma$ || ND) centred around the Br_γ orientation (Figs. 6.12 and 6.13). The formation of weaker intensities around the Cu_γ, S_γ and $(213)[0\bar{2}1]_\gamma$ orientations are also noted. The higher intensities near the ideal $\approx\mathrm{S}_\gamma$ orientation were reported upon the reversion of ε-martensite to γ orientations after annealing at 630 °C for an Fe-22Mn-0.4C steel cold-rolled to 50% thickness reduction [8]. Similar orientations were also observed in an Fe-17Mn-3Al-2Si-1Ni-0.06C steel upon cold rolling to 66% thickness reduction and subsequent annealing at 625 °C [7].

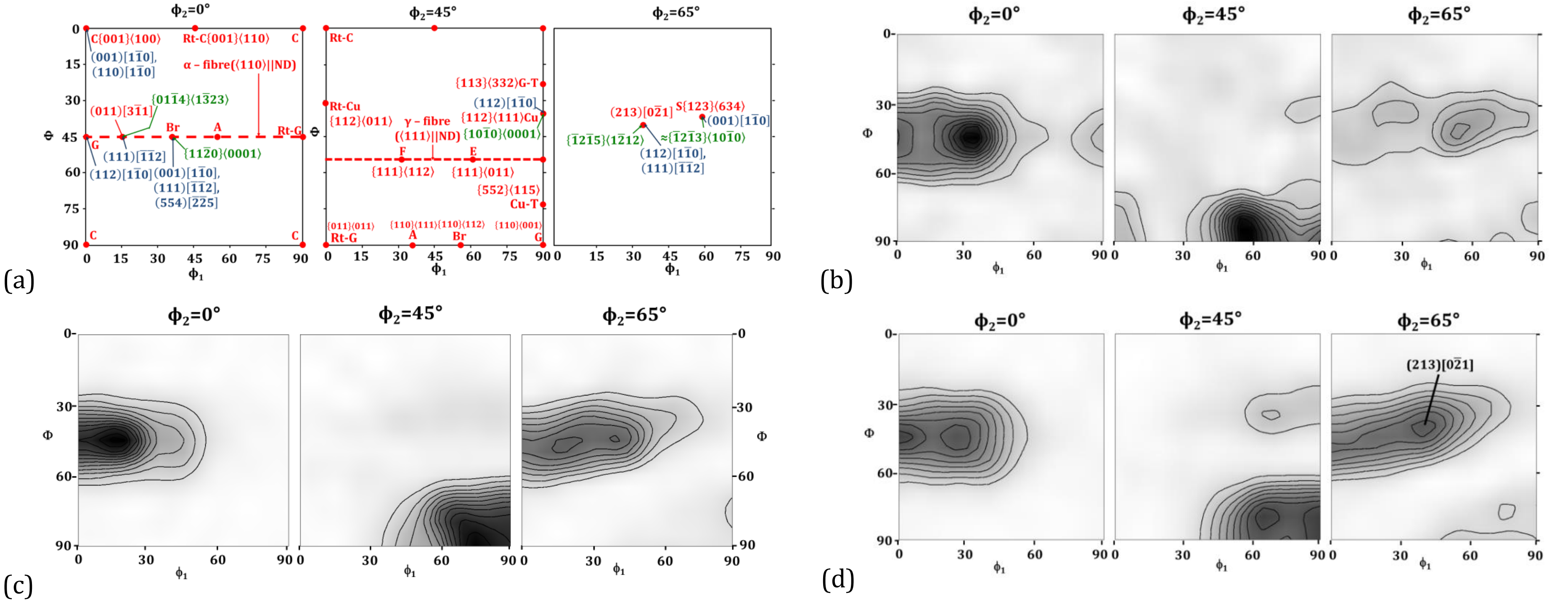

Figure 6.12: ϕ_2 = 0°, 45° and 65° orientation distribution function sections of γ showing (a) ideal orientations (in red), after (b) cold rolling and annealing at (c) 500 °C. In Fig. 6.12a, the particular ε-martensite (in green) and α′-martensite (in blue) orientations are provided for the S-N and K-S orientation relationships, respectively. Contour levels = 0.5×

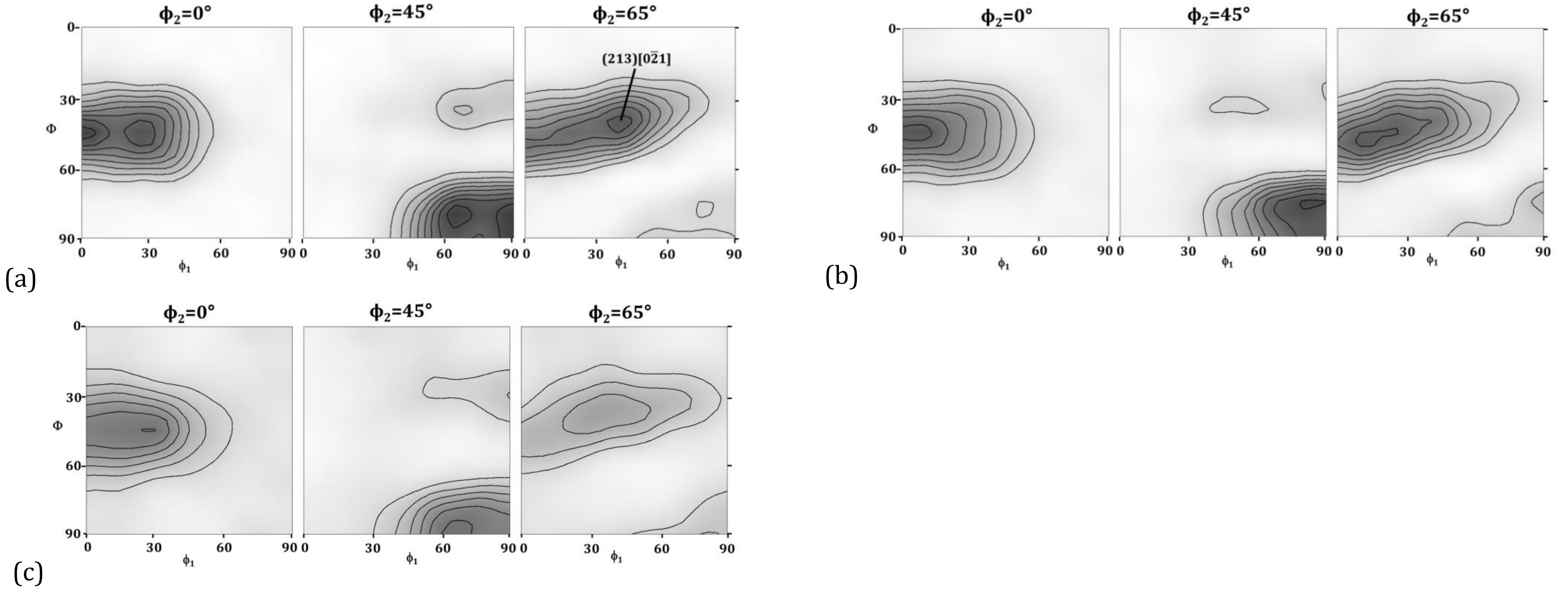

Figure 6.13: ϕ_2 = 0°, 45° and 65° orientation distribution function sections of γ after annealing at (a) 600 °C, (b) 625 °C and (c) 650 °C. Contour levels = 0.5×

The recrystallised γ formed after annealing between 700 and 850 °C (Fig. 6.14) shows weak intensities around the ideal Cube (C_γ, $\{001\}\langle100\rangle_\gamma$), A_γ, Cu_γ and S_γ orientations. The (i) Br_γ, (ii) Cu_γ, (iii) $(213)[0\bar{2}1]_\gamma$ and (iv) S_γ orientations are obtained from the α′-martensite orientations: (i) $(001)[1\bar{1}0]_{\alpha'}$, $(111)[\bar{1}\bar{1}2]_{\alpha'}$ and $(554)[\bar{2}\bar{2}5]_{\alpha'}$, (ii) $(112)[1\bar{1}0]_{\alpha'}$, (iii) $(112)[1\bar{1}0]_{\alpha'}$ and $(111)[\bar{1}\bar{1}2]_{\alpha'}$ and (iv) $(001)[1\bar{1}0]_{\alpha'}$ via the K-S orientation relationship. Alternatively, the Br_γ, Cu_γ, $(213)[0\bar{2}1]_\gamma$ and S_γ orientations can also form from the $\{11\bar{2}0\}\langle0001\rangle_\varepsilon$, $\{10\bar{1}0\}\langle0001\rangle_\varepsilon$, $\{\bar{1}2\bar{1}5\}\langle1\bar{2}12\rangle_\varepsilon$ and $\{\bar{1}2\bar{1}3\}\langle10\bar{1}0\rangle_\varepsilon$ orientations via the S-N orientation relationship, respectively.

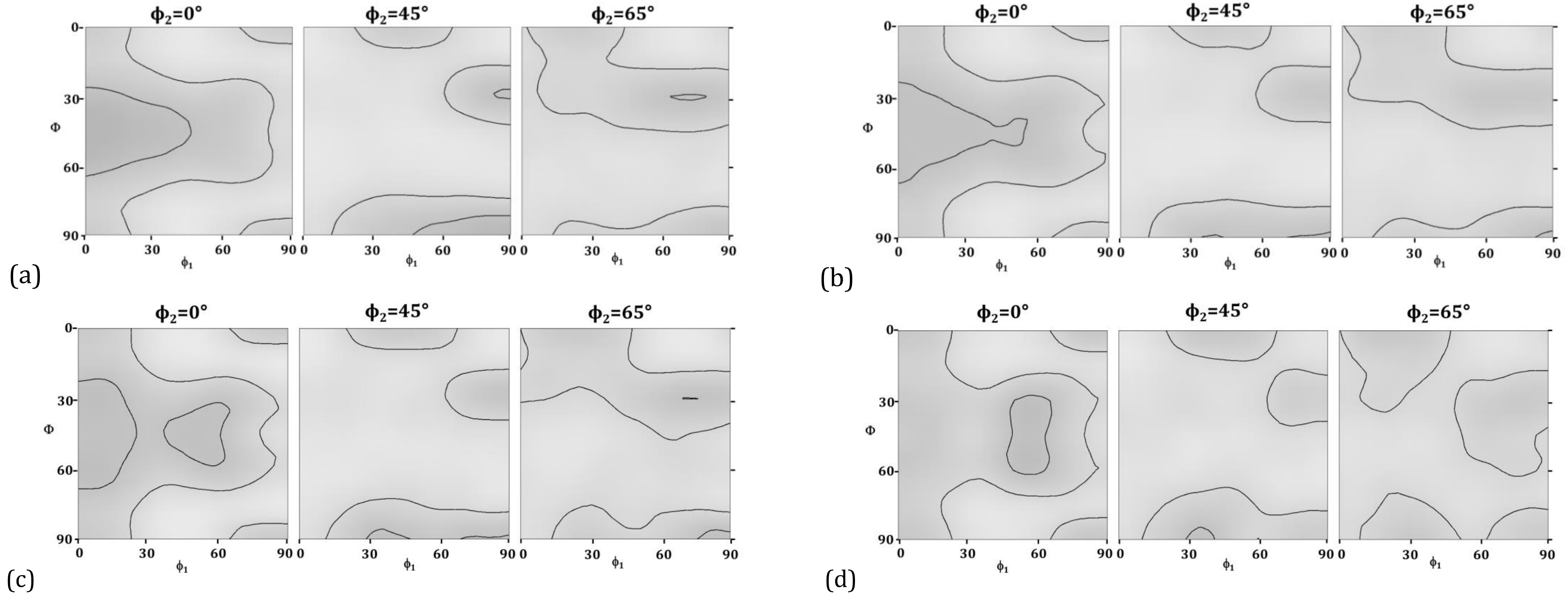

Figure 6.14: ϕ_2 = 0°, 45° and 65° orientation distribution function sections of γ after annealing at (a) 700 °C, (b) 750 °C, (c) 800 °C and (d) 850 °C. Contour levels = 0.5×

Fig. 6.15 shows the ODF sections presenting the orientations of the γ grains segmented into the reverted/recovered and the recrystallised fractions after annealing between 600-650 °C (Figs. 6.4a-6.4c). After annealing, the reverted/recovered γ grains return the formation of strong micro-texture orientations: G_γ/Br_γ and $(213)[\bar{1}\bar{5}2]_\gamma$ after annealing at 600 °C (Fig. 6.15a), G_γ, Br_γ, $(214)[\bar{1}\bar{2}1]_\gamma$ orientations after annealing at 625 °C (Fig. 6.15c) and C_γ, Br_γ orientations after annealing at 650 °C (Figs. 6.15e). The recrystallised γ grains have similar orientations compared to the reverted/recovered γ grains orientations after annealing at 600, 625 and 650 °C (Figs. 6.15b, 6.15d and 6.15f). This indicates that the recrystallised γ grains nucleate from the reverted/recovered γ grains inheriting similar orientations. Similar recrystallisation behaviour was reported during the annealing of other metastable austenitic steels [191].

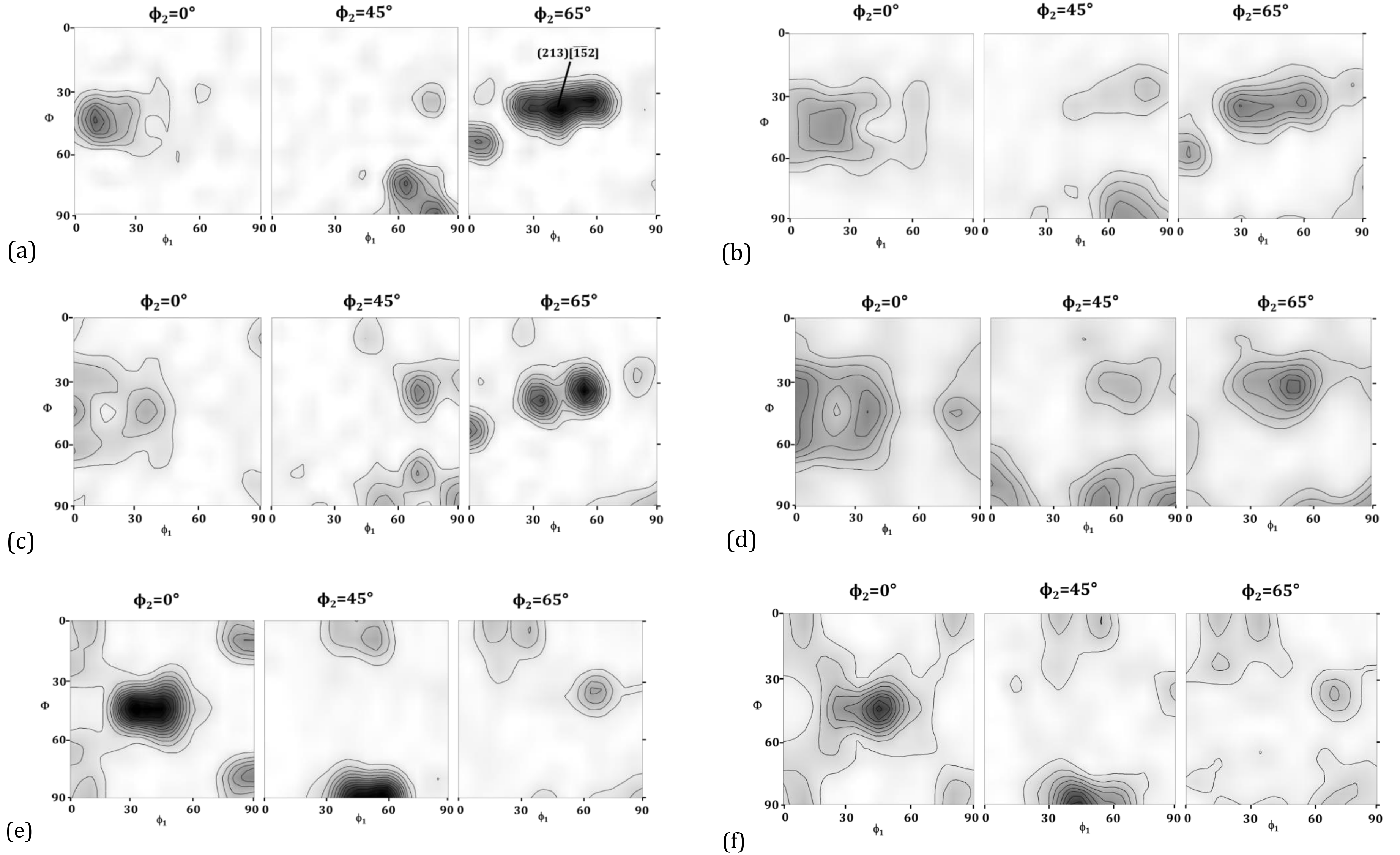

Figure 6.15: ϕ_2 = 0°, 45° and 65° orientation distribution function sections of γ grains segmented into the (a, c, e) reverted/recovered and (b, d, f) recrsytallised fractions after annealing at (a, b) 600 °C, (c, d) 625 °C and (e, f) 650 °C. Contour levels = 0.5×

6.4 Conclusions

The characterisation of the 42% cold-rolled and isochronally annealed samples using electron back-scattering diffraction and transmission electron microscopy led to the following conclusions:

(1) Upon isochronal annealing to 650 °C for 300 s, the reversion of deformation-induced ε and α′-martensite to reverted/recovered γ is observed. The reverted/recovered γ showed the formation of fine twins.

(2) During heating, the nucleation of new γ grains takes place at the boundary of two of the reverted/recovered γ grains after annealing at 600 °C. Upon annealing to 700 °C, the completion of γ recrystallisation is noted with γ grain coarsening taking place upon annealing to temperatures higher than 700 °C.

(3) The calculated value of activation energy for γ grain growth is lower than the lattice self-diffusion energy of γ indicating that γ grain growth takes place via grain boundary diffusion mechanism.

(4) The ε and α′-martensite grain orientations produced the orientations of the reverted/recovered γ grains via phase transformation following the Shoji-Nishiyama and Kurdjumov-Sachs orientation relationships, respectively. Upon γ grain segmentation, the recrystallised γ grains were observed to nucleate with orientations similar to the reverted/recovered γ grain orientations.

CHAPTER 7 EFFECT OF MICROSTRUCTURE ON THE TENSILE BEHAVIOUR OF HIGH MANGANESE STEEL

The high Mn steel was characterised via digital image correlation and electron back-scattering diffraction. The true stress-strain curves of the cold-rolled and 500, 625, 650, 700 and 800 °C samples are presented along with their corresponding strain hardening curves. The digital image correlation results show strain localisation due to the γ phase transformation in the 625, 650, 700 and 800 °C samples upon tensile testing (Section 7.2). The electron back-scattering diffraction maps of the post-mortem microstructures after tension are also presented. The study of micro-texture evolution before and after tensile testing was also undertaken. Finally, the mode of fracture was also analysed.

7.1 Mechanical properties after cold rolling and annealing

Figs. 7.1a and 7.1b are the true stress-strain and strain hardening curves, respectively, for the cold-rolled and the 500, 625, 650, 700 and 800 °C samples. The tensile properties are listed in Table 7.1. The error in the tensile testing machine was 0.5%.

The cold-rolled and the 500 °C samples are observed to fracture at 0.02 true strain, immediately after reaching the YS of 1080 and 1075 MPa (Table 7.1), respectively. The cold-rolled and incompletely recovered states of the predominantly α′-martensite microstructures (Figs. 6.2a and 6.2b) are unable to undertake further deformation, in the cold-rolled and 500 °C samples, respectively, leading to very low elongation values.

In contrast, the shape of the true stress-strain curves for the 625 and 650 °C samples are different from those for the cold-rolled and 500 °C samples (Fig. 7.1a). The initial microstructure consisting of reverted/recrystallising metastable γ and α′-martensite was formed after annealing at 625 and 650 °C (Figs. 6.2c and 6.2d). Upon tension, YS is observed at 810 and 732 MPa (Table 7.1), correspondingly, followed by a linear increase in the stress values reaching the UTS values of 1273 and 1259 MPa (Table 7.1), respectively. Similar trends in the true stress-strain curves were obtained in high Mn steels with an initial microstructure comprising dual phases [155]. In Ref. [155], upon tension the formation of ε and α′-martensite at γ grain boundaries takes place followed by the transformation of the adjacent γ and ε-martensite to α′-martensite. Upon the tension of an Fe-10.6Mn-0.17C-0.5Mo steel annealed at 850 °C for 3 min followed by water quenching, the transformation of metastable lamellar γ to α′-martensite was observed [243]. The tension of the same steel after further annealing at 200 °C for 10-40 min reduced the tendency of α′-martensite formation due to the partition of C in γ, which increases γ stability.

Based upon the slope, the true stress-strain curves and the corresponding strain hardening curves for the 625 and 650 °C samples can be classified into the Regions A_{625} (blue circle, Fig. 7.1a, true strain 0-0.015), A_{650} (orange circles, Fig. 7.1a, true strain 0-0.015), B_{625} (blue triangles, Fig. 7.1a, true strain 0.02-0.15), B_{650} (orange triangles, Fig. 7.1a, true strain 0.02-0.15) and C_{625} (blue stars, Fig. 7.1a, true strain 0.2-0.23), C_{650} (orange stars, Fig. 7.1a, true strain 0.25-0.26) comprising: (i) the elasto-plastic transition (Region A), (ii) uniform strain hardening rate (Region B) and (iii) a reduction in the strain hardening rate with increasing true strain (Region C), respectively.

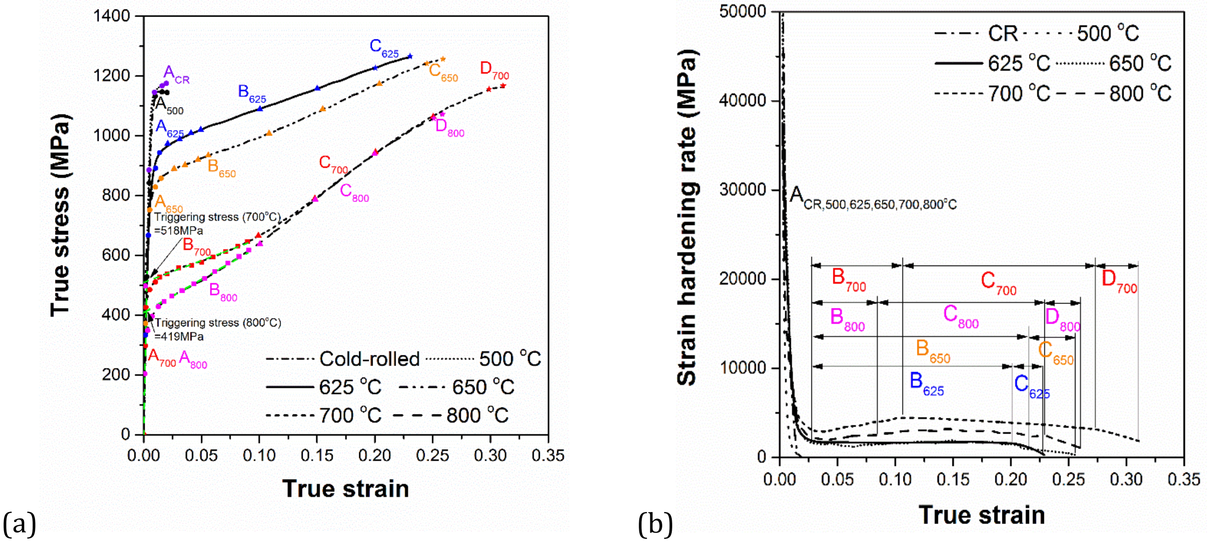

(a) (b)

Figure 7.1: (a) True stress-strain and (b) strain hardening rate curves for the cold-rolled and 500, 625, 650, 700 and 800 °C samples.

Table 7.1 True tensile properties of the cold-rolled and 500, 625, 650, 700 and 800 °C samples.

Tensile properties	**Sample condition**					
	Cold-rolled	500 °C	625 °C	650 °C	700 °C	800 °C
Yield stress (MPa)	1080 ± 3	1075 ± 4	810 ± 5	732 ± 2	465 ± 4	360 ± 2
Ultimate true tensile strength (MPa)	1135 ± 4	1150 ± 3	1237 ± 3	1259 ± 4	1121 ± 3	1067 ± 3
Uniform true elongation	0.02 ± 0.0012	0.02 ± 0.0014	0.23 ± 0.003	~0.26 ± 0.004	0.31 ± 0.003	~0.26 ± 0.002

The Region A with decreasing strain hardening rate shows similar characteristics for all the sample conditions. The reduction in the strain hardening rate in Region A is due to elasto-plastic transition accompanied by the initiation of partial slip in γ via the motion of Shockley partial dislocations. The Region B with the uniform strain hardening rate in the 625 and 650 °C samples is due to the phase transformation of γ to ε and α′-martensite. In-situ neutron diffraction during monotonic uniaxial tensile loading of the present steel cold-rolled and subsequently annealed at 900 °C also displayed the decrease in the fraction of γ with an increase in the fraction of ε and α′-martensite at engineering strains greater than ≈0.025 and ≈0.05, respectively [24]. The formation of deformation-induced ε and α′-martensite leads to the reduction in the mean free path of dislocations which results in strain hardening. Also in Region B, the deformation of pre-existing retained α′-martensite takes place. The Region C for the 625 and 650 °C samples shows a reduction in the strain hardening rate due to the exhaustion of the existing strain hardening mechanisms.

Tensile testing of the 700 and 800 °C samples results in the yielding of the recrystallised metastable γ at 465 and 360 MPa (Table 7.1), correspondingly, followed by a slow stress rising region up to a UTS of 1121 and 1067 MPa (Table 7.1), respectively. The intersection of the linearly extrapolated elastic modulus and the tangent drawn to the slow rise in stress region is defined as the triggering stress [208] and was calculated to be ≈518 and ≈419 MPa for the 700 and 800 °C samples (Fig. 7.1a), respectively. Similar shape of the true stress-strain curve was reported for an Fe-15Mn-3Al-3Si steel with initial microstructures comprising recrystallised γ, α′ and ε-martensite [21]. The triggering stress calculated for the 700 °C sample is higher than that for the 800 °C sample. This is due to the presence of relatively coarse grains in the 800 °C sample, which provides more grain boundary area for the nucleation and subsequent growth of ε and α′-martensite compared to the 700 °C sample.

The YS of the 800 °C sample containing a relatively higher area fraction of ε and α′-martensite formed upon quenching after annealing is lower than that of the 700 °C sample due to the coarsening of the γ grain size from 1.9 ± 1.4 to 4.3 ± 2.7 μm upon annealing at 800 °C (Fig. 6.6). Alternatively, the total elongation is the largest after annealing at 700 °C. This is due to the higher γ area fraction available for phase transformation to deformation-induced ε and α′-martensite leading to a pronounced strain hardening and higher total elongation.

The uniform true elongation obtained for the 800 °C sample is lower in comparison to the 700 °C sample. This was due to a relatively higher area fraction of ε and α′-martensite plate intersections, as well as of γ/α′-martensite interface for the 800 °C sample compared to the 700 °C sample. The presence of interfaces between the α′-martensite was associated with the nucleation and coalescence of cracks upon tension [118].

The true stress-strain curves (Fig. 7.1a) and the corresponding strain hardening rate curves (Fig. 7.1b) for the 700 and 800 °C samples can be roughly divided into the Regions A_{700} (red circle, true strain 0-0.01), A_{800} (fuchsia circle, true strain 0-0.01), B_{700} (red squares, true strain 0.015-0.09), B_{800} (fuchsia squares, true strain 0.015-0.09), C_{700} (red triangles, true strain 0.1-0.25), C_{800} (fuchsia triangles, true strain 0.1-0.2), D_{700} (red stars, true strain 0.3-0.31) and D_{800} (fuchsia stars, true strain 0.25-0.26) comprising: (i) the elasto-plastic transition, (ii) increasing strain hardening rate, (iii) decreasing strain hardening rate and (iv) drastic reduction in the strain hardening rate with true strain, respectively.

The slow rising stress Region B in the 700 and 800 °C samples is due to the onset of the phase transformation of γ to ε and α′-martensite. Similar slow rising stress regions was observed in metastable austenitic steels upon tension [244]. The slope of the Region B in the 700 and 800 °C samples is observed to be different. This is due to the presence of high area fraction of ε and α′-martensite formed upon quenching after annealing at 800 °C compared to the 700 °C sample, which leads to the load partition between γ and ε and α′-martensite in the 800 °C condition. Due to the formation of deformation-induced ε-martensite in the Region B for the 700 and 800 °C samples, the γ is subdivided which increases the strain hardening rate. The Region C for the 700 and 800 °C samples is due to the strain hardening caused by the newly formed deformation-induced ε and α′-martensite along with deformation of the ε and α′-martensite. Also, there is a reduction in the rate of ε and α′-martensite formation in the Region C compared to the Region B for both the conditions. This leads to a decreasing slope in the Region C compared to Region B for the 700 and 800 °C samples which are caused by the decrease in the amount of γ available for transformation to ε and α′-martensite along with the deformation of newly formed α′-martensite. The Region D for these samples is similar to the Region C for the 625 and 650 °C samples where strain localisation due to fracture occurred.

The distinct difference in the duration and shape of the strain hardening rate curves in the Region B_{625} and B_{650} in the 625 and 650 °C samples compared to those of 700 and 800°C samples is due to the combined effects of the additional strain hardening capacity from the pre-existing α′-martensite [155] and from the transformation of γ to ε and α′-martensite. The strain hardening Region B in the 700 and 800 °C samples is only associated with the transformation of γ to ε and α′-martensite. However, the strain hardening Region C in the 700 and 800 °C samples is predominantly due to the deformation-induced phase transformation of ε-martensite to α′-martensite along with the deformation of the remnant ε-martensite and newly formed α′-martensite.

The measured value of Young's modulus for the cold-rolled, 500, 625, 650, 700 and 800 °C samples are 201, 198, 197, 196, 194 and 195 GPa, respectively. This is due to the presence of a mixture of phases (γ, ε and α′-martensite) with different crystal structures and in varying fractions which affects

Young's modulus. The Youngs's modulus of α′-martensite is greater than that of γ due to the coupling of the electron spin moments owing to the ferromagnetic nature of α′-martensite [245]. Thus, on annealing, a decrease in Young's modulus is observed due to the decrease of the α′-martensite fraction. It can be noted from Table 7.1 that the best strength-ductility combination is achieved for the 625 and 650 °C samples.

In relation to the mechanical properties in the literature (Chapter 2, Table. 2.7), the present steel cold-rolled to 42% thickness reduction shows slightly lower YS compared to the same steel cold-rolled to 45% thickness reduction [159]. The present steel after annealing at 700 °C, shows slightly higher YS compared to a single phase Fe-16.8Mn-1.5Al-0.03Si-0.32C steel (YS = 434 MPa) [9]. The UTS achieved for the present steel after annealing at 700 °C is much higher than for the Fe-16.8Mn-1.5Al-0.03Si-0.32C steel (UTS = 1121 MPa). This is ascribed to the formation of both ε and α′-martensite in the present steel compared to the Fe-16.8Mn-1.5Al-0.03Si-0.32C steel in which only the formation of ε-martensite takes place [9]. The hard α′-martensite formed leads to the increase in UTS compared to the Fe-16.8Mn-1.5Al-0.03Si-0.32C steel. However, the Fe-16.8Mn-1.5Al-0.03Si-0.32C steel annealed at 600 °C shows much higher total elongation (≈0.54) compared to the present steel annealed at 700 °C. The deformation-induced α′-martensite can act as nucleation sites for cracks which decreases the elongation [41, 42].

The YS of the high Mn steel after annealing at 800 °C is lower than after annealing at 700 °C due to γ grain coarsening from 1.9 ± 1.4 μm to 4.3 ± 2.7 μm (Chapter 6, Fig. 6.6). Tomota *et al.* [246] reported a higher YS for the annealed samples having a relatively coarse γ grain size due to the higher fraction of plate-like ε-martensite formed upon quenching after annealing. However, in the present study, annealing at 800 °C returns a higher fraction of ε and α′-martensite and lower YS than after annealing at 700 °C.

Alternatively, the total elongation is the largest after annealing at 700 °C due to the higher γ fraction available for phase transformation to deformation-induced ε and α′-martensite. The total elongation obtained after annealing at 800 °C is lower than the above condition on account of the relatively higher fractions of ε and α′-martensite and γ/ε-martensite and γ/α′-martensite interfaces which contribute to the nucleation and coalescence of cracks upon tensile testing [41]. The above results indicate that once γ is fully recrystallised and polygonised, the initial γ grain size has a more significant effect on YS than the ε and α′-martensite phase fractions. Alternatively, the initial ε and α′-martensite fractions tend to affect the total elongation.

7.2 DIC of cold-rolled and annealed samples upon uniaxial tension

The distribution of axial and shear true strains along the entire gauge length and up to the UTS of the cold-rolled and 500, 625, 650, 700 and 800 °C samples is presented in Figs. 7.2-7.8.

For the cold-rolled and 500 °C samples (Fig. 7.2), the distribution of axial true strain is nearly uniform up to 0.005 true strain. This is followed by the onset of localised plastic deformation and subsequent strain localisation above 0.005 true strain, respectively, resulting in higher axial true strains compared to the average true strain values across the gauge length. The onset of local strain concentration upon tension for the cold-rolled sample can be attributed to the microstructures containing predominantly α′-martensite in the cold-rolled condition. Upon tension, the strain localisation in the 500 °C sample is due to the α′-martensite in the incomplete recovered state. Similar strain localisation was noted for an Fe-21Mn-2.5Si-1.6Al-0.11C steel upon uniaxial tensile testing [41].

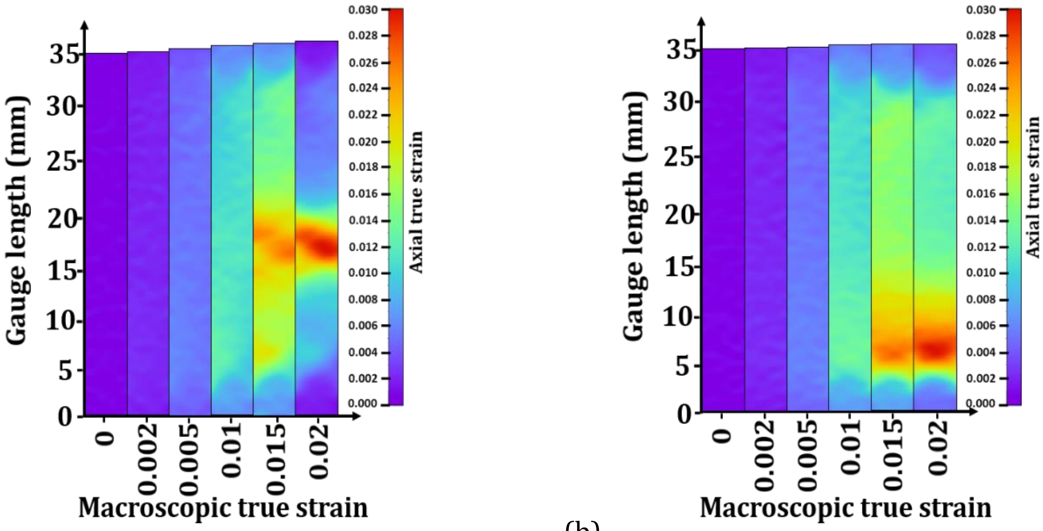

(a) (b)

Figure 7.2: Digital image correlation axial true strain distribution maps of the (a) cold-rolled and (b) 500 °C samples.

Upon tensile testing, the axial true strain distribution for the 625 °C sample (Fig. 7.3a) is observed to show strain localisation occurring at the fracture. In Fig. 7.3b the axial true strain distribution at 0.005 and 0.01 true strains in Region A_{625} shows higher strain regions uniformly distributed throughout the gauge length. As the initial microstructure for the 625 °C sample contains both γ and remnant α′-martensite which are distributed uniformly (Fig. 6.3b), the localised transformation of γ to ε and α′-martensite occurs, but overall the transformation occurs uniformly across the gauge length which can lead to the formation of these uniformly distributed high strain regions across the gauge length. Eskandari *et al.* [41] reported strain localisation before macroscopic yielding in an Fe-21Mn-2.5Si-1.6Al-0.11C steel subjected to tension and ascribed it to the γ to ε-martensite transformation. The appearance of more pronounced strain concentration region in the top part of the gauge section between 0.005 and 0.015 true strain for Region A_{625} in Fig. 7.3b is due to the stress concentration associated with the grip ends. The Region B_{625} shows axial and shear strains (Fig. 7.3a, 7.3c) which are higher in the upper part of the gauge length. The occurrence of load partitioning between γ and newly formed deformation-induced martensite along with the deformation of γ and ε-martensite is the reason for the observed strain localisation. The DIC investigation of strain localisation via the formation and propagation of Lüders bands in an Fe-7Mn-0.14C-0.23Si steel containing initial microstructure comprising γ and α′-martensite were also reported [164, 247, 248]. In that study, the nucleation of Lüders bands at one end of the grip occurred which subsequently propagated towards the other end. Similar to the present study, the strain localisation in Lüders bands was associated with the onset of the deformation-induced α′-martensite formation. μ-DIC strain mapping showed higher strains in γ compared to α′-martensite indicating strain partitioning during tensile deformation of an Fe-12Mn-3Al-0.05C steel [166]. This was attributed to the transformation of γ to ε and α′-martensite and the lower rate of dynamic recovery in γ. Upon tension to 5 and 7% strains, the γ accommodated the majority of the strain. However, on further strain α′-martensite accommodated higher strains compared to γ.

In the Region C_{625} at 0.23 true strain, the local strain concentration at the centre of the gauge length is observed due to fracture. Increase in the shear strain distribution along the gauge length is detected in the B_{625} Region due to the transformation of γ to deformation-induced ε and α′-martensite (Fig. 7.3c). Fig. 7.3d shows the distribution of axial strain across the line AA′ (Fig. 7.3a). For the ≈0.01-0.2 macroscopic true strains, the axial strains are witnessed to increase between 0 and ≈4 mm (in green, Fig. 7.3d) followed by a plateau between ≈4 and 20 mm (in orange, Fig. 7.3d). After 20 mm the axial strain is noted to decrease (in blue, Fig. 7.3d) with an increase in the gauge length.

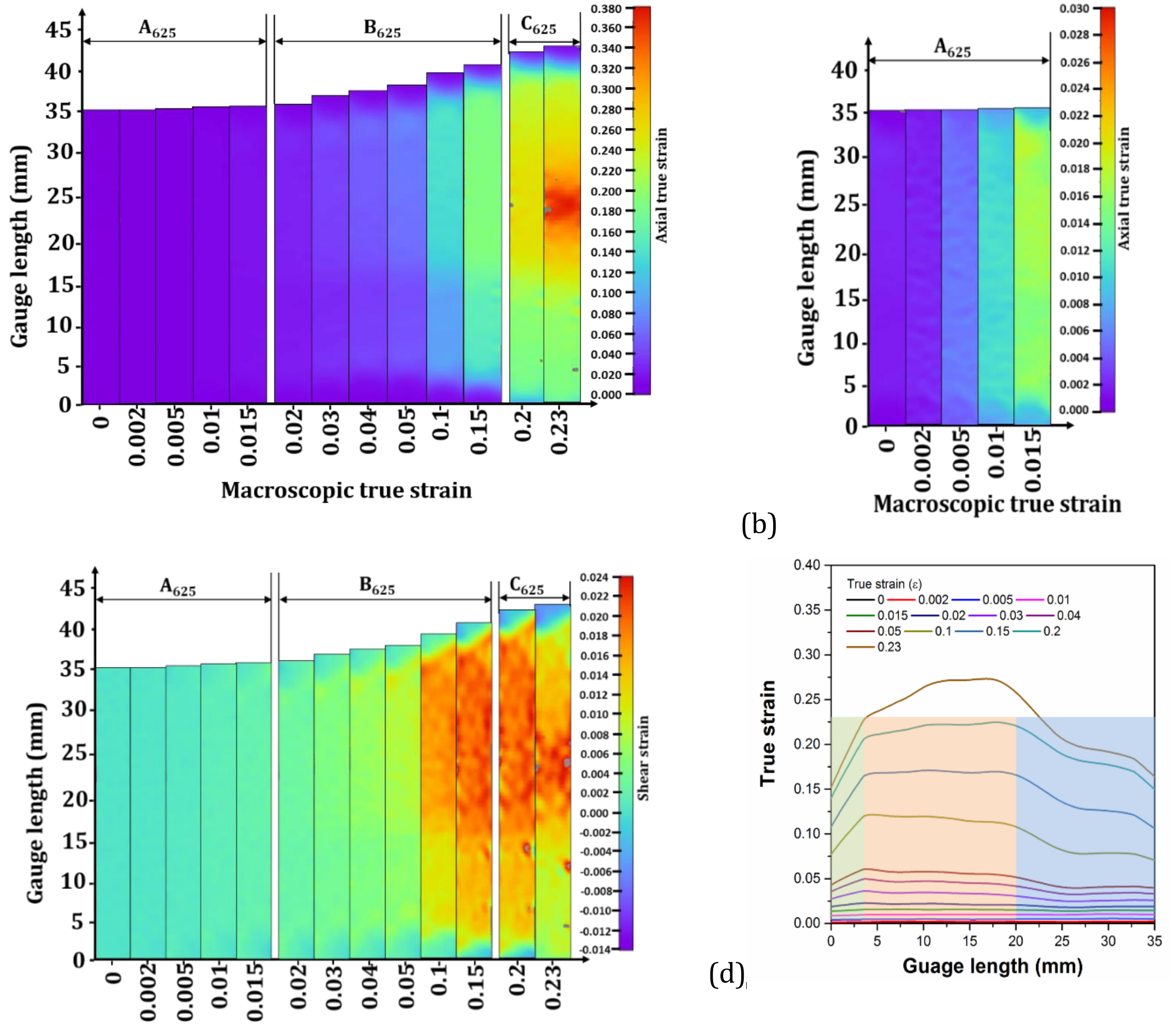

(a) (b) (c) (d)

Figure 7.3: Digital image correlation maps for the 625 °C sample presenting the distribution of (a, b) axial true strain, (c) shear strain and (d) distribution of axial true strain along the line AA′ (Fig. 7.3a). Fig. 7.3b is the scaled axial true strain distribution of the Region A_{625} in Fig. 7.3a.

Upon tension, the axial true strain distribution for the 650 °C sample in Fig. 7.4a shows non-uniform strain distribution along the gauge length similar to the 625 °C condition. In Fig. 7.4a and 7.4c between the axial true strains 0.15 and 0.26, the regions associated with low strain concentration (in blue) in the top part of the gauge length is due to the misindexing of pixels in DIC due to tearing off the paint from the surface. In the Region A_{650}, the true strain distribution at 0.1 true strain shows strain localisation (Fig. 7.4b). This could be due to the strain partitioning between the hard α′-martensite and soft recrystallised γ (Fig. 6.3c). The local regions showing high shear strain concentration distributed uniformly throughout the gauge length can be observed in the Region B_{650}

(Fig. 7.4c). Similar to the 625 °C condition, load partition between the γ and ε/α′-martensite takes place locally to accommodate the strain during tension which leads to strain localisation. Subsequent axial and shear strain localisation observed in the Region C_{650} is due to fracture (Figs. 7.4a and 7.4c). Fig. 7.4d shows the distribution of the axial true strain along the line AA′ in Fig. 7.4a.

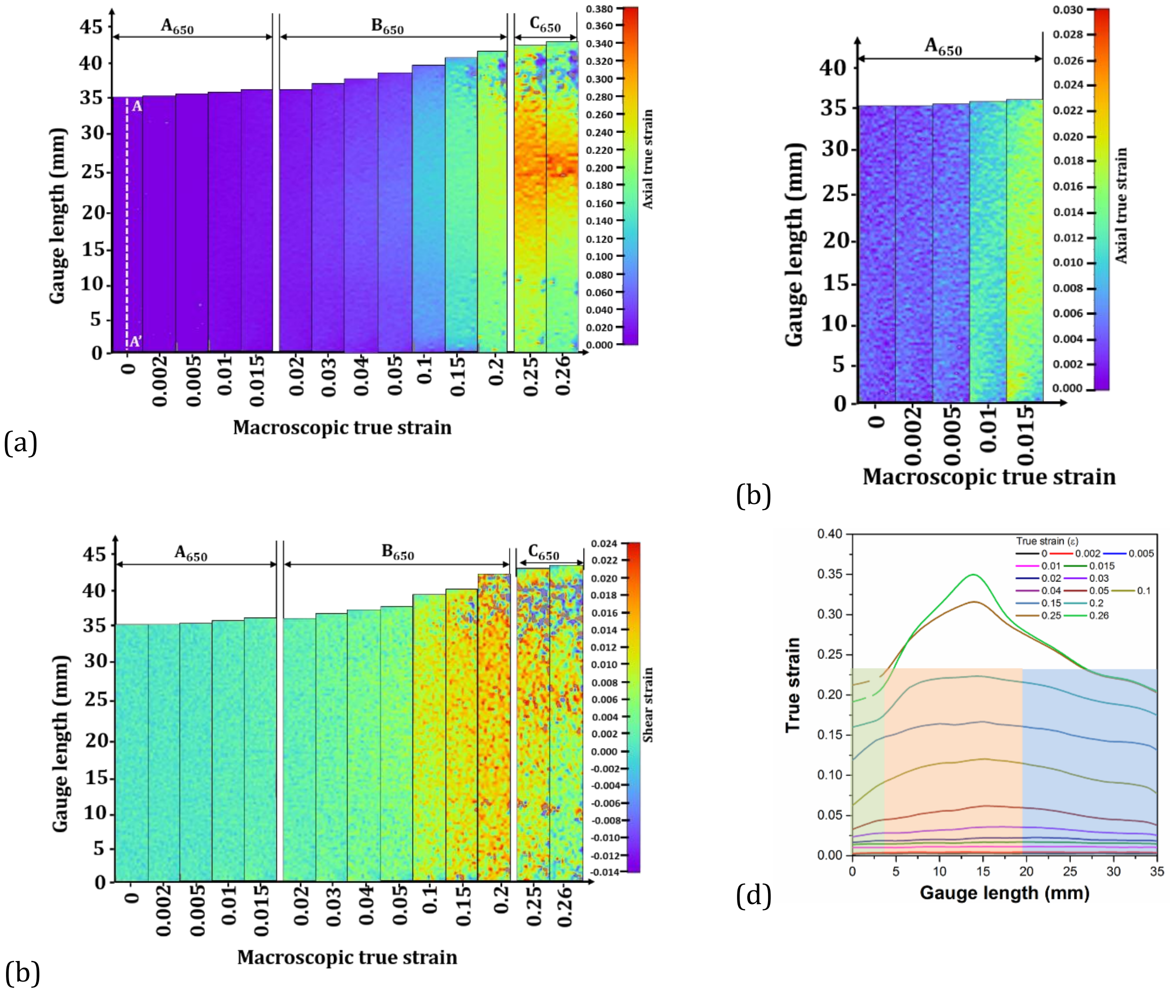

Figure 7.4: Digital image correlation maps for the 650 °C sample presenting the distribution of (a, b) axial true strain, (c) shear strain and (d) distribution of axial true strain along the line AA′ (Fig. 7.4a). Fig. 7.4b is the scaled axial true strain distribution of the Region A_{650} in Fig. 7.4a. The regions of low strain concentration in the upper part of the gauge length in Figs. 7.4a and 7.4c are due to tearing off the paint.

In the 650 °C sample, for the 0.05-0.2 macroscopic true strains, the axial true strain along the gauge length is detected to increase between 0-5 mm (in green, Fig. 7.4d) followed by a nearly constant region between 5 and 20 mm (in orange, Fig. 7.4d). This is followed by a decline in the axial true strain from 20-35 mm (in blue, Fig. 7.4d) along the gauge length. The higher strain region can be ascribed to the formation of deformation-induced ε and α′-martensite. However, at 0.26 macroscopic true strain, the local strain concentration at the centre of the gauge length due to fracture is observed (Fig. 7.4c).

For the 700 °C sample, Fig. 7.5a shows the distribution of axial true strain along the gauge length with increasing strain. Strain localisation can be observed at 0.01 true strain at the end of the Region A_{700} (Fig. 7.5b) and throughout the Region B_{700} (Figs. 7.5c). An example of strain localisation is the increase of local strain to ≈0.033 at the ends of the gauge length for the macroscopic strain of 0.02. This strain localisation is due to the onset of the transformation of γ to deformation-induced ε and α′-martensite. Similar observations were reported during the tensile testing of an Fe-21Mn-2.5Si-1.6Al-0.11C steel [41]. In that study, strain localisation was proposed due to the local transformation of γ to deformation-induced α′-martensite which was verified by magnetic measurements along the gauge length [41].

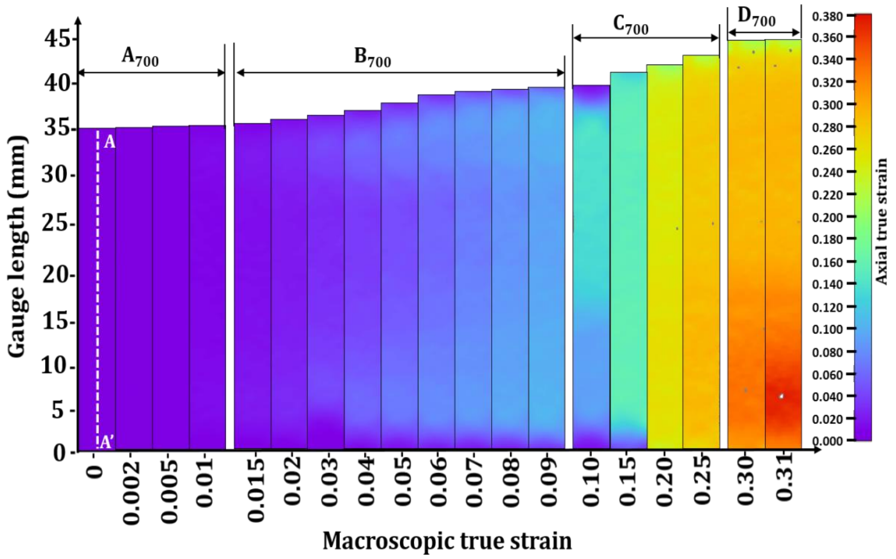

(a)

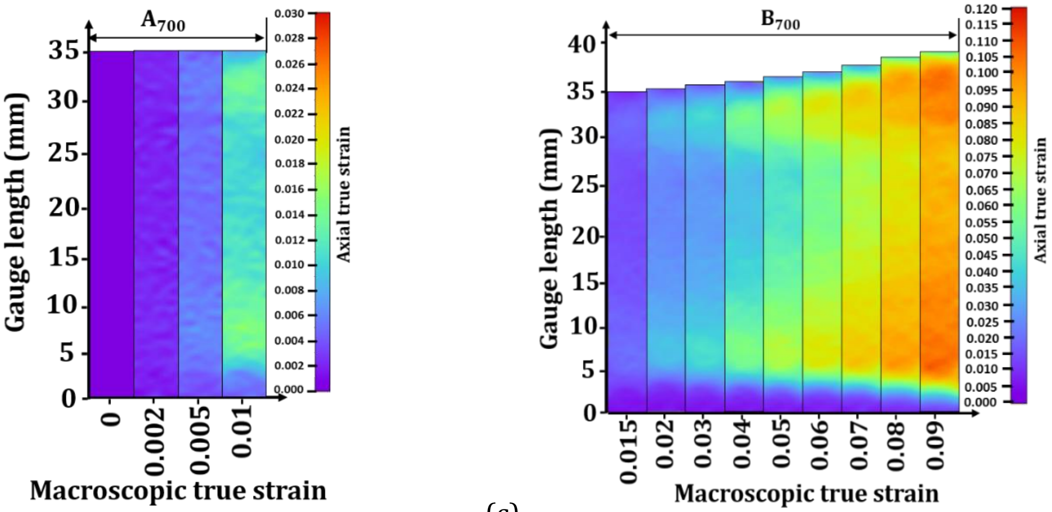

(b) (c)

Figure 7.5: Digital image correlation maps for the 700 °C sample presenting the distribution of (a, b, c) axial true strain. Figs. 7.5b and 7.5c are the scaled axial true strain distribution of the Regions A_{700} and B_{700}, correspondingly, of Fig. 7.5a.

The shear strain distribution in the Region C_{700} shows a nearly uniform strain distribution (Fig. 7.6a). This can be due to the deformation of ε and α′-martensite along with the further transformation of γ to ε and α′-martensite along the gauge length. The strain concentration due to fracture can be observed at the lower end of the gauge section in the Region D_{700} in Fig. 7.6a. Compared to the 625 °C condition, slightly higher shear strains are observed in the 700 °C sample at the macroscopic strain of 0.05 in the Region B_{700}. Also, at 0.1 true strain, localisation of the shear strains at the ends of the gauge length is observed for the 700 °C sample in the Region B_{700} as compared to the 625 °C sample where localisation is observed at the top region of the gauge length at strain 0.1 in the Region B_{625}. This is due to the higher fraction of γ available for the transformation to ε and α′-martensite in the 700 °C sample. Also, for the 625 °C sample, the majority of the ε and α′-martensite formation occurs during the strain hardening Region B_{625} whereas for the 700 °C sample the onset of martensite transformation takes place in the slowly rising stress Region B_{700} and continues in the Region C_{700}.

Fig. 7.6b shows the distribution of the axial true strains along the line AA′ in Fig. 7.5a for various macroscopic true strains. It is apparent that up to ≈0.1 macroscopic true strain, the axial true strains between ≈0-9 mm and ≈27-35 mm (in grey and orange, Fig. 7.6b) are higher near the grip ends than in the middle of the gauge length between ≈9-27 mm (in green, Fig. 7.6b). The axial true strains are lowest at 0 and 35 mm of the gauge length. The local true strain maxima at ≈3 and ≈33 mm are followed by a decrease in the axial true strains up to ≈9 and ≈27 mm (in orange, Fig. 7.6b). Thereafter, the true strain distribution remains constant across the ≈9-27 mm of the gauge length (light green region, Fig. 7.6b). Similar propagation of high strain regions along the gauge length is observed for an Fe-21Mn-2.5Si-1.6Al-0.11C steel between 0.5-0.58 macroscopic true strains upon tension [41]. For the 0.15-0.25 macroscopic true strains, the axial true strain distribution increases to ≈3 and ≈33 mm along the gauge length (in blue, Fig. 7.6b) followed by a nearly constant value between ≈3-33 mm of the gauge length (in aqua, Fig. 7.6b). Beyond macroscopic true strain of 0.3 high strain concentration is observed at ≈30 mm of the gauge length due to fracture.

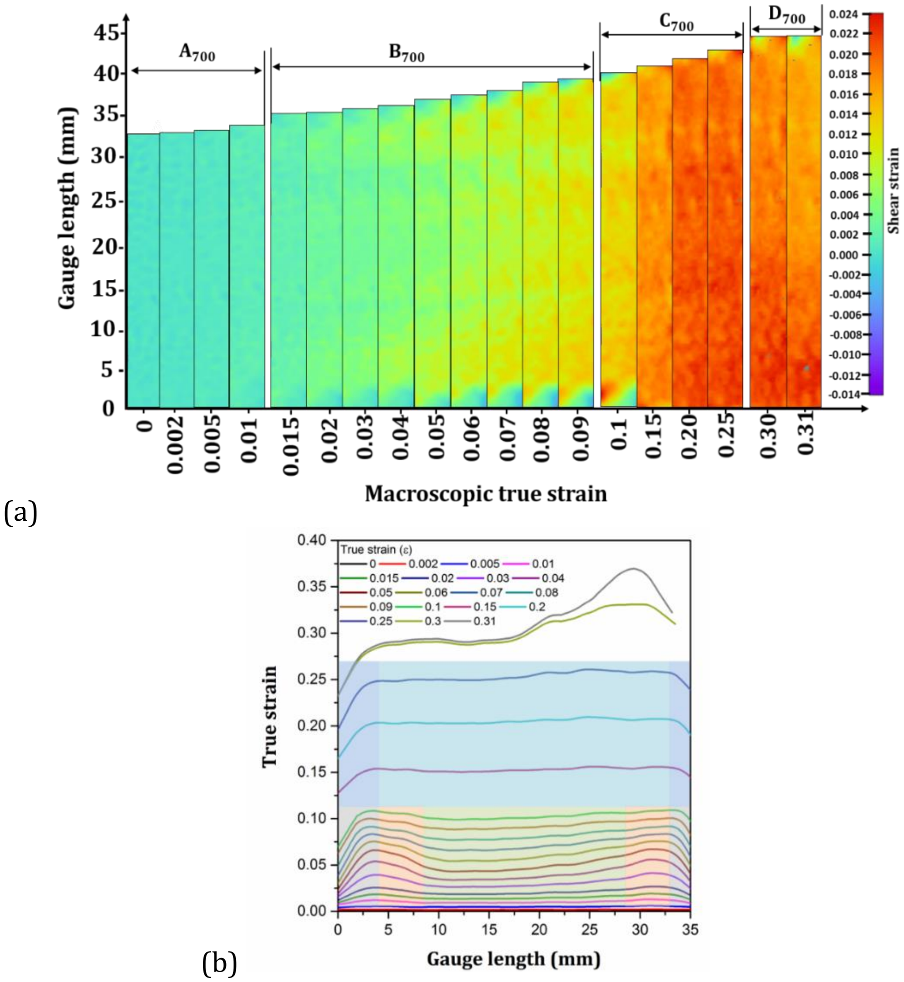

(a)

(b)

Figure 7.6: Digital image correlation maps for the 700 °C sample presenting the distribution of (a) shear strain and (b) axial true strain along the line AA′ in Fig. 7.5a. Regions in grey, blue show increasing, orange show decreasing, green, aqua show uniform axial true strain distribution along the gauge length in Fig. 7.6b.

The total fraction of γ decreases at the gauge end due to the early onset of phase transformation by the stress concentration associated with the grip ends. Thus, the γ at the centre of the gauge length between 3-33 mm is activated for the phase transformation which manifests as a local strain propagation. Once the high strain region nucleates at 3 and 33 mm along the gauge length; it can propagate at stress equal to/lower than the nucleation stress resulting in slow rising stress [249]. The local strain in front of the propagating high strain region (in orange, Fig. 7.6b) is observed to be lower than the macroscopic true strain. This is due to the local partition of higher strain into the γ transforming into ε and α′-martensite in the high strain regions resulting in a lower strain in the nearby γ. The high strain regions at ~3 and ~33 mm along the gauge length propagate towards the centre of the gauge length until the macroscopic true strain becomes approximately equal throughout the gauge length. This corresponds to the end of the Region B_{700}. In the Region C_{700}, the formation and subsequent deformation of the newly formed α′-martensite take place.

Fig. 7.7a shows the distribution of axial true strain along the gauge length with macroscopic true strain for the 800 °C sample. Compared to the 700 °C sample, strain localisation is observed in the lower end of the gauge length at 0.01 macroscopic true strain in the 800 °C sample at the end of the Region A_{800} (Fig. 7.7b). However, a higher strain concentration is visible at the lower end of the gauge length compared to the upper end at 0.01 true strain (Fig. 7.7b). This could be due to the stress concentration associated with the grips. In the Region B_{800} between 0.05-0.09 macroscopic true strains, the strain localisation occurs at both the centre and at the end of gauge lengths (Fig. 7.7c).

As phase transformations start at the ends of the gauge sections at a macroscopic true strain of 0.01 in the Region A_{800}, the deformation-induced phase transformation starts in the centre of the gauge length at true strains between 0.05-0.09. Compared to the Region B_{800}, a significant increase in the shear strains is observed in the Region C_{800} at a macroscopic true strain of 0.2. This is due to the activation of the remnant areas containing γ for transformation to ε and α′-martensite. Finally similar to the 700 °C condition, strain localisation is detected to take place at bottom of the gauge length due to fracture in the Region D_{800}.

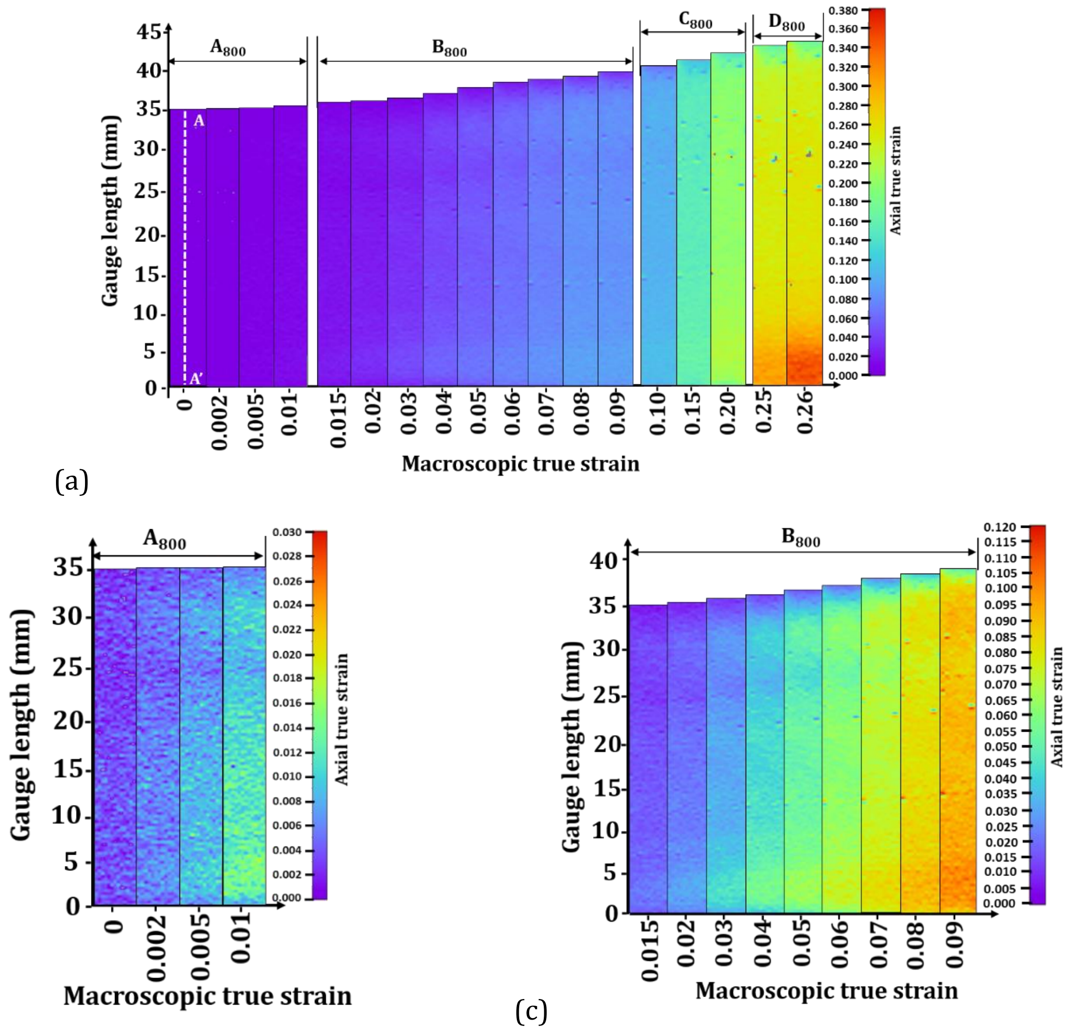

(a)

(b)

(c)

Figure 7.7: Digital image correlation maps for the 800 °C sample presenting the distribution of (a, b, c) axial true strain. Figs. 7.7b and 7.7c is the scaled axial true strain distribution of the Regions A_{800} and B_{800}, correspondingly, of Fig. 7.7a.

The distribution of shear strains and axial strains along the line AA′ (Fig. 7.7a) in the gauge length is presented in Figs. 7.8a and 7.8b, respectively. Up to 0.1 macroscopic true strain, local maxima in the axial true strain distribution is observed at 3 mm of the gauge length (in grey, Fig. 7.8b) followed by a slight decrease in the axial strain between 3 and 8 mm (in orange, Fig. 7.8b). Beyond ≈8 mm of the gauge length, an increase in the axial true strain is observed with the increase in the gauge length (in green, Fig. 7.8b). This indicates that strain localisation at the lower end of the gauge length due to the transformation of γ to deformation-induced ε and α′-martensite. For the 0.15 and 0.20 macroscopic true strains, the axial strain distribution is nearly constant between ~3 and 33 mm of the gauge length (in aqua, Fig. 7.8b). The axial strain distribution is lowest at the ends of the gauge length (in blue, Fig. 7.8b). Beyond, 0.20 macroscopic true strains high strain concentration is detected at ~31 mm along the gauge length due to the fracture of the sample.

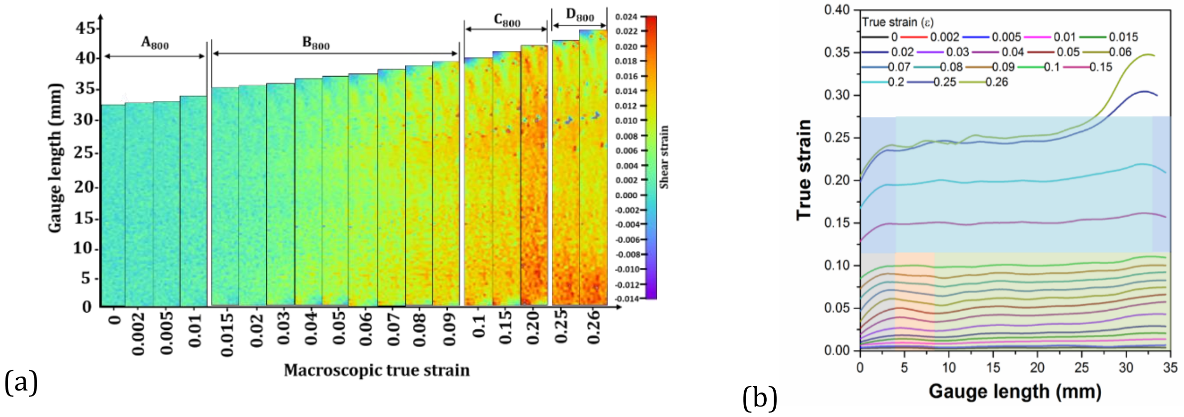

Figure 7.8: Digital image correlation maps for the 800 °C sample presenting the distribution of (a) shear strain and (b) axial true strain along the line AA′ in Fig. 7.7a. Regions light grey, light blue, light green show increasing, light orange show decreasing and light aqua show uniform axial true strain distribution along the gauge length in Fig. 7.8b.

A higher strain accumulation at the bottom of the gauge section may indicate a higher volume fraction of α′-martensite [41]. This leads to the presence of a greater number of crack nucleation sites as the intersection of α′-martensite grains/platelets was reported [41] to nucleate cracks.

In the 800 °C sample, the regions of local high strain concentration are distributed along the gauge length uniformly in the Regions B_{800}, C_{800} and D_{800}. As the initial microstructure for the 800 °C sample (Fig. 6.3f) consists of γ distributed uniformly with ε and α′-martensite; the γ is thus expected to transform locally to ε and α′-martensite resulting in the high strain concentration regions. Another explanation of the local strain concentration can be due to unequal load partitioning between the relatively soft γ and hard α′-martensite.

The DIC axial strain localisation in the stress plateau region of the stress-strain curve in an Fe-7Mn-0.14C-0.23Si steel was observed during the transmission of Lüders bands [164]. In this steel, within the Lüders bands, the transformation of γ to deformation-induced α′-martensite also takes place simultaneously [164]; for which a decrease in the γ volume fraction from 29% to 9% was confirmed by XRD. Thermal measurements via infrared thermography also showed higher heat dissipation during the propagation of Lüders bands which was ascribed to the α′-martensite transformation. In addition, the microstructure within the Lüders bands showed the transformation of γ to α′-martensite compared to the microstructure outside the Lüders bands. Furthermore, the regions deformed by the propagation of Lüders bands showed an increase in hardness due to the transformation to α′-martensite. For this steel, PLC bands were also observed but were associated with serration in the strain hardening curve occurring after the stress plateau region of the tensile stress-strain curve.

A similar transformation of γ to α′-martensite was recorded by XRD during the interrupted tensile testing of an Fe-7Mn-2Al-0.3C steel annealed at 720 °C for 60 min resulting in the strain localisation by the propagation of PLC bands [250]. However, the formation of α′-martensite also leads to the strong resistance to the transmission of PLC bands. Thus, the PLC bands were observed to propagate discontinuously across the gauge section [250].

Lüders band propagation was also witnessed in an Fe-7Mn-0.14C-0.23Si steel deformed at room temperature and also at 100 and 300 °C [165]. Martensite transformation takes place during the tensile testing at room temperature, however, it does not proceed when tensile testing is performed at 100 and 300 °C. Thus, strain localisation can also be caused only by the propagation of Lüders band without the occurrence of martensite transformation [165]. However, in the present investigation, strain localisation was attributed only to martensite transformation as shown in Figs. 2c and 2d without the presence of Lüders or PLC bands.

The DIC axial strain localisation was observed during the uniaxial tension of a metastable Fe-21Mn-2.5Si-1.6Al-0.11C-0.02Nb-0.02Ti-0.01V steel deformed to 0.02 and 0.025 true strains at strain rates of 0.001 and 0.003 s^{-1}, respectively [42]. The optical and EBSD micrographs at strain rates of 0.001 and 0.003 s^{-1} at 0.02 and 0.025 true strains, respectively, showed the formation of only ε-martensite without the formation of α′-martensite. Thus, the transformation of γ to ε-martensite can also lead to strain localisation.

In-situ neutron diffraction tensile testing of the 900 °C sample showed the formation of α′-martensite at a strain of 0.05 which is in the middle of the slowly rising stress region [24]. Also, the onset of γ to ε-martensite transformation was recorded before the start of the ε to α′-martensite transformation. Thus, the strain localisation can be ascribed to the onset of both γ to ε-martensite and ε to α′-martensite transformations.

Figure 7.9 shows the transverse strain distribution at the corresponding fracture strains for the samples after cold rolling and annealing at 500, 625, 650, 700 and 800 °C, respectively. Note that the colour scheme of the transverse strain maps is inverted as compared to the axial true strain distribution maps (Figs. 7.2-7.8), as the transverse strains were recorded as negative by the DIC software. As observed for all the samples, the distribution of transverse strain is uniform along the gauge length with the exception of local transverse strain concentration at the fracture region at the centre or the end of gauge section. The concentration of strains at the ends of the gauge length due to grips is also present.

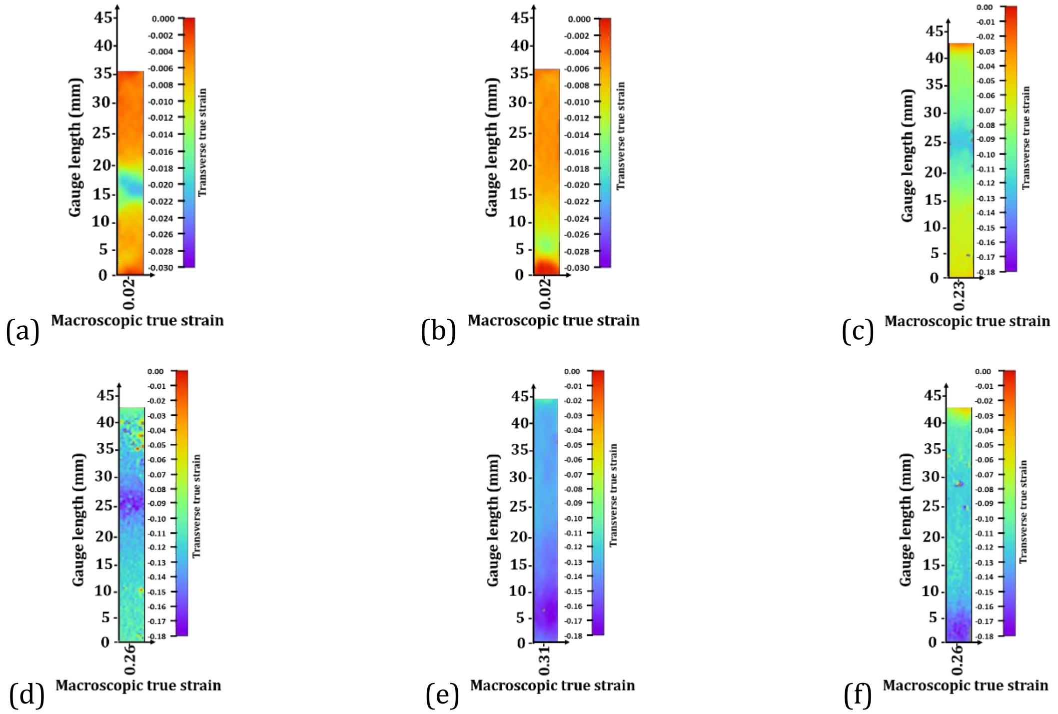

Figure 7.9: Digital image correlation maps showing the distribution of transverse strain at the macroscopic fracture strains for the samples after (a) cold rolling, annealing at (b) 500 °C, (c) 625 °C, (d) 650 °C, (e) 700 °C and (f) 800 °C. The colour scale of the transverse strain distributions is inverted compared to the axial strain distributions.

7.3 Microstructure changes after uniaxial tension

Fig. 7.10 shows the microstructures of the cold-rolled and 500, 625 and 700 °C samples at the true strain corresponding to the UTS. The microstructures of the 650 and 800 °C samples were not examined, as their tensile behaviour was similar to the 625 and 700 °C samples, respectively. The cold-rolled and 500 °C microstructures in Figs. 7.10a and 7.10b have similar morphologies and phase fractions compared to the undeformed samples in Figs. 6.2a and 6.2b, respectively.

The deformation of the 625 and 700 °C samples results in the phase transformation of the reverted and/or recrystallised γ into fine deformation-induced ε and α′-martensite (compare Figs. 7.10c and 7.10d to their undeformed counterparts in Figs. 6.3b and 6.3d). The variation in morphology of the deformation-induced α′-martensite is due to the size differences of the γ grains prior to uniaxial tensile testing. The relative area fraction of the untransformed γ is lower in the 700 °C sample compared to the 625 °C sample. This is due to the higher strain (uniform elongation = 0.31) for the 700 °C sample compared to the 625 °C sample upon tension (uniform elongation = 0.26). The presence of ε-martensite grain containing $\{10\bar{1}2\}\langle\bar{1}011\rangle_{\varepsilon}$ extension twin (inset) in the 700 °C sample after deformation is shown in Fig. 7.10d.

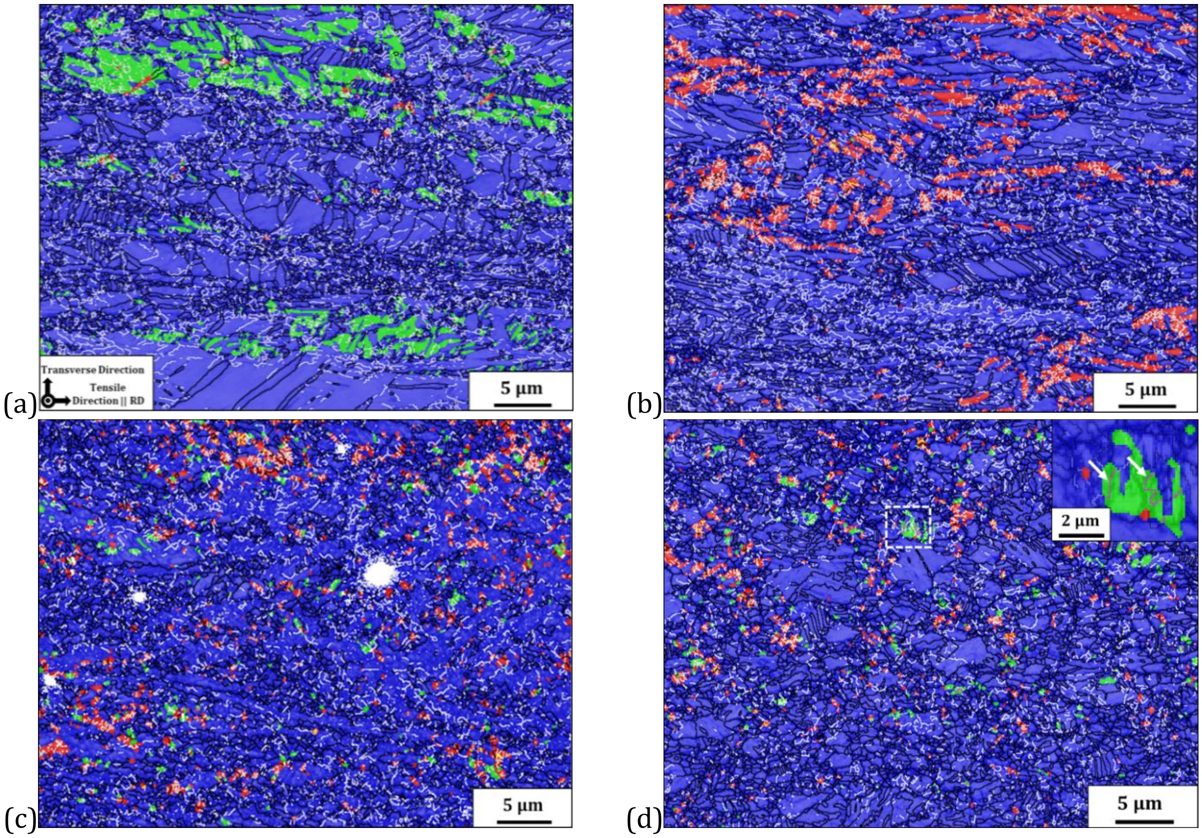

Figure 7.10: Superimposed band contrast and phase maps after subjected to tension for the samples after (a) cold rolling and annealing at (b) 500 °C, (c) 625 °C and (d) 700 °C. Red = γ, green = ε-martensite, blue = α′-martensite, white = unindexed areas, silver = LAGBs, black = HAGBs, yellow = γ twin boundaries and RD || tensile axis = horizontal. Fig. 7.10d (inset) is from the white dashed region showing $\{10\bar{1}2\}\langle\bar{1}011\rangle_{\varepsilon}$ twins in ε-martensite highlighted by white arrows in the inset.

$\{10\bar{1}2\}\langle\bar{1}011\rangle_{\varepsilon}$ twins in ε-martensite were previously reported during the plane strain compression of the same steel (Fig. 4.2d, Chapter 4) and upon the tension of an Fe-30Mn-6Si shape memory alloy [51]. It has to be stated here that for the nucleation of $\{10\bar{1}2\}\langle\bar{1}011\rangle_{\varepsilon}$ extension twin, slip on the basal and pyramidal planes in ε-martensite must be initiated [251]. Thus, the basal and pyramidal planes in ε-martensite accommodate deformation.

Figs. 7.11a-7.11c are the misorientation angle distributions before and after tension for the γ, ε and α′-martensite phases, respectively. The γ, ε and α′-martensite phases record an increase in LAGBs fraction indicating deformation during tension. In the case of the 625 and 700 °C samples, γ shares the applied load via transformation to ε and α′-martensite. With higher tensile strain, deformation accommodation takes place by newly formed ε and α′-martensite and further γ transformation. For the 500, 625 and 700 °C samples, a decrease in the $60°/\langle 111\rangle_{\gamma}$ twin fraction after tension is noted. The α′-martensite also shows a decrease in intensity of the $50°/\langle 110\rangle_{\alpha'}$, $60°/\langle 111\rangle_{\alpha'}$ and $60°/\langle 110\rangle_{\alpha'}$ inter-variant peaks [252] after tensile testing. This is due to the deviation from the twin/matrix or inter-variant misorientation relationships resulting in local lattice rotations via dislocation accumulation at annealing twin [253] or inter-variant boundaries during tension. The ε-martensite phase records a small peak between 86°-90° around the $\langle 11\bar{2}0\rangle_{\varepsilon}$ axis after tension due to $\{10\bar{1}2\}\langle\bar{1}011\rangle_{\varepsilon}$ extension twinning. The formation of parallel $\{10\bar{1}2\}\langle\bar{1}011\rangle_{\varepsilon}$ extension twins with similar orientations inside a single ε-martensite lath during the tension of an Fe-15Mn-0.005C steel were also reported [52]. The formation of $\{10\bar{1}2\}\langle\bar{1}011\rangle_{\varepsilon}$ extension twins at the intersection of different ε-martensite variants were detected in an Fe-30Mn-6Si shape memory alloy [51]. In that study, four different $\{10\bar{1}2\}\langle\bar{1}011\rangle_{\varepsilon}$ extension twin variants of ε-martensite were observed.

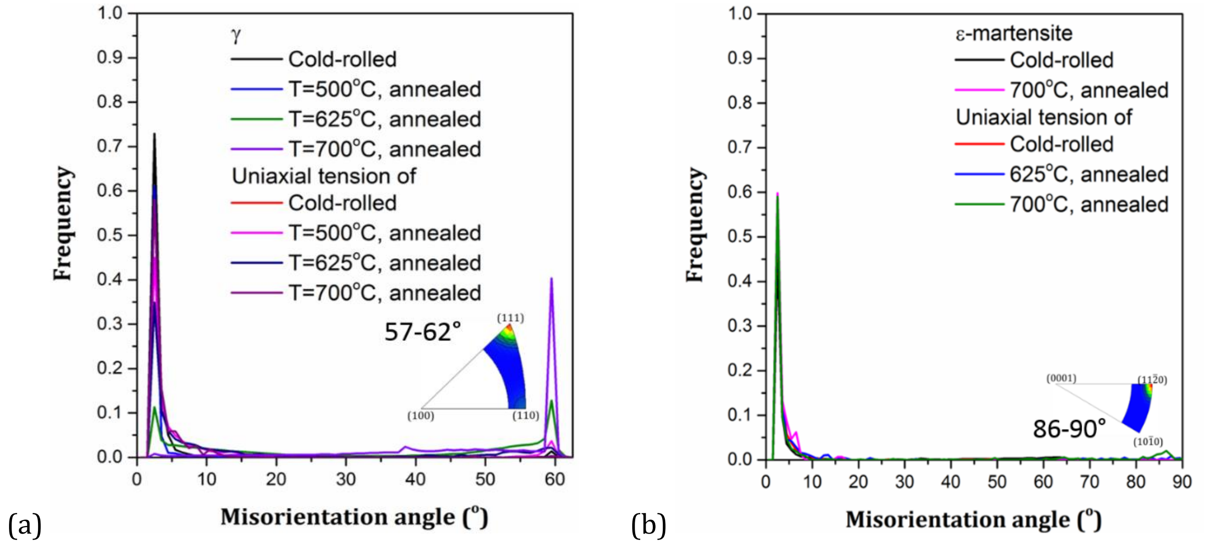

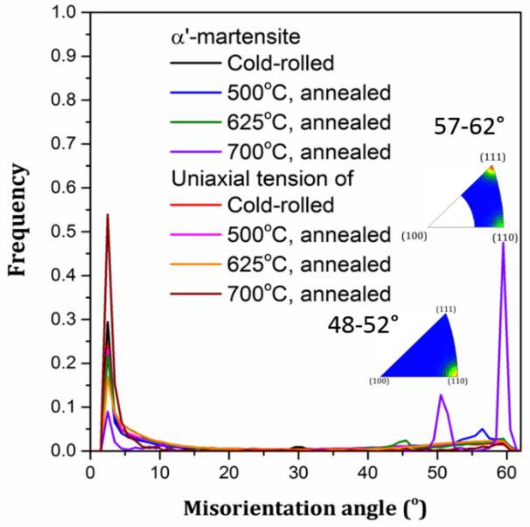

(c)

Figure 7.11: Misorientation angle distributions for (a) γ, (b) ε-martensite and (c) α′-martensite before and after tensile testing for the cold-rolled and 500, 625 and 700 °C samples.

7.4 Micro-texture changes after tension for the cold-rolled and annealed samples

Fig. 7.12 shows the experimental $\{111\}_{\gamma}$, $\{100\}_{\gamma}$, $\{0001\}_{\varepsilon}$ and $\{110\}_{\alpha'}$ pole figures of the cold-rolled and annealed samples before (Figs. 7.12a, 7.12c, 7.12e and 7.12g) and after (Figs. 7.12b, 7.12d, 7.12f and 7.12h) tension with the tensile axis parallel to the RD. Due to the low volume fraction of ε and α′-martensite, the pole figures in the 500, 625 and 700 °C samples are not plotted. The ε-martensite $\{0001\}_{\varepsilon}$ pole figures were plotted using the $[10\bar{1}0]_{\varepsilon}$ || RD and $[0002]_{\varepsilon}$ || ND convention.

For the γ in the cold-rolled samples shown in Fig. 7.12a, the red dashed lines connect the A_{γ} ($\{110\}\langle 111\rangle_{\gamma}$) and Copper ($Cu_{\gamma}$, $\{112\}\langle 111\rangle_{\gamma}$) orientations belonging to the $\langle 111\rangle_{\gamma}$ partial fibre while the blue dash and dot lines connect the Goss (G_{γ}, $\{110\}\langle 001\rangle_{\gamma}$) and Cube ($C_{\gamma}$, $\{001\}\langle 100\rangle_{\gamma}$) orientations belonging to the $\langle 100\rangle_{\gamma}$ partial fibre. The occurrence of the S-N, Burgers and K-S orientation relationships between γ and ε and α′-martensite phases (Fig. 7.10a) was obtained upon superimposing the ideal fcc orientations and partial fibres onto the $\{0001\}_{\varepsilon}$ and $\{110\}_{\alpha'}$ pole figures. The tension in γ results in the typical development of relatively stronger $\langle 111\rangle_{\gamma}$ and a weaker $\langle 100\rangle_{\gamma}$ double-fibre texture parallel to the tensile axis [254] comprising Brass (Br_{γ}, $\{110\}\langle 112\rangle_{\gamma}$), Cu_{γ} and weak G_{γ} orientations (Fig. 7.12f). The evolution of relatively strong $\langle 111\rangle_{\gamma}$ and weak $\langle 100\rangle_{\gamma}$ fibres are ascribed to the increase in latent hardening on non-coplanar systems, which in turn promotes co-planar slip and results in an overall weakening of the $\langle 100\rangle_{\gamma}$ fibre [255]. Similar texture development in γ was reported for an Fe-18.4Mn-3.2Si-3Al steel subjected to tension up to 0.4 true strain [256] and an Fe-17Mn-3Al-2Si steel [24] cycled between +0.035 and -0.028 true strains. Upon the phase transformation of the above γ orientations via the S-N orientation relationship results in the formation of $\{hkil\}_{\varepsilon}$-fibre [182] $\{01\bar{1}3\}\langle 1\bar{1}01\rangle_{\varepsilon}$ orientation where the $\{0001\}_{\varepsilon}$ poles are deviated by ≈24°-30° towards the RD (or tensile axis) (Fig. 7.12f).

The development of the $\langle 110\rangle_{\alpha'}||$ND fibre is observed due to the phase transformation of the above γ and ε-martensite orientations to α′-martensite orientations via the K-S and Burgers orientation relationships, respectively, followed by the α′-martensite deformation accommodation during tension (Fig. 7.12f, 7.12h). In the $\langle 110\rangle_{\alpha'}$ || ND fibre strong intensities around the $(001)[1\bar{1}0]_{\alpha'}$ and $(112)[1\bar{1}0]_{\alpha'}$ orientations are observed due to the transformation from (i) Br_{γ} and Cu_{γ}, G_{γ} orientations, respectively, or (ii) ε-martensite $\{hkil\}_{\varepsilon}$-fibre orientations.

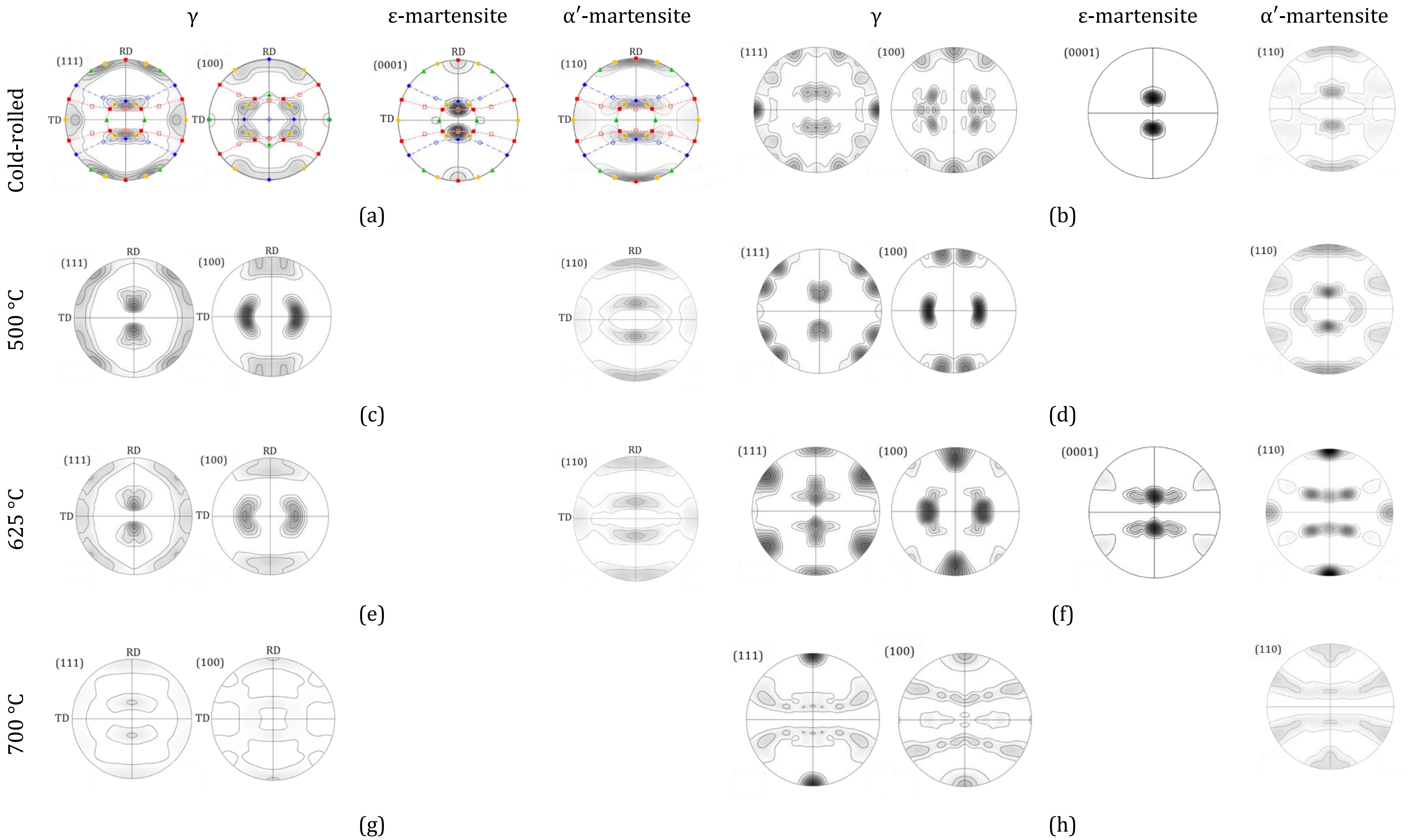

Figure 7.12: γ, ε and α′-martensite pole figures of the (a, b) cold-rolled and annealed at (c, d) 500 °C, (e, f) 625 °C and (g, h) 700 °C samples, (a, c, e, g) before and (b, d, f, h) after tension. In Fig. 7.12a, the ideal fcc orientations on (111) pole figure is superimposed on ε, α′-martensite and $(100)_{\gamma}$, $(111)_{\gamma}$. Key: ◆ $G_{\gamma} = \{110\}\langle 001\rangle_{\gamma}$, ◇ $C_{\gamma} = \{001\}\langle 100\rangle_{\gamma}$, □ $Cu_{\gamma} = \{112\}\langle 111\rangle_{\gamma}$, ■ $A_{\gamma} = \{110\}\langle 111\rangle_{\gamma}$, ● $Br_{\gamma} = \{110\}\langle 112\rangle_{\gamma}$, ▲ Rt-$G_{\gamma} = \{011\}\langle 011\rangle_{\gamma}$ In Figs. 7.12b, 7.12d, 7.12f, 7.12h, RD || tensile axis = vertical. Contours levels = 0.5×.

7.5 Fractography

Figs. 7.13 and 7.14 are the micrographs showing the fracture surfaces of the cold-rolled, 500, 625 and 700 °C samples. The fracture surface of the cold-rolled and the 500 °C sample depicts secondary cracks highlighted by the red arrow in Fig. 7.13a and 7.13b along with flat ledge-like morphologies highlighted by the red arrow in Fig. 7.13b and 7.13d. This shows the occurrence of quasi-cleavage due to rapid crack propagation in α′-martensite [257] and shallow dimples; reminiscent of mixed brittle and ductile fracture modes.

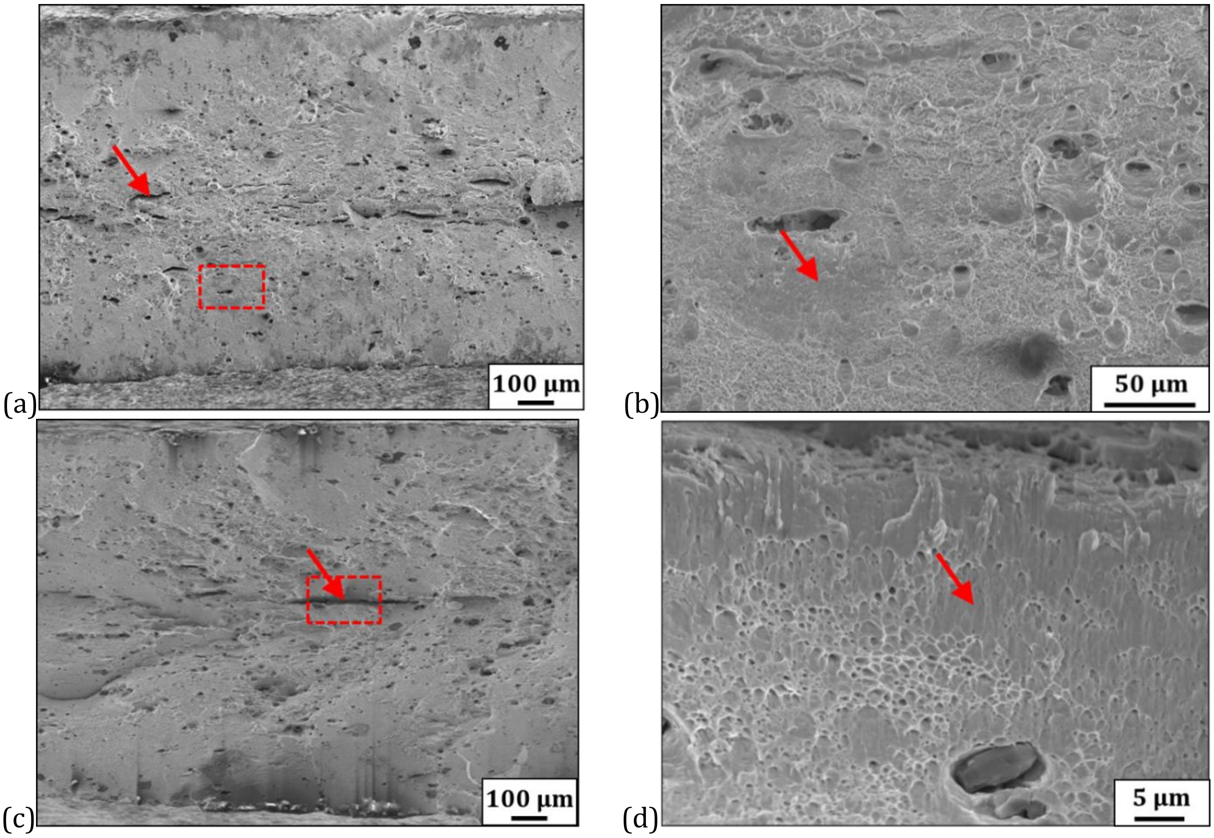

Figure 7.13: Fractography of the fractured tensile samples after (a, b) cold rolling and (c, d) annealing at 500 °C. Figs. 7.13b and 7.13d, are the zoomed-in views of the regions highlighted by red dashed rectangles from Figs. 7.13a and 7.13c, respectively.

The 625 °C (Figs. 7.14a and 7.14b) and 700 °C (Figs. 7.14c and 7.14d) samples return rugged facets and ledge-like morphologies. The zoomed-in views (Figs. 7.14b and 7.14d) of the 625 and 700 °C samples record shallow dimples due to ductile fracture [258-260] and voids caused by particle pull out highlighted by red arrows in Fig. 7.14b. In Fig. 7.14d, coarse particles of ≈5 µm size are present in the voids. On coalescence, micro-voids (see red arrow in Fig. 7.14d) can lead to the formation of shallow dimples.

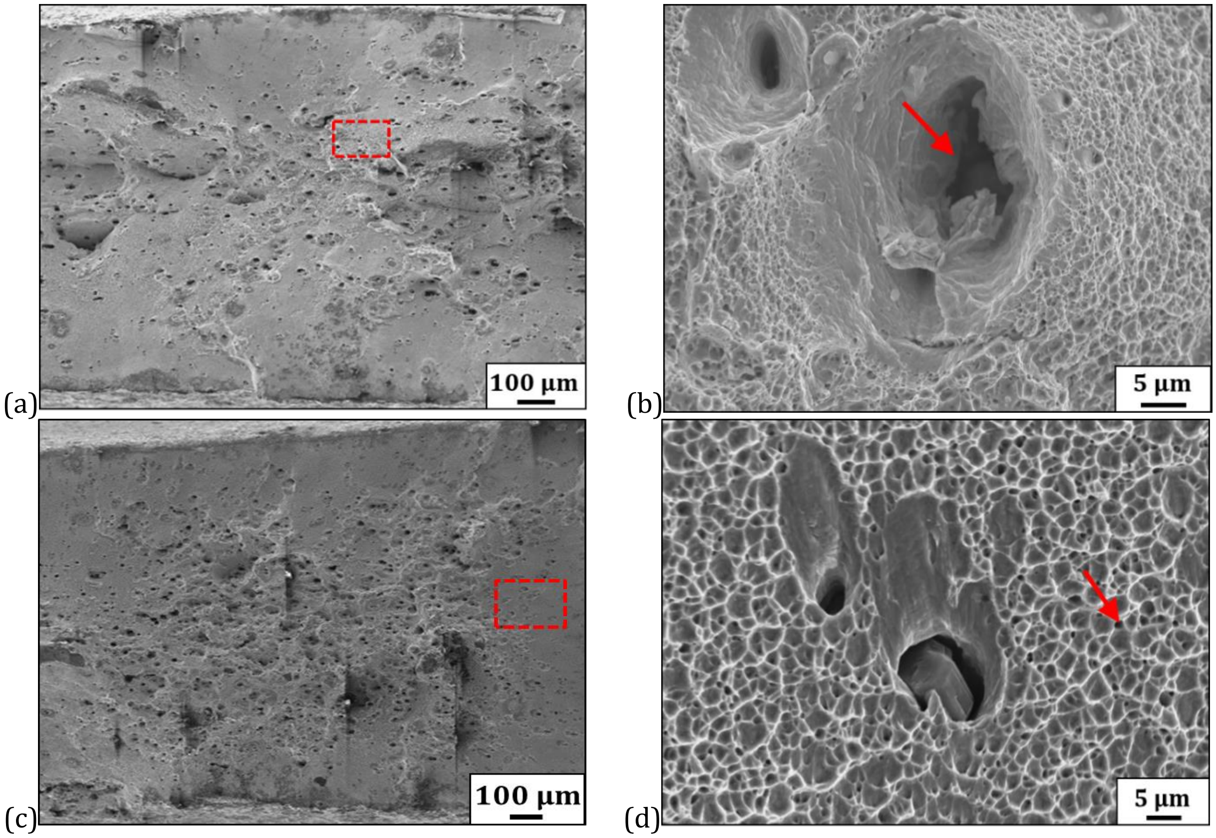

Figure 7.14: Fractography of the fractured tensile samples after annealing at (a, b) 625 °C and (c, d) 700 °C. Figs. 7.14b and 7.14d are the zoomed-in views of regions highlighted by red dashed rectangles in Figs. 7.14a and 7.14c, respectively.

The characterisation of fracture surfaces in an Fe-22Mn-0.6C-0.2V steel also showed the presence of submicron sized dimples indicating limited void growth [261]. The voids nucleated around the fine spherical precipitates of vanadium carbide or at the intersection points between vanadium carbide precipitates and fine twins. The investigation of the fracture surfaces of an Fe-22.3Mn-0.6C-0.2Si steel demonstrated the propagation of quasi-cleavage cracks or formation of a sheet of voids. The voids were less than 1 µm size and were free from inclusions [262].

7.6 Conclusions

Characterisation via digital image correlation during tensile testing and electron back-scattering diffraction of the 42% cold-rolled and 500, 625, 650, 700 and 800 °C samples led to the following conclusions:

(1) The microstructures of the cold-rolled and 500 °C samples contain predominantly α′-martensite and either remnant ε-martensite or γ, respectively. The microstructure remained unchanged upon tensile testing due to the early necking at ≈0.02 true strain. The digital image correlation investigation of the cold-rolled and 500 °C samples showed the axial true strain distribution to be uniform followed by strain localisation at necking. Based on electron back-scattering diffraction and digital image correlation observations, the load was carried by α′-martensite in the cold-rolled and incompletely recovered states for the cold-rolled and 500 °C samples, respectively.

(2) Electron back-scattering diffraction analysis showed that the 625 and 650 °C samples contains reverted/recrystallised γ and α′-martensite. During their tensile loading, the axial strain remains approximately uniform followed by the strain localisation in axial and shear strain in the upper section of the gauge length initiated by the stress concentration associated with the grip ends. The strain localisation is due to the load partitioning between the reverted/recrystallised γ and newly formed deformation-induced ε and α′-martensite along with the deformation of γ, ε and α′-martensite. Also during fracture, strain localisation is observed. Supporting the digital image correlation observations, upon tensile loading the electron back-scattering diffraction map showed that the microstructure consists of deformation-induced ε and α′-martensite in the 625 °C sample.

(3) Electron back-scattering diffraction mapping showed that the 700 °C sample contains fully recrystallised γ. During tensile loading, strain localisation in axial and shear strain in the upper and lower sections of the gauge length is observed in comparison to the upper sections for the 625 and 650 °C samples due to the higher fraction of γ available for the transformation to ε and α′-martensite in the 700 °C sample. Strain localisation for the 700 °C sample is due to the deformation of ε and α′-martensite along with the further transformation of γ to ε and α′-martensite along the gauge length. Upon fracture, strain concentration can be observed in the lower end of the gauge length.

(4) The 800 °C sample contains recrystallised γ along with ε and α′-martensite formed upon quenching after annealing. In comparison to the 700 °C sample, for the 800 °C sample strain localisation is observed at the centre and in the lower end of the gauge length at higher macroscopic true strains and at the bottom of the gauge length at fracture.

(5) The formation of $\{10\bar{1}2\}\langle\bar{1}011\rangle_{\varepsilon}$ extension twins in ε-martensite were also detected after tensile testing of the 700 °C sample, which suggests the deformation of ε-martensite.

(6) The formation of $\langle 111\rangle_{\gamma}$, $\langle 100\rangle_{\gamma}$ double-fibre texture was observed in γ whereas the ε and α′-martensite showed $\{hkil\}_{\varepsilon}$-fibre and $\langle 110\rangle_{\alpha'}$ || ND fibre, respectively, after tensile loading.

(7) The fracture surfaces showed a mixed brittle and ductile fracture mode for the cold-rolled and 500 °C samples and ductile fracture mode for the 625 and 700 °C samples.

CHAPTER 8 CONCLUSIONS AND RECOMMENDATIONS

This chapter recapitulates the general conclusions, key contributions to the original knowledge and also suggests some potential directions for future study.

8.1 General Conclusions

8.1.1 Effect of plane strain compression/cold rolling on microstructure and texture:

- The hot-rolled sample upon quenching shows the presence of ε and α′-martensite in γ. With increasing thickness reduction, the formation of γ-intrinsic stacking faults takes place followed by the deformation-induced ε and α′-martensite formation via (i) γ to ε to α′-martensite (dominant) and (ii) γ to α′-martensite routes. The nucleation of ε-martensite occurs at γ-intrinsic stacking faults and at pre-existing γ annealing twin boundaries. The lateral growth via coalescence leads to the coarsening of ε-martensite plates. The transformation of ε to α′-martensite transpires within the coarse ε-martensite plates and at the intersection of two ε-martensite laths.
- The deformation of ε-martensite occurs via a combination of perfect and partial basal slip, pyramidal slip and $\{10\bar{1}2\}\langle\bar{1}011\rangle_{\varepsilon}$ extension twins. The formation of I_2 type ε-martensite intrinsic stacking faults was observed in relatively thin (thickness between 20-60 nm) ε-martensite laths whereas I_1 type ε-martensite intrinsic stacking faults were present in thick ε-martensite plates. The transition of I_2 to I_1 ε-martensite intrinsic stacking faults occurred due to the deformation accommodation by ε-martensite. The increase in the low angle grain boundary fraction in ε-martensite with an increase in thickness reduction also provides evidence of ε-martensite deformation accommodation.
- Using the orientation distribution function sections correlating the orientations of γ to ε and α′-martensite, it was revealed that during plane strain compression/cold rolling the $\{hkil\}_{\varepsilon}$-fibre orientations are acquired from the $(213)[0\bar{2}1]_{\gamma}$ (ϕ_1 = 32°, Φ = 37°, ϕ_2 = 65°), G_{γ}, $(011)[3\bar{1}1]_{\gamma}$ (ϕ_1 = 20°, Φ = 45°, ϕ_2 = 0°) orientations via the Shoji-Nishiyama orientation relationship. The $\{001\}\langle 110\rangle_{\alpha'}$ orientation is obtained primarily from the $\{11\bar{2}0\}\langle 0001\rangle_{\varepsilon}$ orientation while the $(112)[1\bar{1}0]_{\alpha'}$ orientation is formed from the $\{10\bar{1}0\}\langle 0001\rangle_{\varepsilon}$ orientation. The C_{γ}, Br_{γ}, and Cu_{γ}, G_{γ} orientations transform to $\{001\}\langle 110\rangle_{\alpha'}$ and $(112)[1\bar{1}0]_{\alpha'}$ orientations, respectively, upon increasing thickness reduction.

8.1.2 Microstructure and texture changes during ε and α′-martensite reversion:

- On annealing, the reversion of ε and α′-martensite to γ takes place. In-situ transmission electron microscopy annealing study has shown that ε and α′-martensite reversion occurred by a displacive mechanism without any visible migration of the inclined ε-martensite/γ and α′-martensite/γ interfaces. The transformation resulted in the γ inheriting the shape of either ε or α′-martensite grain via a displacive mechanism and exhibiting the Shoji-Nishiyama and Kurdjumov-Sachs orientation relationships, respectively. The ε and α′-martensite transformation temperatures during the heating of thin foils were observed to be higher than bulk samples.
- The presence of fine twins was observed in the 500, 600, 625 and 650 °C samples in electron back-scattering diffraction and transmission electron microscopy studies. In-situ annealing experiments of the cold-rolled sample elucidated the origin of their formation to be the recovery of reverted γ from ε-martensite. The mechanism was explained based on the glide of Shockley partial dislocations leading to the conversion of γ-ISFs, derived after reversion from faulted ε-martensite to twins.
- The orientation correlation between the three phases showed that the reverted γ orientations originated from both the ε and α′-martensite orientations following the Shoji-Nishiyama and the Kurdjumov-Sachs orientation relationships, correspondingly. The $\{\bar{1}2\bar{1}5\}\langle 1\bar{2}12\rangle_{\varepsilon}$ (ϕ_1 = 90°, Φ = 24°, ϕ_2 = 0°) and (ii) $\{01\bar{1}4\}\langle 1\bar{3}23\rangle_{\varepsilon}$ (ϕ_1 = 72°, Φ = 23°, ϕ_2 = 30°) orientations revert to (i) $(213)[0\bar{2}1]_{\gamma}$ and (ii) $(011)[3\bar{1}1]_{\gamma}$ orientations, respectively. The (i) $(001)[1\bar{1}0]_{\alpha'}$, $(111)[\bar{1}\bar{1}2]_{\alpha'}$ and $(554)[\bar{2}\bar{2}5]_{\alpha'}$, (ii) $(112)[1\bar{1}0]_{\alpha'}$, (iii) $(112)[1\bar{1}0]_{\alpha'}$ and $(111)[\bar{1}\bar{1}2]_{\alpha'}$ and (iv) $(001)[1\bar{1}0]_{\alpha'}$ orientations produce the (i) Br_{γ}, (ii) Cu_{γ}, (iii) $(213)[0\bar{2}1]_{\gamma}$ and (iv) S_{γ} orientations, correspondingly, via the Kurdjumov-Sachs orientation relationship.

8.1.3 Microstructure changes during γ recrystallisation and subsequent grain growth:

- Recrystallisation of the reverted γ grains takes place concurrently with reversion. Electron back-scattering diffraction and transmission electron microscopy micrographs showed the occurrence of nucleation from the reverted/recovered γ grains upon annealing between 600-650 °C. At later stages of recrystallisation, the recrystallised γ grains show the formation of annealing twins. The calculated value of activation energy for γ grain growth (237.2 ± 17.3 kJ/mol) is lower than the self-diffusion of γ (Q = 270 kJ/mol) indicating grain boundary diffusion as a key mechanism for γ grain growth rather than lattice self-diffusion.

8.1.4. The effect of microstructure on the tensile properties:

- The best combination of yield stress and total elongation was observed for the 625 and 650 °C samples due to a microstructure containing nearly equal fractions of highly dislocated reverted γ, soft recrystallised γ and hard α′-martensite. In general, a decrease in the yield stress, ultimate tensile strength and an increase in the uniform true elongation compared to the cold-rolled and 500 °C samples were observed with an increase in the annealing temperature. The decrease in yield stress is due to the decrease in the deformation-induced ε and α′-martensite area fraction upon annealing. The increase in uniform true elongation is due to strain hardening from the transformation of recrystallised γ to deformation-induced ε and α′-martensite. However, the uniform true elongation of the 800 °C sample is lower than that of 700 °C sample due to a higher area fraction of ε and α′-martensite formed upon quenching after annealing in the former and thus providing a higher number of crack nucleation sites.
- The electron back-scattering diffraction maps revealed that no significant changes in the microstructures of the cold-rolled and 500 °C samples occurred upon tensile testing. However, the 625 and 700 °C samples showed the transformation of nearly all γ and ε-martensite to deformation-induced α′-martensite. The digital image correlation axial true strain distribution is in line with the microstructural observation displaying strain concentration after yielding for the cold-rolled and 500 °C sample due to the onset of necking. Upon tension, digital image correlation studies for the 625, 650 and 800 °C samples showed the formation of strain localisation regions which was ascribed to the load partitioning between the γ/α′-martensite phases and phase transformation of γ to ε and α′-martensite. The formation and propagation of strain localisation regions were observed for the 700 °C sample from the ends to the centre of the gauge length. This was only due to the phase transformation of γ.
- The orientations of γ, ε and α′-martensite remained unchanged upon tension for the cold-rolled and 500 °C samples, which is in line with the microstructural observations. The formation of $\{hkil\}_{\varepsilon}$-fibre takes place in ε-martensite upon tension whereas strengthening of the $\{001\}\langle 110\rangle_{\alpha'}$ α′-martensite orientation, $\langle 203\rangle_{\alpha'}$ fibre formation occurs after subjecting to tension for the 625 and 700 °C samples, respectively. Upon tensile testing, the formation of strong $\langle 111\rangle_{\gamma}$ and weak $\langle 100\rangle_{\gamma}$ fibres takes place in the 700 °C sample. The γ and α′-martensite orientations after tension are different to those after plane strain compression/cold rolling. In γ and α′-martensite upon tension, the formation of orientations along the $\langle 111\rangle_{\gamma}$, $\langle 100\rangle_{\gamma}$, $\langle 203\rangle_{\alpha'}$ fibres takes place whereas upon plane strain compression/cold rolling the formation of γ orientations along the α_{γ}-fibre and

α'-martensite orientations belonging to the $\alpha_{\alpha'}$-fibre transpires. This indicates that the strain path affects the texture formation.

- A mixed mode of fracture (ductile and brittle) was noticed for the cold-rolled and 500 °C samples due to rapid crack propagation in α'-martensite whereas a ductile mode of fracture was detected for the 625 and 700 °C samples due to the formation of deformation-induced ε and α'-martensite formation.

8.2 Contribution to the original knowledge

Based on the extensive experiments using advanced characterisation techniques, the following key contributions were made to highlight the plane strain deformation and annealing behaviour of high Mn steels.

- This study for the first time shows the nucleation and growth of ε-martensite upon plane strain compression/cold rolling. The high angle annular dark-field scanning transmission electron microscopy micrographs showed that overlapping γ-intrinsic stacking faults on the $(111)_\gamma$ plane leads to ε-martensite nucleation. The growth of ε-martensite takes place via the coalescence with the existing ε-martensite plates. A mechanism of ε-martensite coarsening via coalescence was proposed involving the motion of Shockley partial dislocations. These observations confirmed the operation of the ε-martensite nucleation mechanism proposed by Fujita and Ueda [15].
- The present investigation using the high angle annular dark-field scanning transmission electron microscopy imaging revealed the evolution of ε-martensite intrinsic stacking faults with increasing thickness reduction. After 10% thickness reduction the presence of I_2-type ε-martensite intrinsic stacking faults was noted. Upon thickness reduction to 15 and 42%, the presence of I_1-type ε-martensite intrinsic stacking faults was detected. The formation of I_1 and I_2-type ε-martensite intrinsic stacking faults upon tension was proposed in an Fe-17Mn-0.02C steel based on X-Ray diffraction analysis [22]. A novel mechanism of the change in ε-martensite stacking fault character via the motion of Shockley partial dislocation was introduced, which indicates the deformation accommodation in ε-martensite with an increase in thickness reduction. The deformation accommodation in ε-martensite also occurred via a combination of perfect and partial basal slip (I_1 and I_2 ε-martensite intrinsic stacking faults), pyramidal slip and $\{10\bar{1}2\}\langle\bar{1}011\rangle_\varepsilon$ extension twinning. The ε-martensite deformation accommodation was also observed where dislocations with a $\langle c\rangle$ component in ε-martensite dissociated into Shockley

partial dislocations in the basal plane during uniaxial tensile testing of an Fe-17Mn steel to 0.05 engineering strain [25].

- A new insight into the reversion mechanism of ε and α′-martensite was obtained in the present study. The reversion of ε-martensite without the nucleation of γ or the motion of γ/ε-martensite inclined interface was noted in the present investigation. The ε-martensite reversion occurred via a displacive mechanism. However, previous in-situ transmission electron microscopy annealing study [34] on ε-martensite reversion showed the nucleation of γ inside and outside of ε-martensite grain leading to the formation of a γ/ε-martensite lamellar structure. Similar to ε-martensite reversion, the reversion of α′-martensite occurred without the motion of ledges or the inclined γ/α′-martensite interface during in-situ annealing at a high temperature of 800 °C for 600 s indicating a displacive mechanism. Previous in-situ annealing study [30] on the α′-martensite reversion showed the operation of the diffusional mechanism via the migration of dislocation ledges at the γ/α′-martensite interface.
- The present study for the first time also explored the formation of fine twins in γ reverted from ε-martensite. The twins in γ were observed to have nanoscale dimensions with a thickness 7.6 ± 2.3 nm, thus excluding them from the category of coarse annealing twins. A novel mechanism via the growth of remnant γ stacking faults retained after ε-martensite reversion was proposed to explain the twins in reverted γ. Similar recovery-induced twins in γ were reported in γ reverted formed from α′-martensite [34].
- The present study carries out a detailed analysis of the ε and α′-martensite orientations formed from γ during deformation and γ orientations formed from the ε and α′-martensite orientations upon reversion during annealing via phase transformations following the Shoji-Nishiyama and Kurdjumov-Sachs orientation relationships, respectively. The presence of such extensive correlation between γ, ε and α′-martensite orientations was lacking in the literature. The previous study by Lü *et al.* [8] showed the formation of $\{123\}\langle 412\rangle_{\gamma}$ orientation from the $\sim\{1129\}\langle 3362\rangle_{\varepsilon}$ orientation after reversion upon annealing. This study fills the gap in the literature and expands the list of γ orientations that are formed during the reversion from ε and α′-martensite orientations via the Shoji-Nishiyama and Kurdjumov-Sachs orientation relationships. As an example, the $\{\bar{1}2\bar{1}5\}\langle 1\bar{2}12\rangle_{\varepsilon}$ orientation obtained after cold rolling to 42% thickness reduction transforms to the $(213)[0\bar{3}1]_{\gamma}$ orientation upon reversion during annealing. This study also correlates the α′-martensite orientations formed from the ε-martensite orientations via phase transformation following the Burgers orientation relationship.

- The present literature lacks experimental data on the calculation of γ grain growth activation energy for phase transforming high Mn steels. A novel image analysis technique was developed in the present study to determine the γ grain size in the 700-850 °C samples to delineate the prior γ/γ grain boundaries. From the γ grain size data, the activation energy of γ grain growth was calculated to be 237.2 ± 17.3 kJ/mol which indicated that grain boundary diffusion is the main mechanism. The calculated activation energies for γ grain growth in the Fe-18Mn and Fe-18Mn-1.5Si-0.6C steels was similar to the one for the present steel [156, 237].

8.3 Future Work

The microstructural evolution during deformation and annealing of a Fe-17Mn-3Al-2Si-1Ni-0.06C steel was studied by electron back-scattering diffraction, transmission electron microscopy and high angle annular dark-field scanning transmission electron microscopy. The mechanical properties of the annealed samples were evaluated using tensile testing via digital image correlation. Some aspects of future work on high Mn steels are given below:

- Plane strain compression between 20 and 42% thickness reduction and subsequent microstructural characterisation via electron back-scattering diffraction, transmission electron microscopy and high angle annular dark-field scanning transmission electron microscopy will provide insight into the drastic microstructural change occurring between 20 and 42% thickness reductions.
- In-situ deformation experiments using electron back-scattering diffraction or transmission electron microscopy will offer direct evidence of the deformation accommodation mechanisms operating in γ, ε and α′-martensite.
- High angle annular dark-field scanning transmission electron microscopy based geometric phase analysis will provide local strain fields at the γ/ε-martensite interfaces, at the tips of growing ε-martensite and at the intersections of ε-martensite plates. This will deepen our knowledge of the presence and interactions of dislocations during the nucleation and growth of ε-martensite plates.
- The modelling of the texture evolution of γ, ε and α′-martensite with increasing thickness reduction and its correlation to tensile properties will further advance our understanding regarding the deformation accommodation mechanisms of γ, ε and α′-martensite.

APPENDIX

A.1 Stacking fault energies of γ and ε-martensite via the weak beam dark-field technique

The γ-SFE was determined using the anisotropic theory of elasticity via calculating the width between the partial dislocations considering the attractive force of the stacking fault and repulsive forces of the partial dislocations which is represented by the following equation [263]:

$$\mathrm{SFE} = \frac{\mu b^2}{8\pi d}\left(\frac{2-\nu}{1-\nu}\right)\left(1 - \frac{2\nu\cos2\alpha}{2-\nu}\right) \tag{A.1}$$

where SFE is the γ-SFE (mJ/m^2), μ_γ and ν_γ are the effective shear modulus and the Poisson's ratio of the $(111)_\gamma$ fault plane, b is the Burgers vector of the partial dislocations, d is the width between the partial dislocations and α is the angle between the Burgers vector and the dislocation line vector.

The effective shear modulus and Poisson's ratio on the $(111)_\gamma$ fault plane was determined using the elastic stiffness constants as follows [263]:

$$\mu_\gamma = \left(C_{44}^\gamma \frac{(C_{11}^\gamma - C_{12}^\gamma)}{2}\right)^{0.5} \tag{A.2}$$

$$\frac{1}{1-\nu_\gamma} = \frac{1}{3\mu_\gamma}\left(\left[\frac{1}{2}C_{11}^\gamma\left(C_{11}^\gamma + C_{12}^\gamma + 2C_{44}^\gamma\right)\right]^{0.5} + C_{12}^\gamma\right)\left[\frac{C_{44}^\gamma(C^\gamma - C_{12}^\gamma)}{C_{11}^\gamma(C^\gamma + C_{12}^\gamma + 2C_{44}^\gamma)}\right]^{0.5}\left(1 + 2\frac{C_{11}^\gamma}{[\frac{1}{2}C_{11}^\gamma(C_{11}^\gamma + C_{12}^\gamma + 2C_{44}^\gamma)]^{0.5}}\right)$$

$$\text{where, } C^\gamma = \left[\frac{1}{2}C_{11}^\gamma\left(C_{11}^\gamma + C_{12}^\gamma + 2C_{44}^\gamma\right)\right]^{0.5} \tag{A.3}$$

The γ single crystal elastic stiffness constants, C_{11}^γ = 163 GPa, C_{12}^γ = 114.5 GPa, C_{44}^γ = 132 GPa were estimated by extrapolating the values from Ref. [264] for the Fe-Mn-Al/Si steels; which in turn were determined by ab-initio calculation. A similar determination of the elastic stiffness constants via interpolation was used in Ref. [265] in the case of an Fe-24Mn-3Al-2Si-1Ni-0.06C steel. Using the Eqs. A.2 and A.3, for the $(111)_\gamma$ fault plane the effective shear modulus and Poisson's ratio was calculated as 57 GPa and 0.4, respectively.

Fig. A.1a shows the WBDF image taken using the g = $[20\bar{2}]_\gamma$ which was verified by the diffraction pattern in the top left inset Fig. A.1a. After 5% thickness reduction, the splitting of a perfect dislocation (red arrows in Fig. A.1a inset) into two Shockley partial dislocations (blue arrows in Fig. A.1a inset) was noticed. Using the $g_\gamma.b = 0$ invisibility criteria and the lattice parameters of γ (a_γ = 0.3602 nm [24]) the Burgers vector was determined as 0.254 nm for the perfect $\frac{a}{2}[10\bar{1}]_\gamma$ dislocation and 0.147 nm for the Shockley partial dislocations with Burgers vector $\frac{a}{6}[11\bar{2}]_\gamma$ and $\frac{a}{6}[2\bar{1}\bar{1}]_\gamma$. Fig. A.1b shows the variation of the width of Shockley partial dislocations with the angle between the Burgers vector and the dislocation line vector. Using Eq. A.3 the average γ-SFE was estimated as 12.3 ± 1.3 mJ/m^2.

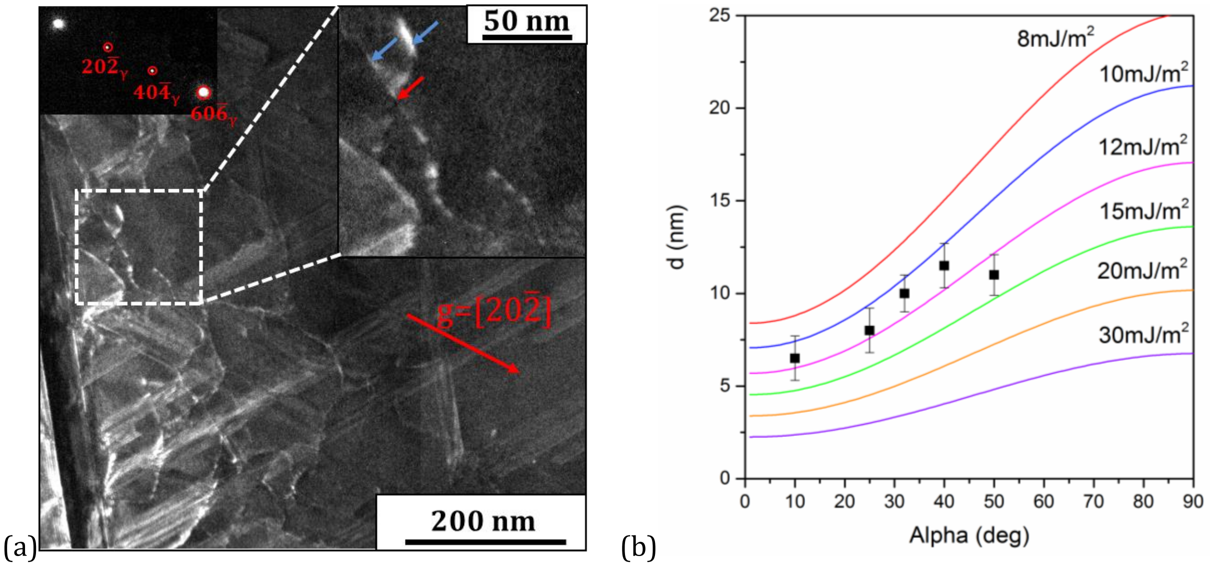

Figure: A.1 Representative (a) weak beam dark-field micrograph and (b) the distribution of the measured width of the Shockley partial dislocations with respect to the angle between the Burgers vector and the dislocation line vector for γ in the sample after 5% thickness reduction. The inset diffraction patterns in Fig. A.1a is from the regions demarcated by a white dashed rectangle in Fig. A.1a using g = [20$\bar{2}$]$_\gamma$. The red and blue arrows in Fig. A.1a show the perfect and Shockley partial dislocations.

It has to be pointed out that Eq. A.1 is based on the repulsion between two Shockley partial dislocations which are under equilibrium separation and the attraction by the γ-stacking fault. In Fig. A.1a a large density of dislocations is observed after the plane strain compression to 5% thickness reduction. The Shockley partial dislocations are observed to be interacting with other dislocations in the γ grain. This will lead to the non-equilibrium separation in the spacing between the Shockley partial dislocations which is expected to be higher than the equilibrium separation between the Shockley partial dislocations. Thus in the present case, the application of Eq. A.1 results in the inaccurate determination of γ-SFE, which is lower than the γ-SFE calculated under the equilibrium separation of Shockley partial dislocations.

For ε-martensite, the basal ε-SFE was also estimated using the Eq. A.1 by calculating the distance between the Shockley partial dislocations with respect to the angle between the Burgers vector and the dislocation line vector. The same approach was used to estimate the basal SFE I_2 -ISFs in Mg-Y alloy subjected to 3-5% cold rolling thickness reductions [219, 266].

Using the isotropic elasticity theory [95] by taking advantage of the isotropy in the basal plane of the hcp crystal structures the determination of the effective shear modulus (μ_ε) and Poisson's ratio (ν_ε)

of the basal $(0001)_\varepsilon$ fault plane was done using the equations:

$$\mu_\varepsilon = (\frac{C_{44}^\varepsilon}{2}(C_{11}^\varepsilon - C_{12}^\varepsilon))^{0.5} \tag{A.5}$$

$$\frac{\mu_\varepsilon}{1-\nu_\varepsilon} = (\bar{C}_{11}^\varepsilon + C_{13}^\varepsilon)[\frac{C_{44}^\varepsilon(\bar{C}_{11}^\varepsilon - C_{13}^\varepsilon)}{C_{33}^\varepsilon(\bar{C}_{11}^\varepsilon + C_{13}^\varepsilon + 2C_{44}^\varepsilon)}]^{0.5}$$

$$\text{where, } \bar{C}_{11}^\varepsilon = (C_{11}^\varepsilon C_{33}^\varepsilon)^{0.5} \tag{A.6}$$

As reported in Refs. [267-269], the single crystal elastic stiffness constants of ε-martensite were calculated from the single crystal elastic stiffness constants of the γ using the equations:

$$\bar{C}_{11}^\varepsilon = \frac{1}{2}(C_{11}^\gamma + C_{12}^\gamma + 2C_{44}^\gamma), \bar{C}_{12}^\varepsilon = \frac{1}{6}(C_{11}^\gamma + 5C_{12}^\gamma - 2C_{44}^\gamma), \bar{C}_{13}^\varepsilon = \frac{1}{3}(C_{11}^\gamma + 2C_{12}^\gamma - 2C_{44}^\gamma),$$

$$\bar{C}_{33}^\varepsilon = \frac{1}{3}(C_{11}^\gamma + 2C_{12}^\gamma + 4C_{44}^\gamma), \bar{C}_{44}^\varepsilon = \frac{1}{3}(C_{11}^\gamma - C_{12}^\gamma + C_{44}^\gamma) \tag{A.7}$$

$$\Delta_\varepsilon = \frac{1}{3\sqrt{2}}(C_{11}^\gamma - C_{12}^\gamma - 2C_{44}^\gamma) \tag{A.8}$$

$$X_1 = \frac{\Delta_\varepsilon^{2^2}}{\bar{C}_{44}^\varepsilon}, X_2 = \frac{2\Delta_\varepsilon^2}{\bar{C}_{11}^\varepsilon - \bar{C}_{12}^\varepsilon} \tag{A.9}$$

$$C_{11}^\varepsilon = \bar{C}_{11}^\varepsilon - X_1, C_{12}^\varepsilon = \bar{C}_{12}^\varepsilon + X_1, C_{13}^\varepsilon = \bar{C}_{13}^\varepsilon, C_{33}^\varepsilon = \bar{C}_{33}^\varepsilon, C_{44}^\varepsilon = \bar{C}_{11}^\varepsilon - X_2 \tag{A.10}$$

By application of Eqs. A.7-A.10, the single crystal elastic stiffness constants for ε-martensite was calculated as: $C_{11}^\varepsilon = 227.9$ GPa, $C_{12}^\varepsilon = 121.5$ GPa, $C_{33}^\varepsilon = 306.7$ GPa, $C_{13}^\varepsilon = 42.7$ GPa, $C_{44}^\varepsilon = 33.3$ GPa. Using the calculated values of single crystal elastic constants in Eq. A.6 produced an effective shear modulus of 42.1 GPa and a Poisson's ratio of 0.46 for the basal $(0001)_\varepsilon$ plane of ε-martensite.

The splitting of a perfect dislocation in ε-martensite into two Shockley partial dislocations can be clearly observed in the inset bright-field image in Fig. A.2a. The Figs. A.2b and A.2c show the WBDF images of a ε-martensite plate after 5% thickness reduction using the g = $[10\bar{1}0]_\varepsilon$ and g = $[0002]_\varepsilon$, respectively. While the perfect and Shockley partial dislocations are visible for the $g_\varepsilon = [10\bar{1}0]$, they are invisible for g = $[0002]_\varepsilon$ (inset Fig. A.2c). Using the $g.b = 0$ invisibility criteria, the dislocations were revealed to be of the basal type with the Burgers vector of perfect dislocation, b = $\frac{a}{3}[11\bar{2}0]_\varepsilon$ and Shockley partial dislocation, b = $\frac{a}{3}[10\bar{1}0]_\varepsilon, \frac{a}{3}[\bar{1}100]_\varepsilon$.

The Burgers vector of the perfect dislocation was calculated as 0.254 nm and 0.147 nm for the perfect and Shockley partial dislocations, respectively, which in turn are associated with the formation of I_2 -type ε-ISFs. The lattice parameters of ε-martensite (a_ε = 0.2545 nm, c_ε = 0.414 nm) used for calculating the Burgers vectors of the perfect and Shockley partial dislocations was obtained from the Rietveld refinement of the neutron diffraction patterns of the same steel composition [24].

Fig. A.2d shows the distribution of the measured width of the Shockley partial dislocations to the angle between the Burgers vector and the dislocation line vector along with the theoretical separations of Shockley partial dislocations for a range of ε-SFE. Using Eq. A1, the ε-SFE for I_2 -type stacking faults was calculated as 4.6 ± 1.4 mJ/m^2.

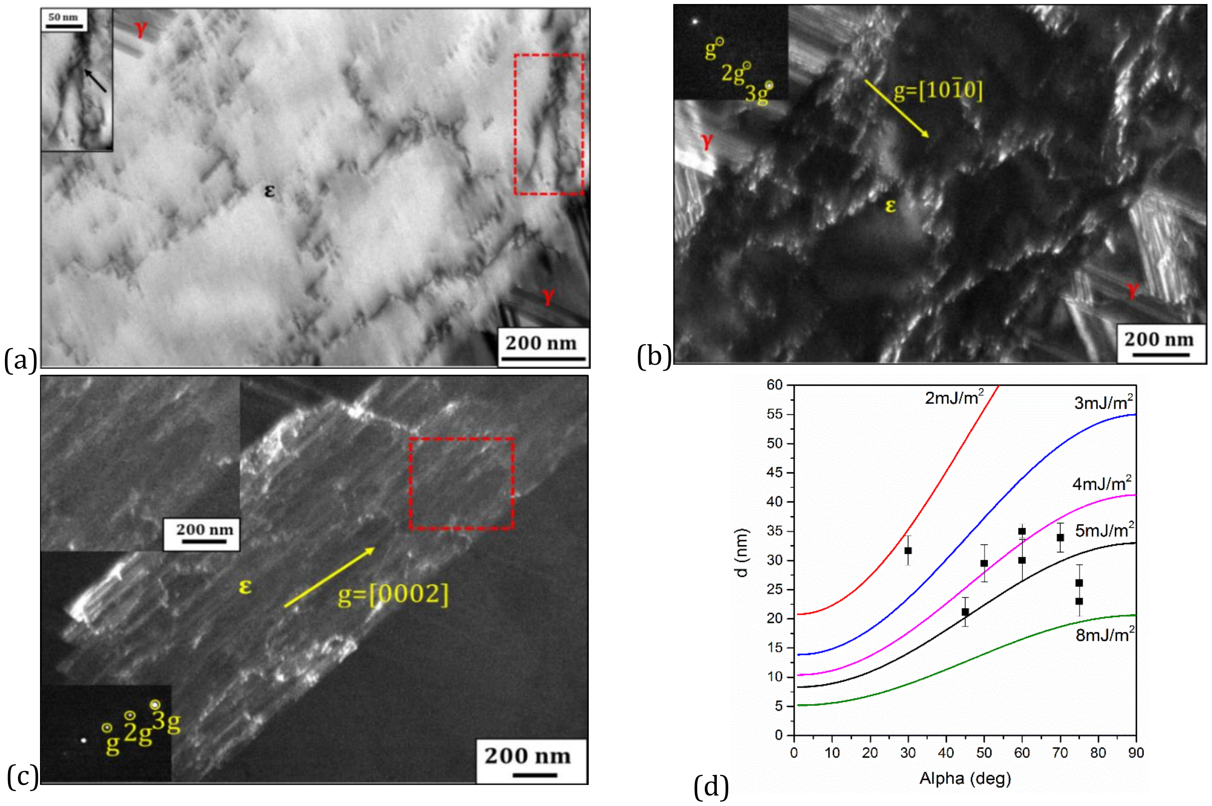

Figure A.2: Representative (a) bright-field image, (b, c) weak beam dark-field images and (d) the distribution of the measured width of the Shockley partial dislocations with respect to the angle between the Burgers vector and the dislocation line vector for ε-martensite after 5% thickness reduction. The inset diffraction patterns in Figs. A.2b, A.2c are from the regions demarcated by red dashed rectangles/squares in Figs. A.2a, A.2c, respectively. The inset diffraction patterns in Figs. A.2b, A.2c use $g = [10\bar{1}0]_{\varepsilon}$ and $g = [0002]_{\varepsilon}$.

The Shockley partial dislocations in Fig. A.2a are observed to be non-parallel to each other producing a non-equilibrium dislocation spacing between the Shockley partial dislocations. This can be attributed to the interaction of Shockley partial dislocations with other dislocations in the ε-martensite grain. Also, the action of image forces on the Shockley partial dislocations can lead to the non-equilibrium spacing between the Shockley partial dislocations. Thus in the present case, the calculated ε-SFE for I_2 -type stacking faults using the non-equilibrium dislocation spacing is lower than when measured under equilibrium Shockley partial dislocations spacing. This can be a possible reason for the lower calculated values of ε-SFE of I_2 -type stacking faults compared to that of the SFE values of I_2 -type stacking faults determined using the density functional theory/first principle calculations [219, 270].

REFERENCES

[1] C. Qiu, The 'Solute-Drag' effect on migrating interfaces during solid-state phase transformations, PhD Thesis, Monash University, Melboure, Australia, 2013.

[2] M. Askari-Paykani, H.R. Shahverdi, R. Miresmaeili, First and third generations of advanced high-strength steels in a FeCrNiBSi system, Journal of Materials Processing Technology 238 (2016) 383-394.

[3] H. Aydin, E. Essadiqi, I.-H. Jung, S. Yue, Development of 3rd generation AHSS with medium Mn content alloying compositions, Materials Science and Engineering: A 564 (2013) 501-508.

[4] D.K. Matlock, J.G. Speer, Third generation of AHSS: microstructure design concepts, Microstructure and texture in steels, Springer, 2009, pp. 185-205.

[5] W.S. Yang, C.M. Wan, The influence of aluminium content to the stacking fault energy in Fe-Mn-Al-C alloy system, Journal of Materials Science 25(3) (1990) 1821-1823.

[6] K. Tsuzaki, S. Fukasaku, Y. Tomota, T. Maki, Effect of prior deformation of austenite on the γ→ ε martensitic transformation in Fe–Mn alloys, Materials Transactions, JIM 32(3) (1991) 222-228.

[7] A.A. Gazder, A.A. Saleh, M.J.B. Nancarrow, D.R.G. Mitchell, E.V. Pereloma, A transmission Kikuchi diffraction study of a cold-rolled and annealed Fe–17Mn–2Si–3Al–1Ni–0.06C wt.% steel, Steel Research International 86(10) (2015) 1204-1214.

[8] Y. Lü, B. Hutchinson, D.A. Molodov, G. Gottstein, Effect of deformation and annealing on the formation and reversion of ε-martensite in an Fe–Mn–C alloy, Acta Materialia 58(8) (2010) 3079-3090.

[9] F. Berrenberg, C. Haase, L.A. Barrales-Mora, D.A. Molodov, Enhancement of the strength-ductility combination of twinning-induced/transformation-induced plasticity steels by reversion annealing, Materials Science and Engineering: A 681 (2017) 56-64.

[10] J. Kowalska, W. Ratuszek, M. Witkowska, A. Zielińska-Lipiec, Development of microstructure and texture in Fe–26Mn–3Si–3Al alloy during cold-rolling and annealing, Journal of Alloys and Compounds 615, Supplement 1 (2014) S583-S586.

[11] J. Kowalska, W. Ratuszek, M. Witkowska, A. Zielińska-Lipiec, T. Tokarski, Microstructure and texture characteristics of the metastable Fe–21Mn–3Si–3Al alloy after cold deformation, Journal of Alloys and Compounds 643, Supplement 1 (2015) S39-S45.

[12] O. Kwon, K.Y. Lee, G.S. Kim, K.G. Chin, New trends in advanced high strength steel developments for automotive application, Materials Science Forum, Trans Tech Publ, 2010, pp. 136-141.

[13] A.A. Saleh, Recrystallisation and deformation behaviour of TWinning Induced Plasticity (TWIP) steel, PhD Thesis, University of Wollongong, Wollongong, Australia, 2012.

[14] T. Kikuchi, S. Kajiwara, Y. Tomota, Microscopic studies on stress-induced martensite transformation and its reversion in an Fe-Mn-Si-Cr-Ni shape memory alloy, Materials Transactions, JIM 36(6) (1995) 719-728.

[15] H. Fujita, S. Ueda, Stacking faults and fcc (γ)→ hcp (ϵ) transformation in 18/8-type stainless steel, Acta Metallurgica 20(5) (1972) 759-767.

[16] Y.F. Shen, X.X. Li, X. Sun, Y.D. Wang, L. Zuo, Twinning and martensite in a 304 austenitic stainless steel, Materials Science and Engineering: A 552 (2012) 514-522.

[17] O. Bouaziz, S. Allain, C.P. Scott, P. Cugy, D. Barbier, High manganese austenitic twinning induced plasticity steels: A review of the microstructure properties relationships, Current Opinion in Solid State and Materials Science 15(4) (2011) 141-168.

[18] J. Wittig, J. Benzing, M. Beigmohamadi, M. Lipinska, J. Mayer, Investigation of the deformation mechanisms and defects in high-Mn austenitic steel, European Microscopy Congress 2016: Proceedings, Wiley-VCH Verlag GmbH & Co. KGaA2016.

[19] S. Allain, J.P. Chateau, O. Bouaziz, S. Migot, N. Guelton, Correlations between the calculated stacking fault energy and the plasticity mechanisms in Fe–Mn–C alloys, Materials Science and Engineering: A 387-389 (2004) 158-162.

[20] K.-T. Park, K.G. Jin, S.H. Han, S.W. Hwang, K. Choi, C.S. Lee, Stacking fault energy and plastic deformation of fully austenitic high manganese steels: effect of Al addition, Materials Science and Engineering: A 527(16) (2010) 3651-3661.

[21] G. Frommeyer, U. Brüx, P. Neumann, Supra-ductile and high-strength manganese-TRIP/TWIP steels for high energy absorption purposes, ISIJ international 43(3) (2003) 438-446.

[22] K.H. Kwon, B.-C. Suh, S.-I. Baik, Y.-W. Kim, J.-K. Choi, N.J. Kim, Deformation behavior of duplex austenite and ε-martensite high-Mn steel, Science and Technology of Advanced Materials 14(1) (2013) 014204.

[23] K. Sato, M. Ichinose, Y. Hirotsu, Y. Inoue, Effects of deformation induced phase transformation and twinning on the mechanical properties of austenitic Fe–Mn–Al alloys, ISIJ international 29(10) (1989) 868-877.

[24] A.A. Saleh, D.W. Brown, E.V. Pereloma, B. Clausen, C.H.J. Davies, C.N. Tomé, A.A. Gazder, An in-situ neutron diffraction study of a multi-phase transformation and twinning-induced plasticity steel during cyclic loading, Applied Physics Letters 106(17) (2015) 171911.

[25] A. Rollett, F.J. Humphreys, G.S. Rohrer, M. Hatherly, Recrystallization and related annealing phenomena, Elsevier Science, oxford, United Kingdom, , 2004.

[26] O. Grässel, L. Krüger, G. Frommeyer, L.W. Meyer, High strength Fe–Mn–(Al, Si) TRIP/TWIP steels development — properties — application, International Journal of Plasticity 16(10) (2000) 1391-1409.

[27] K. Tomimura, S. Takaki, Y. Tokunaga, Reversion mechanism from deformation induced martensite to austenite in metastable austenitic stainless steels, ISIJ International 31(12) (1991) 1431-1437.

[28] Y.H. Wen, H. Peng, H. Si, R. Xiong, D. Raabe, A novel high manganese austenitic steel with higher work hardening capacity and much lower impact deformation than Hadfield manganese steel, Materials & Design 55 (2014) 798-804.

[29] Y.-K. Lee, H.-C. Shin, D.-S. Leem, J.-Y. Choi, W. Jin, C.-S. Choi, Reverse transformation mechanism of martensite to austenite and amount of retained austenite after reverse transformation in Fe-3Si-13Cr-7Ni (wt.%) martensitic stainless steel, Materials Science and Technology 19(3) (2003) 393-398.

[30] F. Mompiou, J. Wu, W.-Z. Zhang, A preliminary in-situ TEM study of martensite/austenite interface migration in an Fe-20Ni-5.4Mn alloy, Materials Today: Proceedings 2 (2015) S651-S654.

[31] J. Wu, J.M. Howe, W.Z. Zhang, An in situ transmission electron microscopy study of interface growth during martensitic transformation in an Fe–Ni–Mn alloy, Acta Mater. 59(8) (2011) 3297-3303.

[32] D. De Knijf, M.J. Santofimia, H. Shi, V. Bliznuk, C. Föjer, R. Petrov, W. Xu, In situ austenite–martensite interface mobility study during annealing, Acta Materialia 90 (2015) 161-168.

[33] H.B. Jiang, X.N. Luo, X.Y. Zhong, H.H. Zhou, C.Y. Wang, J. Shi, H. Dong, In-situ microstructural evolutions of 5Mn steel at elevated temperature in a transmission electron microscope, Journal of Iron and Steel Research, International 24(11) (2017) 1109-1114.

[34] Y. Tomota, Y. Morioka, W. Nakagawara, Epsilon martensite to austenite reversion and related phenomena in Fe- 24Mn and Fe-24Mn-6Si alloys, Acta Materialia 46(4) (1998) 1419-1426.

[35] G. Krauss, Fine structure of austenite produced by the reverse martensitic transformation, Acta Metallurgica 11(6) (1963) 499-509.

[36] S. Lee, B.C. De Cooman, Influence of intra-granular ferrite on the tensile behavior of intercritically annealed 12 pct Mn TWIP+ TRIP steel, Metallurgical and Materials Transactions A 46(3) (2015) 1012-1018.

[37] M. Koyama, T. Sawaguchi, K. Tsuzaki, Premature fracture mechanism in an Fe-Mn-C austenitic steel, Metallurgical and Materials Transactions A 43(11) (2012) 4063-4074.

[38] M. Koyama, T. Sawaguchi, K. Tsuzaki, Effect of deformation temperature on tensile properties in a pre-cooled Fe–Mn–C austenitic steel, Materials Science and Engineering: A 556 (2012) 331-336.

[39] K.H. Kwon, J.S. Jeong, J.-K. Choi, Y.M. Koo, Y. Tomota, N.J. Kim, In-situ neutron diffraction analysis on deformation behavior of duplex high Mn steel containing austenite and ε-martensite, Metals and Materials International 18(5) (2012) 751-755.

[40] D.P. Escobar, S.S.F. Dafé, D.B. Santos, Martensite reversion and texture formation in 17Mn-0.06C TRIP/TWIP steel after hot cold rolling and annealing, Journal of Materials Research and Technology 4(2) (2015) 162-170.

[41] M. Eskandari, A. Zarei-Hanzaki, M. Yadegari, N. Soltani, A. Asghari, In situ identification of elastic–plastic strain distribution in a microalloyed transformation induced plasticity steel using digital image correlation, Optics and Lasers in Engineering 54 (2014) 79-87.

[42] M. Eskandari, M.R. Yadegari-Dehnavi, A. Zarei-Hanzaki, M.A. Mohtadi-Bonab, R. Basu, J.A. Szpunar, In-situ strain localization analysis in low density transformation-twinning induced plasticity steel using digital image correlation, Optics and Lasers in Engineering 67 (2015) 1-16.

[43] J.-K. Kim, B.C. De Cooman, Stacking fault energy and deformation mechanisms in Fe-xMn-0.6 C-yAl TWIP steel, Materials Science and Engineering: A 676 (2016) 216-231.

[44] W.S. Choi, B.C. De Cooman, S. Sandlöbes, D. Raabe, Size and orientation effects in partial dislocation-mediated deformation of twinning-induced plasticity steel micro-pillars, Acta Materialia 98 (2015) 391-404.

[45] W.S. Choi, B.C. De Cooman, Effect of carbon on the damping capacity and mechanical properties of thermally trained Fe-Mn based high damping alloys, Materials Science and Engineering: A 700 (2017) 641-648.

[46] Y. Lü, D.A. Molodov, G. Gottstein, Recrystallization kinetics and microstructure evolution during annealing of a cold-rolled Fe–Mn–C alloy, Acta Materialia 59(8) (2011) 3229-3243.

[47] J.K. Kim, B.C. De Cooman, Observation of dislocations with a Burgers vector containing a <c> component in martensitic hcp ε Fe-17%Mn, Scripta Materialia 128 (2017) 78-82.

[48] A.A. Gazder, A.A. Saleh, A.G. Kostryzhev, E.V. Pereloma, Application of transmission Kikuchi diffraction to a multi-phase TRIP-TWIP steel, Materials Today: Proceedings 2, Supplement 3 (2015) S647-S650.

[49] J. Kowalska, W. Ratuszek, M. Witkowska, A. Zielińska-Lipiec, Influence of cold plastic deformation on the development of the texture in high-manganese austenitic steel, Solid State Phenomena, 2013, pp. 115-120.

[50] X. Zhang, T. Sawaguchi, K. Ogawa, F. Yin, X. Zhao, A structure created by intersecting ϵ martensite variant plates in a high-Manganese steel, Philosophical Magazine 91(35) (2011) 4410-4426.

[51] X. Zhang, T. Sawaguchi, Twinning of deformation-induced ε-martensite in Fe-30Mn-6Si shape memory alloy, Acta Materialia 143 (2018) 237-247.

[52] J. Chen, W.N. Zhang, Z.Y. Liu, G.D. Wang, Microstructural evolution and deformation mechanism of a Fe-15Mn alloy investigated by electron back-scattered diffraction and transmission electron microscopy, Mater. Sci. Eng. A 698 (2017) 198-205.

[53] G. Kurdjumow, G. Sachs, Über den mechanismus der stahlhärtung, Zeitschrift für Physik 64(5) (1930) 325-343.

[54] Y.K. Lee, C.S. Choi, Driving force for γ → ε martensitic transformation and stacking fault energy of γ in Fe-Mn binary system, Metallurgical and Materials Transactions A 31(2) (2000) 355-360.

[55] Y.S. Chang, C.H. Shih, Acta Metallurgica Sinica (English Letters) 7 (1964) 285.

[56] P.Y. Volosevich, V. Gridnev, Y.N. Petrov, Manganese influence on stacking-fault energy in iron-manganese alloys, Fizika metallov i metallovedenie 42(2) (1976) 372-376.

[57] L. Chen, Y. Zhao, X. Qin, Some aspects of high manganese twinning-induced plasticity (TWIP) steel, A review, Acta Metallurgica Sinica (English Letters) 26(1) (2013) 1-15.

[58] J.K. Jung, O.Y. Lee, Y.K. Park, D.E. Kim, K.G. Jin, S.K. Kim, K.H. Song, Journal Korean Institute of Metals and Materials 46 (2008) 627.

[59] I. Gutierrez-Urrutia, D. Raabe, Influence of Al content and precipitation state on the mechanical behavior of austenitic high-Mn low-density steels, Scripta Materialia 68(6) (2013) 343-347.

[60] B.C. De Cooman, O. Kwon, K.G. Chin, State-of-the-knowledge on TWIP steel, Materials Science and Technology 28(5) (2012) 513-527.

[61] J.W. Lee, C.C. Wu, T.F. Liu, The influence of Cr alloying on microstructures of Fe-Al-Mn-Cr alloys, Scripta Materialia 50(11) (2004) 1389-1393.

[62] G.D. Tsay, C.L. Lin, C.G. Chao, T.F. Liu, A new austenitic FeMnAlCrC alloy with high-strength, high-ductility, and moderate corrosion resistance, Materials Transactions 51(12) (2010) 2318-2321.

[63] T.F. Liu, C.M. Wan, DO3 structure in an Fe-Al-Mn-Cr alloy, Scripta Metallurgica 19(7) (1985) 805-810.

[64] T.F. Liu, C.M. Wan, α-Mn structure in a Fe-Al-Mn-Cr alloy, Scripta Metallurgica 19(6) (1985) 727-732.

[65] T.F. Liu, C.C. Wu, β-Mn structure in an Fe-Al-Mn-Cr alloy, Scripta Metallurgica 23(7) (1989) 1087-1092.

[66] S. Takaki, T. Furuya, Y. Tokunaga, Effect of Si and Al additions on the low temperature toughness and fracture mode of Fe-27Mn alloys, ISIJ International 30(8) (1990) 632-638.

[67] Y.N. Petrov, Effect of carbon and nitrogen on the stacking fault energy of high-alloyed iron-based austenite, Zeitschrift für Metallkunde 94(9) (2003) 1012-1016.

[68] I.A. Yakubtsov, A. Ariapour, D.D. Perovic, Effect of nitrogen on stacking fault energy of f.c.c. iron-based alloys, Acta Materialia 47(4) (1999) 1271-1279.

[69] R.E. Schramm, R.P. Reed, Stacking fault energies of seven commercial austenitic stainless steels, Metallurgical Transactions A 6(7) (1975) 1345-1351.

[70] B.X. Huang, X.D. Wang, L. Wang, Y.H. Rong, Effect of nitrogen on stacking fault formation probability and mechanical properties of twinning-induced plasticity steels, Metallurgical and Materials Transactions A 39(4) (2008) 717-724.

[71] S.S.F. Dafé, F.L. Sicupira, F.C.S. Matos, N.S. Cruz, D.R. Moreira, D.B. Santos, Effect of cooling rate on (ε, α') martensite formation in twinning/transformation-induced plasticity Fe-17Mn-0.06 C steel, Materials Research 16(6) (2013) 1229-1236.

[72] J. Kim, S.-J. Lee, B.C. De Cooman, Effect of Al on the stacking fault energy of Fe–18Mn–0.6C twinning-induced plasticity, Scripta Materialia 65(4) (2011) 363-366.

[73] I.-C. Jung, L. Cho, B.C. De Cooman, In situ observation of the influence of Al on deformation-induced twinning in TWIP steel, ISIJ International 55(4) (2015) 870-876.

[74] K. Jeong, J.-E. Jin, Y.-S. Jung, S. Kang, Y.-K. Lee, The effects of Si on the mechanical twinning and strain hardening of Fe–18Mn–0.6C twinning-induced plasticity steel, Acta Materialia 61(9) (2013) 3399-3410.

[75] H. Idrissi, K. Renard, L. Ryelandt, D. Schryvers, P.J. Jacques, On the mechanism of twin formation in Fe–Mn–C TWIP steels, Acta Materialia 58(7) (2010) 2464-2476.

[76] D.T. Pierce, J.A. Jiménez, J. Bentley, D. Raabe, C. Oskay, J. Wittig, The influence of manganese content on the stacking fault and austenite/ε-martensite interfacial energies in Fe–Mn–(Al–Si) steels investigated by experiment and theory, Acta Materialia 68 (2014) 238-253.

[77] X. Tian, Y. Zhang, Effect of Si content on the stacking fault energy in γ-Fe–Mn–Si–C alloys: part I. X-ray diffraction line profile analysis, Materials Science and Engineering: A 516(1) (2009) 73-77.

[78] R.D.K. Misra, S. Nayak, S.A. Mali, J.S. Shah, M.C. Somani, L.P. Karjalainen, On the significance of nature of strain-induced martensite on phase-reversion-induced nanograined/ultrafine-grained austenitic stainless steel, Metallurgical and Materials Transactions A 41(1) (2010) 3-12.
[79] X.-Z. Wu, R. Wang, S.-F. Wang, Q.-Y. Wei, Ab initio calculations of generalized-stacking-fault energy surfaces and surface energies for FCC metals, Applied Surface Science 256(21) (2010) 6345-6349.
[80] L. Vitos, J.O. Nilsson, B. Johansson, Alloying effects on the stacking fault energy in austenitic stainless steels from first-principles theory, Acta Materialia 54(14) (2006) 3821-3826.
[81] D.T. Pierce, J.A. Jiménez, J. Bentley, D. Raabe, J.E. Wittig, The influence of stacking fault energy on the microstructural and strain-hardening evolution of Fe–Mn–Al–Si steels during tensile deformation, Acta Materialia 100 (2015) 178-190.
[82] D.T. Pierce, J. Bentley, J.A. Jiménez, J.E. Wittig, Stacking fault energy measurements of Fe–Mn–Al–Si austenitic twinning-induced plasticity steels, Scripta Materialia 66(10) (2012) 753-756.
[83] L. Rémy, A. Pineau, Twinning and strain-induced f.c.c. → h.c.p. transformation on the mechanical properties of Co-Ni-Cr-Mo alloys, Materials Science and Engineering 26(1) (1976) 123-132.
[84] X.M. Qin, L.Q. Chen, H.S. Di, W. Deng, Some aspects of high Manganese Twinning-Induced Plasticity (TWIP) steel, Acta Metallurgica Sinica (in Chinese) 47 (2011).
[85] D. Hull, D.J. Bacon, Introduction to dislocations, Butterworth-Heinemann, Oxford, United Kingdom, , 2011.
[86] L. Han, Q. An, R. Fu, L. Zheng, S. Luo, Melting of defective Cu with stacking faults, The Journal of chemical physics 130(2) (2009) 024508.
[87] C. Johnson, Diffraction by face-centered cubic crystals containing extrinsic stacking faults, Acta Crystallographica 16(6) (1963) 490-497.
[88] J. Weertman, J.R. Weertman, Elementary dislocation theory, Oxford univeristy press, Oxford, United Kingdom, , 1992.
[89] Z.-X. Qiao, Y.-C. Liu, J.-H. Wang, Y. Meng, D.-A. Wang, Effect of pre-strain on morphology of stress induced epsilon martensite in an Fe-Mn-Si shape memory alloy, Journal of Materials Science and Engineering 26(1) (2008) 46.
[90] K.K. Chawla, M.A. Meyers, Mechanical behavior of materials, Cambridge university press, 2009.
[91] S. Mahajan, G.Y. Chin, Formation of deformation twins in f.c.c. crystals, Acta Metallurgica 21(10) (1973) 1353-1363.

[92] G. Casillas, A.A. Gazder, E.V. Pereloma, A.A. Saleh, Evidencing extrinsic stacking faults in twinning-induced plasticity steel, Materials Characterization 123 (2017) 275-281.

[93] J.-S. Kim, J.B. Jeon, J.E. Jung, K.-K. Um, Y.W. Chang, Effect of deformation induced transformation of epsilon-martensite on ductility enhancement in a Fe-12 Mn steel at cryogenic temperatures, Metals and Materials International 20(1) (2014) 41.

[94] J.A. Venables, The electron microscopy of deformation twinning, Journal of Physics and Chemistry of Solids 25(7) (1964) 685-692.

[95] P.M. Anderson, J.P. Hirth, J. Lothe, Theory of dislocations, Cambridge university press, Cambridge, United Kingdom, , 2017.

[96] I. Karaman, H. Sehitoglu, Y.I. Chumlyakov, H.J. Maier, I.V. Kireeva, Extrinsic stacking faults and twinning in hadfield manganese steel single crystals, Scripta Materialia 44(2) (2001) 337-343.

[97] D.A. Porter, K.E. Easterling, Phase transformations in metals and alloys, Taylor & Francis, Boca Raton, United States of America, , 1992.

[98] S. Takaki, H. Nakatsu, Y. Tokunaga, Effects of austenite grain size on epsilon martensitic transformation in Fe-15%Mn alloy, Materials Transactions, JIM 34(6) (1993) 489-495.

[99] R.D.K. Misra, S. Nayak, S.A. Mali, J.S. Shah, M.C. Somani, L.P. Karjalainen, On the significance of nature of strain-induced Martensite on phase-reversion-induced nanograined/ultrafine-grained austenitic stainless steel, Metallurgical and Materials Transactions A 41(1) (2009) 3.

[100] M. Humbert, B. Petit, B. Bolle, N. Gey, Analysis of the γ–ε–α′ variant selection induced by 10% plastic deformation in 304 stainless steel at– 60° C, Materials Science and Engineering: A 454 (2007) 508-517.

[101] N. Bergeon, G. Guenin, C. Esnouf, Characterization of the stress-induced ε-martensite in a Fe–Mn–Si–Cr–Ni shape memory alloy: microstructural observation at different scales, mechanism of formation and growth, Materials Science and Engineering: A 238(2) (1997) 309-316.

[102] A.K. De, D.C. Murdock, M.C. Mataya, J.G. Speer, D.K. Matlock, Quantitative measurement of deformation-induced martensite in 304 stainless steel by X-ray diffraction, Scripta Materialia 50(12) (2004) 1445-1449.

[103] G.B. Olson, M. Cohen, A mechanism for the strain-induced nucleation of martensitic transformations, Journal of the Less Common Metals 28(1) (1972) 107-118.

[104] Z. Ding, S. Li, W. Liu, Y. Zhao, Modeling of stacking fault energy in hexagonal-close-packed metals, Advances in Materials Science and Engineering 2015 (2015) 8.

[105] Z. Nishiyama, M.E. Fine, M. Meshii, C.M. Wayman, Martensitic transformation, Academic Press, New York, United States of America, , 1978.

[106] L. Bracke, L. Kestens, J. Penning, Transformation mechanism of α′-martensite in an austenitic Fe–Mn–C–N alloy, Scripta Materialia 57(5) (2007) 385-388.

[107] E. Pereloma, A. Gazder, I. Timokhina, Retained austenite: transformation-induced plasticity, Encyclopedia of Iron, Steel, and Their Alloys (2016) 3088-3103.

[108] W.G. Burgers, On the process of transition of the cubic-body-centered modification into the hexagonal-close-packed modification of zirconium, Physica 1(7) (1934) 561-586.

[109] L. Germain, S.R. Dey, M. Humbert, N. Gey, Determination of parent orientation maps in advanced titanium based alloys, Journal of Microscopy 227(3) (2007) 284-291.

[110] S. Morito, H. Tanaka, R. Konishi, T. Furuhara, T. Maki, The morphology and crystallography of lath martensite in Fe-C alloys, Acta Materialia 51(6) (2003) 1789-1799.

[111] S. Li, G. Zhu, Y. Kang, Effect of substructure on mechanical properties and fracture behavior of lath martensite in 0.1C–1.1Si–1.7Mn steel, Journal of Alloys and Compounds 675 (2016) 104-115.

[112] A. Stormvinter, G. Miyamoto, T. Furuhara, P. Hedström, A. Borgenstam, Effect of carbon content on variant pairing of martensite in Fe–C alloys, Acta Materialia 60(20) (2012) 7265-7274.

[113] J.S. Bowles, J.K. Mackenzie, The crystallography of martensite transformations I, Acta Metallurgica 2(1) (1954) 129-137.

[114] J.R. Patel, M. Cohen, Criterion for the action of applied stress in the martensitic transformation, Acta Metallurgica 1(5) (1953) 531-538.

[115] R. Naraghi, Martensitic transformation in austenitic stainless steels, 2009.

[116] C. Haase, L.A. Barrales-Mora, D.A. Molodov, G. Gottstein, Texture evolution of a cold-rolled Fe-28Mn-0.28 C TWIP steel during recrystallization, Materials Science Forum, Trans Tech Publ, 2013, pp. 213-216.

[117] H.R. Wenk, S. Matthies, R.J. Hemley, H.K. Mao, J. Shu, The plastic deformation of iron at pressures of the earth's inner core, Nature 405(6790) (2000) 1044-1047.

[118] H. Ding, H. Ding, D. Song, Z. Tang, P. Yang, Strain hardening behavior of a TRIP/TWIP steel with 18.8% Mn, Materials Science and Engineering: A 528(3) (2011) 868-873.

[119] H. Beladi, G.S. Rohrer, A.D. Rollett, V. Tari, P.D. Hodgson, The distribution of intervariant crystallographic planes in a lath martensite using five macroscopic parameters, Acta Materialia 63 (2014) 86-98.

[120] O. Grässel, L. Krüger, G. Frommeyer, L. Meyer, High strength Fe–Mn–(Al, Si) TRIP/TWIP steels development—properties—application, International Journal of Plasticity 16(10) (2000) 1391-1409.

[121] S. Martin, S. Wolf, U. Martin, L. Krüger, Influence of temperature on phase transformation and deformation mechanisms of cast CrMnNi-TRIP/TWIP steel, Solid State Phenomena, 2011, pp. 172-177.

[122] X. Liang, J.R. McDermid, O. Bouaziz, X. Wang, J.D. Embury, H.S. Zurob, Microstructural evolution and strain hardening of Fe–24Mn and Fe–30Mn alloys during tensile deformation, Acta Materialia 57(13) (2009) 3978-3988.

[123] S. Lee, Y. Estrin, B.C. De Cooman, Effect of the strain rate on the TRIP–TWIP transition in austenitic Fe-12 pct Mn-0.6 pct C TWIP steel, Metallurgical and Materials Transactions A 45(2) (2014) 717-730.

[124] R.D. Doherty, D.A. Hughes, F.J. Humphreys, J.J. Jonas, D.J. Jensen, M.E. Kassner, W.E. King, T.R. McNelley, H.J. McQueen, A.D. Rollett, Current issues in recrystallization: A review, Materials Science and Engineering: A 238(2) (1997) 219-274.

[125] C. Celada-Casero, B.M. Huang, M.M. Aranda, J.R. Yang, D.S. Martin, Mechanisms of ultrafine-grained austenite formation under different isochronal conditions in a cold-rolled metastable stainless steel, Materials Characterization 118(Supplement C) (2016) 129-141.

[126] J. Han, Y.-K. Lee, The effects of the heating rate on the reverse transformation mechanism and the phase stability of reverted austenite in medium Mn steels, Acta Materialia 67(Supplement C) (2014) 354-361.

[127] K. Tominiura, Y. Kawauchi, S. Takaki, Y. Tokunaga, Effect of prior deformation on grain refining process of martensitic shear reversion in metastable austenitic stainless steel, Tetsu-to-Hagane 77(9) (1991) 1519-1526.

[128] S. Rajasekhara, L.P. Karjalainen, A. Kyröläinen, P.J. Ferreira, Microstructure evolution in nano/submicron grained AISI 301LN stainless steel, Mater. Sci. Eng. A 527(7) (2010) 1986-1996.

[129] M.O. Spindola, S.S.F. Dafé, D.J. Carmo, D.B. Santos, Microstructural characterization and mechanical behavior of a low-carbon 17%Mn steel, Materials Research 17 (2014) 694-699.

[130] R.D.K. Misra, Z. Zhang, P.K.C. Venkatasurya, M.C. Somani, L.P. Karjalainen, Martensite shear phase reversion-induced nanograined/ultrafine-grained Fe–16Cr–10Ni alloy: The effect of interstitial alloying elements and degree of austenite stability on phase reversion, Materials Science and Engineering: A 527(29) (2010) 7779-7792.

[131] P.T. Wakefield, M. Hatherly, Nucleation and recrystallization texture development in rolled Cu–10Zn brass, Metal Science 17(2) (1983) 55-62.

[132] J. Huber, M. Hatherly, Nucleation of recrystallized grains in heavily cold-worked α-brass, Metal Science 13(12) (1979) 665-669.

[133] K. Rajan, Nucleation of recrystallization in a Co-Cr-Mo alloy, Metallurgical and Materials Transactions A 15(7) (1984) 1335-1338.

[134] D.P. Escobar, S.S.F. Dafé, K. Verbeken, D.B. Santos, Effect of the cold rolling reduction on the microstructural characteristics and mechanical behavior of a 0.06% C–17% Mn TRIP/TWIP steel, Steel Research International (2015).

[135] J. Han, Y.K. Lee, The effects of the heating rate on the reverse transformation mechanism and the phase stability of reverted austenite in medium Mn steels, Acta Mater. 67(Supplement C) (2014) 354-361.

[136] H. Koohdar, M. Nili-Ahmadabadi, M. Habibi-Parsa, H.R. Jafarian, T. Bhattacharjee, N. Tsuji, On the stability of reversely formed austenite and related mechanism of transformation in an Fe-Ni-Mn martensitic steel aided by electron backscattering diffraction and atom probe tomography, Metallurgical and Materials Transactions A 48(11) (2017) 5244-5257.

[137] P.R. Rios, F. Siciliano Jr, H.R.Z. Sandim, R.L. Plaut, A.F. Padilha, Nucleation and growth during recrystallization, Materials Research 8(3) (2005) 225-238.

[138] S.F. Medina, J.E. Mancilla, Static recrystallization of austenite and strain induced precipitation kinetics in titanium microalloyed steels, Acta Metallurgica et Materialia 42(12) (1994) 3945-3951.

[139] E. Palmiere, C. Garcia, A. DeArdo, The influence of niobium supersaturation in austenite on the static recrystallization behavior of low carbon microalloyed steels, Metallurgical and Materials Transactions A 27(4) (1996) 951-960.

[140] H. Miura, T. Sakai, A. Belyakov, G. Gottstein, M. Crumbach, J. Verhasselt, Static recrystallization of SiO 2-particle containing {011}<100> copper single crystals, Acta Materialia 51(6) (2003) 1507-1515.

[141] C. Haase, M. Kühbach, L.A. Barrales-Mora, S.L. Wong, F. Roters, D.A. Molodov, G. Gottstein, Recrystallization behavior of a high-Manganese steel: experiments and simulations, Acta Materialia 100 (2015) 155-168.

[142] K.K. Jee, J.H. Han, W.Y. Jang, Measurement of volume fraction of ε martensite in Fe–Mn based alloys, Materials Science and Engineering: A 378(1–2) (2004) 319-322.

[143] F. de las Cuevas, A.F. M. Reis, G. Pratolongo, L. P. Karjalainen, V. García Navas, J.G. Sevillano, Kinetics of recrystallization and grain growth of cold rolled TWIP steel Advanced Materials Research 89-91 (2010) 153-158.

[144] M. H Razmpoosh, A. Zarei-Hanzaki, N. Haghdadi, J.-H. Cho, W.J. Kim, S. Heshmati-Manesh, Thermal stability of an ultrafine-grained dual phase TWIP steel, Materials Science and Engineering: A 638(0) (2015) 5-14.

[145] V. Randle, Mechanism of twinning-induced grain boundary engineering in low stacking-fault energy materials, Acta Materialia 47(15) (1999) 4187-4196.

[146] A.A. Saleh, E.V. Pereloma, A.A. Gazder, Texture evolution of cold-rolled and annealed Fe–24Mn–3Al–2Si–1Ni–0.06C TWIP steel, Materials Science and Engineering: A 528(13–14) (2011) 4537-4549.

[147] B.X. Huang, X.D. Wang, Y.H. Rong, L. Wang, L. Jin, Mechanical behavior and martensitic transformation of an Fe–Mn–Si–Al–Nb alloy, Materials Science and Engineering: A 438(Supplement C) (2006) 306-311.

[148] H. Ding, Z.Y. Tang, W. Li, M. Wang, D. Song, Microstructures and mechanical properties of Fe-Mn-(Al, Si) TRIP/TWIP steels, Journal of Iron and Steel Research, International 13(6) (2006) 66-70.

[149] J. Han, S.-J. Lee, J.-G. Jung, Y.-K. Lee, The effects of the initial martensite microstructure on the microstructure and tensile properties of intercritically annealed Fe–9Mn–0.05C steel, Acta Materialia 78(Supplement C) (2014) 369-377.

[150] M.C. McGrath, D.C. Van Aken, N. Medvedeva, J.E. Medvedeva, Work hardening behavior in steel with multiple TRIP mechanisms, Metallurgical and Materials Transactions A 44(10) (2013) 4634-4643.

[151] A. Pétein, P.J. Jacques, On the relationship between mechanical properties and mechanisms of plastic deformation in metastable austenitic steels, Steel Research International 75(11) (2004) 724-729.

[152] H.C. Choi, T.K. Ha, H.C. Shin, Y.W. Chang, The formation kinetics of deformation twin and deformation induced ϵ-martensite in an austenitic Fe-C-Mn steel, Scripta Materialia 40(10) (1999) 1171-1177.

[153] P. Behjati, A. Kermanpur, L. Karjalainen, A. Järvenpää, M. Jaskari, H.S. Baghbadorani, A. Najafizadeh, A. Hamada, Influence of prior cold rolling reduction on microstructure and mechanical properties of a reversion annealed high-Mn austenitic steel, Materials Science and Engineering: A 650 (2016) 119-128.

[154] P. Behjati, A. Kermanpur, A. Najafizadeh, H.S. Baghbadorani, J.-G. Jung, Y.-K. Lee, Influence of precooling and deformation temperature on microstructure and mechanical properties in a high-Manganese austenitic steel, Materials Science and Engineering: A 614 (2014) 232-237.

[155] H.W. Yen, S.W. Ooi, M. Eizadjou, A. Breen, C.Y. Huang, H.K.D.H. Bhadeshia, S.P. Ringer, Role of stress-assisted martensite in the design of strong ultrafine-grained duplex steels, Acta Materialia 82 (2015) 100-114.

[156] S. Lee, B.C. De Cooman, Tensile behavior of intercritically annealed 10 pct Mn multi-phase steel, Metallurgical and Materials Transactions A 45(2) (2014) 709-716.

[157] B.C. De Cooman, S.J. Lee, S. Shin, E.J. Seo, J.G. Speer, Combined intercritical annealing and Q&P processing of medium Mn steel, Metallurgical and Materials Transactions A 48(1) (2017) 39-45.

[158] J. Hu, W. Cao, C. Wang, H. Dong, J. Li, Austenite stability and its effect on the ductility of the cold-rolled medium-Mn steel, ISIJ International 54(8) (2014) 1952-1957.

[159] D. Pérez Escobar, S. Silva Ferreira de Dafé, D. Brandão Santos, Martensite reversion and texture formation in 17Mn-0.06C TRIP/TWIP steel after hot cold rolling and annealing, Journal of Materials Research and Technology 4(2) (2015) 162-170.

[160] D.W. Suh, S.J. Park, C.H. Lee, S.J. Kim, Microstructure and mechanical behaviors of 0.1 C-13Mn metastable austenitic steel, Metallurgical and Materials Transactions A 40(2) (2009) 264-268.

[161] A. Arlazarov, M. Gouné, O. Bouaziz, A. Hazotte, G. Petitgand, P. Barges, Evolution of microstructure and mechanical properties of medium Mn steels during double annealing, Materials Science and Engineering: A 542(Supplement C) (2012) 31-39.

[162] O. Grässel, G. Frommeyer, C. Derder, H. Hofmann, Phase transformations and mechanical properties of Fe-Mn-Si-Al TRIP-steels, Le Journal de Physique IV 7(C5) (1997) 383-388.

[163] H.-W. Yen, S.W. Ooi, M. Eizadjou, A. Breen, C.-Y. Huang, H. Bhadeshia, S.P. Ringer, Role of stress-assisted martensite in the design of strong ultrafine-grained duplex steels, Acta Materialia 82 (2015) 100-114.

[164] X.G. Wang, L. Wang, M.X. Huang, Kinematic and thermal characteristics of Lüders and Portevin-Le Châtelier bands in a medium Mn transformation-induced plasticity steel, Acta Mater. 124 (2017) 17-29.

[165] X.G. Wang, M.X. Huang, Temperature dependence of Lüders strain and its correlation with martensitic transformation in a medium Mn transformation-induced plasticity steel, Journal of Iron and Steel Research, International 24(11) (2017) 1073-1077.

[166] A. Dutta, D. Ponge, S. Sandlöbes, D. Raabe, In situ µ-DIC measurements of strain partitioning in medium Mn steel, in: M.M.S. The Minerals (Ed.) Advanced High-strength Steels, TMS Annual Meeting & Exhibition, Springer International Publishing, Pheonix, Arizona, USA, 2018.

[167] C.C. Tasan, M. Diehl, D. Yan, C. Zambaldi, P. Shanthraj, F. Roters, D. Raabe, Integrated experimental–simulation analysis of stress and strain partitioning in multiphase alloys, Acta Materialia 81 (2014) 386-400.

[168] C.C. Tasan, J.P.M. Hoefnagels, M. Diehl, D. Yan, F. Roters, D. Raabe, Strain localization and damage in dual phase steels investigated by coupled in-situ deformation experiments and crystal plasticity simulations, International Journal of Plasticity 63 (2014) 198-210.

[169] D. Yan, C.C. Tasan, D. Raabe, High resolution in situ mapping of microstrain and microstructure evolution reveals damage resistance criteria in dual phase steels, Acta Materialia 96 (2015) 399-409.

[170] Y.B. Das, A.N. Forsey, T.H. Simm, K.M. Perkins, M.E. Fitzpatrick, S. Gungor, R.J. Moat, In situ observation of strain and phase transformation in plastically deformed 301 austenitic stainless steel, Materials & Design 112(Supplement C) (2016) 107-116.

[171] Y.B. Das, A.N. Forsey, T.H. Simm, K.M. Perkins, M.E. Fitzpatrick, S. Gungor, R.J. Moat, In situ observation of strain and phase transformation in plastically deformed 301 austenitic stainless steel, Materials & Design 112 (2016) 107-116.

[172] F. Di Gioacchino, J. Quinta da Fonseca, Plastic strain mapping with sub-micron resolution using digital image correlation, Experimental Mechanics 53(5) (2013) 743-754.

[173] B. Sun, N. Vanderesse, F. Fazeli, C. Scott, J. Chen, P. Bocher, M. Jahazi, S. Yue, Discontinuous strain-induced martensite transformation related to the Portevin-Le Chatelier effect in a medium manganese steel, Scripta Materialia 133(Supplement C) (2017) 9-13.

[174] M. Callahan, O. Hubert, F. Hild, A. Perlade, J.-H. Schmitt, Coincidence of strain-induced TRIP and propagative PLC bands in medium Mn steels, Materials Science and Engineering: A 704(Supplement C) (2017) 391-400.

[175] P.J. Jacques, Q. Furnémont, F. Lani, T. Pardoen, F. Delannay, Multiscale mechanics of TRIP-assisted multiphase steels: I. characterization and mechanical testing, Acta Materialia 55(11) (2007) 3681-3693.

[176] L.M. Roncery, S. Weber, W. Theisen, Mechanical properties of (20–30)Mn12Cr(0.56–0.7)CN corrosion resistant austenitic TWIP steels, Steel Research International 83(4) (2012) 307-314.

[177] P.D. Zavattieri, V. Savic, L.G. Hector, J.R. Fekete, W. Tong, Y. Xuan, Spatio-temporal characteristics of the Portevin–Le Châtelier effect in austenitic steel with twinning induced plasticity, International Journal of Plasticity 25(12) (2009) 2298-2330.

[178] M. Kuntz, Verformungsmechanismen hoch manganlegierter austenitischer TWIP-stähle, Thesis, Stuttgart University, Stuttgart, Germany, 2008.

[179] A. Bäumer, Verfestigungsverhalten von hochmanganhaltigen Stählen mit TWIP-Effekt / von Annette Bäumer, PhD Thesis, RWTH Aachen University, Aachen, Germany, 2009.

[180] S. Wesselmecking, L. Tataurova, W. Bleck, Digital image correlation (DIC) analysis of temperature and strain rate influence on the serrated flow behaviour of high-Mn steels, in: M.M.S. The Minerals (Ed.) Advanced High-strength Steels, TMS Annual Meeting & Exhibition, Springer International Publishing, Pheonix, Arizona, USA, 2018.

[181] H. Wenk, P. Van Houtte, Texture and anisotropy, Reports on Progress in Physics 67(8) (2004) 1367.

[182] Y.N. Wang, J.C. Huang, Texture analysis in hexagonal materials, Materials Chemistry and Physics 81(1) (2003) 11-26.

[183] S. Suwas, R.K. Ray, Crystallographic texture of materials, Springer-Verlag London, London, United Kingdom, , 2014.

[184] R.E. Smallman, D. Green, The dependence of rolling texture on stacking fault energy, Acta Metallurgica 12(2) (1964) 145-154.

[185] J. Hirsch, K. Lücke, M. Hatherly, Overview No. 76: Mechanism of deformation and development of rolling textures in polycrystalline fcc Metals—III. The influence of slip inhomogeneities and twinning, Acta Metallurgica 36(11) (1988) 2905-2927.

[186] A. Weidner, P. Klimanek, Shear banding and texture development in cold-rolled α-brass, Scripta Materialia 38(5) (1998) 851-856.

[187] A.A. Gazder, A.A. Saleh, E.V. Pereloma, Microtexture analysis of cold-rolled and annealed twinning-induced plasticity steel, Scripta Materialia 65(6) (2011) 560-563.

[188] K.H. Oh, J.S. Jeong, Y.M. Koo, D.N. Lee, The evolution of the rolling and recrystallization textures in cold-rolled Al containing high Mn austenitic steels, Materials Chemistry and Physics 161 (2015) 9-18.

[189] P.H. Chapellier, R.K. Ray, J.J. Jonas, Prediction of transformation textures in steels, Acta Metallurgica et Materialia 38(8) (1990) 1475-1490.

[190] R.D. Doherty, Recrystallization and texture, Progress in Materials Science 42(1–4) (1997) 39-58.

[191] M.C. Somani, P. Juntunen, L.P. Karjalainen, R.D.K. Misra, A. Kyröläinen, Enhanced mechanical properties through reversion in metastable austenitic stainless steels, Metallurgical and Materials Transactions A 40(3) (2009) 729-744.

[192] S.G. Chowdhury, S. Datta, B.R. Kumar, P. De, R. Ghosh, Randomization of texture during recrystallization of austenite in a cold rolled metastable austenitic stainless steel, Materials Science and Engineering: A 443(1-2) (2007) 114-119.

[193] G.E. Dieter, Mechanical metallurgy, McGraw-Hill, Singapore, , 1976.

[194] J. Mahieu, B. De Cooman, J. Maki, Phase transformation and mechanical properties of Si-free CMnAl transformation-induced plasticity-aided steel, Metallurgical and Materials Transactions A 33(8) (2002) 2573-2580.

[195] B.J. Davis, The effect of separations on the assessment of charpy impact tests, PhD Thesis, School of Mechanical, Materials, and Mechatronic, and Biomedical Engineering, University of Wollongong, Wollongong, Australia, 2017.

[196] Quantax EBSD manual, in: Bruker (Ed.) Bruker Nano GmBH, Berlin.

[197] A.A. Gazder, F. Al-Harbi, H.T. Spanke, D.R. Mitchell, E.V. Pereloma, A correlative approach to segmenting phases and ferrite morphologies in transformation-induced plasticity steel using electron back-scattering diffraction and energy dispersive X-ray spectroscopy, Ultramicroscopy 147 (2014) 114-132.

[198] G. Palumbo, K. Aust, Structure-dependence of intergranular corrosion in high purity nickel, Acta Metallurgica et Materialia 38(11) (1990) 2343-2352.

[199] J.J. Fundenberger, B. Beausir, JTEX software for texture analysis, University de Lorraine-Mtez, 2015.

[200] M.H. Alvi, S. Cheong, H. Weiland, A.D. Rollett, Recrystallization and texture development in hot rolled 1050 aluminum, Materials Science Forum 467-470 (2004) 357-362.

[201] A.A. Gazder, M. Sánchez-Araiza, J.J. Jonas, E.V. Pereloma, Evolution of recrystallization texture in a 0.78 wt.% Cr extra-low-carbon steel after warm and cold rolling, Acta Materialia 59(12) (2011) 4847-4865.

[202] J.M.M. Pérez, J. Pascau, Image processing with ImageJ, Packt Publishing, 2013.

[203] C.A. Schneider, W.S. Rasband, K.W. Eliceiri, NIH Image to ImageJ: 25 years of image analysis, Nature methods 9(7) (2012) 671-675.

[204] D.R.G. Mitchell, B. Schaffer, Scripting-customised microscopy tools for Digital Micrograph™, Ultramicroscopy 103(4) (2005) 319-332.

[205] L.C. Chang, H.K.D.H. Bhadeshia, Austenite films in bainitic microstructures, Materials Science and Technology 11(9) (1995) 874-882.

[206] D.R.G. Mitchell, DiffTools: electron diffraction software tools for DigitalMicrograph™, Microscopy Research and Technique 71(8) (2008) 588-593.

[207] P.A. Stadelmann, EMS - a software package for electron diffraction analysis and HREM image simulation in materials science, Ultramicroscopy 21(2) (1987) 131-145.

[208] T.W. Duerig, J. Albrecht, D. Richter, P. Fischer, Formation and reversion of stress induced martensite in Ti-10V-2Fe-3Al, Acta Metallurgica 30(12) (1982) 2161-2172.

[209] D.B. Santos, A.A. Saleh, A.A. Gazder, A. Carman, D.M. Duarte, É.A. Ribeiro, B.M. Gonzalez, E.V. Pereloma, Effect of annealing on the microstructure and mechanical properties of cold rolled Fe–24Mn–3Al–2Si–1Ni–0.06 C TWIP steel, Materials Science and Engineering: A 528(10) (2011) 3545-3555.

[210] U.F. Kocks, H. Mecking, Physics and phenomenology of strain hardening: the FCC case, Progress in Materials Science 48(3) (2003) 171-273.

[211] S. Vercammen, B. Blanpain, B.C. De Cooman, P. Wollants, Cold rolling behaviour of an austenitic Fe–30Mn–3Al–3Si TWIP-steel: the importance of deformation twinning, Acta Materialia 52(7) (2004) 2005-2012.

[212] X. Li, L. Chen, Y. Zhao, R.D.K. Misra, Influence of manganese content on ε-/α′-martensitic transformation and tensile properties of low-C high-Mn TRIP steels, Materials & Design 142 (2018) 190-202.

[213] A.A. Saleh, E.V. Pereloma, A.A. Gazder, Microstructure and texture evolution in a twinning-induced-plasticity steel during uniaxial tension, Acta Materialia 61(7) (2013) 2671-2691.

[214] J.H. Yang, C.M. Wayman, On secondary variants formed at intersections of ϵ martensite variants, Acta Metallurgica et Materialia 40(8) (1992) 2011-2023.

[215] J. Brooks, M. Loretto, R. Smallman, In situ observations of the formation of martensite in stainless steel, Acta Metallurgica 27(12) (1979) 1829-1838.

[216] X.S. Yang, S. Sun, H.H. Ruan, S.Q. Shi, T.Y. Zhang, Shear and shuffling accomplishing polymorphic fcc γ → hcp ε → bct α martensitic phase transformation, Acta Materialia 136 (2017) 347-354.

[217] E.I. Galindo-Nava, P.E.J. Rivera-Díaz-del-Castillo, Understanding martensite and twin formation in austenitic steels: A model describing TRIP and TWIP effects, Acta Materialia 128 (2017) 120-134.

[218] K. Guy, E.P. Butler, D.R.F. West, ε and α' martensite formation and reversion in austenitic stainless steels, Le Journal de Physique Colloques 43(C4) (1982) 575-580.

[219] S. Sandlöbes, M. Friák, S. Zaefferer, A. Dick, S. Yi, D. Letzig, Z. Pei, L.F. Zhu, J. Neugebauer, D. Raabe, The relation between ductility and stacking fault energies in Mg and Mg–Y alloys, Acta Materialia 60(6) (2012) 3011-3021.

[220] B. Li, E. Ma, Pyramidal slip in magnesium: dislocations and stacking fault on the {1011} plane, Philosophical Magazine 89(14) (2009) 1223-1235.

[221] H. Yu, Q. Dong, Z. Yao, M.R. Daymond, Stacking faults observed in {101−2} extension twins in a compressed high Sn content Zr alloy, Scripta Materialia 141(Supplement C) (2017) 72-75.

[222] D.B. Williams, C.B. Carter, Transmission electron microscopy: a textbook for materials science, Springer, 2009.

[223] C. Hitzenberger, H. Karnthaler, A. Korner, In situ TEM study of the hcp to fcc martensitic phase transformation in CoNi single crystals, Acta Metallurgica 36(10) (1988) 2719-2728.

[224] A.A. Gazder, A.A. Saleh, A.G. Kostryzhev, E.V. Pereloma, Application of transmission Kikuchi diffraction to a multi-phase TRIP-TWIP steel, Mater. Today: Proc. 2(Supplement 3) (2015) S647-S650.

[225] N. Nakada, T. Tsuchiyama, S. Takaki, D. Ponge, D. Raabe, Transition from diffusive to displacive austenite reversion in low-alloy steel, ISIJ International 53(12) (2013) 2275-2277.

[226] R. Abbaschian, L. Abbaschian, R.E. Reed-Hill, Physical metallurgy principles, 4th edition, Cengage Learning, USA, 2008.

[227] F.S. Buffington, K. Hirano, M. Cohen, Self diffusion in iron, Acta Metallurgica 9(5) (1961) 434-439.

[228] H. Bibring, G. Lenior, F. Sebilieau, Rev. Metall. 56 (1959) 279.

[229] J.A. Klostermann, W.G. Burgers, Surface martensite in iron-nickel, Acta Metallurgica 12(4) (1964) 355-360.

[230] J. Pak, D.W. Suh, H.K.D.H. Bhadeshia, Displacive phase transformation and surface effects associated with confocal laser scanning microscopy, Metallurgical and Materials Transactions A 43(12) (2012) 4520-4524.

[231] B.B. He, M.X. Huang, A.H.W. Ngan, S. Van Der Zwaag, Effect of free surface on the stability of individual retained austenite grains in a duplex stainless steel, Metall. Trans. A 45(11) (2014) 4875-4881.

[232] J.D. Escobar, G.A. Faria, L. Wu, J.P. Oliveira, P.R. Mei, A.J. Ramirez, Austenite reversion kinetics and stability during tempering of a Ti-stabilized supermartensitic stainless steel: Correlative in situ synchrotron x-ray diffraction and dilatometry, Acta Mater. 138 (2017) 92-99.

[233] A. Bojack, L. Zhao, P.F. Morris, J. Sietsma, In-situ determination of austenite and martensite formation in 13Cr6Ni2Mo supermartensitic stainless steel, Mater. Charact. 71 (2012) 77-86.

[234] S. Kajiwara, Nearly perfect shape memory effect in Fe–Ni–C alloys, Trans. Japan Int. Met. 26(8) (1985) 595-596.

[235] A. Gilbert, W.S. Owen, Diffusionless transformation in iron-nickel, iron-chromium and iron-silicon alloys, Acta Metallurgica 10(1) (1962) 45-54.

[236] Y. Tomota, N. Sekido, S. Harjo, T. Kawasaki, W. Gong, A. Taniyama, In situ observations of transformation behavior upon heating for a 1.5Mn-1.5Si-0.2C steel -comparison between neutron diffraction, XRD, EBSD and dilatometry, ISIJ International 57(12) (2017) 2240-2247.

[237] J.-H. Jun, C.-S. Choi, Variation of stacking fault energy with austenite grain size and its effect on the MS temperature of γ→ε martensitic transformation in Fe–Mn alloy, Materials Science and Engineering: A 257(2) (1998) 353-356.

[238] M.H. Razmpoosh, A. Zarei-Hanzaki, N. Haghdadi, J.-H. Cho, W.J. Kim, S. Heshmati-Manesh, Thermal stability of an ultrafine-grained dual phase TWIP steel, Materials Science and Engineering: A 638 (2015) 5-14.

[239] B.P. Kashyap, K. Tangri, Grain growth behaviour of type 316L stainless steel, Materials Science and Engineering: A 149(2) (1992) L13-L16.

[240] L. Kaufman, Coupled phase diagrams and thermochemical data for transition metal binary systems-III, Calphad 2(2) (1978) 117-146.

[241] F. Lu, P. Yang, L. Meng, F. Cui, H. Ding, Influences of thermal martensites and grain orientations on strain-induced martensites in high Manganese TRIP/TWIP steels, Journal of Materials Science & Technology 27(3) (2011) 257-265.

[242] R.K. Ray, J.J. Jonas, M.P. Butrón-Guillén, J. Savoie, Transformation textures in steels, ISIJ International 34(12) (1994) 927-942.

[243] Y.-U. Heo, D.H. Kim, N.H. Heo, C.W. Hong, S.-J. Kim, Deformation behavior in medium Mn steel of nanometer-sized α′+ γ lamellar structure, Metallurgical and Materials Transactions A 47(12) (2016) 6004-6016.

[244] T. Ogawa, M. Koyama, C.C. Tasan, K. Tsuzaki, H. Noguchi, Effects of martensitic transformability and dynamic strain age hardenability on plasticity in metastable austenitic steels containing carbon, Journal of Materials Science 52(13) (2017) 7868-7882.

[245] S. Münstermann, Y. Feng, W. Bleck, Influencing parameters on elastic modulus of steels, Canadian Metallurgical Quarterly 53(3) (2014) 264-273.

[246] Y. Tomota, M. Strum, J.W. Morris, Microstructural dependence of Fe-high Mn tensile behavior, Metallurgical Transactions A 17(3) (1986) 537-547.

[247] H. Luo, H. Dong, M. Huang, Effect of intercritical annealing on the Lüders strains of medium Mn transformation-induced plasticity steels, Materials & Design 83 (2015) 42-48.

[248] X. Wang, L. Wang, M. Huang, In-situ evaluation of Lüders band associated with martensitic transformation in a medium Mn transformation-induced plasticity steel, Materials Science and Engineering: A 674 (2016) 59-63.

[249] D. Jiang, S. Kyriakides, C.M. Landis, K. Kazinakis, Modeling of propagation of phase transformation fronts in NiTi under uniaxial tension, European Journal of Mechanics - A/Solids 64 (2017) 131-142.

[250] F. Yang, H. Luo, E. Pu, S. Zhang, H. Dong, On the characteristics of Portevin–Le Chatelier bands in cold-rolled 7Mn steel showing transformation-induced plasticity, International Journal of Plasticity 103 (2018) 188-202.

[251] R.L. Bell, R.W. Cahn, The dynamics of twinning and the interrelation of slip and twinning in zinc crystals, Proceedings of the Royal Society of London A 239(1219) (1957) 494-521.

[252] E.V. Pereloma, F. Al-Harbi, A.A. Gazder, The crystallography of carbide-free bainites in thermo-mechanically processed low Si transformation-induced plasticity steels, Journal of Alloys and Compounds 615 (2014) 96-110.

[253] S.K. Mishra, S.M. Tiwari, A.M. Kumar, L.G. Hector, Effect of strain and strain path on texture and twin development in austenitic steel with Twinning-Induced plasticity, Metallurgical and Materials Transactions A 43(5) (2012) 1598-1609.

[254] A.A. Saleh, E.V. Pereloma, B. Clausen, D.W. Brown, C.N. Tomé, A.A. Gazder, Self-consistent modelling of lattice strains during the in-situ tensile loading of twinning induced plasticity steel, Materials Science and Engineering: A 589(Supplement C) (2014) 66-75.

[255] A.T. English, G.Y. Chin, On the variation of wire texture with stacking fault energy in f.c.c. metals and alloys, Acta Metallurgica 13(9) (1965) 1013-1016.

[256] P. Yang, T.Y. Liu, F.Y. Lu, L. Meng, Orientation dependence of martensitic transformation in high Mn TRIP/TWIP steels, Steel Research International 83(4) (2012) 368-373.

[257] J. Han, A.K. da Silva, D. Ponge, D. Raabe, S.M. Lee, Y.K. Lee, S.I. Lee, B. Hwang, The effects of prior austenite grain boundaries and microstructural morphology on the impact toughness of intercritically annealed medium Mn steel, Acta Materialia 122 (2017) 199-206.

[258] H. Choi, S. Lee, J. Lee, F. Barlat, B.C. De Cooman, Characterization of fracture in medium Mn steel, Materials Science and Engineering: A 687 (2017) 200-210.

[259] A.S. Hamada, L.P. Karjalainen, M.C. Somani, The influence of aluminum on hot deformation behavior and tensile properties of high-Mn TWIP steels, Materials Science and Engineering: A 467(1) (2007) 114-124.

[260] E. Bayraktar, F.A. Khalid, C. Levaillant, Deformation and fracture behaviour of high Manganese austenitic steel, Journal of Materials Processing Technology 147(2) (2004) 145-154.

[261] J. Lorthios, M. Mazière, X. Lemoine, P. Cugy, J. Besson, A.-F. Gourgues-Lorenzon, Fracture behaviour of a Fe–22Mn–0.6 C–0.2 V austenitic TWIP steel, International Journal of Mechanical Sciences 101 (2015) 99-113.

[262] Z.C. Luo, M.X. Huang, Revealing the fracture mechanism of Twinning Induced Plasticity steels, Steel Research International (2018) doi.org/10.1002/srin.201700433.

[263] E. Aerts, P. Delavignette, R. Siems, S. Amelinckx, Stacking fault energy in silicon, Journal of Applied Physics 33(10) (1962) 3078-3080.

[264] T. Gebhardt, D. Music, D. Kossmann, M. Ekholm, I.A. Abrikosov, L. Vitos, J.M. Schneider, Elastic properties of fcc Fe–Mn–X (X = Al, Si) alloys studied by theory and experiment, Acta Materialia 59(8) (2011) 3145-3155.

[265] A.A. Saleh, E.V. Pereloma, B. Clausen, D.W. Brown, C.N. Tomé, A.A. Gazder, On the evolution and modelling of lattice strains during the cyclic loading of TWIP steel, Acta Materialia 61(14) (2013) 5247-5262.

[266] Z. Pei, L.-F. Zhu, M. Friák, S. Sandlöbes, J. von Pezold, H.W. Sheng, C.P. Race, S. Zaefferer, B. Svendsen, D. Raabe, Ab initio and atomistic study of generalized stacking fault energies in Mg and Mg–Y alloys, New Journal of Physics 15(4) (2013) 043020.

[267] S.L. Wong, M. Madivala, U. Prahl, F. Roters, D. Raabe, A crystal plasticity model for twinning- and transformation-induced plasticity, Acta Materialia 118 (2016) 140-151.

[268] R.M. Martin, Relation between elastic tensors of wurtzite and zinc-blende structure materials, Physical Review B 6(12) (1972) 4546-4553.

[269] E.R. Fuller, W.F. Weston, Relation between elastic-constant tensors of hexagonal and cubic structures, Journal of Applied Physics 45(9) (1974) 3772-3776.

[270] N. Chetty, M. Weinert, Stacking faults in magnesium, Physical Review B 56(17) (1997) 10844-10851.